Universidade do Minho
Escola de Ciências

Patrícia Daniela Cabral da Silva

Immuno-Field-Effect Tansistor Platforms Based on 2D Materials for Early Detection of Biomarkers of Ischemic Stroke

dezembro de 2021

Immuno-Field-Effect Tansistor Platforms Based on 2D Materials for Early Detection of Biomarkers of Ischemic Stroke

Patrícia Daniela Cabral da Silva

UMinho | 2021

Universidade do Minho
Escola de Ciências

Patrícia Daniela Cabral da Silva

Immuno-Field-Effect Tansistor Platforms Based on 2D Materials for Early Detection of Biomarkers of Ischemic Stroke

Doctoral Thesis
Doctoral Program in Physics

Work supervised by
Professor DoutorJoão Pedro Santos Hall A. Alpuim
Doutora Elisabete Ramos Fernandes

dezembro de 2021

DIREITOS DE AUTOR E CONDIÇÕES DE UTILIZAÇÃO DO TRABALHO POR TERCEIROS

ACKNOWLEDGMENTS

First of all, I would like to acknowledge my supervisors João Pedro Santos Hall A. Alpuim and Elisabete Ramos Fernandes for the patience, support and fruitful work discussions. They were always present to make this project happen and to motivate me to continue every day.

I would also like to acknowledge all the team of the 2D Materials group at INL with which I shared a lot of my time both for work and for leisure. In particular, I acknowledge Jérôme Borme who was my very helpful mentor in the clean-room, always ready to help me to improve my work.

To Fátima Cerqueira, for all the help and lessons on Raman spectroscopy.

To George Machado Jr. and Cláudia Coelho for the friendship and the help in the characterization of the graphene field-effect transistors.

To Marco Martins and Ivo Colmiais for providing the acquisition system for transistor measurements and the availability to help in the never-ending problems that appeared.

To the Nanodevices group, in particular Elisabete Fernandes and Briliant Prabowo, for the opportunity to collaborate and learn more about microfluidic devices and sample processing.

To INL for the amazing facilities and people who helped me through my PhD.

To FCT for the funding through the PhD scholarship SFRH/BD/128579/2017 and Covid extension funding COVID/BD/151846/2021.

To MAP-Fis for the opportunity to learn more and know students with different backgrounds and experiences.

To all my friends which helped lighten the mood in the most difficult times of the PhD and were always ready for good laughs and out of this world discussions.

My final thanks are to my family and my beloved cat which supported and bared with me through these years, in particular to my husband, Daniel, who has been my rock during this time.

STATEMENT OF INTEGRITY

I hereby declare having conducted this academic work with integrity. I confirm that I have not used plagiarism or any form of undue use of information or falsification of results along the process leading to its elaboration.

I further declare that I have fully acknowledged the Code of Ethical Conduct of the University of Minho.

RESUMO

A deteção precoce de biomarcadores clinicamente relevantes é um dos principais desafios no diagnostico de doenças. Os avanços mais recentes na microeletrónica abriram caminho para o desenvolvimento de biossensores eletrónicos, em que é possível alcançar dispositivos de elevada sensibilidade e velocidade. Em particular, os biossensores baseados em transístores de efeito de campo têm potencial para a miniaturização e integração em processos de fabricação eletrónica, ao mesmo tempo permitindo deteção rápida, paralela e sem marcação. Este potencial pode ser explorado para desenvolver ferramentas de diagnostico mais eficazes para a avaliação de pacientes de AVC isquémico. O AVC isquémico é uma das maiores causas de morte e incapacidade no mundo e a aplicação de tratamento é condicionada pelo curto espaço de tempo em que o tratamento com o Ativador do plasminogénio tecidual pode ser aplicado. Assim sendo, o desenvolvimento de um biossensor para analise rápida do estado do paciente pode proporcionar estratificação para a aplicação terapêutica atempada, podendo aumentar o número de pacientes tratados e reduzindo o risco de transformação hemorrágica nos pacientes tratados.

Com esta problemática em mente, o trabalho apresentado focou-se no desenvolvimento de transístores de efeito de campo baseados em materiais 2D para a deteção de biomarcadores relevantes para a estratificação de pacientes com AVC isquémico. Transístores de efeito de campo com grafeno como material do canal foram testados e otimizados para interação com biomoléculas. A transferência de grafeno e passivação dos contactos foi otimizada para fornecer transístores de efeito de campo compatíveis com a funcionalização de superfícies e bio reconhecimento de proteínas. A funcionalização do grafeno foi estudada, garantindo a consistência do método, a estabilidade dos anticorpos imobilizados e a redução de ligações não-especificas. Os transístores funcionalizados foram testados com proteínas standard para estudar o mecanismo de deteção. Os testes realizados com as proteínas biomarcadoras de AVC isquémico, Matrix Metallopeptidase 9 e Fibronectina celular, mostraram potencial para a deteção simultânea dos biomarcadores graças à ausência de interação cruzada entre eles. A exposição dos dispositivos à matriz biológica de interesse revelou que é possível detetar especificamente os biomarcadores em amostras de soro diluído, no entanto em amostras mais complexas algumas limitações surgem devido à ocorrência de eventos de ligação não-especifica. Além disso, a reprodutibilidade dos transístores mesmo não sendo perfeita (11% intra e 26% inter variabilidade) revela um grande potencial para a continuação do desenvolvimento desta tecnologia para a deteção rápida de biomarcadores de AVC isquémico para a estratificação de pacientes.

Palavras-chave: AVC Isquémico, Biomarcadores, Biossensor, Materiais 2D, Transístores de Efeito de Campo

ABSTRACT

Early detection of clinically relevant biomarkers (proteins, DNA, or others) is nowadays considered the holy grail of diagnostics for modern medicine. The recent advancements in micro-electronics have opened the path for bioelectronics-based sensors, where devices of greatly improved sensitivity and speed of detection are achieved. In particular, biosensors based on field-effect transistors hold the potential for miniaturization and integration in electronic manufacturing processes while allowing parallel label-free sensing and fast response times. This potential can be explored to develop practical diagnostic tools for evaluating ischemic stroke patients. Acute ischemic stroke is a leading cause of death and disability worldwide, and treatment is still conditioned due to the narrow time window of intravenous thrombolysis with tissue plasminogen activator (tPA). As such, developing a biosensing tool for fast analysis of the condition of ischemic stroke patients can provide stratification for therapy application, potentially increasing the number of treated patients and reducing the risk of hemorrhagic transformation.

With this in mind, the focus of this work was the development of 2D material-based field-effect transistors for the detection of biomarkers clinically relevant to the stratification of ischemic stroke patients. Field-effect transistors using graphene as the channel material were tested and optimized for selective biomolecular recognition. Graphene transfer and contact passivation were optimized using clean-room processes to provide field-effect transistors compatible with surface functionalization and bio-recognition. Graphene functionalization was studied to ensure a consistent method for stable immobilization of probe antibodies and reduction of non-specific binding. The functionalized graphene field-effect transistors were tested against standard protein biomarkers to access the detection mechanism. The tests performed with stroke protein biomarkers, Matrix Metallopeptidase 9, and cellular Fibronectin showed great potential for their simultaneous detection due to the absence of cross-reactivity between these proteins.

The graphene field-effect transistors exposure to the interest biological sample matrix (human serum) revealed that specific detection could be achieved in diluted serum samples. However, some limitations arise in more complex samples (raw serum) due to non-specific binding events. Moreover, although not perfect, the reproducibility of the measurements (11% intra-variability and 26% inter-variability) shows the great potential to further develop this technology for fast and label-free detection of ischemic stroke-related biomarkers patient stratification.

Key-words: Ischemic Stroke, Biomarkers, Biosensor, 2D Materials, Field-Effect Transistors

Table of Contents

Figures Index

Tables Index

Acronyms List

2D – Bidimensional; AFM – Atomic Force Microscopy; ALD – Atomic layer deposition ;APTES - (3-Aminopropyl)triethoxysilane; BE – Binding Energy; BSA – Bovine Serum Albumin; c-Fn – cellular Fibronectin; CV – Variation coefficient; CVD – Chemical vapor deposition; DMF – Dimethylformamide; DNA – desoxyribonucleic acid; DOS – Density of states; DR – Dynamic range; ECR – Electron cyclotron resonance; EDL – Electrical double layer; EDX – Energy-dispersive X-ray spectroscopy; EG- – Electrolyte-gated; ETA – Ethanolamine; FET – Field-effect transistor; HOPG – Highly oriented pyrolytic graphite; HT – Hemorrhagic transformation; ICP – Inductively coupled plasma; ISFET – ion-sensitive FET; I_{SD} – Source-drain current; L – length; LoB – Limit of blank; LoD - Limit of detection; LPE – Liquid-phase exfoliation; MMP9 – Matrix metallopeptidase 9; MOS – Metal–oxide semiconductor; NHS-ester - N-Hydroxysuccinimide Ester; NW – Nanowire; PBSE - 1-pyrenebutyric acid n-hydroxysuccinimide ester; PMMA - Poly(methyl methacrylate); PoC – Point-of-care; QCM – Quartz crystal microbalance; R – resistance; rGO – reduced Graphene Oxide; RIE – Reactive ion etching; SLG – single-layer graphene; TMAH - Tetramethylammonium hydroxide; TMDC – transition metal dichalcogenide; tPA - tissue plasminogen activator; V_{CNP} – Charge neutrality point voltage; V_G – gate voltage; V_{SD} – source-drain voltage; V_{TH} – Threshold voltage; XPS - X-ray photoelectron spectroscopy; W – width.

Chapter I

1. Introduction

The last decades of diagnostics research witnessed a tremendous effort invested in developing new and improved diagnostics systems for healthcare. The development of new devices for the bioanalytical study of relevant biomarkers for clinical diagnosis [1–4] has made biosensors research a growing and multidisciplinary field, requiring knowledge of physics, biology, chemistry, materials science, and engineering [1,5]. Biosensors can be defined as devices that integrate biorecognition elements and transducers to provide qualitative or quantitative information regarding a specific bio-analyte, such as a protein, a nucleic acid (DNA or RNA), a cell, or another small biomolecule [1,2].

In short, a biosensor is composed of a recognition layer (probe) that provides specificity to the desired target. A transducer layer converts the probe-target interaction into a measurable signal [1,6] that can then be processed to provide the relevant information regarding the pathology under study. The variety of elements that can compose the biosensor layers is illustrated in Scheme 1.

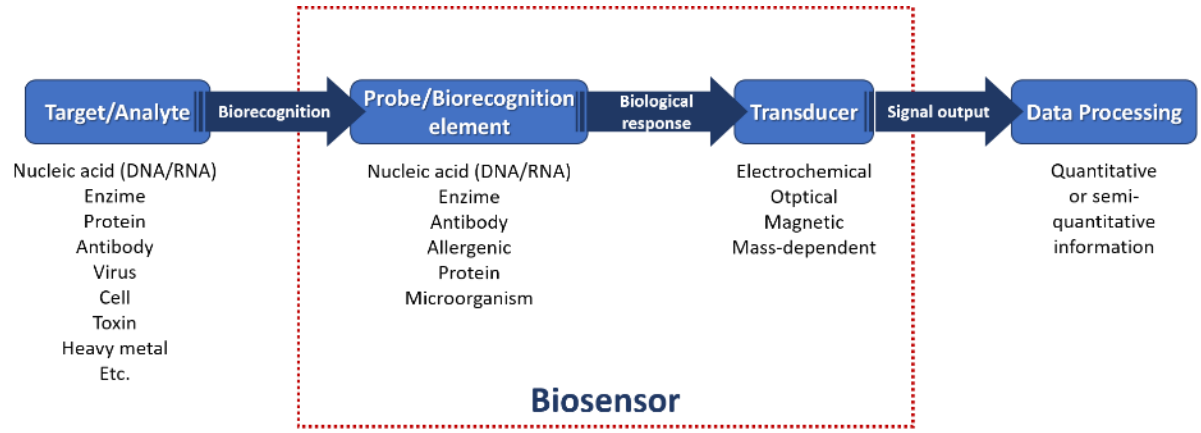

Scheme 1. *A sequence of detection of an analyte for clinically relevant information. The multitude of elements that can be used both for biorecognition of the analyte and transduction of this interaction shows how rich and adaptable is the biosensing research field. Adapted from [1].*

When the probe-target interaction is an immunogenic reaction (antibody-antigen), the biosensor can be designated as an immunosensor. The use of such reactions in bioanalytical detection is relatively mature, being widely used in laboratory immunoassays with excellent specificity [2]. Methods such as enzyme-linked immunosorbent assays (ELISA) have provided considerable support for clinical diagnosis [2]. However, these methodologies require the use of specialized personnel, labeling of the targets (source of instability), and extensive protocols that render the methods difficult [7] and therefore impossible to

implement for the quick analysis often required in clinical applications [2]. The development of new technologies and methods for biosensing systems is key to enhancing clinical diagnostics and improving healthcare [2,3].

Biosensors can be classified according to the detection methodology into label-based and label-free. Label-based biosensors perform detection using characteristics inherent to the label, be it fluorescence, magnetism, or other. Label-free systems perform detection using characteristics of the target itself or of the probe-target interaction, which can be a mass change [8–10], optical properties [7,11,12], and electrical properties [3,7,10], among others [7]. Label-based systems can be advantageous for detection in complex matrices [13], but labels can induce changes in the probe-target interaction impairing the sensing capability [3,7]. Besides, labeling of the target molecule introduces additional sample processing steps that hinder applicability for fast detection required in many clinical applications [3,7]. As such, label-free methods have gained much attention in recent years, mainly with the incorporation of nanomaterials/nanotechnology in the transduction systems that pushed biosensors to new boundaries [3,7], allowing high-sensitivity, low sample consumption, reduced interference with the bio-analytes, portability, and automation of the detection systems [3,7].

In particular, label-free biosensors based on electronic transduction have become very popular thanks to their inherent advantages [3,5,13]. The use of electronic components for signal transduction allows for fast and straightforward signal acquisition with potential for integration with existing technologies for data acquisition and processing [5,13,14], facilitating the incorporation in miniaturized systems [5,13–15], meaning these systems can be easily adapted for point-of-care (PoC) applications. The production of miniaturized devices also allows for implementing multiple devices in a small area, improving reliability and signal stability, and allowing for multiple target detection, i.e., multiplex biosensors [14].

One of the most promising systems for electronic transduction of biorecognition events (probe-target interaction) is based on field-effect transistors (FETs) [3,6,7]. These charge-sensitive devices are considered ideal for the development of PoC systems [3] due to their real-time response to changes in their surface dielectric environment [3,7] and ease of miniaturization [6] that allow for cost-effective fabrication, integration with other electronic components, and small sample volumes [3]. Additionally, surface-based sensors with electronic transduction can achieve specificity and selectivity without target labeling [3,6]. In particular, 2D material-based FETs have been proposed to develop ultra-sensitive biosensors due to the extremely high surface ratios and the possibility of exposing such materials directly to the biological sample [3,6,7], enhancing sensitivity and response time.

In the following sections, FETs' working principles as biosensors are discussed (section 1.1), focusing on the use of 2D materials (section 1.2) and their application to a clinical condition (section 1.3). Later, 2D materials in biosensing are discussed in section 2 (State of the Art) of this chapter.

1.1. Field-Effect Transistors

1.1.1. Operation principles

Field-effect transistors are the most frequently used electronic transducers for biosensing [7] and respond to the changes in the gate dielectric environment induced by charged biomolecules via modulation of the charge carriers in the transistor channel [3,6,14,16]. This mechanism directly converts the biorecognition event into an electrical signal, allowing for real-time detection with high sensitivity and selectivity [3].

In a typical FET structure, the electrical current flows through a conductive channel that connects the source and drain electrodes, as shown in Figure 1. A voltage applied to a third electrode, the gate, modulates the conductance between these two electrodes. In a metal-insulator-semiconductor (MOS) FET, gate voltage couples capacitively to the channel through a solid dielectric layer [3,17,18], controlling the charge distributions at the semiconductor/dielectric interface, which can be accumulation, depletion, and inversion. MOSFET devices typically work in enhancement mode, where the channel consists of an inversion layer. For example, take an n-channel MOSFET, built in a p-doped wafer with n^+ implanted source and drain contacts. Applying a small positive gate voltage results in charge carrier depletion in the channel, decreasing the conductivity. However, increasing the gate voltage to more positive values will form a thin conductive inversion layer, the n-channel [3]. Because the n^+ contacts are blocking for holes, the device will conduct (turn ON) only when the inversion layer forms. The transistor electrical characteristics can be accessed by a transfer curve, which shows the current between the source and drain electrodes (I_{DS}) as a function of the gate voltage (V_G) for a fixed drain-source voltage (V_{DS}).

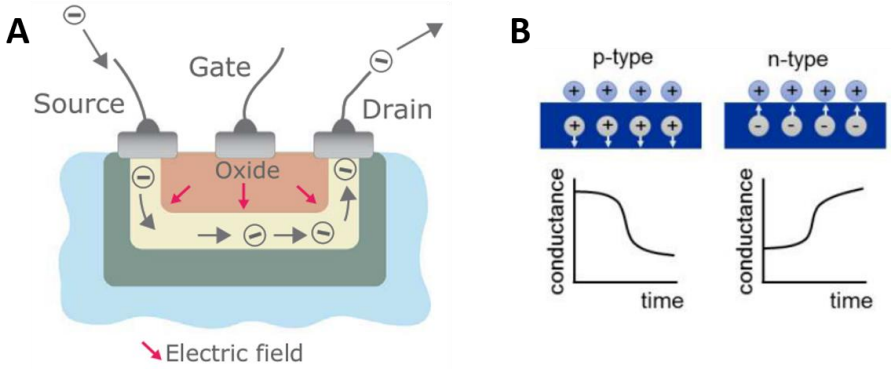

Figure 1. *Typical configuration of a Field-effect Transistor and effect of charged elements in its properties. (A) A solid-gated FET is shown, with arrows schematically depicting current flow between the source and drain electrodes. (B) Result of modulation of the channel conductance by applying positive voltage via gating on p-type or n-type channels. Adapted from [3,14].*

If an aqueous solution replaces the solid gate dielectric (Figure 2A), the ions in the solution can provide the capacitance required to couple the gate voltage to the electrostatic channel potential [17]. In which case, we speak of a liquid-gate FET. The possibility of using liquids for channel conductance modulation [3,7] allows for using FETs as biosensors with liquid samples, such as saline buffers, plasma, blood, saliva, and others, where the biomolecules are more stable [3]. In electrolyte-gated FETs (EG-FETs), the conductance between source and drain electrodes is modulated by the electrolyte whenever voltage is applied to a reference electrode (here-on called gate) [3]. The gate voltage modulates the thickness of electrical double layers (EDLs) at the gate/electrolyte and electrolyte/semiconductor interfaces.

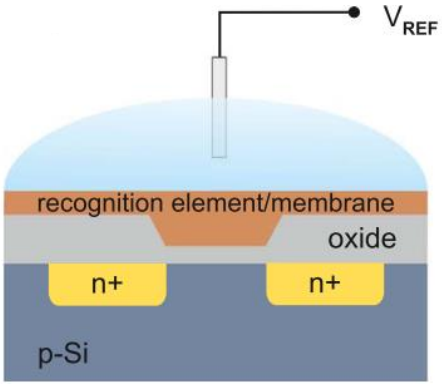

(A)

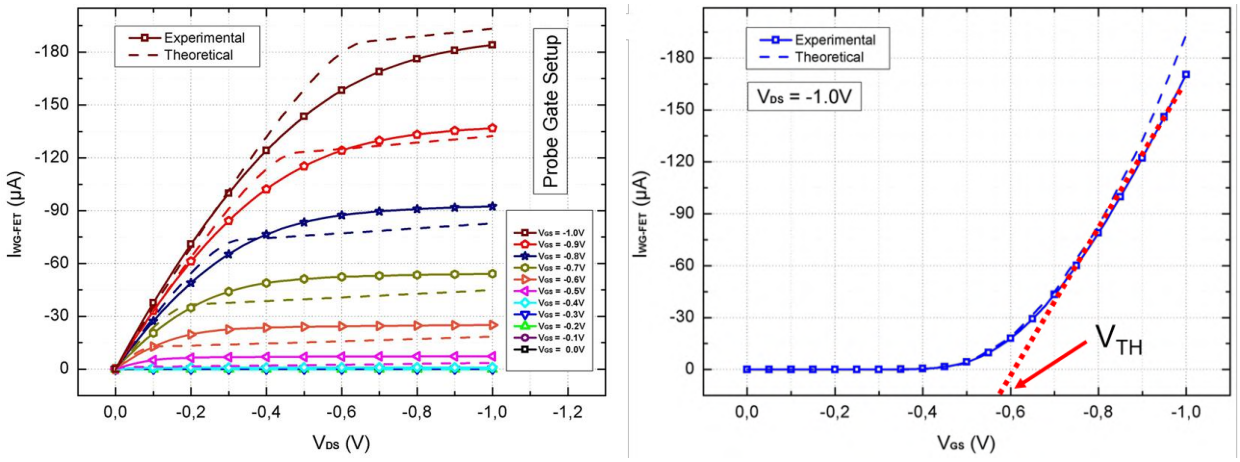

(B) (C)

Figure 2. *Typical metal-oxide FET (MOSFET) with an electrolyte and a reference gate electrode, replacing the traditional solid gate (A). (B) Typical I-V curve obtained for different values of applied gate-source voltage. (C) Transistor transfer curve obtained for a fixed drain-source voltage showing the threshold voltage (V_{TH}) at which the conduction of charge carriers begins. Adapted from [14,19].*

Applying a small gate potential disrupts the equilibrium at the space-charge regions and forces a redistribution of the ions and dipoles at the interface within the EDLs, expanding or contracting them [6]. The first layer to be considered is the stationary layer, or Stern layer, formed by counterions firmly bound to the solvated electrode surface [6]. This layer acts as a solid dielectric, and the electric potential decreases linearly with the distance from the electrode surface, as shown in Figure 3A (right-side region of the electrolyte). After the stationary layer, the counter- and co-ions enter a diffusive regime, where ion concentration is dependent on the distance to the electrolyte/electrode interface [6]. In the diffusive layer, counter and co-ions concentrations follow Maxwell-Boltzmann statistics, and the electric potential profile can be found by solving the Poisson-Boltzmann equation [20] (Figure 3A, central region of the electrolyte). At a small distance from the electrode surface, which depends on the electrolyte ionic strength, we reach the electrolyte bulk where the solution is neutral [6] Figure 3A, left-side region of the electrolyte). At the boundary between the diffusive layer and the solution bulk, the potential reaches e^{-1} of its interface value [6]. Detection of charged analytes can only occur within the layers where the electrolyte interacts with the solid surface, meaning it occurs within the stationary and diffusive layers [6] (Figure 3A, Debye layer). The distance that goes from the surface to the boundaries of the diffusive layer is often referred to as Debye length [6] and defines the longest distance at which an analyte can influence the semiconductor channel characteristics [3,6].

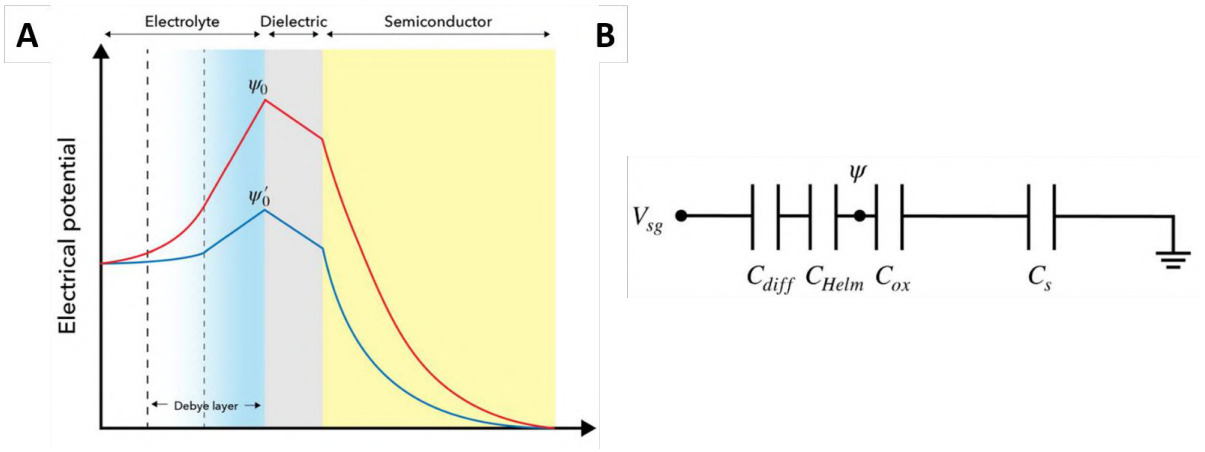

Figure 3. *Models for the interaction of the electrolyte with the semiconductor channel of FETs. (A) The electrical potential model comprises three electrolyte layers (Stern, diffusive, and bulk solution). (B) The equivalent capacitor model where C_{Helm} (Helmholtz capacitance) is equivalent to the stationary layer and C_{diff} (diffusive capacitance) is equivalent to the diffusive layer. C_{ox} is the dielectric capacitance, and C_S is the semiconductor capacitance. Adapted from [6].*

The electrical double layers can also be modeled as virtual capacitors [16] formed between the fixed charges located on the solid (C_{ox}) and the solution sides of the liquid-solid interface, as shown in Figure 3B. The electrolyte interaction can be modeled as a series of two capacitors that represent the behavior of the stationary layer, C_{Helm}, and the diffusive layer, C_{Diff}, as represented in Figure 3B [6]. C_{Helm} follows the Helmholtz model, which defines the fixed charged plane of the Stern layer). The EDL is diffusive at a finite electrolyte temperature and extends beyond the Helmholtz plane modeled by the second capacitor, C_{Diff} [6]. The equivalent capacitor circuit can then be described considering a fixed or tunable voltage source applied to C_{Diff} [6]. The tunable C_{Diff} model considers the re-distribution of ions in the diffusive layer in response to different analytes, which is converted into a capacitance change [6]. The fixed-voltage model considers a fixed value of C_{Diff} while the electrical potential applied on the capacitor changes to positive or negative depending on the charges carried by the analytes [3,6]. Based on these models, it is possible to understand that the charged analyte will cause changes in the charge distribution near the channel surface (within the Debye length), which will change the effective gate voltage, resulting in changes in the drain current, measurable acquiring I-V output curves (Figure 2B) or transfer curves (Figure 2C) of the FET devices [6].

As mentioned, the thickness of the EDL in the electrolyte is given by the Debye length. To determine this value, one has to consider the behavior of the ions in solution, in the Stern and diffusive layers, and the interface charge density, σ, associated with it, given by:

$$\sigma = \sqrt{8\varepsilon\varepsilon_0 k_B T c_0}\sinh\left(\frac{z q_e \psi_0}{2 k_B T}\right) \quad (1)$$

where ε is the dielectric constant of the electrolyte, k_B is the Boltzmann constant, T is the temperature of the solution, c_0 is the salt concentration of the electrolyte (or ionic strength, I), z is the valence number of the salts composing the electrolyte, and ψ_0 is the surface potential [17]. Considering that the measurements are performed in solution, with low surface potentials (bellow 25 meV) [17], (1 can be simplified to $\sigma = \frac{\varepsilon\varepsilon_0\psi_0}{\lambda_D}$, where λ_D is the Debye length and can be given by:

$$\lambda_D = \sqrt{\frac{\varepsilon\varepsilon_0 k_B T}{2 q_e^2 c_0 N_A}} \quad (2)$$

It is possible to observe in $\lambda_D = \sqrt{\frac{\varepsilon\varepsilon_0 k_B T}{2 q_e^2 c_0 N_A}}$ that the maximum distance (λ_D) at which the analytes can electrostatically perturb the charge distribution in the channel is dependent on the salt concentration / ionic strength of the solution containing the analytes [3], meaning that for high salt concentrations, the Debye length is reduced, implying a stronger screening of charged analytes in solution and less interaction with the FET channel, i.e., reducing sensitivity [3,17]. The screening effect is one of the significant limitations in developing FETs as biosensing platforms [7], and its understanding is key to developing new methods to improve the sensitivity and reliability of the FET as a biosensor.

1.1.2. EDL screening

Ideally, FET biosensors should have high probe density (antibodies, DNA, etc.), a capacitive interface for detecting highly charged targets, and low salt concentration solutions to allow complete 'visualization' of the surface events [3]. In reality, most clinical samples (blood, serum, saliva) have high concentrations of salts and other non-specific elements, reducing the Debye length and limiting the detection accuracy [3,17]. Additionally, the complex composition of clinical samples can mean variable ionic strength, composition, and pH between samples, which affect the FET conductance without relation to the actual target [15]. In fact, for undiluted clinical samples or buffers, the Debye length is estimated to be about 0.8 nm which is much lower than the typical probe size (typical antibody size is about 12 nm, Figure 4A) [3], meaning that the target-probe interaction is mostly screened in the bulk solution without directly affecting the transistor characteristics [17], hence losing sensitivity.

Proposals to overcome charge screening - also referred to as Debye screening - have been explored [3,15,17], with the simplest method being pre-treatment of the analyte-containing solution (buffers or biological samples) [3]. In this approach, the solution is pre-treated using centrifugation, filtration, or dilution strategies to achieve low ionic-strength solutions in which a measurable effect of the analyte can

be achieved in the FET biosensors [3]. However, for samples with a low target concentration or highly sensitive to the solution composition, pre-treatment can be disadvantageous since it can worsen the detection probability (for low target concentrations) and lead to misleading results (sensitive targets) due to non-specific adsorption events.

Other approaches try to reduce the probe size to fit within the Debye length, replacing antibodies with small oligonucleotide sequences (aptamers) [3,12] or by fragmenting probe antibodies to immobilize only the specific region for detection (Figure 4B) [3,21]. Some concerns are raised regarding the specificity of the probe in both strategies. Aptamers often need to be stabilized with the addition of functional groups that can hinder affinity, but cross-reactivity is often problematic [22]. The formation of antibody fragments through enzymatic reactions can also alter the inherent affinity of the specific region that is immobilized onto the sensor surface and reduce the stability of the probe molecule [23,24]. Regardless of these strategies, it is also proposed that when the probe, i.e., antibodies, is immobilized without directional control, it will not be perfectly aligned with the surface but rather in various configurations, as exemplified in Figure 4C. Consequently, upon target recognition, the reaction is occurring partially within the Debye length providing a channel conductance variation in the FET sensor, hence a biosensor signal [3].

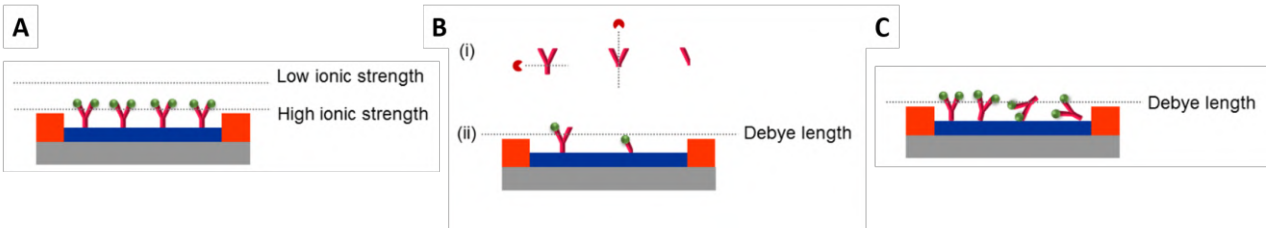

Figure 4. *Strategies to overcome Debye screening. (A) Sample dilution to increase Debye length. (B) Antibody fragmentation to reduce probe size. (C) Random immobilization of antibodies in the sensor surface. Adapted from [3].*

1.1.3. Drift and 1/f noise

It is common for EG-FETs to use an oxide layer as a substrate for sensing. However, the use of oxides originates a monotonic signal drift that is usually attributed to buried charged defects in the oxide [14]. This drift is more intense when the sensor surface is exposed to an electrolyte and tends to stabilize over time as the protonation and deprotonation events at the buried sites stabilize [14]. Additionally, the signal from EG-FETs can also drift due to the random fluctuations, or 1/f noise [14]. The 1/f noise can be attributed to the FET operation, specifically to leakage currents in the measuring setup [14]. The existence of leakage currents can lead to experimental artifacts and electrolysis depending on the electrolyte composition and applied potentials in the system. However, it can help to predict and compensate signal

drift, provided that leakage currents can be measured [14,18]. Leakage currents can be reduced if the gate electrode and sensing surface perform properly, making choosing the structure and materials critical to implementing a system with stable properties [14]. This choice is ever more critical when dealing with nano-sized materials or devices since the channel current becomes more affected by interfaces and surface trap states [16], increasing the 1/f noise. The level of signal fluctuation (noise) combined with the actual sensing response ultimately limits the molecular detection in FETs [16].

Note that exposure to the environment and aging of the device materials can increase noise, which might be avoided by protecting the devices through capping or functionalization [16,18]. Encapsulation of graphene and functionalization of silicon nanowires (Si NWs) showed improved noise performances due to the passivation of surface traps and interface states at the sensor's surface [16].

Additionally, it is proposed that using a reference sensor that does not have the specific probe immobilized at its surface but is exposed to the same solution as the active sensor can improve signal reliability [17]. In that way, the influence of high salt concentration, unspecific elements in solution, and sample-to-sample variability is measured in the reference, allowing to obtain specific target interaction from the difference between the active sensor signal and the reference [17].

1.1.4. Microfabrication for sensing applications

Despite the promising features of field-effect transistors for biosensing applications, limitations are found in the stability and miniaturization of the devices [14], mainly due to the need for exposure to liquid and biological samples. Encapsulating standard ion-sensitive FETs (ISFET) is proposed to separate the FET device from the sensing region to improve stability [14]. In alternative to the encapsulation of standard transistors (Figure 1A), FETs using low-dimensional materials have been proposed with the transistor channel exposed to the environment [7,25–28]. In this configuration, all the transistor is exposed (source, drain, gate, and channel), providing alternatives for the sensing region of the FET device. As such, two main strategies are proposed to apply FETs as biosensors: Use of external gate electrodes that can be mass-produced with low complexity and low-cost and connected to the gate standard ISFETs [29–32]; or fabrication of FETs using materials stable under liquid environments (1D and 2D materials) to allow direct exposure to the sample [7,25–28].

Although the first strategy allows improving the stability and life-time of ISFETs, the use of bulky external Au gate electrodes for sensing can introduce significant drift, reducing the reliability and sensitivity of ISFETs as biosensors [14]. Regarding the second strategy, the study and application of low-dimensional materials (1D and 2D) have been particularly successful since materials like silicon nanowires, graphene,

and others have shown to be chemically stable even under liquid environments [3,15,25], allowing to expose the transistor channel for sensing and taking advantage of the sensitivity of the channel materials. In particular, 2D material-based FETs have been studied due to improved control over material properties and orientation compared with 1D materials (e.g., Si nanowires, carbon nanotubes) [25].

Microfabrication of FETs for biosensing needs to consider application features, including device stability under salt-rich solutions and clean surfaces after microfabrication. Stability of the FET devices in electrolyte-gate configurations (preferred for biosensing) implies passivation of semiconductor and dielectric materials prone to host ions that diffuse inside their lattice, degrading the materials or rendering electronic measurements unstable. Therefore, the passivation of all surfaces contacting the electrolyte, except the surface where biorecognition occurs, is recommended [19]. The passivation layer can be done by coating the wafer surface with photoresist [19], epoxy resin [33], or silicon nitride (SiN_x) and silicon oxide (SiO_2) layers [34,35]. An adequate protection strategy allows to place the electrolyte over a large number of devices without cross-talking [36], reduce leakage current [33], reduce drift due to ion diffusion, and prevent damage of the metallic electrodes [36]. Thus, when designing a biosensor, it is essential to consider permeability to salts and solvents before choosing the passivation layer material. If polymers are chosen, they must be resistant to saline solutions [36] to avoid degradation upon exposure to biological solutions. If silicon-based materials are used, one must consider that SiO_2 is much more permeable to ions than SiN_x. A higher permeability may allow ions from the test solution to get trapped in the dielectric or reach the current lines and cause noise, drift, cross-talking between electrodes, or corrosion of the metallic contacts [36].

Additionally, during microfabrication with 2D materials grown on catalysts, the material transfer process is often a source of residues and contaminations that can affect all the FET surfaces [37,38], including the gate electrode if a planar-gate model is chosen (preferred for scalability and design flexibility [19,39]). These residues pose a challenge for biosensing development, hindering surface functionalization and increasing variability and non-specific interactions with the FET devices [17]. As such, microfabrication processes for bio-FETs need to be optimized considering the final surfaces and the intended application.

1.2. 2D Materials

Two-dimensional (2D) materials are defined by the reduced number of atomic layers, which result in materials with few to tens of nm in thickness and sizeable lateral dimensions that can reach several centimeters [18]. This class of materials is explored due to the unique physical and chemical properties that can be exploited for label-free transduction of biorecognition events with high sensitivity [1,3,18,25]. One of the significant advantages of 2D materials compared with analogous 0D, 1D, or 3D materials is

the record-high surface-to-volume ratio, providing maximum surface availability for interaction with the biomolecules, which ultimately leads to higher sensitivity reaching even single-molecule detection [18,40]. 2D materials can be divided into different families and exhibit a great variety of electrical properties, varying from metals to insulators and semiconductors with bandgap energies from ultraviolet to infrared, as schematized in Figure 5.

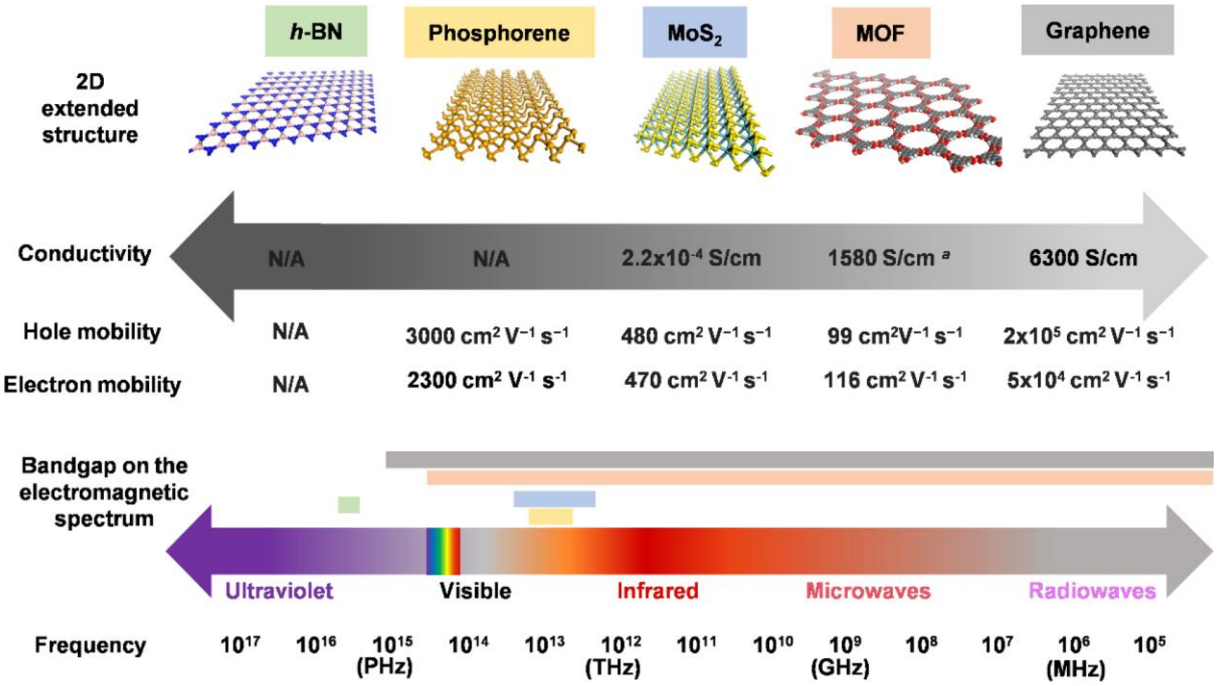

Figure 5. *Examples of 2D materials exhibiting a wide range of chemical structures, conductivities, carrier mobilities, and bandgaps. N/A: no known reports of this value exist. Adapted from [18].*

The following section focus on 2D materials used as biorecognition surfaces in FET-based biosensors: graphene and 2D transition-metal dichalcogenides (TMDCs).

1.2.1. Graphene

Properties

Graphene is a one-atom-thick sheet of sp^2-hybridized carbon atoms arranged in a honeycomb lattice [3,25,41], with a lattice parameter of 2.46 Å [41]. Graphene has remarkable electronic, mechanical, and chemical properties, including high surface area (≈2630 $m^2 \cdot g^{-1}$), optical transmittance (97.7 % transmittance in the entire visible spectrum), strength (tensile strength 130.5 GPa), and flexibility (Young's modulus ≈1 TPa), record-high electrical conductivity (10^4 $S.cm^{-1}$), carrier mobility (2×10^5 $cm^2V^{-1}s^{-1}$) at low carrier density (10^{12} cm^{-2}), hydrophobicity (contact angle with water ≈95°) and chemical resistance [3,18,41,42]. The confinement of charge carriers in the graphene hyperconjugated π-orbital system

results in high carrier mobility and electrical conductivity, particularly in single-layer graphene (SLG), where hopping between stacked monolayers is absent [3,18,41]. The lattice and electronic structure of graphene are shown in Figure 6.

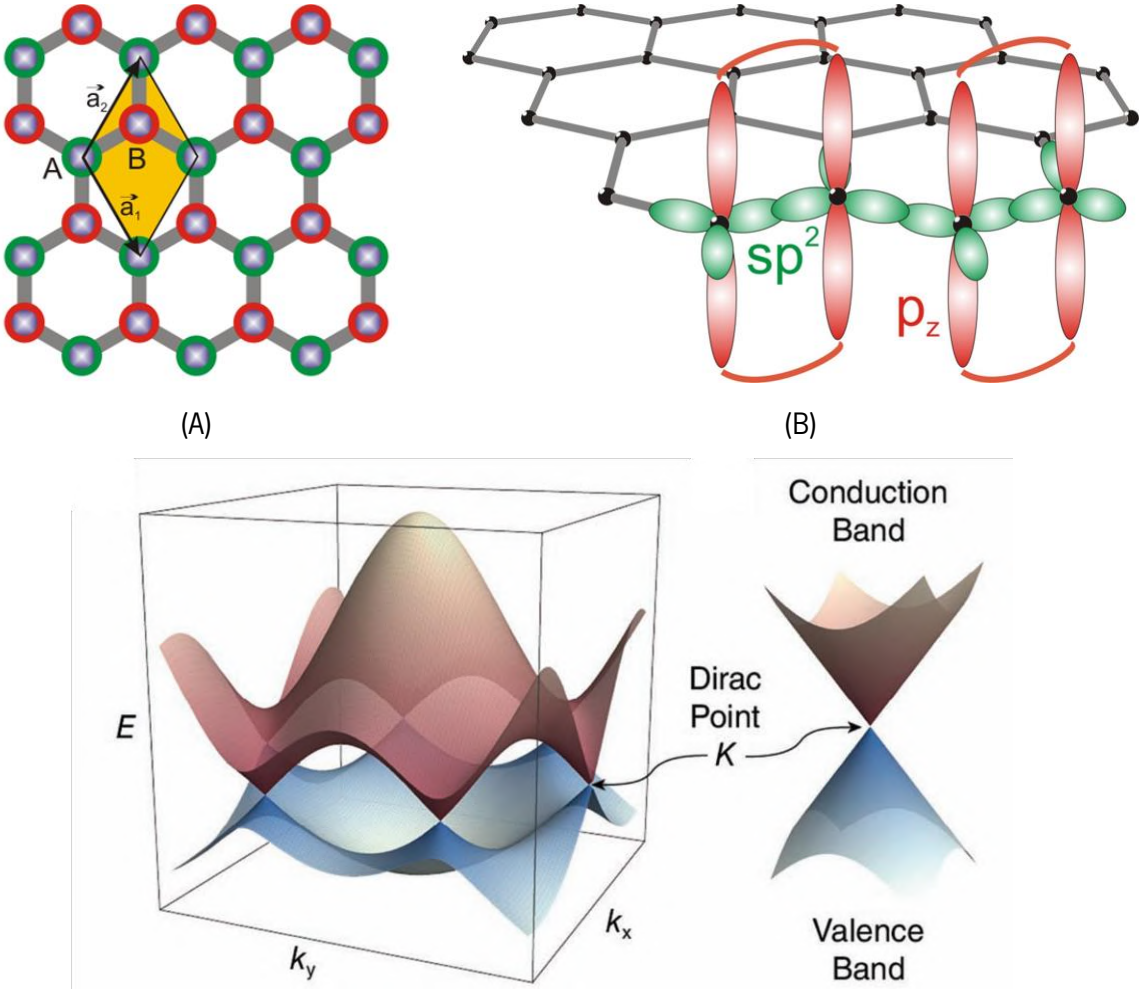

Figure 6. *Graphene lattice and band structure. (A) Graphene honeycomb lattice structure, considering the Bravais lattice as the superposition of two triangular sub-lattices A (green atoms) and B (red atoms). (B) Graphene lattice structure with sp^2-hybridized carbon atoms by σ-bonds, leaving the p_z-orbitals free for π-π bonds. (C) Electronic band structure of graphene showing the Dirac cones intersecting at the Dirac points. Adapted from [41,43].*

Graphene is a zero-bandgap semiconductor because its electronic density of states (DOS) has a singularity where the conduction and valence bands meet, the so-called Dirac point. In the vicinity of the Dirac point, a linear dispersion of the electron energy-momentum relation is observed, going almost symmetrically towards the valence and conduction bands, forming the so-called Dirac cones. As a zero-bandgap semiconductor, graphene exhibits ambipolar transport since the Fermi level can move continuously

between bands, which has significant consequences in the characteristics of graphene field-effect transistors. The conductance minimum arises when the Fermi energy level (E_F) is as close as possible to the Dirac point because then the DOS is at its minimum. This point is also known as the charge neutrality point (CNP) or Dirac point [3,18,41]. The E_F level can be moved in FET devices by applying an electrostatic potential. Gate voltages or the addition of charged or polar objects close to graphene can move the Fermi level. In the latter case, the effect is known as local gating, and it is the basis for the detection of charged biomolecules [3,18,41]. Besides, graphene's high surface area can be explored for functionalization to provide specific interaction with the charged biomolecules of interest, making graphene an excellent candidate for highly sensitive and selective biosensors [3].

Growth

As a single-atom-thick material, graphene can be obtained by several methods, which, depending on the method, can result in pristine single-layer graphene (SLG) or slightly oxidated forms of graphene. The first reported method for the obtention of graphene was mechanical exfoliation ("Scotch tape" method) of highly oriented pyrolytic graphite (HOPG) [44], which allows obtaining pristine graphene films with record-high conductivity due to the absence of contaminants [44]. However, this method is random and artisanal, providing little control over the number of layers and giving small-sized samples with nanometric of micrometric lateral dimensions. Therefore, it is unsuitable for the up-scaling of graphene-based devices, as required for developing applications [18]. Other top-down techniques have been used to exfoliate graphene. Liquid-phase exfoliation (LPE) refers to a group of techniques to exfoliate van der Waals solids into their corresponding isolated layers by applying energy to disrupt the weak inter-layer bonds in a liquid medium attracted considerable attention. It is a cost-effective and up-scalable methodology for producing defect-free graphene flakes liquid dispersions.[33,34] LPE techniques can be classified into electrochemical and physical exfoliation. Physical exfoliation encompasses processes such as ultrasonic exfoliation [45] and several shear exfoliation approaches [46], e.g., high shear mixing and wet jet milling [47].

Apart from these top-down techniques, a vast effort has been dedicated to developing bottom-up graphene growth, with atomic control of the growth process and the resulting graphene structure. Most important among bottom-up techniques, due to the high electronic quality of the resulting material, comparable to that of mechanically exfoliated flakes, is chemical vapor deposition (CVD)[48]. Graphene grown by thermal CVD on metal catalysts or the Si face of SiC wafers is currently the preferred solution to provide high-quality graphene over a large area [37]. CVD using a copper catalyst is the most popular because of its lower cost and high versatility [37], allowing single-layer graphene growth and its transfer onto virtually

any substrate type. If precise control of the oxygen supply to the Cu surface during growth is put in place, colossal crystal size and carrier mobility can be achieved [49]. Graphene grown on SiC wafers has the advantage of growing natively on a transparent insulating substrate and enables transfer-free fabrication of optoelectronic devices [50]. However, monocrystalline SiC substrates are too expensive to be used in large-scale production, and graphene grain size is limited by the atomic terraces' sub-micrometer width, unlike in CVD graphene grown on the copper catalyst.

Although graphene growth by CVD is an excellent choice for producing high-quality graphene for electronic applications, other applications, less demanding in terms of electronic properties, can use low-cost methods based on graphene oxide. Oxidation of graphite using strong acids is used to promote chemical exfoliation, and the cleaved films can be posteriorly treated thermally or chemically to reduce the oxidation level of the material, producing reduced-graphene oxide (rGO) [17,18]. rGO is a low-cost alternative for CVD graphene since it can also be produced with high throughput. However, there is less control over the layers' number, spatial distribution over the substrate, and increased defects and scattering points. Still, for applications that do not require high-quality graphene, rGO presents itself as an alternative for low-cost applications [17,18].

FET operation in biosensing

Graphene's ambipolar character in the FET configuration makes it ideal for sensing charged biomolecules, with either negative or positive charge [3]. Using graphene as a conductive channel between source and drain electrodes, it is possible to detect charged biomolecules by changes in the channel conductance because of the Fermi energy movement in the DOS due to doping by local gating [3,7,15,16].

In a graphene FET, measuring the transfer curve shows the variations in the Fermi energy, for example, by tracking the gate voltage at the charge neutrality point [15]. Figure 7 shows an example of Fermi energy shift by exposure to a positively charged biomolecule and the consequent change in the voltage of the charge neutrality point (V_{CNP}).

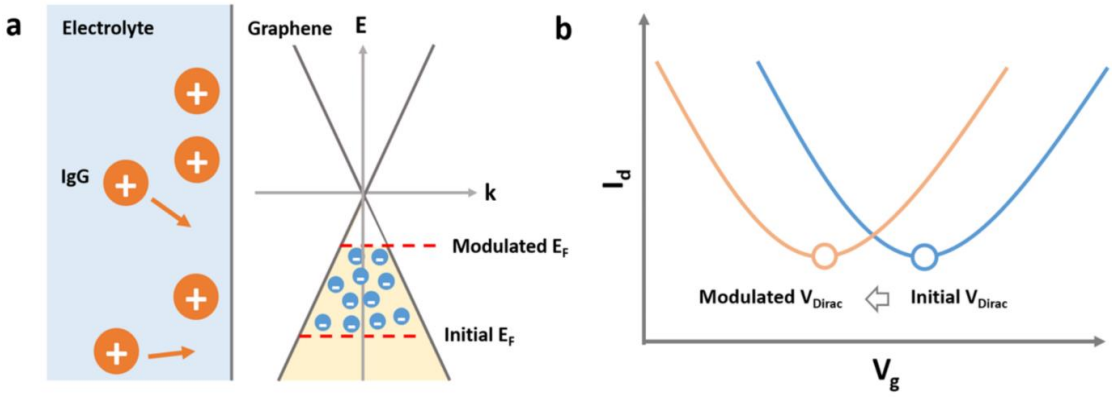

Figure 7. *Effect of charged biomolecules on the charge carrier distribution in an electrolyte-gated graphene FET (EG-GFET). (a) The EF of a p-doped EG-GFET is raised by the depletion of holes (positive charge carriers), reducing the voltage necessary to reach the minimum conductivity point, VCNP (b). Adapted from [15].*

In graphene FETs, GFETs, the current modulation schematized in Figure 7 can be expressed as a function of the excess carrier density, Δn, which is related to the amount of charged molecules (N) on the graphene surface:

$$\Delta I_{SD} = \frac{w}{l} V_{SD} e \mu \Delta n, \quad \Delta n \propto N \tag{3}$$

With ΔI_{SD} being the variation of the source-drain current for a fixed gate-voltage, W and L being the width and length of the FET channel, e the elementary charge and μ the carrier mobility, assumed as constant [16]. As shown in Equation (3), the sensing response of the EG-GFET should be proportional to the total amount of charged molecules adsorbed on the channel surface; however, the quantitative monitoring of biomolecules is challenging due to the uncertainty related to the number of charges presented by a given biomolecule, which can depend on its configuration upon adsorption [51], and the identification of the sensing reactions occurring at the graphene surface [16].

Considering Equation (3), the sensor response, S, can be defined by the change in the current, ΔI_{SD}, caused by the interaction of a biomolecule of charge e, in an amount N: $S = \Delta I_{SD}/N$. According to eq.(3), the sensor response is thus proportional to the carrier mobility in the channel, μ, implying that high mobility graphene has an improved sensor response (as well as improved signal-to-noise ratio, SNR) [16].

In an electrolyte-gate configuration, graphene FETs (GFETS) are exposed directly to the electrolyte, and consequently, the device's electrical characteristics will be influenced by the electrolyte composition [15]. Application of a gate voltage through the electrolyte leads to the modulation of the electrical double-layers (EDL) at the solid-liquid interfaces that serve as the gate dielectric [15]. The EDL thickness (Debye length)

at the graphene-electrolyte interface is critical [3] since charge modulation by charged biomolecules occurs at/or very close to this layer. The Debye length is dependent on the electrolyte composition, being reduced in the presence of salt-rich solutions due to charge screening [3]. It is argued that biosensing of large molecules should not be possible with EG-GFETs due to the distance of the charges to graphene, which is often more extensive than the Debye length. However, the random orientation of immobilized probes and the use of solutions with low salt concentration for measurements with EG-GFETs can help overcome this limitation [3,15].

1.2.2. Transition-Metal Dichalcogenides

The discovery of graphene opened the path for the exploration of other 2D materials which exhibit significantly different properties [1]. In particular, 2D transition-metal dichalcogenides (TMDCs) have shown great potential for electronic applications due to their inherent direct band-gap, which is lacking in graphene [1]. Transition metal dichalcogenides (TMDCs) are materials composed of hexavalent transition metal (M, e.g., Mo, W) and a divalent chalcogen (X, e.g., S, Se, Te) in the stoichiometry MX_2 [18]. Some of these TMDCs crystallize in layered structures that are stacked together through van der Walls forces and can be separated and used as a single TMDC layer (3 atomic layers), resulting in materials with different properties from their bulk (3D) counterpart [18]. In this section, some properties of TMDCs are explored and their potential for FET biosensors.

Properties

Most reports in biosensing with 2D TMDCs use MoS_2 or WS_2 as a channel semiconductor material, with the first one being the more common [1]. As such, only the general properties of those materials are reported below.

MoS_2 is a layered material, in which each layer is composed of a central atomic layer of Mo encapsulated by two S atomic layers, bound in either trigonal prismatic symmetry (D_{3h}) or trigonal antiprismatic symmetry (D_{3d}) [18] as exposed in Figure 8.

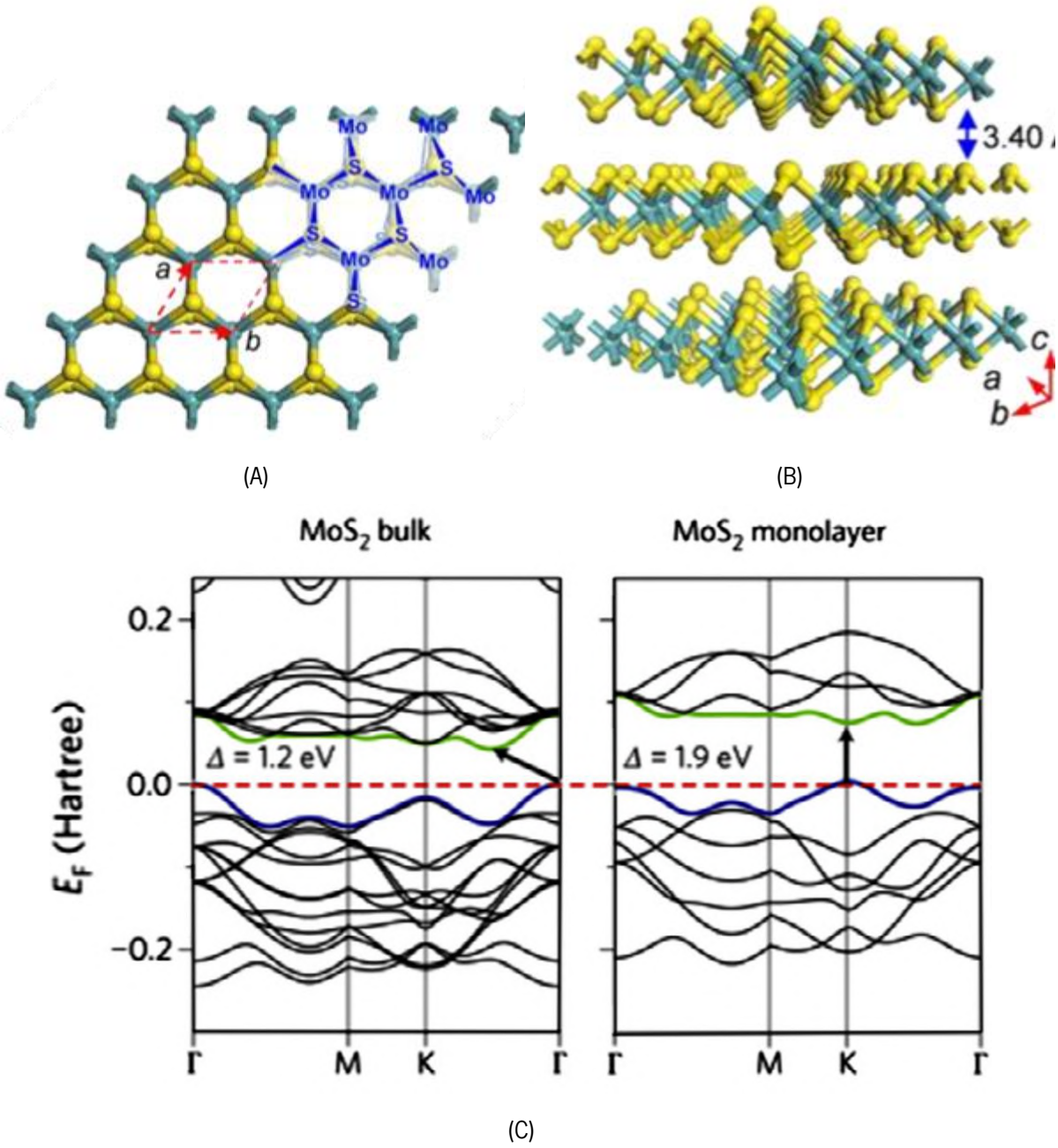

Figure 8. *MoS_2 lattice and band structure. (A) MoS_2 binding symmetry within one layer, between Mo and S. (B) Bulk MoS_2 layered structure and inter-layer distance. (C) Band structure of MoS_2 as a bulk material (left) and as a 2D material (right). Adapted from [18,52].*

MoS_2, like graphene, possesses attractive properties for the development of biosensors such as a sizeable surface-area ratio, mechanical strength, and high carrier mobility (when combined with a high-k dielectric material) [53]. A single layer of MoS_2 is 6.5 Å thick and can be easily cleaved from the bulk crystal using mechanical exfoliation processes [52], as used in graphene [52], and was first reported in 2010 [18]. However, in contrast to graphene, which is considered as a zero-bandgap material, MoS_2 has a direct bandgap of about 1.9 eV, which can lower the leakage current and improve the FET significantly on/off

ratios while keeping acceptable carrier mobility of approximately 200 $cm^2.V^{-1}s^{-1}$ (with a high-k dielectric) [53]. MoS_2 has a lattice constant of 3.13 Å at 77 K and electrical properties tunable with the number of layers due to the changes in symmetry and quantum confinement effects [52]. Bulk MoS_2 has an indirect band-gap of 1.2 eV, which increases to a direct bandgap of 1.9 eV with the decrease in the number of layers [18,52]. The direct bad-gap of 2D MoS_2 is of high interest for FET development since it allows to obtain FETs with high carrier mobility and a high on-to-off ratio [1].

Tungsten sulfide (WS_2), similar to MoS2, is a layered material composed of a W layer between two S layers, shown in Figure 9A.

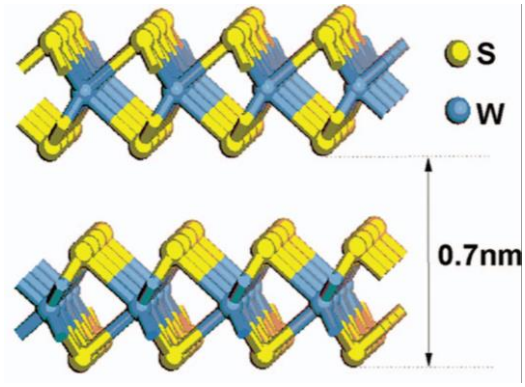

(A)

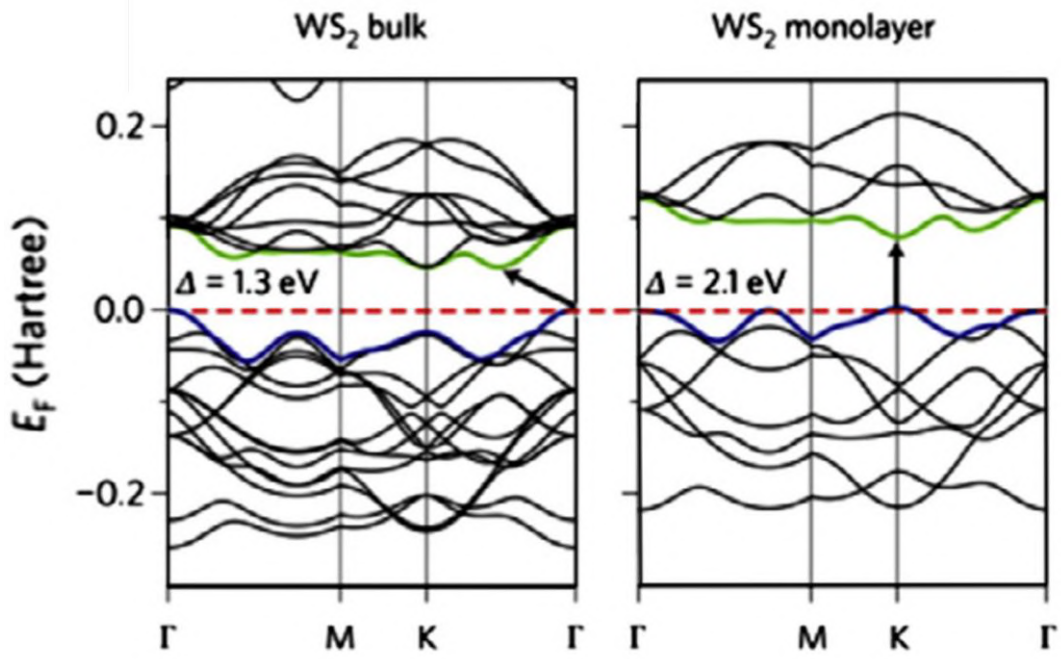

(B)

Figure 9. *MoS_2 lattice and band structure. (A) Bulk MoS_2 layered lattice structure and inter-layer distance. (B) Band structure of MoS_2 as a bulk material (left) and as a 2D material (right). Adapted from [52,54].*

Alike its TMDC semiconductor counterpart, MoS_2, the bandgap of WS_2 changes from an indirect bandgap of 1.3 eV in the bulk material to a direct bandgap of 2.1 eV in monolayer form [52,54], making it attractive

for use in a new generation of 2D material-based FETs, with lower leakage currents and potential for improved dynamic ranges in sensing devices, when compared to graphene [55].

Growth

Both MoS_2 and WS_2 can be obtained by mechanical exfoliation like other layered materials, like graphene. Although this method allows obtaining pristine crystals, there is a lack of control of the sample size and number of layers [18,54]. Liquid phase exfoliation and hydrothermal synthesis have also been reported for the obtention of few-layer MoS_2 and WS_2, but the method that has provided better results for large-scale growth of these 2D TMDCs is chemical vapor deposition (CVD) using Mo or W and S precursors [18,52,54]. Still, large-scale synthesis of 2D TMDCs remains a challenge due to the difficulty in controlling the edges composition and presence of S vacancies which affect the interaction of the materials with the environment [52,54].

FET operation in biosensing

Using TMDCs in a FET configuration provides a similar detection mechanism to that studied for graphene, although the transistor characteristics are different from the carbon-based material. Shortly, the presence of charged biomarkers acts as a dopant element, shifting the threshold voltage of the FETs (similar to V_{CNP} shift in graphene). This shift is often followed by the change in source-drain current for a fixed source-drain voltage [55,56]. However, unlike graphene, which has inherent high carrier mobility, MoS_2 and WS_2 interfaced with a high-k dielectric, like Hafnium oxide (HfO_2), are often used for improved channel mobility and suppressed scattering effects [53] as represented in the scheme of Figure 10A.

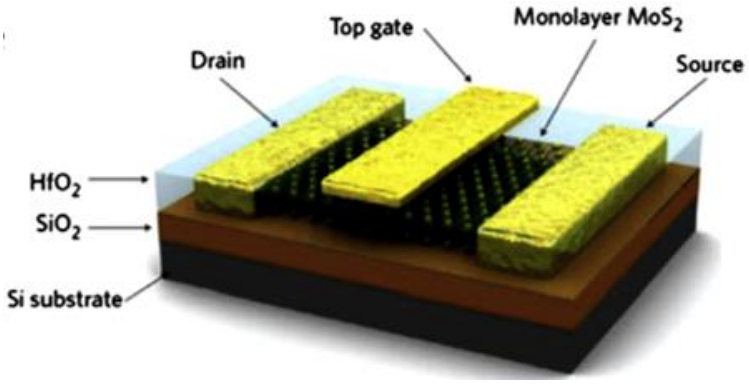

(A)

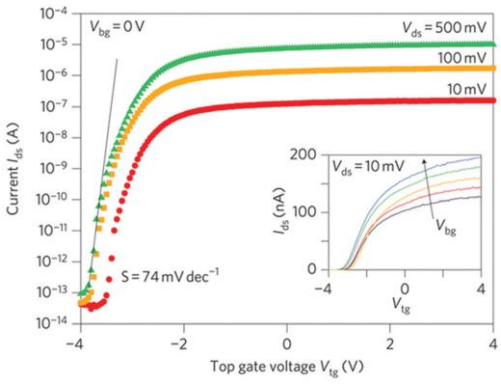

(B)

Figure 10. *A field-effect transistor using a 2D TMDC (MoS_2) as channel material (A), and correspondent transfer curve for different source-drain fixed voltage values (10 to 500 mV). Reproduced from [52,57].*

The use of the high-k dielectric for stabilization of the electrical properties of TMDCs is not consensual as it can reduce the sensitivity for biosensing due to the increased distance between the 2D channel and the biorecognition events. As such, biosensor development strategies using HfO_2 and without dielectric are explored as exemplified in Figure 11.

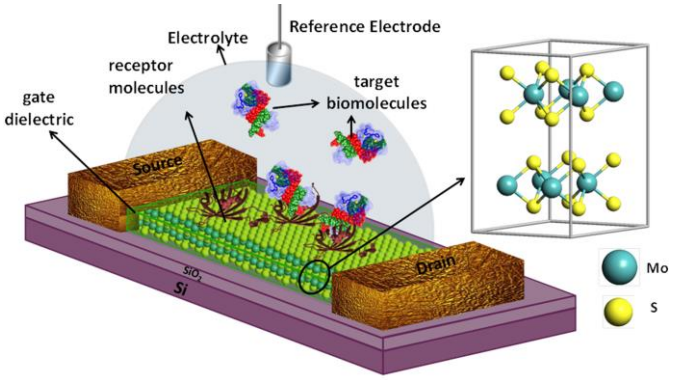

(A)

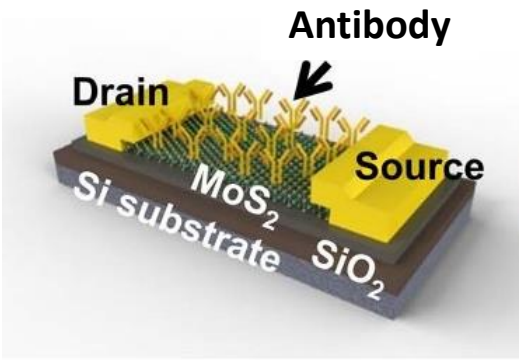

(B)

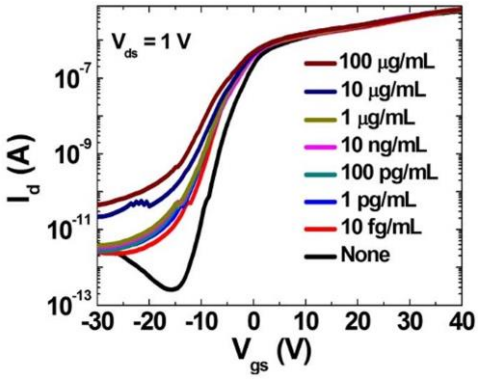

(C)

Figure 11. *MoS_2-based FETs for biosensing. (A) MoS_2-based FET with biorecognition at the high-k gate dielectric (HfO_2) used to improve the electrical properties of the TMDC channel. (B) MoS_2-based FET with biorecognition directly at the TMDC channel. (C) MoS_2-FET transfer curves with exposure to increasing concentrations of a positively charged protein. Reproduced from [58,59].*

In the devices with high-k dielectric, the sensing occurs at the dielectric interface with the charge of biomarker being capacitively-coupled with the TMDC channel, shifting the threshold voltage of the FET without significant changes in the transconductance [58–60]. In FETs without high-k dielectric, biorecognition occurs directly on the TMDC surface with the biorecognition event modulating the on-state transconductance, attributed to disordered potentials forming at the MoS_2 layers [58–60]. It is proposed

that the use of the high-k dielectric improves the electrical properties of the TMDC semiconductor, reaching carrier mobility values up to 200 $cm^2.V^{-1}s^{-1}$ [53,60]; however, it is argued that the inherent hydrophilic nature of the dielectric requires the use of more extensive functionalization processes which increase the distance between the surface and the biorecognition event, reducing the device sensitivity [59,60]. As such, it is still unclear which approach is more advantageous for the operation of TMDC-based FETs for biosensing.

1.3. Application: Hemorrhagic Transformation

Ischemic stroke is a complex disease and a significant public health problem requiring an early detection system to reduce human disability and deaths worldwide. Thrombolytic therapy with tPA (tissue Plasminogen Activator) is the only pharmacological therapy effective for acute cases of ischemic stroke [61], restoring blood circulation in the occluded vessel, but it is tightly restricted in its therapeutic window (< 4.5 hours from stroke onset) [61]. Moreover, hemorrhagic transformation (HT) is a side effect commonly associated with the thrombolytic treatment, caused by disruption of the damaged vessel upon restoration of blood circulation [61–63]. Stratification of the patients is performed based on general risk factors, such as blood pressure, weight, and neuroimaging, which can provide information on diffusion-perfusion mismatch, infarct volume, proximal occlusion, and leukoaraiosis, that indicate increased risk [62] of HT. However, this stratification strategy does not accurately predict lesion growth and hemorrhagic transformation risk [64], mainly due to the time required to analyze neuroimaging data [64].

Thanks to the knowledge of ischemic stroke pathophysiology, several protein biomarkers have been studied and appointed as predictors of the risk of HT after stroke onset [62,63,65,66]. Based on the stratification of the patients using these biomarkers, the number of patients treated increases, reducing the mortality and morbidity associated with stroke [67]. Part of the problem of detecting the risk of HT is the heterogeneity of ischemic stroke [61], implying that several markers must be simultaneously studied to give a safe diagnostic. In terms of protein biomarkers, some have been proposed for their role in different physiological processes of ischemic stroke that can lead to HT: Matrix Metallopeptidase 9 (MMP9), cellular Fibronectin (c-Fn), Platelet-Derived Growth Factor-CC (PDGF-CC), Angiopoietin-1 (Ang1), Neuroserpin and Calcium-binding protein S100β.

Several studies correlate elevated levels of MMP9 present in blood serum with the higher risk of developing HT [64,68–70]. MMP9 belongs to the family of metallopeptidases, proteins involved in the destruction of microvascular integrity by degradation of the extracellular matrix and the basal lamina. Within MMPs, MMP9 is the only one that can be independently correlated with blood-brain barrier

disruption (also a risk factor for HT) and HT. Several reports suggest a cutoff value for MMP9 with concentrations equal to or higher than 140 ng/mL [62,65].

High cellular Fibronectin (c-Fn) levels have also been reported as a predictive factor of HT [65]. Fibronectin is a type of adhesive glycoprotein that promotes cell-cell and cell-matrix interaction. Plasma fibronectin (p-Fn) is usually produced by hepatocytes (liver), but in plasma, we can also find small concentrations of c-Fn, produced by endothelial cells [71]. As c-Fn is mainly confined in endothelial tissue (blood vessels component), high concentration levels of this protein in serum might indicate endothelium damage, i.e., vascular injury [71]. c-Fn plasma concentrations higher than 3.6 μg/mL predict HT development with high sensitivity [62,65]. Although detection of c-Fn shows low specificity for HT when combined with the detection of MMP9, the specificity increases to 87%, providing a safer diagnosis [65].

It is also reported that increased PDGF-CC levels are related to the development of HT [68,72]. PDGF-CC is an isoform of the family of platelet-derived growth factors (PDGFs) involved in cell proliferation processes and regulation of the survival and migration of mesenchymal cells, such as smooth muscle and glial cells [72]. PDGFs are also involved in the extracellular matrix and tissue remodeling regulatory processes and are crucial for angiogenesis and hematopoiesis [72]. Even though PDGFs exist in four different isoforms, from A to D, only isoform PDGF-CC is activated by tPA, increasing blood-brain barrier (BBB) permeability, and it has been shown that blockage of PDGF-CC receptor, PDGFα, reduces tPA related complications in mice models [68,72]. Although more research is required, a 175 ng/mL cutoff value was proposed for HT prediction with a sensitivity of 90% and specificity of 88% [72].

Angiopoietin-1, a specific growth factor for endothelial cells, known for its role in vascular remodeling, maturation, and stability, was shown to have decreased expression after the ischemic event [73].

Neuroserpin is a specific serine protease inhibitor for the brain and is involved in brain development, neuronal survival, and synaptic plasticity [61]. Neuroserpin is known to react with tPA inhibiting the plasminogen action, and so it is considered to have a neuroprotective effect in brain ischemia [61,74]. It has been reported that neuroserpin levels are negatively correlated with MMP-9 and cFN levels within 24h of stroke onset, and low levels of neuroserpin have been correlated with brain damage [61,74]. Reports established that a poor outcome of stroke patients could be predicted for serum levels of neuroserpin below 70 ng/mL. Furthermore, there is a significant association between the cutoff value of neuroserpin and the levels of the previously mentioned brain injury biomarkers (MMP-9 ≥ 140 ng/mL, cFN > 3.6 μg/mL) [74].

Another protein related to increased HT risk is the calcium-binding protein S100β [62,66,75]. S100β is a glial protein related to intracellular calcium regulation with cellular differentiation and motility [66]. When

present at low concentrations, it has a protective and trophic role; however, high levels of this protein are toxic and pro-apoptotic [66]. It is known that in humans, S100β is at concentrations 40 times higher in the cerebrospinal fluid than in serum, and so an increase of this protein in serum is indicative of BBB disruption/damage [75]. It is proposed that concentrations above 0.23 μg/mL can be associated with HT risk, but the authors advise that for diagnostic, single protein detection is not enough [62,75]

In line with the above discussion, several authors have mentioned that the single protein-based diagnosis is not enough to safely analyze the risk of HT development in a patient [64,73,74]. Therefore, multiplex assays are the key to obtaining a more reliable stratification of stroke patients, as exemplified by the increase in specificity of diagnostic provided by the addition of the analysis of MMP9 levels to the c-Fn level analysis [65].

The major challenge for stratification using protein biomarkers is related to the developing detection systems that can detect multiple markers and be adapted to have different sensitivities and dynamic ranges for each biomarker. Approaches to this problem are further discussed in Section 2.2 of this chapter.

2. State of the art

2.1. Field-effect transistors for biosensing

In FETs made of 1D and 2D materials, provided the material is chemically stable, the low-dimensionality allows the channel to be directly exposed to the target-containing electrolyte. It is not the case in conventional FETs made of bulk materials, where the channel is buried at the interface between a solid-state dielectric and the semiconductor. Compared to bulk materials, graphene is a highly advantageous option due to its 2D nature and intrinsic properties, such as high carrier mobility, low electrical noise, and chemical stability [16]. As so, the use of this material as a channel for FET devices unlocks the potential for highly sensitive and fast FET-based biosensors. Devices based on 1D materials present similar advantages. However, their use is limited because of the difficulty and cost of large-scale fabrication of 1D materials [76].

Moreover, precise control of their structural and electronic properties is so far elusive, resulting in significant variability in device performance [59]. Therefore, 2D materials, compatible with standard planar technology, are logic alternatives for FET-based biosensor development. This chapter discusses the recent developments in biosensing using 2D-material-based FETs, focusing on graphene and MoS_2.

2.1.1. Graphene bio-FETs

Surface functionalization

The unique fundamental properties of graphene [44], particularly the chemical stability and extreme sensitivity to near-surface charges and electric fields, suggest its use for biomolecular detection [77–79]. However, the hydrophobicity and high sensitivity to charges and electrical fields result in substantial interference from nonspecific molecular adsorption and thus poor selectivity of unmodified graphene sensors for bioanalytes when operating in an aqueous physiological environment. Accordingly, graphene surfaces need to be functionalized [79–81] with specific biomolecular probes to produce selective and specific biosensors, thereby minimizing nonspecific adsorption and ensuring that the biorecognition of the target dominates the surface binding events.

Several strategies have been proposed to functionalize graphene surfaces, as summarized in Table 1, ranging from direct immobilization of probe molecules to non-covalent modification with a linker molecule [79–83].

Initially proposed graphene FETs (GFETs) for biosensing used direct exposure to the target to show the ability for sensing of charged biomolecules, showing non-specific detection of BSA [84] and cholesterol [85], among others. However, to provide specific detection of the biomolecules, probes are essential. Some authors have proposed direct immobilization of probes on graphene, including nanoparticle-tagged antibodies and DNA probes [80,86–88], odorant-binding proteins [89], DNA [90], and antibodies [79]. Although these systems can provide specific detection of the intended biomarkers, prevention of non-specific binding to the graphene surface is not accounted for. Additionally, some probe biomolecules can lose conformation in contact with graphene due to the high surface hydrophobicity, hindering the specificity to the probe.

The most common strategy for biosensor development with GFETs is using a linker molecule between graphene and the probe. This linker allows the preservation of the electrical characteristics of graphene and provides stabilization to the probe molecule [42]. The linker can be immobilized in the surface by covalent bonding in graphene or rGO defects [81,91,92], or by non-covalent π-π interactions [89,93–106]. Graphene's covalent functionalization introduces sp3 centers in the sp2 network as reaction sites. Specific detection of pharmaceutical compounds [107], insulin [92], and virus [81] was achieved using diazonium chemistry to create carboxylic acid sites, which are then activated and stabilized with 1-ethyl-3-[3-(dimethylamino)propyl]-carbodiimide hydrochloride/sulfo-N hydroxysuccinimide (EDC/s-NHS) [81,92,107]. The probes are then immobilized by reaction with the NHS group. Although covalent modification is highly reliable, it destroys the aromaticity of the graphene lattice, leading to poorer electrical characteristics when compared with pristine graphene.

Non-covalent functionalization allows rendering the graphene surface specific for detection while keeping the 2D lattice intact. One common non-covalent approach is aromatic linkers that self-assemble on the graphene surface by π-π interaction (hydrophobic stacking). This interaction is quite stable and achieves binding energy of almost 0.1 eV per carbon atom [16]. Aromatic linkers allow the modification of graphene with functional groups and the immobilization of antibodies, DNA, nanoparticles, or other biomolecules [16,108]. The use of aromatic compounds, mainly pyrene-based compounds, as linkers is a general approach for biosensor development in GFETs due to the preservation of graphene properties and the possibility for covalent binding with virtually any biomolecule. The linker which appears more often is a 1-pyrene butyric acid n-hydroxysuccinimide ester (PBSE), which allows immobilization of probe biomolecules through the NHS-ester group. This linker is reported in the development of GFETs for biosensing by several authors [42,83,89,93–103,109,110] for detection of proteins [42,94,95,98,99,101,109,110], DNA [83,93,96,100], aromatic compounds [89] and others [102]. PBSE has been reported as an effective linker for GFET biosensors due to its strong adhesion to graphene [111–115] and simple chemistry for probe immobilization [116,117].

The probes for biomolecular recognition are the main element to provide specificity to the biosensor in development. As in other systems, using a linker with an NHS-ester group allows reaction with amino groups of biomolecules, creating a covalent amide bond between the linker and the probe [116,117]. This reaction is readily achieved in proteins (including antibodies), which are rich in amine groups [3] but can also be achieved with DNA probes or aptamers if the molecule is modified to have an amine-group at the extremity intended for binding with the linker [118]. From the reported studies in Table 1, it is possible to observe that the probe's choice is mainly related to the intended biomolecular target (DNA, protein, odorants, etc.).

DNA single-strand sequences immobilized into the GFET surface provide excellent specificity, distinguishing even between the complementary strand and a strand with a single base-pair mismatch [83,87,118,119]. The main limitation regarding DNA detection is the often-small amount of genetic material available in samples for detection. However, GFETs have shown extremely high sensitivity for these biomolecules due to their negative charge, and small size (immobilization of probe and recognition close to graphene), indicating this technology is suitable for developing highly sensitive geno sensors [16].

Two main approaches were reported for detecting other biological targets such as proteins, viruses, bacteria, and others: using antibodies and aptamers as probes. Antibodies are large proteins composed of two heavy polypeptide chains (about 50 kDa each) and two light chains (about 25 kDa each) linked by disulfide bonds, which are organized into constant and variable regions [3]. The variable regions of

antibodies provide the specificity to a protein/antigen and correspond to the region where biorecognition occurs [3]. Antibodies are obtained by exposure to the immunogenic agent in an organism that will generate a specific immunological response, hence antibodies that can be extracted. Antibodies are widely used as a probe for biosensors in general, and in GFETs, several reports use this probe to provide specific detection of proteins [79,86,92,94,95,101,103], viruses [81], and toxins [98,120], among others.

Aptamers are short single-stranded DNA or RNA sequences which fold into well-defined 3D structures that form binding regions for specific targets [121]. Specific aptamers are obtained synthetically from a library of millions of sequences selected through affinity reactions with the target [121]. Aptamers have been proposed to replace antibodies due to the low fabrication cost. However, selecting a specific aptamer is still costly and time-consuming, while the library of antibodies is much more developed. Still, there are many reports of the use of specific aptamers for the detection of antibiotics [102], toxic metals [105], and proteins [97,109,110].

Independently from the chosen probe element (DNA, antibodies, aptamers), it is vital to consider the probe's affinity and stability, which is key to a well-functioning and specific GFET based biosensor. Additionally, the functionalization process is most likely not perfect in terms of probe surface coverage, meaning that after probe immobilization, some linker molecules can be left unreacted, and graphene can still be partially exposed. Consequently, there is the need for a passivation/blocking strategy to avoid the non-specific binding of sample elements to the linker or the graphene surface. Although some reports overlook this step, it has been shown that it is critical to improve specificity and reduce noise [3,16]. Strategies for chemical surface passivation mainly focus on the inactivation of free NHS-ester groups of the linkers used, with ethanolamine and bovine serum albumin (BSA) being widely reported as blocking agents [42,79,100–102,120,81,83,92–97]. Still, some reports also concern the passivation of exposed graphene to avoid non-specific interactions, using either surfactant-containing buffers [82,86] or polyethylene glycol (PEG) based compounds [81,92,99,103,110]. Chemical passivation of the GFETs is key to improving detection in biological samples, rich in salts and non-specific elements that can interact with the graphene surface. Some reports suggest an increase in sensitivity by reducing the Debye screening using PEG molecules between the probe molecules [29,103,110,122], making the passivation step highly important for biosensor development for clinical applications.

Applications

Graphene FETs can detect a wide range of targets depending only on the surface functionalization to provide biorecognition specificity. There are extensive reports for detecting DNA, proteins, toxins, and other targets for various applications. The focus of this work is on medical applications. Therefore, the explored state-of-the-art research is mainly directed to this application area. A resume of explored biomarkers and general biosensor parameters achieved in bio-GFETs is presented in Table 2.

Although graphene FETs for biosensing can be operated with back gating or electrolyte gating, the second system seems to be preferred due to the possibility of using the sample solution as an electrolyte for the measurement. As such, there are more reports for electrolyte-gated graphene FETs (EG-GFETs) than for other GFET architectures, as noted in Table 2.

Still, some reports propose biosensing with back-gated GFETs to detect proteins, DNA, and other biomolecules with high sensitivity, with reported LoD in the femtomolar range [79,94,100–102,107]. One such example reports human chorionic gonadotropin (hCG) [94], a protein biomarker of trophoblastic and testicular cancer and an indicator of fetus development during pregnancy. This GFET system (using CVD-grown graphene) uses a four-probe electrical measurement to extract the transistor characteristics with a solid back-gate. After non-covalent functionalization with a pyrene-based linker, specific antibody (anti-hCG antibody) immobilization and passivation with bovine serum albumin (BSA), exposure to hCG at concentrations ranging from 0.1 pg/ml to 1 ng/ml increased the normalized resistance with increasing concentration, with an LoD of about 0.1 pg/ml (~27 fM). Zheng et al. [100] report a system with a similar architecture for the detection of DNA. The CVD-grown graphene was functionalized with PBSE (π-π hydrophobic stacking), then an amine-modified DNA sequence was immobilized, and passivation for non-specific interactions with ethanolamine followed [100]. The functionalized devices were exposed to complementary DNA (cDNA), one-base mismatched, and non-complementary DNA (non-DNA), showing a high sensitivity with an LoD of 10 fM, and a wide dynamic range up to 100 pM. Although the proof-of-principle results with the back-gated architecture seem promising, there is a lack of further development of these sensors, with some research groups switching from back-gated systems to electrolyte-gated ones [92,107] due to the possibility of using the sample solution as the electrolyte for real-time measurements. One such example is reported by Lerner et al., who report the detection of an opioid (Naltrexone) graphene FETs with a LoD of 29 pM [107] using back-gate architecture, and later reports immune-detection of insulin in an electrolyte gated system, with a similar LoD (100 pM). Further work from the same research group used preferentially electrolyte-gated GFETs to detect clinical biomarkers (e.g., zika virus [81]).

Several EG-GFETs systems are under development with great potential, as evidenced by the proof-of-principle reports summarized in Table 2. Several approaches have been considered to access

biorecognition-induced variations in the EG-GFETs signal, with the voltage variation of the minimum conductivity point (a.k.a. Dirac point voltage) and the source-drain current variation being the most reported parameters for signal extraction. The signal extraction method does not seem to be related to the kind of biomarker detected, although the evaluation of source-drain variation seems to be preferred in rGO-based devices which do not operate as well as FETs as the CVD-graphene based ones (extraction of V_{CNP} might be more difficult in rGO-based FETs).

EG-GFETs are reported for DNA detection with high sensitivity reaching an LoD of 25 aM [83]. Attomolar sensitivity is also reported for detecting thyroid-stimulating hormone (TSH) [103] by immunosensing, reaching an LoD of 200 aM in saline solution and 800 aM in whole serum, with detection up to 10 nM. This variation in sensitivity between buffer and human serum is critical for developing clinical applications since, ideally, the EG-GFET should be able to detect the biomarker of interest in a biological sample/complex medium. Several reports explore detection in saline solutions, exhibiting promising features in terms of LoD and dynamic range for detecting elusive biomarkers. However, research still needs to be done to detect biological samples and multiplexing biomarker detection to push the EG-GFETs technology to a clinical biosensor.

2.1.2. Transition-Metal Dichalcogenide bio-FETs

Surface functionalization

Functionalization is a crucial step to provide specificity to the FET biosensor. In the case of TMDC-based FETs, the functionalization approach changes with the biorecognition surface since it can either be the TMDC material or a high-k gate dielectric (Section 1.2.2, FET operation in biosensing). In general, for devices where biorecognition occurs directly in the TMDC layer, no linker is used, being the immobilization of the specific probe dependent on the hydrophobic nature of the TMDC [56,59,123]. Such systems have been reported for specific detection of antibodies [59,123], cancer biomarkers [59,123], and glucose [56]. Other reports propose probe immobilization by modification of the probe with Ni ions which are to interact with MoS_2 [124] or surface modification with silanes, (3-Aminopropyl)triethoxysilane (APTES), and glutaraldehyde for probe covalent immobilization [60,125].

The APTES + glutaraldehyde method is more commonly associated with HfO_2 coated TMDC-FETs since there is an extensive literature on the modification of oxide surfaces for biomolecules immobilization using this method [58,60,126]. One of the reported studies in Table 1 [60] uses this surface modification system in MoS_2-FETs with and without HfO_2 coating to immobilize Anti-Human TNF-α to compare the biosensor properties of both transistor structures.

Applications

Semiconductor TMDC use in biosensing is residual compared with the use of graphene, mainly due to the maturity of the growth methods for those materials, which still need much improvement to allow wafer-scale device fabrication as it is done with graphene-based devices. Still, some reports have explored the potential for biosensing with MoS_2-based FETs, as it is the most researched TMDC. Most of these reports focus on detecting using back-gated FETs (Table 2) even though the earlier reports of biosensing with MoS_2 are in electrolyte-gated configurations [55,58].

Sarkar et reported the first-ever working MoS_2-based FET for biosensing [58]. In this work, HfO_2-coated MoS_2 was modified with APTES, and streptavidin was immobilized for specific detection of biotin as a proof-of-principle biosensor. As shown in Figure 12A, exposure to 10 μM of streptavidin reduces the source-drain current and positively shifts the threshold voltage (V_{TH}) [58] as expected by the capacitive coupling effect caused by the accumulation of negatively charged biomarkers at the dielectric surface.

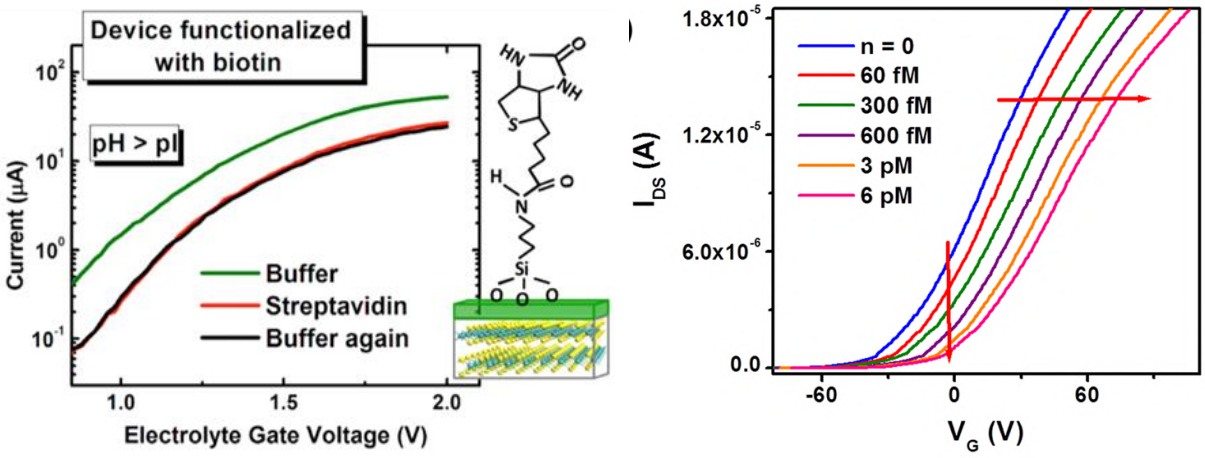

(A) (B)

Figure 12. *Transfer curves of MoS_2-based transistors with a high-k dielectric coating over the semiconductor channel. (A) Electrolyte-gated system for streptavidin detection in the functionalized HfO_2 surface [58]. (B) Back-gated system for detection of TNF-α in the functionalized HfO_2 surface [60]. Adapted from [58,60].*

In back-gate configurations using the HfO_2 dielectric over the MoS_2 semiconductor channel, the charge accumulation effects are similar, with the difference of the device operating at much higher voltages. As shown in Figure 12B, exposure to increasing concentrations of a negatively charged biomarker (TNF-α, pI < pH of buffer) shifts the threshold voltage positively, without changing the shape of the transfer curves, indicating preservation of the electrical properties of the device [60]. However, many of the back-gated MoS_2 FETs suggested in the literature for biosensing do not use the high-k dielectric over MoS_2 to promote

direct detection at the channel as reported for graphene. The detection of TNF-α in HfO_2-coated channels and exposed MoS_2 was compared in the same report [60]. In insulator-free sensors, the group reported a consistent reduction in the source-drain current with increasing concentrations of the biomarker, indicating a reduction of the transconductance (or the charge carrier mobility) [60], meaning that although detection is also achieved in the dielectric-free system, it comes at the cost of degradation of the electrical properties of the FET device.

1 ***Table 1.*** *Resume of functionalization strategies used on different configurations of 2D-materials based FETs for biosensing.*

Architecture	Signal	Surface	Linker	Probe	Passivation	Target	Ref.
Back gate	Channel Resistance variation, normalized to R_0	Graphene	-	Anti-IgG (Au NPs label)	-	IgG	[80]
				Anti-ANXA2 + Anti-VEGF + Anti-EN01	BSA	ANXA2 VEGF EN01	[79]
			PBSE	Anti-hCG		hCG	[94]
		rGO	- (Au NPs)	Anti IgG	Blocking buffer	IgG	[86]
	Dirac point voltage variation	Graphene	Diazonium chemistry (covalent) + EDC/Sulfo-NHS	μ-opioid receptor (protein)	-	Naltrexone (opioid)	[91]
			PBSE	PNA	Ethanolamine	DNA	[100]
	Source-Drain current variation	Graphene	-	-	-	Cholesterol	[85]
			PBSE	Anti-CEA	Ethanolamine	CEA	[101]
				Aptamer		Kanamycin A	[102]
		MoS_2	-	-	-	IgG	[59]
				Anti-PSA		PSA	
				-		Glucose	[56]
				Anti-PSA	BSA	PSA	[123]
				Anti-IgG		IgG	
			Ni-based chemistry	μ-opioid receptor (protein)	-	DAMGO	[127]
			APTES + glutaraldehyde	NHS-biotin		Streptavidin	[125]
				Anti-IL-1β		IL-1β	
		MoS_2/ HfO_2	APTES + glutaraldehyde	Anti-Human TNF-α		TNF-α	[60]
Electrolyte gate	Gate voltage variation	Graphene	Pyrene Butyric Acid (PBA) + N-(1-pyrenyl)maleimide (PyMal)	Anti-TSH (F'(ab))	Thiol-PEG	TSH	[103]

			PBSE	Aptamer	-	Thrombin	[104]
			Alginate-calcium microcubes	GOD		Glucose	[128]
				Urease		Urea	
				Anti-APOA1 coated magnetic beads		APOA1	
Electrolyte gate	Dirac point voltage variation	Graphene	PBSE	DNA	Ethanolamine	cDNA	[83]
				Aptamer	Amino-PEG + Ethanolamine	PSA	[110]
			Diazonium chemistry + Pyrene chemistry + EDC/Sulfo-NHS	Anti-insulin		Insulin	[92]
			Pyrene chemistry	Aptamer, 8-17 DNAzyme	-	Lead (PB^{2+})	[105]
			-	DNA	-	cDNA	[90]
			-	Au NPs + Thiol-DNA	-		[87]
			PBSE	DNA	Ethanolamine		[93]
			Pyrene-1-boronic acid	Pyrene-1-boronic acid	-	Glucose	[106]
		rGO	PBSE	Anti-PSA		PSA-act	[95]
			PBSE	PNA	Ethanolamine	DNA	[96]
	Gate capacitance variation, normalized to C_0	Graphene	Diazonium chemistry + Pyrene chemistry	Anti-Zika NS1	Amino-PEG +Ethanolamine	Zika virus	[81]
			-	-	-	BSA	[84]
		rGO	Ply-L-Lysine	Anti-AFB1	BSA	AFB1	[120]
	Source-Drain current variation	Graphene	PBSE	Aptamer	Ethanolamine	IgG	[97]
Electrolyte gate	Source-Drain current variation, normalized to I_0	rGO	-	OBP14	-	Homovanillic acid	[98]
			PBSE	Anti-BSA		BSA	
				Anti-aflatoxin B1		AFB1	
				OBP14		Methyl Vanillate Eugenol	[89]

		Biotin	PEG	Streptavidin	[99]
		-		Fibronectin	
rGO + NPs	Cysteamine + glutaraldehyde	Ebola antibody	0.1% SuperBlock Tween 20 in PBS	Ebola antigen	[82]
	-	Thiol-DNA	-	DNA	[88]
MoS_2 / HfO_2	APTES + glutaraldehyde	Anti-PSA	-	PSA	[55]
	APTES	(sulfo-NHS)-biotin		Streptavidin	[58]

NPs – nanoparticles; Au NPs – gold NPs; EDC/Sulfo-NHS - 1-ethyl-3-[3-(dimethylamino)propyl]- carbodiimide hydrochloride/sulfo-N hydroxysuccinimide ; PEG – polyethylene glycol; PBSE - 1-pyrenebutyric acid n-hydroxysuccinimide ester; BSA – bovine serum albumin; hCG – human chorionic gonadotropin; CEA – carcinogembryonic antigen; PSA – prostate specific antigen; IgG – immunoglobulin G; GOD – glucose oxidase; OBP14 – odorant binding protein 14; AFB1 – Aflatoxin B1; APTES – (3-Aminopropyl)triethoxysilane; DAMGO – ([D- Ala2, N-MePhe4, Gly-ol]-enkephalin); IL-1β – Inter Leucin 1β; TNF-α - Tumor necrosis factor α; DNA – Deoxyribonuclease; TSH – Thyroid stimulating hormone; ANXA2 – Annexin A2; VEGF – Vascular Endothelial Growth Factor; ENO1 – α-enolase 1.

2

Table 2. *Resume of biomarkers detected using different configurations of 2D-materials based FETs, with the limit-of-detection (LoD) and dynamic range reported.*

LoD and Dynamic range units were homogenized to molarity for easier comparison between reports.

Architecture	Signal	Surface	Sensor type (by recognition element)	Target	LoD	Dynamic Range	Ref
Back gate	Channel Resistance variation, normalized to R_0	Graphene	Immunosensor	IgG	13 pM	-	[80]
				ANXA2	21 – 25 fM	25 fM – 25 nM	[79]
				VEGF		26 fM – 26 nM	
				ENO1		21 fM – 21 nM	
				hCG	< 27 fM	27 fM – 27 pM	[94]
		rGO		IgG	1.3 pM	1.3 pM – 1.3 µM	[86]
	Dirac point voltage variation	Graphene	Protein-based sensor	Naltrexone (opioid)	29 pM	29 pM – 29 µM	[91]
			DNA sensor	DNA	10 fM	1 fM – 100 pM	[100]
	Source-Drain current variation	Graphene	-	Cholesterol	-	3 mM – 21 mM	[85]
			Immunosensor	CEA	< 600 fM	600 fM – 600 pM	[101]
			Aptamer	Kanamycin A	10 nM	1 nM – 1 µM	[102]
		MoS_2	-	IgG	-	67 fM – 667 nM	[59]
			Immunosensor	PSA	36 fM	36 fM – 360 pM	
			Enzymatic sensor	Glucose	300 nM	300 nM – 30 mM	[56]
			Immunosensor	PSA	36 pM	36 pM – 29 nM	[123]
				IgG	36 pM	36 pM – 60 nM	
			Protein-based sensor	DAMGO	3 nM	-	[127]
			Biotin-Streptavidin sensor	Streptavidin	1 fM	1 fM – 300 fM	[125]
			Immunosensor	IL-1β	1 fM	1 fM – 500 fM	
		MoS_2 / HfO_2	Immunosensor	TNF-α	60 fM	60 fM – 60 pM	[60]

Electrolyte gate	Gate voltage variation	Graphene	Immunosensor	TSH	200 aM 800 aM (whole serum)	10 fM – 10 nM	[103]
			Aptamer	Thrombin	-	10 nM – 300 nM	[104]
				Hemagglutinin H5		500 zM–500 pM	
			Immunosensor	α-fetoprotein	145 pM	145 pM – 14.5 nM	[129]
			Protein-based sensor	IgE	5.3 pM	5.3 pM – 526 pM	[130]
			Biotin-Streptavidin sensor	Streptavidin	-	5 µM	[131]
	Dirac point voltage variation	Graphene	DNA sensor	cDNA	25 aM	1 aM – 100 pM	[83]
			Aptamer-based sensor	PSA	10 nM	1 nM – 1 µM	[110]
			Immunosensor	Insulin	100 pM	100 pM – 10 µM	[92]
			Aptamer-based sensor	Lead (PB^{2+})	180 pM	180 pM – 115 nM	[105]
			DNA sensor	cDNA	1 pM	1 pM – 100 nM	[90]
					100 pM	100 pM – 500 nM	[87]
					100 fM	100 fM – 1 nM	[93]
			Metabolite sensor	Glucose	-	2 µM – 25 mM	[106]
		rGO	Immunosensor	PSA-act	3.8 fM	3.8 fM – 38 nM	[95]
			DNA sensor	DNA	100 fM	10 fM – 1 nM	[96]
	Gate capacitance variation, normalized to C_0	Graphene	Immunosensor	Zika virus	450 pM	-	[81]
			-	BSA	300 pM	300 pM – 300 nM	[84]
		rGO	Immunosensor	AFB1	300 zM (10^{-4} ppt)	300 zM – 3 fM (10^{-4} – 1 ppt)	[120]
	Source-Drain current variation	Graphene	Aptamer-based sensor	IgG	290 pM	290 pM – 340 nM	[97]
	Source-Drain current variation, normalized to I_0	rGO	Immunosensor	BSA	100 pM	1 nM – 25 µM	[98]
				AFB1	33 pM	33 pM – 10 nM	
			Odorant sensor (Protein-based)	Homovanillic acid	-	100 nM – 100 µM	[89]
				Methyl Vanillate	-	100 nM – 200 µM	
				Eugenol	-	100 nM - 250 µM	

	Biotin-Streptavidin sensor	Streptavidin	300 nM	300 nM – 20 µM	[99]
	-	Fibronectin	0.5 nM	0.5 nM – 220 nM	
rGO + NPs	Immunosensor	Ebola Antigen	26 pM	26 pM – 12 nM	[82]
	DNA sensor	DNA	2.4 nM	48 nM – 5 µM	[88]
MoS_2 / HfO_2	Immunosensor	PSA	375 fM	375 fM – 3.75 nM	[55]
	Biotin-Streptavidin sensor	Streptavidin	-	100 fM – 10 µM	[58]

rGO – reduced Graphene Oxide; NPs- nanoparticles; BSA – bovine serum albumin; hCG – human chorionic gonadotropin; CEA – carcinogembryonic antigen; PSA – prostate specific antigen; IgG – immunoglobulin G; GOD – glucose oxidase; OBP14 – odorant binding protein 14; AFB1 – Aflatoxin B1; DAMGO – ([D- Ala2, N-MePhe4, Gly-ol]-enkephalin); IL-1β – Inter Leucin 1β; TNF-α - Tumor necrosis factor α; DNA – Deoxyribonuclease; TSH – Thyroid stimulating hormone; ANXA2 – Annexin A2; VEGF – Vascular Endothelial Growth Factor; ENO1 – α-enolase 1.

5

2.2. Biosensors for clinical applications

Part of this section is reproduced from the publication "The Challenges of Developing Biosensors for Clinical Assessment: A Review" by Briliant Adhi Prabow, Patrícia D. Cabral, Paulo Freitas and Elisabete Fernandes, in Chemosensors 9(11) (2021) 299 (https://doi.org/10.3390/chemosensors9110299)

Personal Contribution: Writing of section 5, editing, and reviewing of the full article.

Initiating research in biosensing applied to the diagnosis of diseases is still challenging for researchers, be it in the preferences of biosensor platforms, selection of biomarkers, detection strategies, or other aspects (e.g., cutoff values) to fulfill the clinical purpose. There are two sides to developing a diagnostic tool: biosensor development and clinical. From the development side, the research engineers seek the typical characteristics: sensitivity, selectivity, linearity, stability, and reproducibility. On the other side are the physicians who expect a diagnostic tool that provides fast acquisition of patient information to obtain an early diagnosis or an efficient patient stratification, consequently making assertive and efficient clinical decisions. The development of diagnostic devices always involves assay developer researchers working as pivots to bridge both sides whose role is to find detection strategies suitable to the clinical needs by understanding (1) the intended use of the technology and its basic principle and (2) the preferable type of test: qualitative or quantitative, sample matrix challenges, biomarker(s) threshold (cutoff value), and if the system requires a mono- or multiplex assay format.

Although different biosensor technologies are available and under development, this thesis focuses on 2D material-based field-effect transistors as a technology, meaning that the development challenges discussed here will focus on the biomarker detection and clinical requirements discussed in the published review [10].

2.2.1. Biosensor development challenges

In the development of a biosensing system, the analytical performance allows us to understand the capabilities and limitations of the technology and essentially analyze if it addresses a specific application or not. Several general parameters indicate the performance of a biosensor, such as the sensitivity, limit of detection (LoD), specificity, reproducibility, and dynamic range (DR). Therefore, it is essential to have an intended clinical purpose before developing a biosensor. For example, diagnosing some complex diseases requires the detection of multiple biomarkers with specific cutoff values, meaning that those biomarkers may exist in an ordinary person but at constant or low concentrations. This issue is one of

the most challenging aspects to address in developing a diagnostic tool. The device needs to look for multiple rather than individual biomarkers and distinguish between certain levels of those biomarkers, rather than distinguishing a minimal concentration from zero. In this case, the biosensors' sensitivity, dynamic ranges, and resolutions may be critical parameters to address. Therefore, the detection strategy should be optimized considering the complexity of the biomarker(s), the affinity of the biorecognition elements, the clinical cutoff values, the relevant dynamic range, and the sample matrix. [10]

The biosensor sensitivity, i.e., response signal for every unit of the target sample's concentration, is typically enhanced by improvements on the signal-to-noise ratio (SNR), which can be achieved by the use of sandwich assays [132–134], nanoparticle-based labels [135–137], or use of high surface area materials (1D or 2D materials) [124,138–140]. 2D materials for the advanced sensing structure can be graphene [81,141,142] that enhances the detection down to attomolar to femtomolar ranges [143–145]. Other 2D materials, such as molybdenum disulfide (MoS_2), reported being able to boost the detection down to the femtomolar range for protein [58] and DNA detection [146], respectively. [10]

The dynamic range is the concentration window between the signal response's maximum and minimum usable indication. Nevertheless, the signal response does not always increase proportionally to the target concentration in the dynamic range, particularly in the extremely low or high concentration target. Therefore, another term that biosensor experts use is the linear dynamic range to determine the biosensor signal response in the linear region of the fitting curve. The linear dynamic range is a trade-off parameter compared with the sensitivity (i.e., when the sensitivity value is high, the detection range will be small). On the other hand, if the application requires a significant linear range performance, the sensitivity of the biosensor will be lower [147,148]. The dynamic range can be enhanced by increasing the surface area of the sensing. However, when developing detection strategies for clinical biomarkers, determining the valid dynamic range is the cutoff value (threshold) of the interest biomarkers. Technology may allow a log-linear range, but depending on the device's intended use, the researcher may need to adjust several parameters (if possible) to obtain a narrower dynamic range. The use of different structures of sensing [148,149], diluted and label tailoring [67], varying the concentration of biorecognition elements [150], and the use of antibodies with different affinities [151] are some of the parameters that can be manipulated to achieve the pretended sensitivity and dynamic range. [10]

The general concept of sensing is distinguishing a particular substance from others (selective) and capturing a particular target (specific). Therefore, the biosensing system should be configured to detect a specific target through selective and robust affinity binding with the specific biorecognition element. The quality of the biological components will determine the specificity and, consequently, the sensitivity of the

developed detection strategy. Moreover, complex samples may require two labels (dual-labeling) to increase the assay specificity [152]. Measurements of the non-complementary samples are compared to those with the specific target to evaluate specificity. A functional biosensor should distinguish these different samples producing significantly different response signals. Ideally, the non-specific target's resulting signal level is similar to the zero-concentration measurement of the biosensor. Nevertheless, in the presence of a high concentration of non-specific targets, a false positive or drift signal can appear due to non-specific bindings and interferences. Several attempts have been reported to improve the specificity and low fouling binding during the biosensing measurements, either in competitive assays or complex media such as serum or whole blood. For example, by blocking assays [153–155], polymer brush, and zwitterionic functionalization surface [156–159], also by using label and sandwich assays to obtain a specific signal [160–162]. In immunoassays, monoclonal antibodies are also recommended to obtain high specificity and lower cross-reactivity events [163]. [10]

Besides the challenges associated with the mentioned analytical performance parameters, in the case of complex diseases in medical science, analyzing a single biomarker is not enough to evaluate the biological or pathogenic process. Therefore, assessing a panel of biomarkers is required to improve the specificity and accuracy of the diagnosis. In the case of complex diseases in medical science, analyzing a single biomarker is not enough to evaluate the biological or pathogenic process. Therefore, assessing a panel of biomarkers is required to improve the specificity and accuracy of the diagnosis. For example, Duffy 2020 [164] noted that PSA single biomarker detection is not enough to assess the prostate cancer state. The study proposed additional biomarkers such as PHI (Prostate Health Index), 4K score, and prostate cancer gene 3 (PCA3) as the panel biomarkers. The 4K score itself contains the total PSA, free PSA, intact PSA (a form of free PSA), and human kallikrein 2 (hK2) [164]. Another panel of biomarkers has been proposed to evaluate colorectal cancer (CRC). In clinical practice, the RAS gene family (KRAS and NRAS), BRAF, HER2, and microsatellite instability (MSI) have been reported as candidates for the panel of biomarkers [165]. A panel of biomarkers has also been proposed for ovarian cancer assessment [166]. These findings in medical sciences can be a valuable milestone for the clinical application of biosensors to perform panel biomarkers simultaneously. [10]

A cutoff value needs to be considered for each of the biomarkers of interest for clinical diagnosis since this value can help provide the stage for disease diagnosis [10]. Therefore, a comprehensive analysis of the biomarkers in the context of the clinical diagnostic is critical for developing a biosensing method able to improve clinical decisions. For example, in the case of prostate cancer, a study suggested a clinical cutoff value for the PSA biomarker of 4 ng/ml in blood. In patients, the PSA concentration can reach up

to 104 ng/mL, while it is usually below 0.1 ng/mL in healthy people. As such, patients with a PSA concentration higher than 4 ng/mL are required to perform a biopsy analysis. Another study recommended that the range of 2–4 ng/mL be considered the grey area, although it will decrease the TP rate [167]. Although only one biomarker is detected, if the biosensor is sensitive enough (LoD below 4 ng/mL), it can increase the chance for diagnostic of prostate cancer at an earlier stage of the disease, improving the chances of a positive outcome for the patient. Another option could be the inclusion of multiple biomarkers in the initial analysis as suggested by Duffy 2020 [164], which proposed the use of additional biomarkers such as prostate cancer gene 3 (PCA3), and the Prostate Health Index (PHI), 4K score. These biomarkers must be thoughtfully studied to determine a cutoff value and the entire panel for clinical analysis. [10]

The cutoff value for multiple biomarkers must be determined to achieve precision and accuracy in the clinical diagnostic tools of complex diseases. One such example can be seen for stratification ischemic stroke patients for tPA) therapy. A group of researchers from clinical neurosciences proposed a panel of biomarkers that reflect patients undergoing ischemic stroke [63]. It was proposed that for levels of cellular-Fibronectin (c-Fn) above 3.6 µg/mL [62,65], Matrix Metalloproteinase 9 (MMP9) above 140 ng/mL [62,65], Platelet-derived Growth Factor-CC (PDGF-CC) above 175 ng/mL [72], Neuroserpin below 70 ng/mL [74], and the calcium-binding protein S100β above 230 ng/mL [62,75], the patients can be at a higher risk on developing a hemorrhagic transformation (HT) after tPA treatment. Although the detection of each biomarker is not specific for HT risk, the combination of at least two biomarkers (c-Fn and MMP9) can provide a detection specificity of 87%, increasing the chances of a safe diagnosis and improving clinical decision [65]. [10]

It is also essential to notice that the same biomarkers could be used to diagnose other diseases as long as the cutoff values and biomarker combination are adjusted to the clinical condition at the study. Wood et al. [168] also reported optimizing multiple parameters in a particle-based platform to achieve detection of 3 different analytes (multiplex assay) with different ranges of relevant concentrations. Parameters such as particle concentration [67,168], capture antibody affinity [67,168], measuring conditions [67], and sample preparation (e.g., dilutions) [67,168] affect the outcome of the developed assay and can be tuned to fit the necessary cutoff for the clinical application being targeted. [10]

As such, biosensor platform application to the clinical environment depends on adjusting its dynamic range to cover the clinical cutoff concentration of the biomarkers and provide multiple biomarker detection to provide specific diagnostics. [10]

2.2.2. Hemorrhagic transformation risk assessment

As mentioned previously (sections 1.3 and 2.2.1), to tackle the clinical emergency of ischemic stroke, a single biomarker is not enough to provide a clear assessment of the risk of hemorrhagic transformation (HT) after tPA therapy [65,74,75]. However, to the moment, few biosensor technologies reported detection of the interest biomarkers [67,169–172], and only one report was found dedicated to a biomarker of the panel in the context of HT risk assessment [67].

The detection of MMP9 and cFn has been reported by using different technologies [67,169–172]. Mohseni and colleagues used surface Plasmon Resonance (SPR) to develop an immuno-sensor for MMP9 detection, which achieved limits of detection (LoD) in the order of pg/mL by refractive index changes in the sensor upon the recognition event [170]. Recently, using a similar technique, Sankiewicz and colleagues developed an SPR imaging system for immuno-detection of fibronectin, achieving an LoD in the ng/mL range [172]. Other authors report MMP9 detection using electrochemical techniques with LoD in the range of pg/mL [169,171] to ng/mL [173]. However, consideration for the clinical relevance of the biosensor parameters is lacking in these reports. In the case of HT risk assessment, the biosensor must be tuned to provide a linear dynamic range that covers the relevant cutoff value, i.e., 3.6 µg/mL for cellular fibronectin. A recent report by Fernandes et al. [67], which results from a partnership between the assay developers and the clinical staff, explores the specific detection of cellular fibronectin and tuning of the biosensor performance to match the clinically relevant parameters of the biomarker [67].

The significant challenges for developing effective assays for HT risk assessment within the relevant time window for tPA therapy are related not only to the fine-tuning of the sensitivity and dynamic range reported [67] but also with the multiple biomarker analysis (multiplex assay) and sample processing to reduce operator influence and effects of the complex samples on the sensing system..

3. Motivation

As reviewed in the previous sections, there is a lack of diagnostic tools for the stratification of stroke patients. A panel of six biomarkers (Angiopoietin-1, Cellular Fibronectin, Matrix Metallopeptidase -9, Neuroserpin, Platelet-Derived Growth Factor-CC, and S100β) can be used to predict which patients have the risk of developing HT, allowing the assessment of the adequate and efficient clinical treatment of stroke [70–72,74]. The main goal of this thesis is the application of 2D material-based immuno-FETs to detect the defined panel of biomarkers. Using a widely studied 2D material (graphene) as a sensing surface in a FET configuration will be explored to provide label-free and fast analysis of the biomarkers of interest, focusing on MMP9 and c-Fn for initial assessment of the biosensing technology.

Field-effect transistors are tested and optimized for biosensing, considering the application's needs for chemical and biological exposure often overlooked in microfabrication. The graphene surface is further studied to confirm its potential for biofunctionalization and specific detection of protein biomarkers. Biosensor development is then reported combining the graphene FETs and the biofunctionalization methodology, using reference biomarkers (e.g., BSA) and then the clinically relevant biomarkers.

Biosensor development allows studying the devices' sensing parameters and assessing how they fit the clinical application. Besides, the effects of the biological sample and potential for direct detection are accessed, keeping in mind that sample processing using operator-free systems (microfluidics) might need to be developed later to optimize biomarker detection.

The present document is divided into six chapters. The first chapter (Chapter I – Introduction) reviews field-effect transistors as biosensors, the properties of 2D materials that make them appropriate for biosensing applications, and the current state of the art applying of these materials. This chapter (Chapter I – Introduction) also reviews the clinical ischemic stroke physiopathology and limitations in current analysis and treatment derived from lack of efficient stratification tools and the most recent advances in biosensing development for complex diseases. Chapter II (Microfabrication and characterization of EG-FETs) reports the development and optimization of the microfabrication processes for EG-GFETs compatible with biosensing applications. Chapter III (Biofunctionalization of 2D materials) reports the study of the surface chemistry to achieve a consistent and stable functionalization methodology for graphene surfaces. Chapter IV (Assessment of graphene immuno-FETs for detecting stroke-related biomarkers) discusses the effects of the exposure of charged proteins in EG-GFETs, specific detection of the interest protein biomarkers (MMP9 and c-Fn), and variability within and between EG-GFETs from the same batch. Chapter V (Biological Matrix studies) reports the effects of the exposure of EG-GFETs and mimic surfaces to the clinical sample of interest (human serum) and shows the potential of the developed devices for real-sample analysis. The final chapter (Chapter VI – Future Work) resumes the limitations of the present work with proposals for improvement of the technology and assays. Supplementary information to the chapters is found in the Appendixes at the document's end.

Chapter II – Microfabrication and characterization of EG-FETs

The contents of this section are present in the publication " Clean-Room Lithographical Processes for the Fabrication of Graphene Biosensors" by Patrícia D. Cabral, Telma Domingues, George Machado, Jr., Alexandre Chicharo, Fátima Cerqueira, Elisabete Fernandes, Emília Athayde , Pedro Alpuim and Jérôme Borme, in Materials 13 (2020) 5728 (https://doi.org/10.3390/ma13245728).

Personal Contribution: Methodology development, data processing and analysis, investigation, original draft writing, reviewing, and editing.

1. Introduction

Since first obtained by the exfoliation of graphite [44], graphene has been explored in numerous applications [16,174,175] due to its outstanding properties, such as high carrier mobility [16,174], low intrinsic electronic noise [16,94], chemical stability [16,39,94], high sensitivity to electric charges in its vicinity [16,174], and record surface-to-volume ratio [94,174]. Graphene has been used as the building block for various electronic biosensing systems, with high sensitivity [175]. Among them, electrochemical sensors [176] and field-effect transistors (FETs) are the most common. Graphene FETs (GFETs) make use of graphene sensitivity to electric fields and charges [16,177] to produce the output signal of the sensor, operating at low voltages [177]. Additionally, GFETs are compatible with the upscaling of the sensor fabrication process [177]. GFETs can be found as top-gated, back-gated, or in a combined geometry, for the detection of a variety of molecules/biomolecules and ions [175], including pH [84], glucose [175], deoxyribonucleic acid (DNA) [175], proteins [94], and hormones [175]. Graphene is a zero-bandgap material that generates electrons and holes under an applied transverse electric field, which is a process known as electrostatic gating [16]. Therefore, an electron or hole drain current is generated for positive or negative gate voltages, with a minimum value at the charge neutrality point (CNP), where graphene is considered non-doped [6,16]. In a top gate GFET, a liquid electrolyte can replace the commonly used solid dielectrics (electrolyte-gate GFET, EG-GFET), usually a thin Al_2O_3 or SiO_2 film [39]. In this configuration, the gate potential falls in the nanometer-thick electrical double-layers (EDL) forming at the solid–electrolyte interfaces, providing a high gate capacitance to operate the transistor at a very low voltage. The possibility of detecting small changes in GFET transfer characteristics due to minute changes in the interfacial charge distribution that modulates the gate capacitance paves the way for ultrasensitive biosensing. Thus, EG-GFETs are ideal candidates for molecular sensing with electronic transduction [6,19]. EG-GFETs are commonly built without the reference gate electrode (Figure 13), which is then added as an external, cumbersome metallic wire (made of gold, platinum, or silver) used for measurements [19]. Making the gate electrode part of the wafer, coplanar with the source, and drain electrodes allows for planar technology single-lithographic mask contact fabrication as well as design flexibly regarding the transistor layout [19,39].

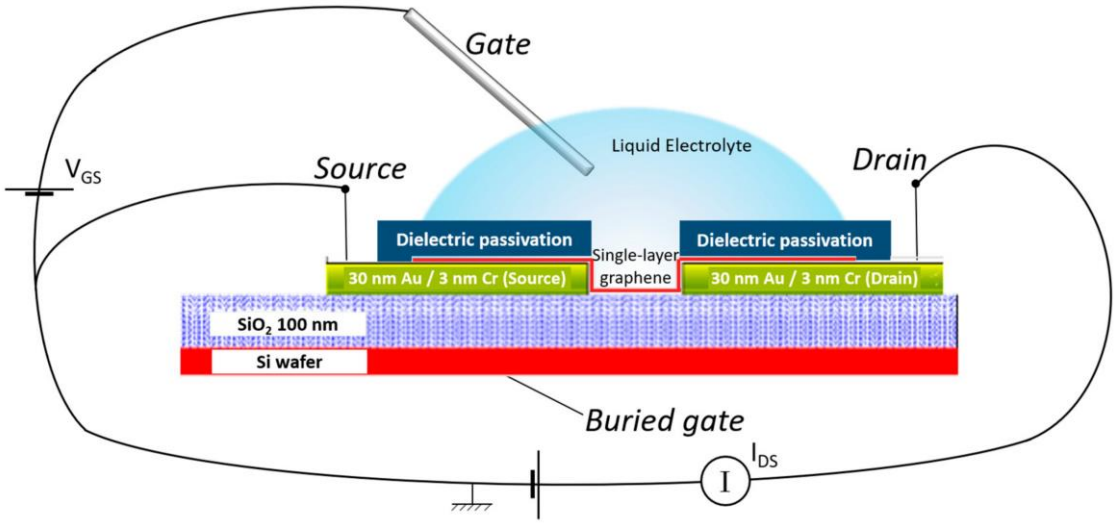

Figure 13. *Working model of a typical graphene field-effect transistor in which a liquid electrolyte replaces the commonly used solid dielectrics (EG-GFET). A fixed voltage is applied between the source and drain contacts, and the current output is measured as a function of the gate-source voltage. Dielectric passivation is applied on top of the source and drain contacts to avoid interaction of the electrolyte at these regions to improve signal stability. V_{GS}—gate-source voltage, I_{DS}—drain-source current.*

When designing EG-GFETs, it is crucial to consider their application, e.g., the device's environment, to decide design and fabrication steps. Electrolyte gating implies using liquids on top of semiconductor materials that typically degrade upon contact with aqueous solutions. Moreover, semiconductor and dielectric materials are prone to host ions that diffuse inside their lattices, degrading the materials or making electronic measurements unstable. Therefore, except graphene, the passivation of surfaces in contact with the electrolyte is recommended to prevent/minimize such effects [19]. The passivation layer can be done by coating the wafer surface with photoresist [19], epoxy resin [33], or silicon nitride (SiN_x) and silicon oxide (SiO_2) layers [34,35]. An adequate protection strategy allows to place the electrolyte over a large number of devices without cross-talking [36], reduce leakage current [33], reduce drift due to ion diffusion, and prevent damage of the metallic electrodes [36]. Thus, when designing a biosensors process, it is essential to consider permeability to salts and solvents to choose the passivation layer material. If polymers are chosen, they must be resistant to saline solutions [36] to avoid degradation upon exposure to biological solutions. If silicon-based materials are used, one must consider that SiO_2 is much more permeable to ions than SiN_x. A higher permeability may allow ions from the test solution to reach the current lines and cause drift, cross-talking between electrodes, or corrosion of the metallic contacts [36].

For example, dimethylformamide (DMF) as a graphene cleaning agent after wafer fabrication and as a solvent in the graphene's non-covalent functionalization [42] would not be allowed in polymeric passivation. Although DMF does not dissolve SU-8, it degrades and unseals continuous films [178]. One of the initial stage designs developed in this work and tested with a master student observed that DMF damages the direct-write epoxy resist mrDWL1x, promoting its release from the surface and re-deposition elsewhere, which renders the device unusable [179]. Passivation using SiO_2 or SiN_x layers allows exposing the devices to all solvents without compromising the passivation. However, it implies more complex lithographic and etching processes, thus increasing the fabrication cost.

In conclusion, it is of paramount importance to keep in mind the application of the EG-GFET when designing the passivation of current lines. An important consideration is to decide at which point of the fabrication process the passivation layer should be added. Overall, lithographic processes involving aggressive patterning steps (e.g., dry etches, lift-off processes) should be avoided once graphene is transferred onto the wafer since they increase the number of residues left on graphene [39]. Therefore, inorganic passivation layers should be patterned before graphene transfer. However, this leaves the source and drain contacts unprotected since they receive graphene in a subsequent step. Leaving those contacts exposed to the electrolyte contributes to signal instability due to varying electrolyte potential during gate voltage sweeps [19] and device-to-device variability due to uneven coverage of the large electrode area with graphene, namely at its edges. In summary, the passivation layer's optimized design recommends adding it only after graphene transfer, protecting all surfaces except the graphene channel and the metal gate electrode, which is exposed to the electrolyte. However, this collides with the earlier stated principle of avoiding lithography of hard layers in the presence of graphene.

Passivation based on photoresists is done in a relatively straightforward process, using one lithographic step only followed by development in solution (a mild process) and sometimes a final bake to harden the layer. However, for passivation based on SiN_x/SiO_2, the process implies more aggressive steps, e.g., plasma-based etching or sputtering depositions that can affect graphene integrity [39]. Some authors avoid dry etching steps by patterning the passivation layer via wet etch using a strong basis or acid [180]. However, chemically dangerous solutions (e.g., buffered hydrofluoric acid (HF)) should be avoided for safety. Moreover, it is common to observe an undercut when performing wet etch, promoting the passivation layer's peeling. An alternative proposal combines the two strategies, avoiding dry etch directly on graphene (partial dry etch) and reducing the times required for wet etch to limit the undercut effects. Dependence on wet etch processes always limits reproducibility and process upscaling [34].

There are additional constraints that need to be met when considering dry etching on graphene. The suggestion of the presented work is to use a stopping layer on the graphene active regions preceding the passivation layer's deposition. The stopping layer serves two purposes: protect graphene during dry etching and provide a dry etch-resistant surface signaling the process's end. For the deposition of the stopping layer, atomic layer deposition (ALD), thermal evaporation, and sputtering can be considered. ALD, owing to its low deposition rate, can only be deposited in thin layers. The ALD of aluminum oxide is beneficial for the thin gate dielectric in transistor structures. However, because graphene is hydrophobic, the ALD of aluminum on graphene must be preceded by an evaporated aluminum layer, which turns into an oxide layer by natural oxidation and presents a good surface for the ALD growth [181,182]. However, for a thin aluminum oxide stopping layer, there is no necessity to use ALD provided physical vapor deposition systems are used under conditions that minimize graphene damage. Here, we chose the stopping layer material from those possible to grow under milder sputtering conditions.

Another critical step in EG-GFET fabrication is graphene transfer. For applications requiring electronic grade material, there are few choices available beyond mechanically exfoliated graphene from highly oriented pyrolytic graphite (HOPG), Chemical Vapor Deposition (CVD) being one of them [48]. Still, mechanical exfoliation is not an alternative when a large area is required (wafer-scale fabrication). Graphene grown by thermal CVD on copper catalysts or the Si face of SiC wafers is currently the preferred solution to provide high-quality graphene over a large area [37]. The first approach is the most popular because of its low cost and high versatility [37], allowing the transfer of graphene onto virtually any substrate type. If precise control of the oxygen supply to the Cu surface during growth is put in place, huge crystal size and carrier mobility can be achieved [49]. Graphene grown on SiC wafers has the advantage of growing natively on a transparent insulating substrate and enables transfer-free fabrication of optoelectronic devices [50]. However, monocrystalline SiC substrates are too expensive to be used in large-scale production, and graphene grain size is limited by the atomic terraces' sub-micrometer width, unlike CVD graphene. Although wet transfer methods of CVD-grown graphene give the most promising results for the large-area fabrication of GFETs, there are still challenges related to surface contaminants [37,38] often overlooked in the biosensing field [17]. After graphene transfer and patterning, visible residues of different origins (polymethylmethacrylate (PMMA), metal residues) are almost always found on the device surface. Residues on the sensing surface hinder functionalization and promote the non-specific binding of biomolecules in undesired areas [17]. It is crucial to search for new strategies to improve surface cleaning after graphene transfer and patterning. After etching graphene from undesired surfaces (e.g., from the gate electrode), the residues attached to it (mainly metal contaminants) are not

entirely removed from the surface, bringing reproducibility usability issues to the biosensing device. In this work, we address strategies to improve surface cleaning after graphene patterning. Those issues are critical in fabricating EG-GFET biosensors with the highest sensitivity and lowest limit of detection.

2. Materials & Methods

2.1. Materials

Table 3. *Materials and reagents.*

	Description	Supplier
Materials	Cu foil, 99.99 + % purity	Good Fellow
	200 mm Si wafer, P-doped, 1–100 Ω cm, < 100 >	Silicon Valley Microelectronics, Inc.
	Si wafer with thermal oxide, 100 nm	Siegert Wafer
	Hexamethyldisilazane (HMDS)	Technic
	PMMA 15 kDa, powder	Sigma-Aldrich
	PMMA 550 kDa, powder	Alfa Aesar
	$FeCl_3$, 98%	
	KOH flakes, 90%	Sigma-Aldrich
Solvents	Dimethylformamide (DMF), 99.75%	Sigma-Aldrich
	Anisole, ≥99%	
	Acetone, 99.5%	Honeywell
	Isopropanol (IPA), 99.8%	
Photoresists	AZ1505	Microchemicals GmbH
	AZP4110	
	AZ400k 1:4	
	mrDWL1_XP	Micro Resist Technology
	AR 300.47	Allresist
	mrDev600	Micro Resist
Solutions	HCl, 37%	Sigma-Aldrich

2.2. Clean-Room Fabrication Tools

2.2.1. Deposition Tools

For thin film deposition on the 200 mm wafer and 4 × 4 cm samples, different sputtering, and chemical vapor deposition (CVD) tools are used depending on the material requirements. A Kenosistec DC

magnetron sputtering system is used to deposit thin metallic films of Cr, Au (contacts), Cu, and Ni (stopping layer). The base sputtering pressure is between 5×10^{-7} and 8×10^{-7} mbar. The sputtering conditions are 20 sccm Ar, 80 W, 300 mA for Cr; 6 sccm Ar, 100 W, 200 mA for Au; 20 sccm Ar, 100 W, 100 mA for Cu; and 15 sccm Ar, 100 W, 300 mA for Ni.

A Timaris FTM RF sputtering system is used to deposit films of Al_2O_3 (RF cathode, 200 sccm Ar, 2570 W), TiW(N) (DC cathode, 200 sccm Ar, 40 sccm N, 1000 W, 3 A), and AlSiCu (DC cathode, 200 sccm Ar, 2250 W, 6 A) for the sacrificial and stopping layers. All sputtered materials are obtained from high purity sputter targets. The AlSiCu mass composition is $Al_{98.5}Si_1Cu_{0.5}$ (mass fraction). TiW(N) is obtained from $Ti_{10}W_{90}$ (mass fraction) and sputtered in N plasma.

An SPTS MPX plasma-enhanced CVD, Newport, United Kingdom, is used to deposit films of SiO_2 and Si_xN_y for the passivation layer.

Single-layer graphene (SLG) was grown by chemical vapor deposition in a load-locked quartz tube 3-zone furnace (FirstNano EasyTube® 3000) onto 99.99 + % purity copper (Good Fellow) foils (25 µm thickness). For growth, a gaseous mixture of methane/hydrogen at a gas flow rate ratio of CH4:H2 1:60 was used. Graphene grows on both sides of the copper foil.

2.2.2. Lithographic Tools

The wafer/samples for lithography are prepared as follows. HMDS silanization is performed with YES Vapor Prime Oven 310TA, Livermore, CA, USA, to improve photoresist adhesion. Coating with the photoresists AZ1505 and AZP4110 is performed with Suss Microtec Gamma Cluster tracks, Garching bei München, Germany, with baking temperatures of 100 °C and 110 °C, respectively.

Patterning of the photoresist films is done using Direct Write Laser Lithography—DWL2000 with 405 nm laser. The masks for patterning are prepared with LibreCAD software.

2.2.3. Dry Etch Tools

The tools for dry etching are divided into two groups: the patterning of thin films and graphene. For contact layer patterning, a Nordiko Ion Milling system, Havent, UK, is used, with 300 s of etching at an angle of 40° between the normal to the wafer plane and the incident ionic stream. The Ar plasma is 440 W with a working pressure of 4×10^{-4} Torr, and a −3200 V grid accelerates the ions before neutralization.

For patterning of the passivation layer, an SPTS APS SiO_2 Etcher, Newport, UK, is used with 150 s of plasma, for complete etching of the passivation, including 25% over etch. The reactive mixture contained C_4F_8 50 sccm, H_2 30 sccm, and the working pressure is 6×10^{-3} mbar.

High-power O_2 plasma in a Roth & Rau cold wall plasma-enhanced CVD system is used to clean the back side of the graphene catalyst Cu foil for 4 min (8 cycles of 30 s plasma) under 200 W of plasma and pressure 4×10^{-1} mbar. For patterning graphene, low-power O_2 plasma is used in a PVA TEPLA Plasma Asher, Wettenberg, Germany, for 18 min (3 cycles of 6 min plasma) in conditions: 230 W, O2:Ar 1:1, 0.5 mbar, or high-power O_2 plasma is used in a SPTS ICP system for 30 s in conditions: 1200 W, O2 100 sccm, 3×10^{-2} mbar.

2.2.4. Dicing Tools

To cut 4 cm by 4 cm testing samples and to dice the wafer into individual chips, a Disco DAD 3500 Automatic Dicing Saw, Tokyo, Japan, is used, with a Mikrokerf 2.187-10-30H (hub-type blade, 254 µm width, 30 µm diamond grit in hard resin). Previously to dicing, the wafers are coated with AZ1505 photoresist to keep the devices free of debris. The blade water flux is reduced to half the usual value to prevent damage to the graphene surfaces. The blade is spinning at 30 krpm, and the feed speed is 8 mm/s.

2.3. Characterization Techniques

2.3.1. Raman Spectroscopy

Confocal Raman spectroscopy (WITec Alpha 300R, Ulm, Germany) is used to confirm single-layer graphene presence in transferred samples and detect variations in graphene quality after microfabrication processes. Raman data analysis is done using WITec Project FOUR+ software, Ulm, Germany. All samples are analyzed using a 532 nm Nd:YAG laser for excitation. The laser beam with power in the range 2 to 3 mW is focused on the sample by a ×50 lens (Carl Zeiss, Jena, Germany), and the spectra are collected with a 600 groove/mm grating using 5 acquisitions each with 2 s acquisition time. Within each experiment, the laser power is fixed to allow a comparison of the acquired data.

2.3.2. Scanning Electron Microscopy/Energy-Dispersive X-ray Spectroscopy

Scanning Electron Microscopy (SEM), FEI NovaNanoSEM 650, Hillsboro, OR, USA, is used to study surface features and energy-dispersive X-ray spectroscopy (EDX) analysis. SEM images are collected in the secondary electron imaging mode at a 5 mm working distance and an operating voltage of 5.0 or 10.0 kV, depending on the materials to be analyzed and the probing depth desired.

EDX acquisition using Oxford Instruments INCA software, Oxfordshire, UK, is performed on selected regions from SEM images to confirm surface chemical composition and detect surface contaminants after completing the fabrication process.

2.3.3. Mechanical Profilometer

KLA–Tencor P-16 Surface Profiler, Scotia, NY, USA, is used to measure photoresist films' step height after O_2 plasma-based etching steps.

2.3.4. Optical Interferometer

OPM Nanocalc–Optical Profilometer/Interferometer, Ettlingen, Germany, is used to estimate SiO_2 and SiN_x films' thickness, using a deuterium–tungsten halogen light source. The thickness is determined by fitting to a model using reflected light between 40 and 800 nm.

2.3.5. Optical Microscope

Nikon Ni-E optical microscopes, Tokio, Japan, are used to assess the sample surface after each fabrication step visually.

2.3.6. Graphene EGFET Electrical Characterization

For acquisition on the transfer curves of the fabricated EG-GFET samples, the source and drain contacts of each transistor are connected to a Keithley 4687 Picoammeter, Cleveland, OH, USA, which applied a constant (1 mV) source–drain voltage (V_{SD}), and the source–drain current (I_{SD}) is measured. The high-impedance gate circuit is formed between gate and source contacts. It is biased by applying a voltage (V_{GS}) by a Keithley 2400 source meter, Cleveland, OH, USA, which is programmed to apply voltage ramps from 0.2 to 1.2 V in steps of 0.01 V. All the measurements were performed using 10 mM phosphate buffer as gate electrolyte to close the circuit.

For full-wafer characterization, an automated wafer probe station is used. The graphene channels' resistance is analyzed by applying a constant voltage between source and drain (1 mV) and measuring the channel's current, using a Keithley 2400 source meter. No liquid electrolyte is added to the devices, and no gate voltage is applied (the gate contact is left floating). Channel resistance values by the device are obtained by processing the current measurements using MATLAB scripts.

2.4. Microfabrication Methods

2.4.1. Dry Etch Patterning

For dry etch patterning, the samples were coated with positive photoresist AZ1505, and the pattern was written using a DWL2000 optical lithography system with a CAD mask and 405 nm laser. After exposure, the samples were developed with AZ400k 1:4 developer for pre-determined times according to the film

thickness. According to the etched layer, the dry etch was performed using different equipment (described in section 2.2.3.).

2.4.2. Fabrication of Metal Contacts and Interconnects

Following the strategy of maximizing lithography process steps before graphene transfer, we start the fabrication of the EG-GFET by depositing and patterning the source, drain, and gate contacts. A 200 mm Si wafer with 100 nm of thermal oxide is coated by sputtering with an adhesion layer of chromium (Cr, 3 nm) followed by a conductive layer of gold (Au, 35 nm) and a sacrificial layer of alumina (Al_2O_3, 10 nm). The contacts were patterned into 513 square dies of 6.75 mm side using optical lithography and ion milling for etching the unprotected Cr/Au/Al_2O_3 into the desired pattern. The etching process is followed by Secondary Ion Mass Spectroscopy (SIMS) using the extinction of the Cr signal as endpoint criterion. The gap between source and drain contacts (the channel length) is fixed at 25 µm, and the width of the gold contacts is 83 µm in all devices (the channel width is 75 µm). The layout of the contacts is made to accommodate 20 graphene EG-GFETs divided into 4 groups of 4 FETs and 2 groups of 2 FETs, which is a layout specifically developed to perform multiplex assays in biosensing. The Si wafer is diced in chips of 4 × 4 cm2, each containing 36 dies, before performing the tests described in the following sections.

2.4.3. Graphene Transfer

For graphene transfer, a temporary poly(methyl methacrylate) (PMMA) substrate was used. PMMA was spin-coated onto the top side of the graphene/Cu/graphene sample, and copper was further dissolved by dipping the PMMA/graphene/Cu into a 0.5 M $FeCl_3$ solution for 2 h. PMMA/graphene was cleaned in 2% HCl solution to remove metal precipitates and washed in deionized water three times.

PMMA/graphene films were transferred to the pre-patterned silicon/silicon dioxide (Si/SiO_2) wafer substrate. After transfer, the sample is dried in the air overnight. Then, the PMMA is removed using acetone. Graphene quality, i.e., the homogeneity of the obtained graphene film after the transfer, is first investigated by optical images. Confocal Raman spectroscopy was used to confirm the presence of SLG.

3. Results & discussion

3.1. Graphene Transfer and Pattern Leaving a Clean Wafer Surface

In this study, graphene was grown by CVD in a hot-wall reactor (First Nano ET3000, New York, NY, USA) on high-purity Cu catalysts and transferred. The process was optimized to achieve monolayer films with low defect density, as shown by the Raman spectra in Figure 14. Graphene is transferred to the final substrate using a temporary polymeric substrate (PMMA) as described in section 2.4.3 of this chapter.

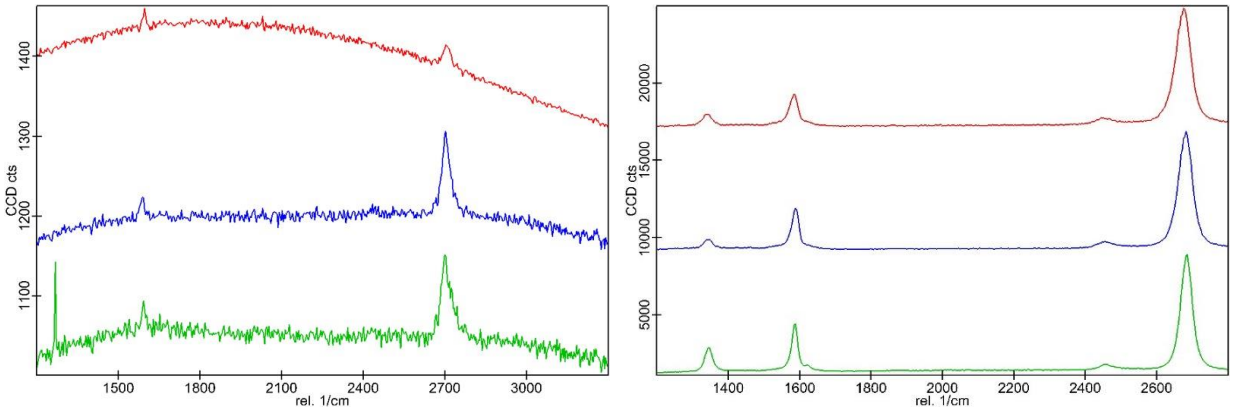

***Figure 14**. Raman spectra of graphene as grown in Cu foil (A) and after transfer to a SiO_2 substrate with gold contacts (B) in three different sample points (red, blue, and green represent individual sample points).*

Graphene transfer and patterning are crucial steps in the fabrication of graphene devices. Except for automated, continuous transfer systems [183], which are not universally available yet, the wet graphene transfer limitations are mostly user-related, requiring a trained hand to achieve reproducible results.

At least two kinds of transfer-borne residues can come from the transfer process. Apart from polymeric residues, copper residues from the foil or iron precipitates from the $FeCl_3$ etching solution may attach to the graphene film's bottom side, later sticking to the surfaces onto which graphene is transferred, shown in Figure 15. Precipitates can be reduced by using a metal-free etchant such as ammonium persulfate or using the HCl solution to dissolve the iron. Air bubbles present in the copper foil can lead to undissolved copper clusters after the dissolution process. Using fresh $FeCl_3$ solutions and sequential dissolutions can improve the removal of Cu clusters. Regardless, small Cu atomic clusters and ions are consistently observed in the surfaces after graphene transfer, as shown by PIXE studies [184]. Those particles may not influence graphene's surface processes since they are performed on the top side (the residues are mostly trapped at the interface between the substrate and graphene) but are transferred to other exposed

wafer surfaces. In our design, where the top gate electrode is coplanar with the transistor channel, the exposure of this electrode during transfer leads to adsorption of the residues on the gold surface, as evidenced in Figure 15D. This contamination is also a source of parasitic signal because exposure to biological solutions leads to non-specific protein adsorption at the particle sites. In particular, if such sites are located on the gate electrode, changes in the voltage drop at the gate–electrolyte interface are observed [14,122]. This effect changes the biosensor's concentration-dependent behavior to a random behavior hindering interpretation, optimization, and device use.

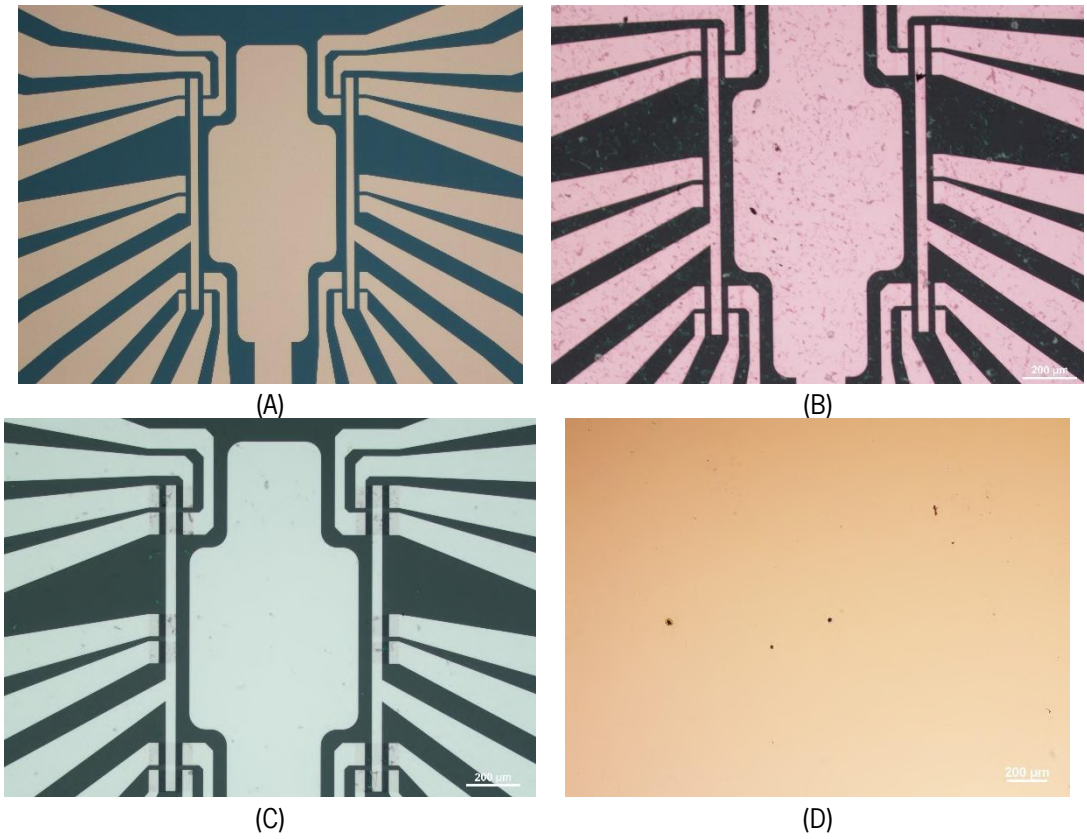

Figure 15. *Optical microscopy photographs of a chip surface before and after graphene transfer. (A) Pristine surface with no visible contaminants with 5× magnification. (B) After graphene transfer, a great number of small particles are visible, even at 5× magnification. (C) After graphene removal through O_2 plasma etching, the particles/contaminants are still visible at 5× magnification, meaning they are permanently attached to the surfaces. (D) Transfer-borne residues on gold surface after graphene removal at 5× magnification. Scale bar of 200 µm for all photographs.*

3.1.1. Dry Etching

The most common way to pattern graphene is reactive ion etching, using an oxygen plasma that readily attacks and removes carbon (Figure 16). For dense patterns or smaller features where mask transfer

accuracy is critical, a plasma technique with some ion bombardment level is necessary, such as commonly used inductively coupled plasma sources (ICP). Electron cyclotron resonance remote plasma sources (ECR) are suitable for isolated and micrometer-sized features. When using dry etching methods, the patterning material, photoresist, must be considered carefully to ensure it sustains the etching process while being easily removed after patterning, leaving few residues on graphene. The etch process's critical parameters are the radiofrequency (RF) power and the O_2 partial pressure since they influence the etching efficiency and the exposure time that the photoresist can sustain. However, the process is dependent on the size of the etched area. For example, etching small substrates with a few tens of square centimeters is very different in etching time and uniformity than etching a 200 mm-wafer due to changes in the plasma current at the surface of the sample [185,186].

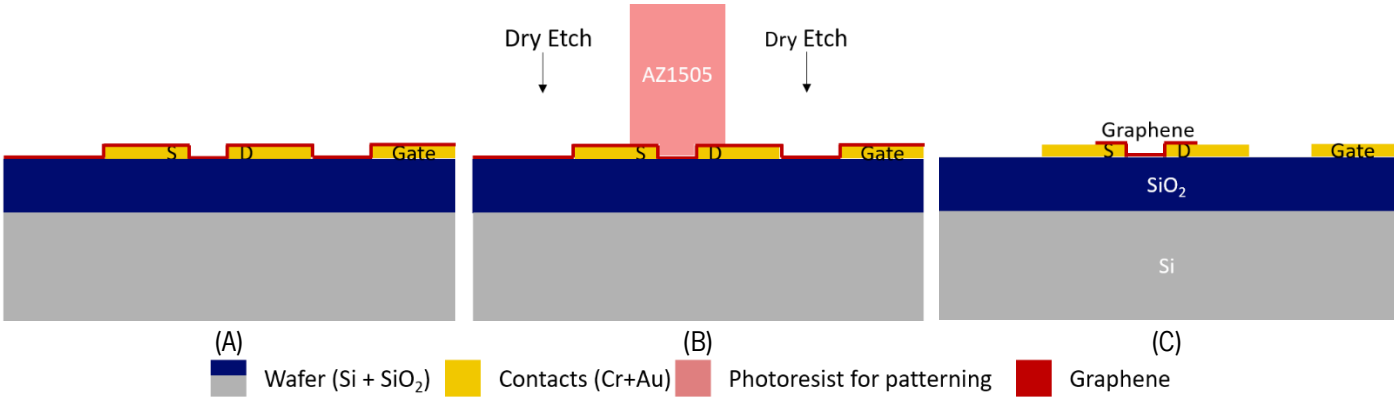

Figure 16. *Graphene patterning, after wet transfer, by standard O2 plasma etching. (a) After wet transfer, graphene covers all the surfaces of the devices. (b) Use of AZ1505 photoresist to protect the channel, source, and drain during O2 plasma etch of excess graphene. (c) Patterned sample with graphene covering the source and drain contacts and the channel between them.*

Two positive photoresists (AZ1505 and AZP4110) were exposed to plasma etching in a barrel reactor ECR plasma asher and an ICP reactive ion etching system. We first obtained conditions suitable for graphene etching in the two systems; then, we obtained the resist etch rate. To this goal, we measured the remaining thickness of 25 µm × 75 µm isolated resist features using a mechanical profilometer (KLA–Tencor P-16 Surface Profiler) in between etching steps as a function of the total etching time (Figure 17). The figures for photoresist height variation with O_2 plasma time indicate that the photoresist is etched much faster when using the ICP O_2 reactive ion etching (RIE) (Figure 17B) than when using the ECR O2 plasma source (Figure 17A). ECR shows different etch rates between the two photoresist masks (Figure 17C and 17D). The high-power (1200 W) ICP leads to a ≈700 nm/min etching rate for both photoresists.

The low-power (230 W) ECR asher, with a sample temperature lower than 100 ◦C, leads to an etch rate of ≈30 nm/min for AZ1505 and of ≈70 nm/min for AZP4110.

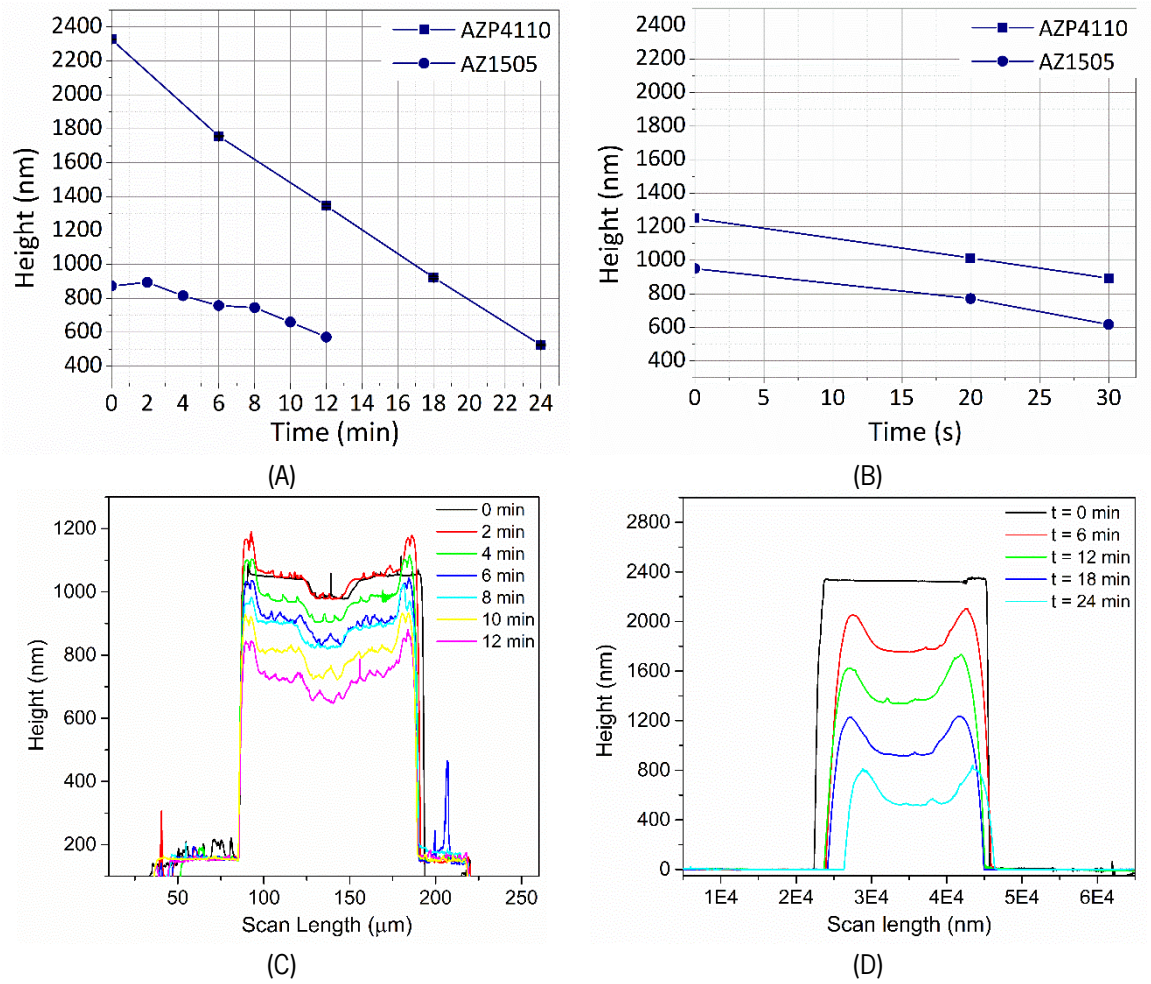

Figure 17. *Effect of exposure time to O2 plasma using electron cyclotron resonance (ECR) plasma source and inductively coupled (ICP) plasma source on different positive photoresists. (A) Thickness variation of different positive photoresists as a function of exposure time to O2 plasma using ECR (low power) plasma source and (B) ICP (high power) plasma source. (C) AZ1505 photoresist profiles after each 2 min exposure to ERC (low power) O2 plasma, with an initial thickness of ≈1 µm, showing decrease in photoresist thickness in each additional 2 min step. (D) Profile of AZP4110 photoresist after each 6 min of ERC (low power) O2 plasma, with initial thickness of ≈2.4 µm, showing a decrease in photoresist thickness in each additional 6 min step.*

Considering the etching times allowed by both methods, samples with pre-patterned contacts and graphene are patterned. For the ECR plasma source, the sample is coated with AZP4110 at 2200 nm (nominal thickness) to maximize the etch time. The sample is etched for a total time of 18 min divided into 6 min etching periods (to allow better temperature control of the sample). For the ICP plasma source,

the sample is coated with AZ1505 at 1035 nm (nominal thickness) and etched for 10 s. According to the values in Figure 17, both samples should end up with approximately the same photoresist thickness, ensuring proper protection of the graphene channels. The optical photographs in Figure 18 show efficient graphene removal for both methods. However, transfer-borne residues are also visible with high density.

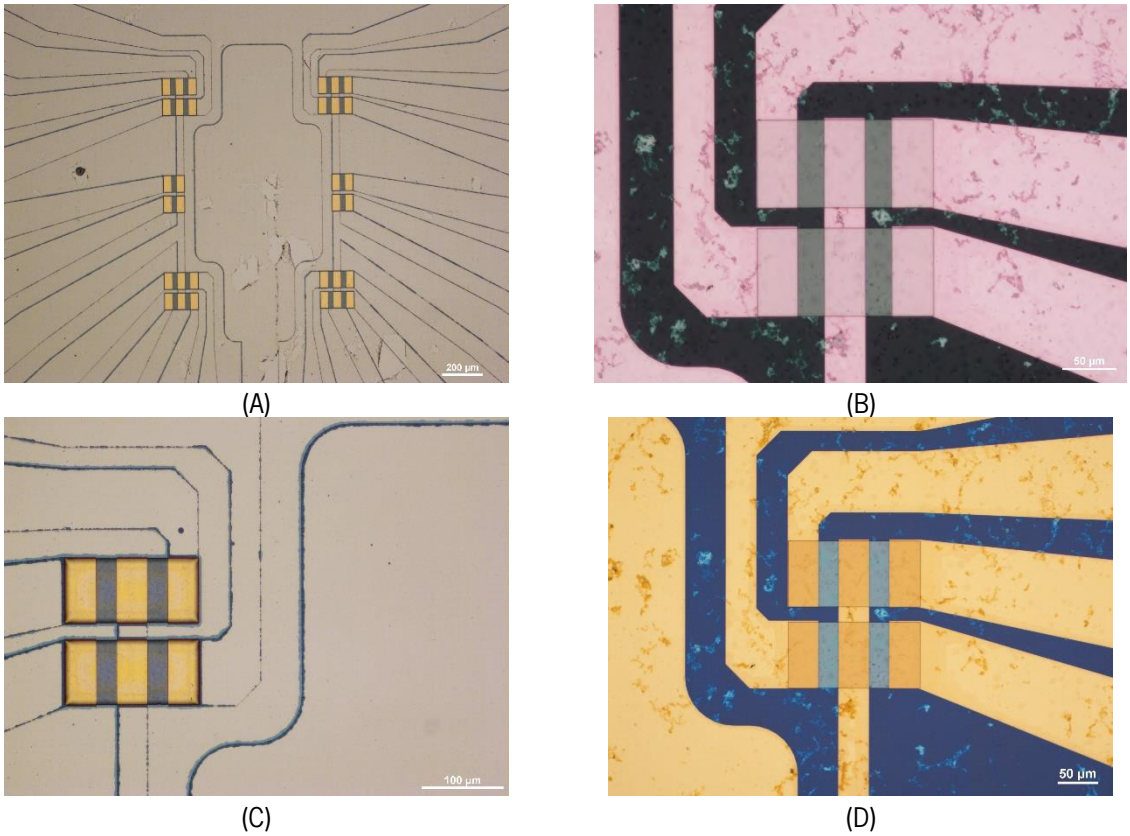

Figure 18. *Optical microscope images of sample surface before graphene patterning (A, B) and after patterning with electron cyclotron resonance (ECR) (low power) O_2 plasma source (C) and inductively coupled (ICP) (high power) O_2 plasma source (D). Scale bars represent 200 µm for (A), 100 µm for (C), and 50 µm for (B) and (D).*

High power processes (above 1000 W [187]) are highly effective in removing graphene, with 10 s being enough for complete 200 mm-wafer patterning. However, removal of the photoresist mask is also swift, on the one hand, and high temperatures can be quickly achieved, increasing the risk of photoresist burning on the other. Consequently, the photoresist thickness and time of exposure to high power plasma needs optimization to ensure that the photoresist endures the process without being burnt/removed. The ICP O_2 plasma is also expected to remove graphene transfer-related residues (e.g., PMMA) from the surface. However, the optimal time for graphene patterning without removing the photoresist is usually not enough to achieve good surface cleaning.

The use of low ECR-power O_2 plasma requires an increased process time. Still, it allows for improved control of the system temperature, improves photoresist stability, and reduces at least 10 times the photoresist etch rate. Over time, organic residues' removal from the surface is also improved, and graphene is efficiently etched from an entire 200 mm wafer in less than 18 min. Therefore, in the following work, ECR-O_2 plasma is preferred whenever the dry etching of graphene is required.

The limitation for ECR-O_2 plasma etching is removing metallic particles or other non-organic transfer-borne residues. As detailed in the introduction, these residues that come adsorbed to the backside of graphene upon transfer are not removed by O_2 plasma and hinder device performance. A more elaborate strategy is necessary, preventing direct contact between residues and chip surfaces. In the next section, a lift-off process is studied to limit the wafer surface's contamination by debris resulting from the graphene transfer process.

3.1.2. Lift-Off Based Transfer

A lift-off inspired process could be an alternative to the standard dry etch patterning, allowing minimum graphene contact with unnecessary/undesired surface regions and achieving a cleaner fabrication process. Previous results from the 2DMD group with microelectrodes [176] show that when transferring graphene over a surface with relatively steep steps (above 100 nm), the film likely breaks and tears apart (crack propagation) at the step region. Therefore, we use a lift-off technique to transfer graphene only to the wafer regions where transistor channels form.

For lift-off assisted wet transfer, a sample with gold contacts is spin-coated with a photoresist (AZ1505 1035 nm or AZP4110 2200 nm) and patterned by optical lithography. The transfer region is left unprotected, as schematically shown in Figure 19.

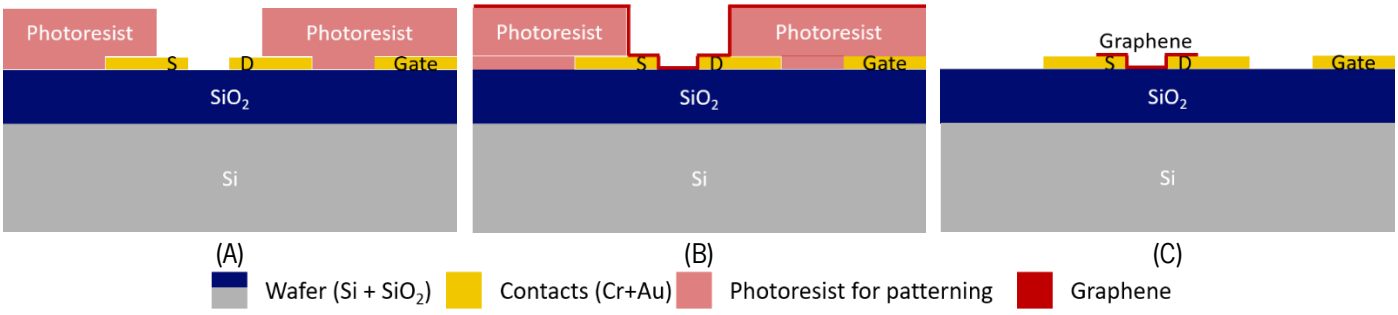

Figure 19. *Lift-off assisted graphene transfer and patterning. First, the sample is patterned by optical lithography to leave the source and drain electrodes and channel exposed (a). During graphene transfer,*

the remaining surface is protected with photoresist (b) that is removed along with PMMA, leaving the surface of the devices clean (c). Graphene is represented as a red line.

Graphene transfer is performed as described in section 2.4.3 using PMMA as a transfer substrate. The samples are annealed in a low vacuum (desiccator) for 2 h after the transfer to improve graphene adhesion. Photoresist dissolution coincides with PMMA removal. After PMMA removal, the samples are observed by optical microscopy to assess the lift-off process's success. The optical images in Figure 20(A and B) clearly show that the lift-off process quality is dependent on the size and distribution of the features patterned on the surface. Although a systematic breaking of the graphene film in the outer edges of features with a sub-millimeter area (≈0.4 mm^2) in size is observed (Figure 20B), in more minor features (≈0.012 mm^2), the breaking occurs randomly in regions out of the delimited pattern (Figure 20A, red rectangles), creating floating parts of the film that end up on top of the region of interest. For graphene features separated by short gaps (less than ≈20 µm), the graphene film does not break between the gaps even with 2.2 µm height steps, keeping its structural integrity instead of adhering to the surface after the photoresist removal.

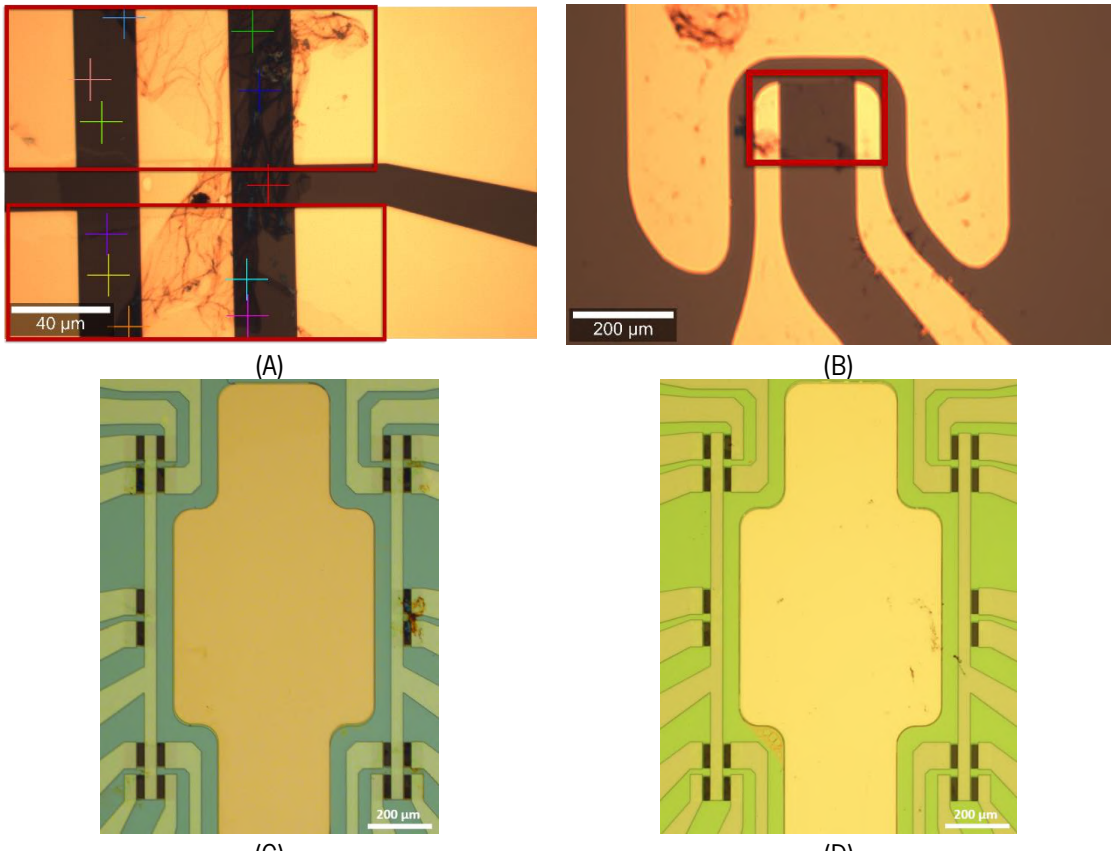

Figure 20. *Optical microscope images of samples with pre-patterned gold contacts after graphene transfer/patterning. The size and density of the structures influences the efficiency in controlling the*

breaking step of lift-off patterning, with small features (A) becoming poorly patterned and big features (B) becoming well defined. The final surfaces appear cleaner after graphene lift-off-based transfer and patterning (C) than with standard patterning by dry etch (D). The scale bars represent 200 µm, with exception of (A) where the scale bar represents 40 µm.

The clear advantage achieved with the lift-off strategy is the final quality of the device surface. Figure 20C shows a cleaner gold surface when compared to the final surface of chips fabricated by dry etch techniques (Figure 20D), but it is only suitable for designs where the devices are separated from each other by at least some millimeters.

3.1.3. Combined Approach

Based on the results of Sections 3.1.1 and 3.1.2, particularly concerning the downsides of the dry etch (surface dirtiness) and the lift-off method (lack of patterning precision), a new combined strategy to improve the process is envisaged as shown in Figure 21.

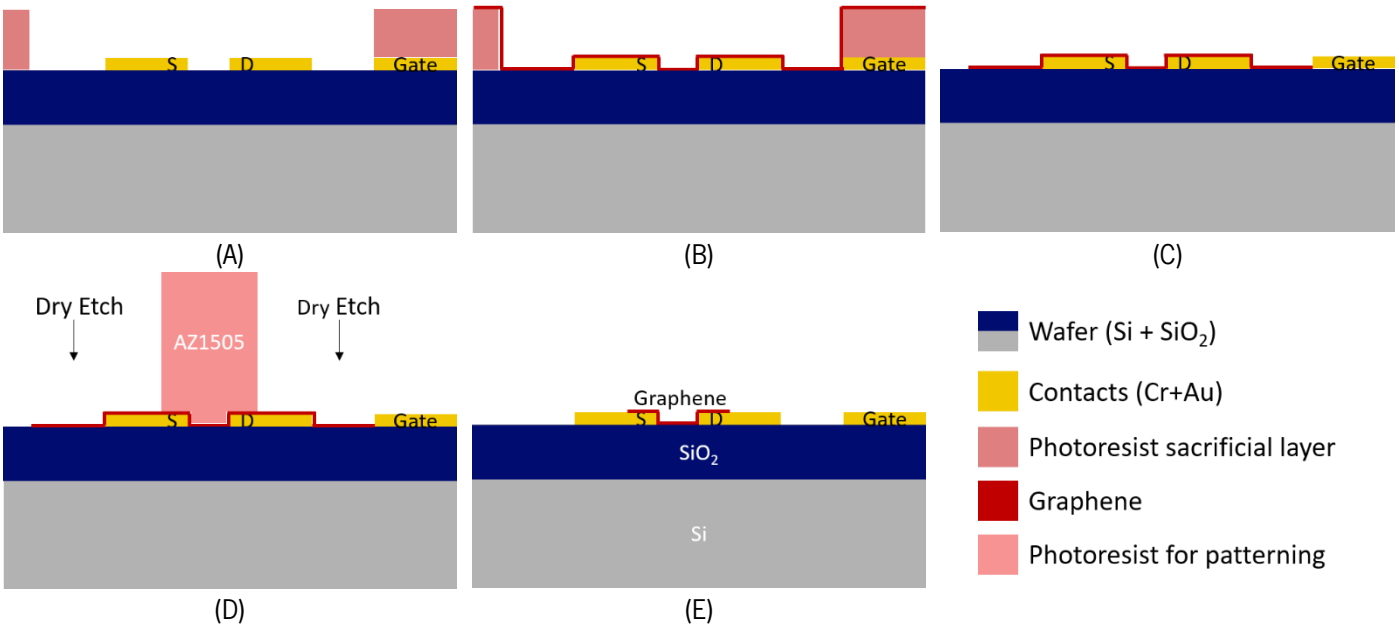

Figure 21. *Graphene transfer and patterning using a combined lift-off and O2 patterning method. (A) A photoresist sacrificial layer promotes the initial patterning of graphene and prevents the accumulation of transfer-related residues at the gate electrode. (B) During the transfer of graphene, the 2D material breaks at the borders of the photoresist. (C) Sample after initial patterning. (D) Standard O_2 plasma etching for*

fine-tuning of graphene patterning. (E) Patterned sample with graphene covering the source and drain contacts and the channel between them.

As breaking occurred at the expected region for extensive features, this can be used to perform a pre-patterning of graphene that keeps the relatively large (≈0.7 mm2) in-plane gate electrode clean after the transfer. Then, dry etching is used for precise graphene patterning in the channel area, leaving the gate electrode free of residues. An extra lithographic step is added, as schematized in Figure 21A-B and Figure 22A, consisting of a large square area around the region of interest where graphene can contact and adhere to the surface. Inside that square, the photoresist protects the gate electrode, keeping it as clean as possible. After photoresist and PMMA dissolution, the graphene channels should then be patterned by RIE.

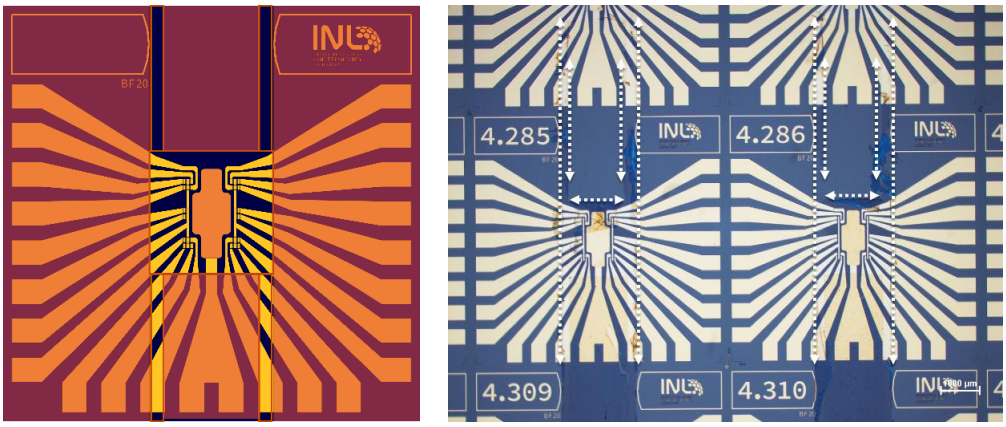

(A) (B)

Figure 22. *Proposal (A) and execution (B) of the modified lift-off strategy for graphene transfer and patterning in two steps. Only the result of the first step (lift-off assisted transfer) is shown in (B) since the goal of gate protection is not achieved. The white arrows show the regions where graphene cracked in the mask limits. The darker region on the gate of device 4.285 is evidence of the re-deposition of loose graphene pieces during the lift-off process. In device 4.286, it is also visible that graphene did not break along the gate features, which were also protected with photoresist before the transfer.*

A test sample was prepared using a 2200 nm AZ4110 photoresist to transfer lift-off assisted graphene (Figure 22B). After transfer and PMMA removal, inspection by optical microscopy was performed to assess the patterning quality. Although the features were large and well separated, Figure 22B shows that crack propagation in graphene occurred only systematically in the photoresist mesa's outer limits, i.e., where distances between the photoresist steps were in the order of millimeters. The photoresist protection was dissolved in the region of interest, i.e., the gate electrode, without breaking the graphene

film. Therefore, the combined strategy was abandoned since graphene's mechanical properties make lift-off a technique hard to master for patterning this material, leading to the accumulation of residues in the gate electrodes originating from the wet transfer process surface, compromising the performance of the device for biosensing.

3.1.4. Pre-Transfer Sacrificial Layer

The previous sections showed that lift-off patterning of graphene films returns inferior results compared to the patterning of standard materials by the same technique. Consequently, a novel methodology was designed, as schematically shown in Figure 23. A hard mask is used not to pattern graphene but to protect the substrate during graphene transfer and patterning by O_2 plasma using a photoresist mask. Any contaminants not removed by the oxygen plasma are removed together with the hard sacrificial mask. The contaminants possibly deposited with graphene on the source and drain are not avoided. Still, they should not significantly affect the device performance since they are not in contact with the biological solutions.

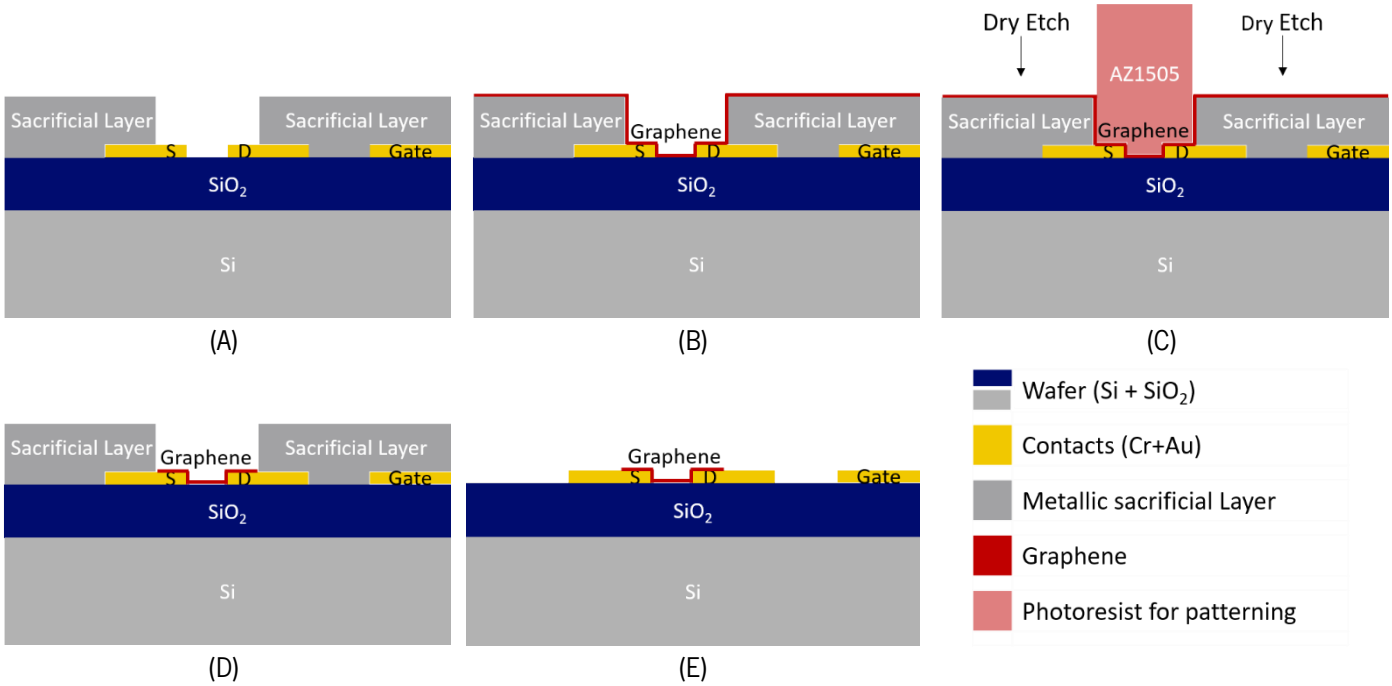

Figure 23. *Pre-transfer sacrificial layer to protect the chip surface from residues. (A) Preparation of the sacrificial layer via lift-off, leaning only the channel region and source and drain electrodes exposed for the graphene transfer. (B) Graphene transfers over the protected devices, where it only contacts the actual surface where desired. (C) Graphene patterning using O_2 plasma (dry etching). (D) The exposed sacrificial*

layer is removed by wet etch, removing the residues left on the transfer process's surface. (E) Finalized graphene transfer and patterning process, leaving the gold surfaces free of residues.

The sacrificial layer should withstand the standard transfer process and patterning of graphene, and it should also be easily removed (e.g., dissolution), leaving the graphene intact. With that in mind, it was designed as follows: first, a buffer Al_2O_3 film was sputtered for physical separation of the Au surfaces from the sacrificial metal layers, avoiding inter-layer diffusion. Films with 10 and later 20 nm of Al_2O_3 were used to ensure this layer's stability during aluminum etch (the etchant is the same for both AlSiCu and Al_2O_3). The next layer in the stack is AlSiCu, the protective layer that avoids residues to deposit on the devices' surface. The capping layer is TiW(N) to allow all lithographic processes (the photoresist developer quickly dissolves AlSiCu and is too reflective for precise laser exposure). Al_2O_3 may replace TiW(N) as a capping layer to avoid repeated use of H_2O_2 to etch TiW(N), which increases the risk of damaging graphene (section 3.2.2).

At the point of the fabrication sequence where the sacrificial layer is added, only the contacts have been patterned, and so a standard lift-off can be used with no risk of damaging underlying layers. Thus, after a lithographic step that leaves the photoresist protecting the source, drain, and channel, the sacrificial layer stack is deposited by sputtering followed by lift-off using acetone and ultrasonic bath (Figure 24A). Next, graphene is transferred by wet transfer and PMMA is removed with acetone (Figure 24B), Then, graphene is patterned using three cycles of 6 min of a low power ECR-O2 plasma (Figure 24C and Section 3.1.1). Wet etching of the sacrificial layer follows, using the photoresist from the previous step to protect graphene. H_2O_2 removes TiW(N), or AZ400k 1:4 developer removes Al_2O_3, depending on which material was used as the capping layer. AZ400k can etch both Al_2O_3 and AlSiCu, so it is used to etch the adjacent AlSiCu layer. The etch rate of AlSiCu is 10 times higher than that of Al_2O_3, so the etch time is adjusted to preserve the Al_2O_3 buffer layer. However, optical images after the process (Figure 24D, red circled regions) show the total removal of the Al_2O_3 film in certain areas due to the over-etch required for removal of the AlSiCu film (non-homogeneous etch). This forces to stop the fabrication process since gold is no longer protected.

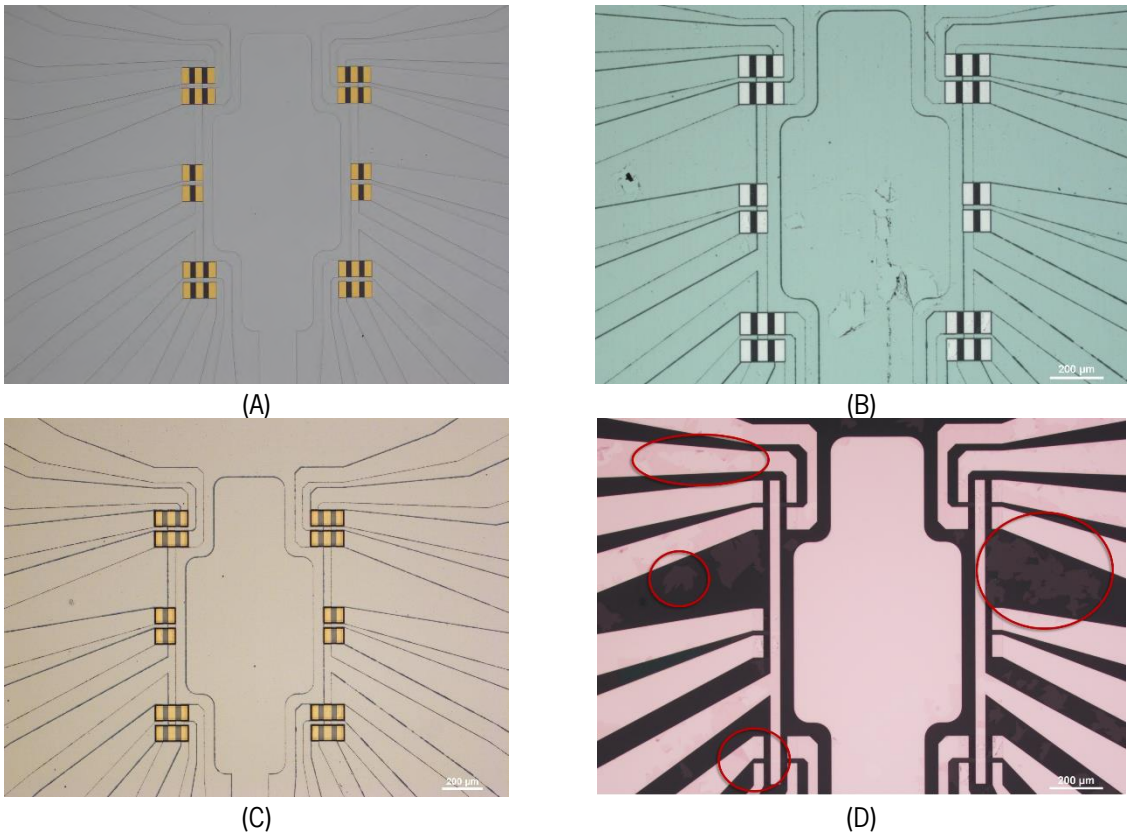

Figure 24. *Graphene transfer and patterning using a protective sacrificial layer. After preparing the sacrificial layer by lift-off (a), graphene was transferred (b) and patterned using O2 plasma (c). The sacrificial layer was removed (d) by wet etch while keeping the patterning photoresist on the sample. Scale bar of 200 µm for all photographs.*

A further increase in Al_2O_3 thickness could improve this result. However, it is difficult to envision because Al_2O_3 needs to be later selectively removed (before the dielectric passivation deposition, Section 3.2) by wet etching using an alkaline solution, causing unwanted dark erosion of the AZP4110 photoresist mask. Consequently, 20 nm seemed to be the maximum Al_2O_3 thickness compatible with this process. As an alternative, a thin layer of TiW(N) was deposited between the buffer layer of Al_2O_3 and AlSiCu. In this way, the wet etch of AlSiCu is accomplished with no attack on the Al_2O_3. Following the above process, a new sample is prepared and observed with the optical microscope revealing spotless surfaces with well-patterned graphene transistors, as seen in Figure 25, which shows that the process is successful.

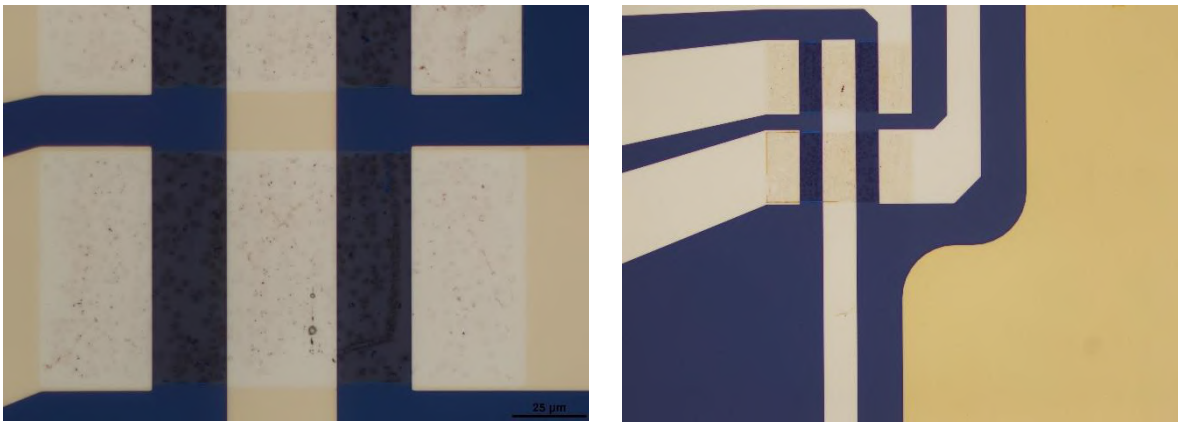

(A) (B)

Figure 25. *Optical microscope images reveal well-defined patterning of graphene (a) and clean surfaces after removing the sacrificial layer (b).*

A final comment on using TiW(N) or Al_2O_3 as a capping layer: partial removal of the sacrificial layer occurs upon graphene transfer (Figure 26) due to HCl residues trapped between graphene and the Al_2O_3 layer. If the graphene is transferred in a single step, this is irrelevant, and the Al_2O_3 capping layer can be used. However, if multiple transfers of graphene patches are required to cover the wafer, TiW(N) should be chosen because HCl does not degrade TiW(N). It should be as thin as possible to reduce the photoresist/graphene exposure time to H_2O_2 TiW (N) etch.

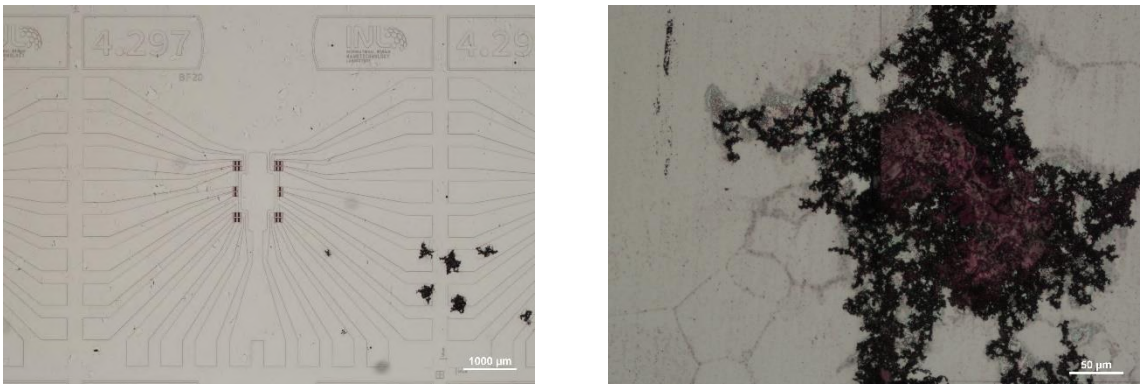

(A) (B)

Figure 26. *Sacrificial layer damage induced by HCl residues of the graphene transfer process. (A) Damage occurs in small areas, as observed by the darker coloring of the sacrificial layer. Scale bar represents 1000 µm. (B) Inset of one of the damaged regions, exhibiting the TiW(N) layer beneath the "attacked" AlSiCu. Scale bar represents 50 µm.*

For these reasons, the sacrificial layer stack was defined as TiW(N) 5 nm/AlSiCu 100 nm/TiW(N) 15 nm. The wet etching process to remove it was H_2O_2 30% 150 s, then AZ400K 1:4 240 s, H_2O_2 30% 50 s. This

stack proved helpful in avoiding residues in the gold gate electrode since, after this process, the Al_2O_3 film on top of gold is particle-free (Figure 25B).

3.2. Fabrication of the Dielectric Passivation Layer

Before designing the passivation layer, several points need consideration. First, consider the final use of the devices. In our case, a clean biosensing interface is obtained by using strong solvents (e.g., DMF) [42] that attack polymeric materials, including photoresists. For example, we observed that DMF damages the direct-write epoxy resist mrDWL1x, promoting its release from the surface and re-deposition elsewhere, which renders the device unusable (Appendix I – Microfabrication of EG-GFETs). Second, along all stages of biofunctionalization, bio-recognition, and transducing, the devices are exposed to salt-containing solutions (e.g., phosphate buffer, PB), which recommends that the top layer of the passivation has minimum permeability to ions. With these considerations in mind, a protective coating consisting of a stack of five alternated SiO_2 and SiN_x films with a total thickness of 250 nm was designed, starting with a layer of SiO_2 to take advantage of the good adhesion of SiO_2 to graphene and the substrate, and terminating with SiN_x to take advantage of the superior impermeability of SiN_x. The multilayer, deposited by plasma-enhanced CVD (PECVD), hinders native nucleation centers and breaks the propagation of defects through the layers, creating tortuous diffusion paths for water and other small molecules [188,189]. All tests are performed after this rugged, chemically stable passivation layer is in place.

For testing, samples of 4 × 4 cm^2, each containing 36 chips of 20 EG-GFETs, were fabricated as described in Section 2.4.2. Figure 27 shows the general design of each chip (Figure 27A) and the disposition of the graphene channels (gray) and gate electrode (yellow) (Figure 27B).

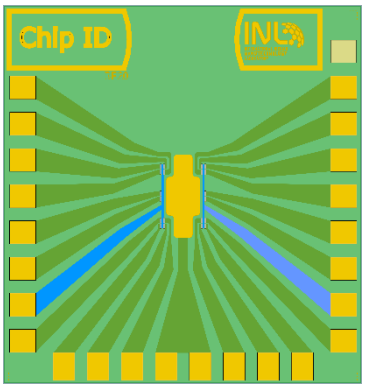

(A)

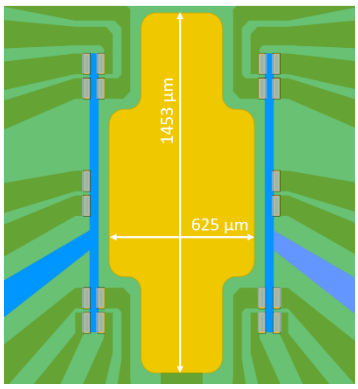

(B)

Figure 27. *Layout for graphene-based biosensors. Layout total size is 6.75 mm by 6.75 mm (A), composed of 20 transistor channels with individual drain electrodes, a common source electrode for each 10 transistors, and a common in-plane gate electrode (B).*

3.2.1. Combined Reactive Ion Etching and Wet Etch Strategy

Some reports refer to dry etching methods [92] to open access vias to graphene in the passivation layer, while others prefer wet etch methods based on HF [180]. Although dry etch is a highly controlled process and very efficient in the etching of dielectric materials, its use directly in a layer adjacent to single-layer graphene would damage graphene due to the plasma-based process. Although less controlled (it often produces an undercut under the edge of the patterned zone), wet etch can be used without damaging graphene. Therefore, a mixed strategy combining dry and wet etching techniques was proposed and tested to open the access vias on the passivation layer on top of graphene without compromising the graphene quality. First, dry etching is used to open the top layer of the passivation stack (Figure 28C), and then wet etch with a strong basis or acid opens the remaining layers of the passivation stack (Figure 28D).

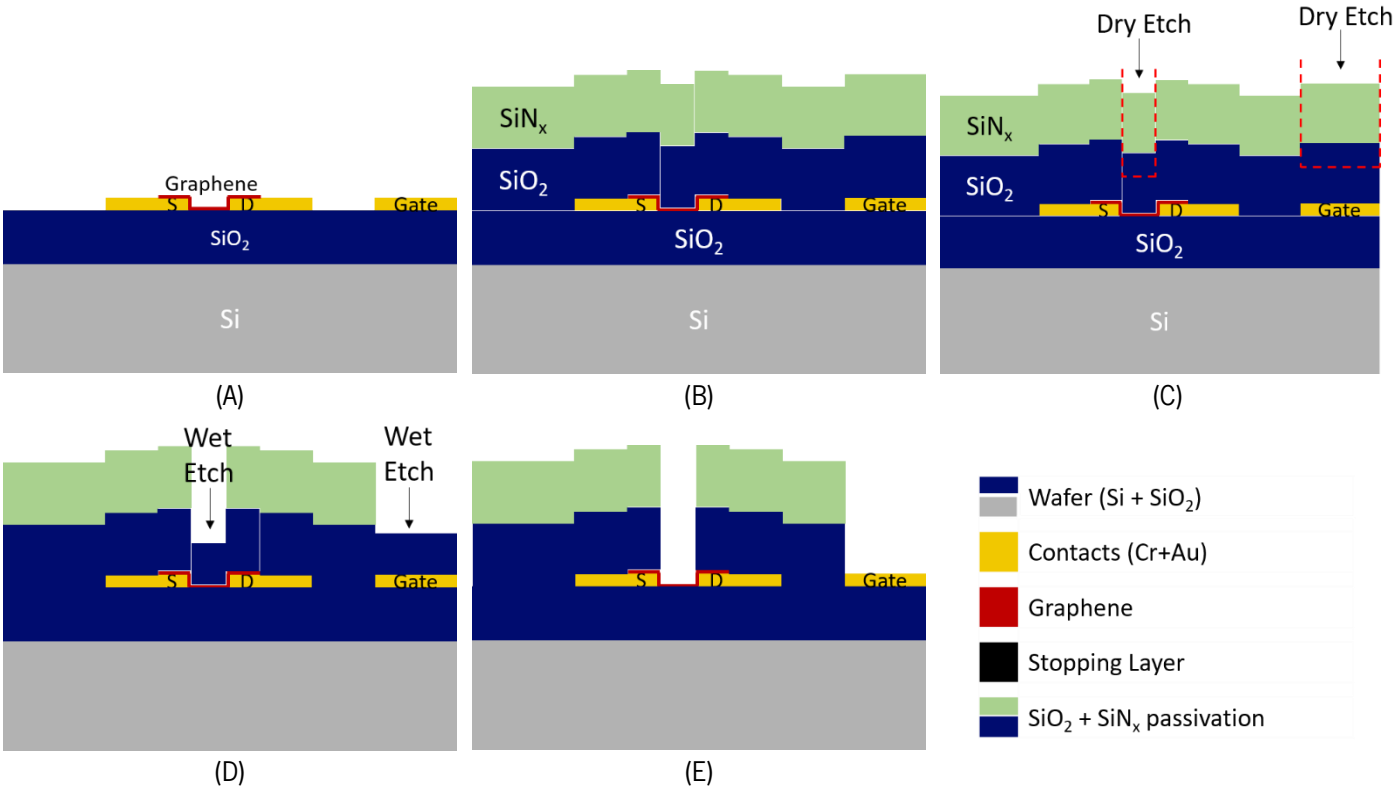

Figure 28. *Patterning of dielectric passivation by combined reactive ion etching (RIE) and wet etch methods. (A) Sample after graphene transfer and patterning, ready for dielectric passivation. (B) Deposition by PECVD of SiO_2 and SiN_x dielectric passivation. (C) Dry etch patterning of the passivation,*

reaching the SiO_2 layer. The remaining thickness allows graphene to be protected during RIE and is removed later by wet etch. (D) Wet etch with KOH at 60 ◦C to remove remaining SiO_2 from graphene and the gate electrode. (E) The final device with only the graphene channel and the gate electrode is exposed to the electrolyte.

Two test wafers were prepared to measure the dry and wet etch rates of the passivation layer, as follows: Si wafers are coated, using PECVD, with 90 nm of SiO_2 and 50 nm of SiN_x on Test Wafer #1, and 120 nm of SiO_2 and 50 nm of SiN_x on Test Wafer #2. For thickness estimation with an interferometer, millimeter-sized patterns were patterned by optical lithography. Optical microscopy images of the samples can be found in Appendix I – Microfabrication of EG-GFETs. Based on previous etching recipe parameters, historical values of etch rates for SiO_2 (116 nm/min) and SiN_x (274 nm/min) are used to estimate the time required to completely etch the top SiN_x layer and about half of the SiO_2 layer. Test Wafer #1, was etched over times ranging from 20 to 30 s. After performing reactive ion etching (RIE), an interferometer was used to measure the remaining thickness of the SiO_2 film in the pattern. The estimated thicknesses are presented as a function of etching time in Figure 29A. Due to the fast decrease of the SiO_2 thickness, shown in Figure 29A (black squares), which increases the error in estimating the post-etch film thickness, a new wafer was prepared (Test Wafer #2) with an increased thickness of the SiO_2 layer. For this thicker film, after 25 to 30 s of etching time (Figure 29A), red dots) approximately 40 nm of SiO_2 is left on top of the hypothetic graphene, thus preventing damage to the 2D film.

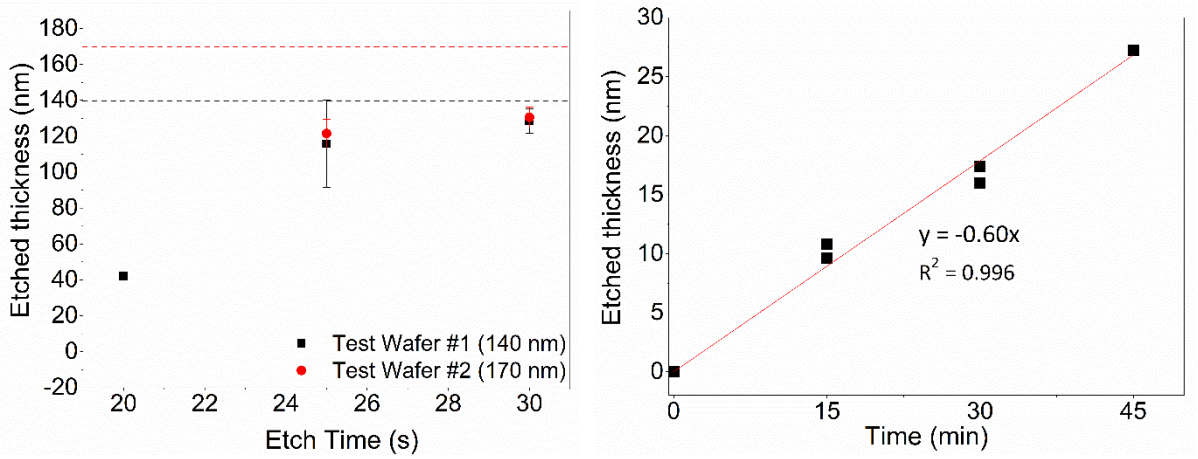

Figure 29. *Film thickness after different etching times for SiN_x and SiO_2. (A) Dry etch of SiN_x and SiO_2 stack for two different initial thicknesses. The dashed lines refer to the reference thickness for each test wafer. (B) Wet etch of SiO_2 films by KOH 1 M at 60 °C over time.*

Many oxidizing agents, such as piranha or aqua regia, react strongly with organic Si compounds. Thus, they must be avoided. Phosphoric acid (often used as Al etchant) is known to create pores in graphene [190], and solutions based on hydrofluoric acid (HF), which is also a graphene dopant, should be avoided for safety. On the other hand, base solutions, such as KOH and tetramethylammonium hydroxide (TMAH), are not known to attack graphene and are good candidates for the wet etch of the dielectrics. Thus, KOH 1 M was used as the etchant for the second step of the passivation patterning.

Wet etch was tested using features previously patterned by RIE. The Test Wafers #1 and #2 are diced in samples of 2×2 cm^2 and exposed to KOH 1M for different times and temperatures until a satisfactory etching rate is obtained. When exposed to KOH 1 M at 45 °C, the etch rate is about 5 nm/h, which is similar to the room temperature rate [14]. Increasing the temperature to 60 °C leads to a 7-fold increase in etch rate, to approximately 36 nm/h. The etch rate was estimated by exposing several samples to KOH for 15 min, 30 min, or 45 min. The thickness of the SiO_2 film is measured using the interferometer, before and after etching, and the difference is plotted as a function of time. A least-squares fit estimates the etch rate, as shown in Figure 29B. Once both steps of the passivation layer were optimized on featureless un-patterned films a sample with patterned contacts (as described in Section 3.1) was prepared to undergo the same procedure, mimicking the complete process to be performed at wafer scale. After graphene transfer and patterning, the passivation layer (120 nm of SiO_2 and 50 nm of SiN_x) was deposited, and lithography was performed to expose the channel and gate areas to the RIE. Since the features are too small for thickness estimation by interferometry, AFM is used to measure the remaining thickness of SiO_2 after RIE and estimate the time required for the subsequent wet etch step. The data from the AFM measurement, as shown in Figure 30, gives a step of approximately 100 nm, i.e., there is still 70 nm of SiO_2 left on top of the graphene channel. Based on the wet etch study performed in the test wafers, the sample is immersed for 2 h in the KOH 1 M etching solution at 60 °C. However, after this process, severe peeling-off of the passivation layer is noticeable even to the naked eye, as shown in Figure 30B-D.

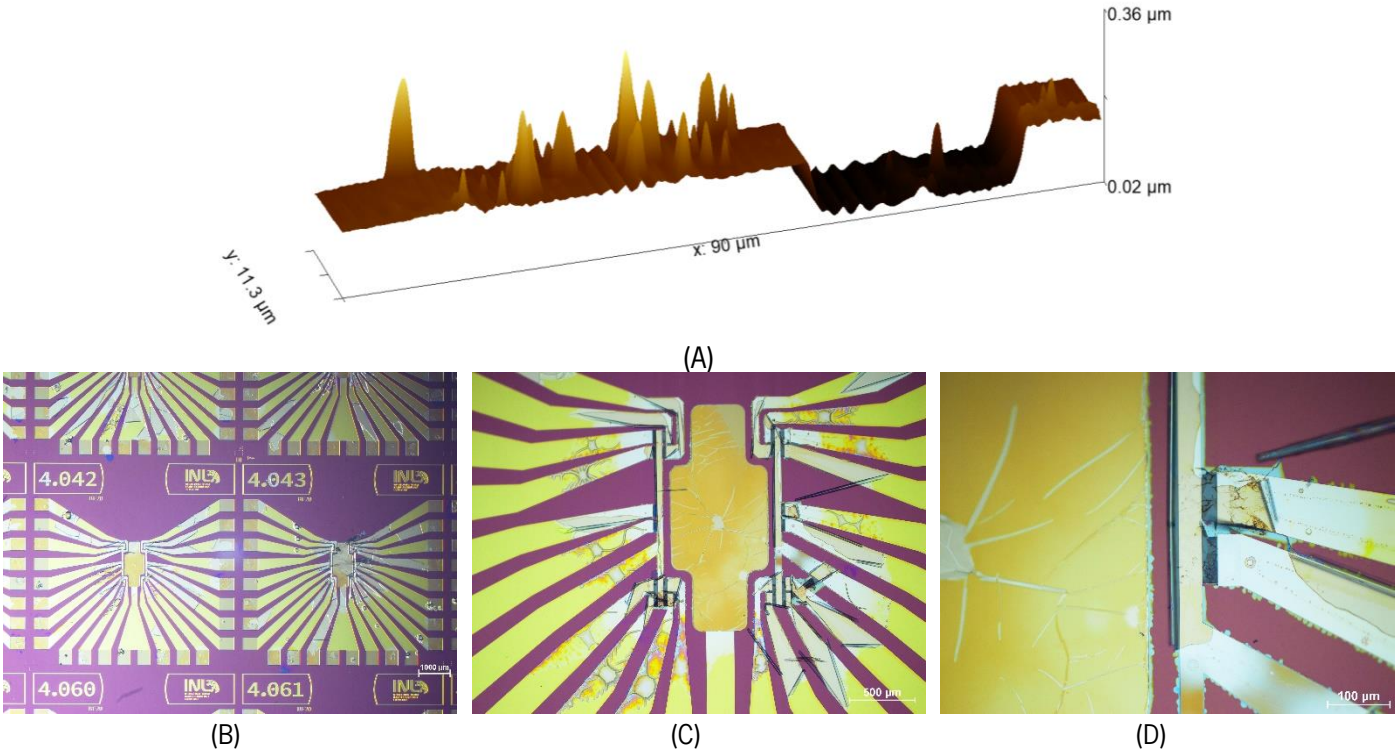

Figure 30. *Patterned sample after dry etch (A) and after wet etch in KOH 1M at 60 °C (B-D). A peeling effect is very clear even at 1× magnification (B). Increasing the magnification to 5×, it is noticeable that the peeling is starting at the channels region, which is confirmed at 20× magnification (D), indicating that the peeling is caused by an undercut of the SiO_2 during wet etch with KOH. Scale bars represent 1000 µm (B), 500 µm (C), and 100 µm (D), respectively.*

The results indicate that the wet etch step is systematically causing the SiO_2/SiN_x stack delamination, as shown in Figure 30B-D. It is hypothesized that delamination could be caused by the undercut of the SiO_2 film under the SiN_x during the KOH wet etch process, promoting the top layer's stress release by peeling and rendering the devices unusable. An approach to overcome this issue could be using HF vapor in a vacuum instead of liquid etchant. Still, when up-scaling to the wafer-size, the process steps' economy and homogeneity over a large area are essential. HF vapor etching is typically used for the complete removal of oxides with large over-etch times. In contrast, the use for patterned etching is highly non-homogeneous due to the anisotropy of the vapor flow, which is an effect that is difficult to compensate when removing relatively thin films (<100 nm) [191]. Therefore, a satisfactory solution, combining wet and dry etching, could not be found for the graphene EG-FET fabrication.

3.2.2. Stopping Layer-Assisted Reactive Ion Etching of Dielectric Passivation

As the combination of dry and wet etch presents significant limitations due to the wet etch step, other alternatives were sought in the literature to achieve patterning of passivation layers through reactive ion etching (RIE) [92]. However, none of them discuss how the graphene surface can be protected during this process. For the deposition of the stopping layer, atomic layer deposition (ALD), thermal evaporation, and physical vapor deposition (PVD) can be considered. ALD, owing to its very low deposition rate, can only be deposited in very thin layers. ALD of aluminum oxide is useful as a thin gate dielectric for transistor structures, so this technique has been studied for GFETs. However, because graphene is hydrophobic, the ALD of aluminum on graphene must be preceded by a thin evaporated aluminum layer, which turns into an oxide layer by natural oxidation and presents a good surface for the ALD growth [181,182]. However, there is no real advantage in using ALD if another technique precedes it for a stopping layer composed of aluminum oxide. Therefore, physical vapor deposition systems are tuned to provide mild deposition conditions of relevant materials to minimize graphene damage. We propose a specific solution, consisting of the insertion of a stopping layer between graphene and the dielectric to be etched, as schematized in Figure 31.

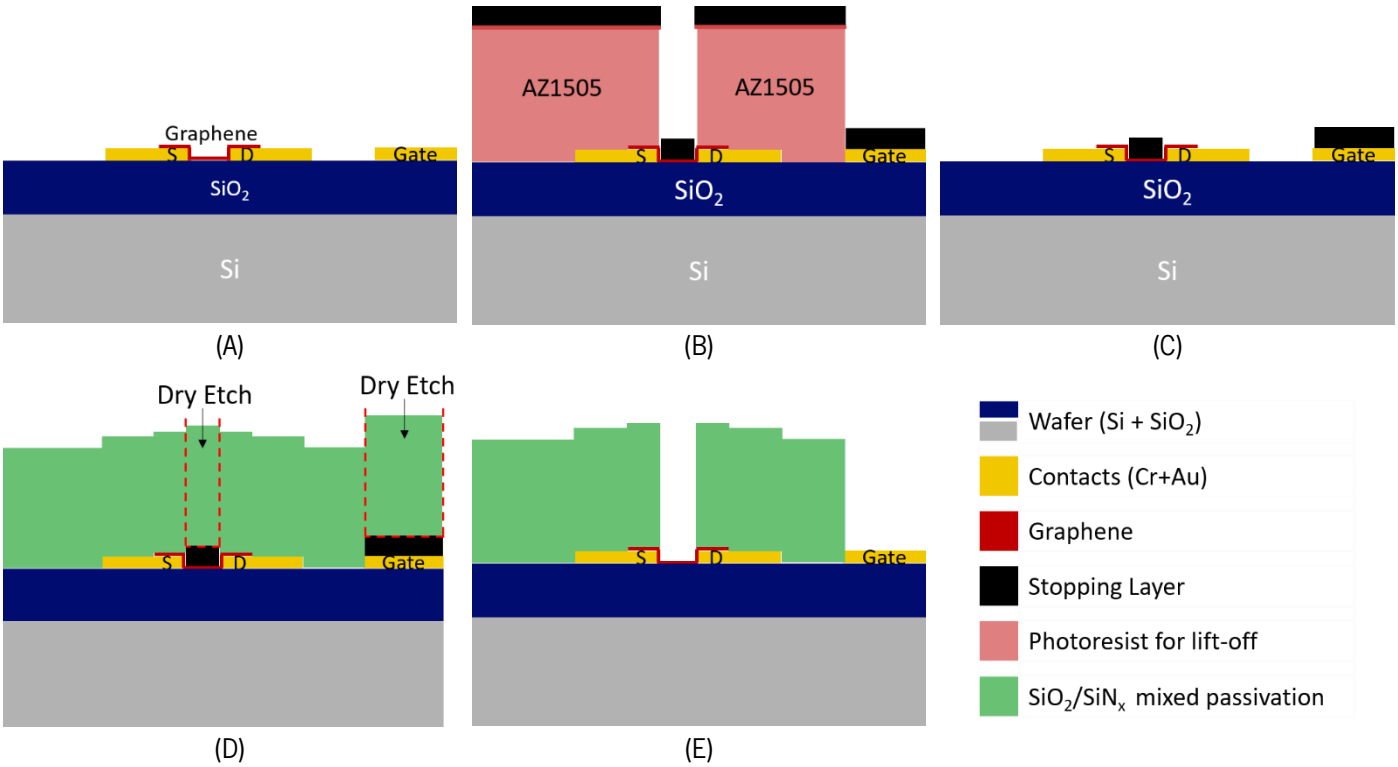

Figure 31. *Patterning of the dielectric passivation by RIE using a sacrificial/stopping layer. (a) Sample after graphene transfer and patterning, ready for dielectric passivation. (b) Preparation of the metallic stopping layer by ultrasonication-free lift-off. (c) Stopping layer after patterning covering the graphene channel and the gate electrode. (d) Deposition by PECVD of SiO_2 and SiN_x dielectric passivation and*

standard RIE patterning. (e) After wet, final device etch of the stopping layer, with only the graphene channel and the gate electrode exposed for contact with the electrolyte.

When a plasma etching is performed on graphene, a stopping layer must be prepared on top of it to prevent the etching from damaging graphene. For reactive ion etching of silicon oxide, the typical stopping layer is based on aluminum, either metallic or oxidized, which is not etched by fluorine chemistry. Still, graphene integrity must also be taken into consideration while building this layer. We performed the graphene integrity study as follows: six different materials (Al_2O_3, AlSiCu, TiW(N), Al, Cu, and Ni), ranging from metals to insulators, were sputtered (RF or DC with low and high power) on top of several graphene samples. After sputtering, a wet etch of those materials was performed at room temperature and with mild agitation for all samples. Different etching agents are used to match the material to etch AZ 400k 1:4 for Al_2O_3, AlSiCu and Al, H_2O_2 30% for TiW(N), and $FeCl_3$ 0.5 M for Cu and Ni. The etching process was stopped when the samples seemed clean. The graphene quality of these samples was analyzed by Raman Spectroscopy before sputtering and after wet etch of the sputtered material. The comparison of Raman spectra for all combinations shown in Figure 32 indicates that sputtering of most of these materials is very damaging to graphene. However, when sputtering Cu and Ni, the damage is not significant.

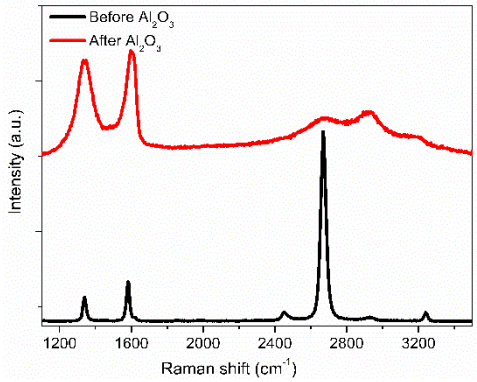

(A)

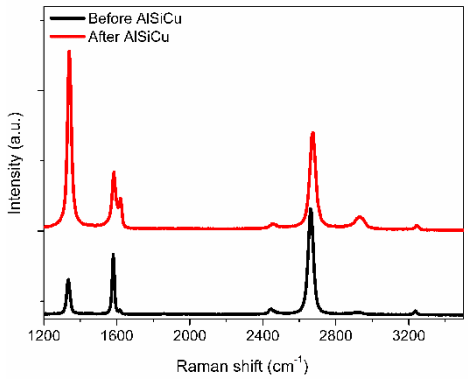

(B)

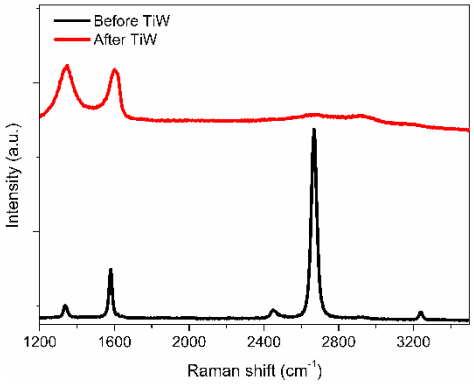

(C)

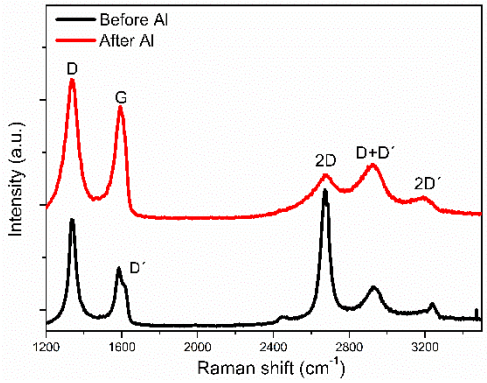

(D)

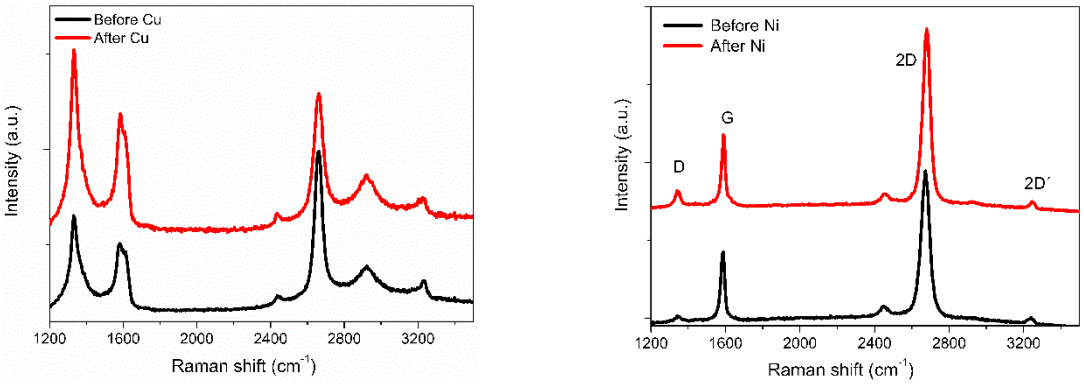

(E) (F)

Figure 32. *Raman spectra of graphene samples before and after sputtering and wet etch of Al_2O_3 (A), AlSiCu (B), TiW(N) (C), Al (D), Cu (E), and Ni (F).*

DC sputtering of AlSiCu and TiW(N) at 2 kW and 1 kW, respectively, and RF sputtering of aluminum oxide at 2.5 kW were found to damage or altered the material extensively. The deposition of AlSiCu also induced many defects that could be originated by the high-power plasma of the sputtering system with an additional contribution from mechanical damage during the dissolution of aluminum, where bubbling was observed. The deposition of oxide films, such as Al_2O_3, seems to induce the oxidation of graphene. A similar situation occurs with TiW(N), where the etchant H_2O_2 30% leads to the complete oxidation of graphene.

A low power (100 W) sputtering system with a sizeable target-sample distance of 30 cm (larger than in the system previously used) was tested. While the RF sputtering of pure aluminum leads to the damage of graphene after its removal, the DC sputtering of Cu and Ni did not induce a significant increase in the Raman defects peak (D mode: ≈1350 cm−1, Figure 32E,F). Interestingly, these metals are also well-known catalysts for graphene growth, and their deposition on graphene was reported as healing graphene [192].

Once graphene is protected by a thin layer of Cu or Ni, further depositions of varied materials and higher powers can be successfully performed without damaging graphene. Thus, an effective stopping layer for dry etching of the passivation layer without compromising graphene integrity is achieved.

The next challenge for the preparation of the stopping layer is patterning. Patterning by wet etch should be avoided if we are to precisely control the features' size, and patterning by standard lift-off is limited, since ultra-sonication is forbidden due to the graphene underlayer. Therefore, the lift-off process was changed as follows. Soaking the photoresist with a TMAH-based developer (AR 300.47, diluted 4:3 in water) before exposure creates a top hardened layer that behaves differently upon exposure and development. Development occurs faster in the remaining photoresist than in the hardened layer,

producing "mushroom hat"-like features, or a negative profile, which creates a shadow during metal deposition and, therefore, facilitates lift-off. Since this feature forms at the top photoresist surface, immersion in a solvent peels-off this layer, where the sputtered materials are adhered. Testing this methodology on samples with pre-patterned contacts and graphene was highly effective and reproducible even at a wafer scale (see Appendix I – Microfabrication of EG-GFETs).

Based on the obtained results, samples with pre-patterned gold contacts were prepared to test the passivation patterning process by dry etching using the best protective stopping layers. Samples with gold contacts and graphene were prepared as follows: the samples are coated with 600 nm of AZ1505 photoresist and soaked in the developer (AZ400k 1:4) previously to optical lithography. After lithography and development, each sample was sputter-coated with copper (Cu, 10 nm) or nickel (Ni, 10 nm), which was followed by aluminum alloy (AlSiCu, 30 nm) and titanium-tungsten (TiW(N), 5 nm). Then, the samples were immersed in acetone for 1 h at room temperature and then rinsed with an acetone wash bottle to promote the loose material's release. The soaking method avoids sonication, preventing the damage/delamination of graphene. Next, the passivation layer was deposited as a stack of two 50 nm films of SiO_2 and three 50 nm films of SiN_x with 250 nm of final thickness. The passivation stack was patterned using 1035 nm of AZ1505 photoresist and optical lithography, followed by RIE using previously optimized parameters. After removing the remaining photoresist, the channels and the gate electrode are released by wet etch of the stopping layer (AZ 400K 1:4 for AlSiCu and $FeCl_3$ 0.5 M for Cu or Ni). The removal of the stopping layer was followed by EDX over the gate electrode, allowing the final devices to be process contaminants free. The EDX spectrum in Figure 33 shows the stopping layer's condition after patterning the passivation.

The RIE etching step etches away the SiO_2/SiN_x passivation stack and the capping layer of TiW(N) and stops at the AlSiCu layer. The removal of AlSiCu by an alkaline solution (AZ400k) is confirmed in the spectrum of Figure 33B, where the peak of Al is significantly reduced. A small signature of Al is still visible due to the protective Al_2O_3 that is beneath the Cu of the stopping layer. The spectrum confirms the removal of the Cu by $FeCl_3$ 0.5 M in Figure 33C by the absence of any Cu related peak. The surface's final status can be observed in Figure 33D, after removing the protective Al_2O_3 from the gold surfaces and showing no evidence of significant contaminants at the surface of the device.

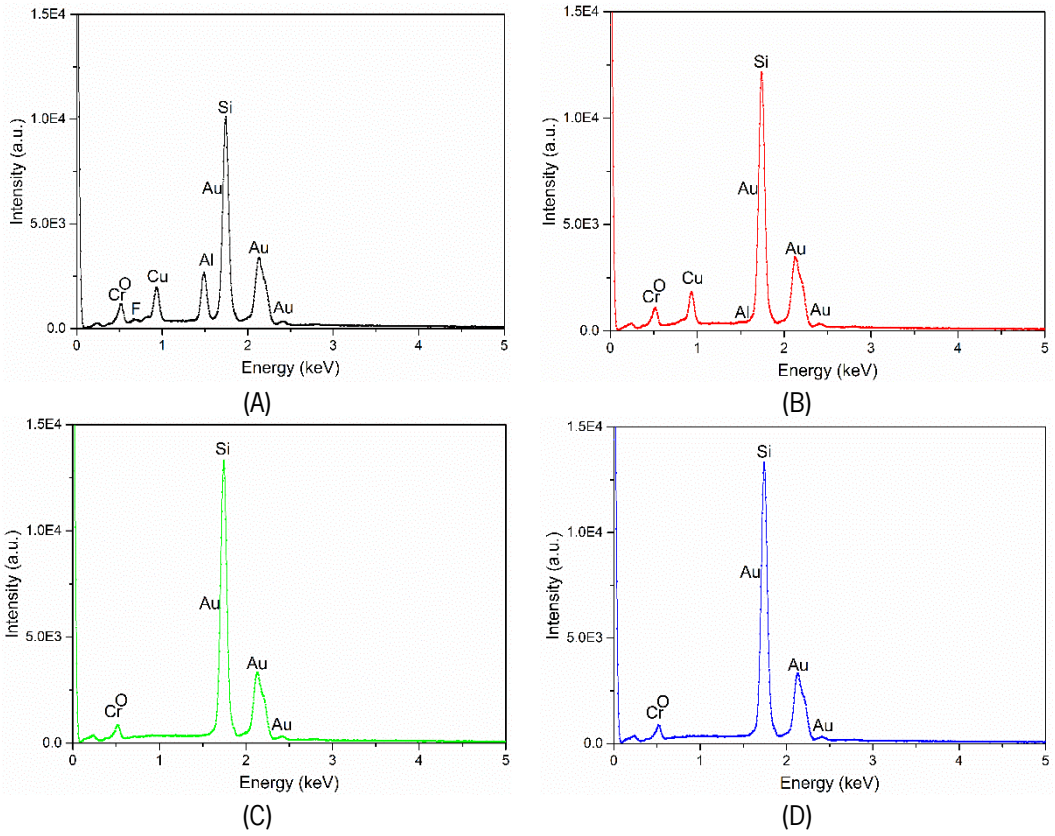

Figure 33. *Energy-dispersive X-ray spectroscopy (EDX) spectra at the gate electrode after patterning of the dielectric passivation (a) and after each step of the wet etch. (b) After AlSiCu removal by AZ400k 1:4. (c) After Cu removal by $FeCl_3$ 0.5 M. (d) After Al_2O_3 removal by AZ400k 1:4.*

Confirming the results shown in Figure 32, the Raman spectra in Figure 34A and the map of full width at half maximum (FWHM) for the 2D mode in Figure 34B show that the process using Cu as a protective layer does not induce significant damage on graphene. Only a slight increase of the defect peak is observed after processing. The same can be observed in the sample using Ni as a protective stopping layer in Figure 34C and Figure 34D. Confirmation of the electrical contact is performed by acquiring transfer curves in electrolyte–gate configuration, as shown in Figure 34E,F. Both transfer curves exhibit the typical ambipolar behavior of EG-GFETs with the minimum conductivity point (V_{CNP}) indicating intrinsic p-doping of the devices. We obtain a field-effect mobility for electrons and holes of $\mu_e \approx 1700$ $cm^2 V^{-1} s^{-1}$ and $\mu_h \approx 1300$ $cm^2 V^{-1} s^{-1}$, respectively, by fitting the transfer curves to a model describing the DC conductivity of single-layer graphene (SLG), σ, as a function of gate voltage. The model is based on carrier resonant scattering due to the strong short-range potentials originating from impurities adsorbed at the graphene surface [39,193].

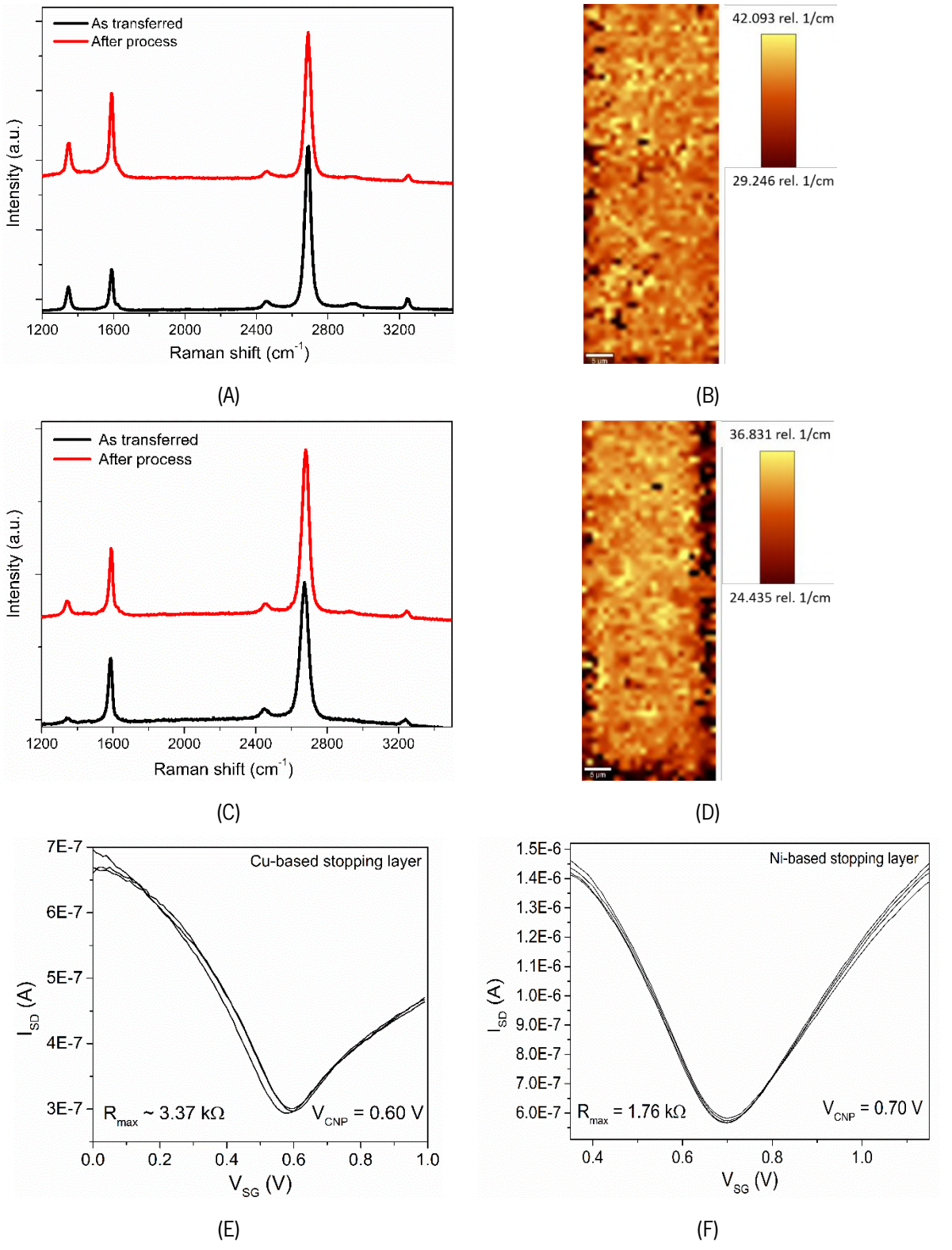

Figure 34. *Characterization of EG-GFETs fabricated with dielectric passivation. Raman spectroscopy characterization before sputtering of the stopping layer (black) and after complete processing (red) using Cu (A) or Ni (C) as the basis. Full width at half maximum (FWHM) of the 2D mode of graphene after process using a Cu-based stopping layer (B) and after the process using an Ni-based stopping layer (D). The electrical characterization of the respective EG-GFETs in deionized (DI) water shows transistor*

behavior of the devices and similarity in the transfer curve characteristics both for a Cu-based process (c) and Ni-based process (d).

3.3. Case Study: Fabrication at 200 mm Wafer Scale of Graphene Electrolyte Gated FETs

This study's main goal is to develop a process for the wafer-scale fabrication of high electronic quality devices for biosensing applications. The final devices produced at the 200 mm wafer-scale following the proposed process are resistant to all the solvents used for graphene functionalization [42] and have low ion permeability, which increases their electrical stability.

After the previous study (sections 3.1 and 3.2), in which each step of the fabrication process was optimized using small area substrates, a complete microfabrication process is performed on a 200 mm Si wafer covered with 100 nm of thermal SiO_2. The chip design is for 20 graphene transistors per chip, with a common source electrode for each group of 10 FETs, a top gate electrode in the center of each chip, and a back-gate access pad to allow double-gating of the transistors. The fabrication sequence is briefly presented in Figure 35.

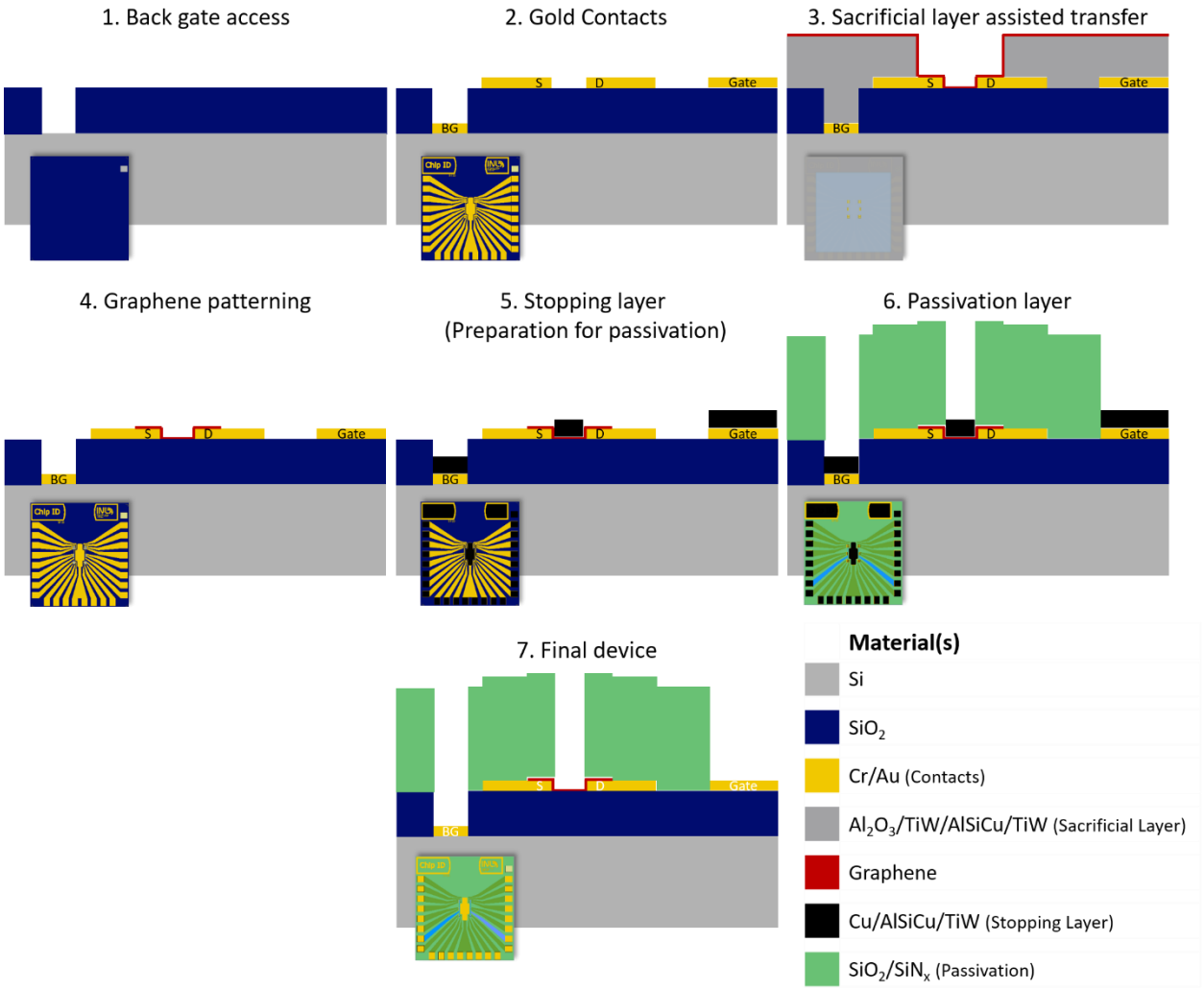

Figure 35. *Graphical overview of the optimized fabrication process for wafer-scale production of EG-GFETs for biosensing. Steps 1 and 2 refer to contact patterning. In step 3, the sacrificial layer is used during graphene transfer to avoid transfer-borne residues on gold surfaces (e.g., gate electrode). After complete transfer and PMMA removal, graphene is patterned by dry etching, and the sacrificial layer is removed, as shown in step 4. In step 5, the stopping layer is prepared on top of graphene, based on Cu or Ni, which is followed by deposition and dry etch patterning of the passivation stack (step 6). Finally, the stopping layer is dissolved, and the final device is achieved (step 7). The color code for the layers/materials is presented at the bottom right corner of the figure.*

The first step is to open the back-gate access using optical lithography and reactive ion etching (Figure 36A). Then, a contact layer stack is sputtered on the wafer: 3 nm of the Cr adhesion layer, 35 nm of the Au conductive layer, and 20 nm of the Al_2O_3 protective layer following the results of section 3.1.4. The contacts are patterned using optical lithography and ion milling (Figure 36B) over 180 square dies, 18 dies of side 20.25 mm, and 162 dies of side 6.75 mm (see Appendix I – Microfabrication of EG-GFETs).

Source and drain contacts are 75 µm wide (channel width, W), separated by a gap (channel length, L) of 25 µm. The gate electrode is circularly shaped with ≈20 mm2 area for the 20 mm dies and rectangular shaped with ≈0.7 mm2 area for the 6.75 mm dies.

The sacrificial layer for graphene transfer is prepared by lift-off following section 3.1.4, using TiW(N) in the top layer to ensure the sacrificial layer's stability during the multiple graphene transfer steps. Optical microscopy is used to confirm the lift-off process's completion (Figure 36C).

The processed PMMA/graphene films are transferred onto the wafer's desired regions until full coverage is achieved (Figure 36D). After PMMA removal, graphene is patterned with low power ECR-O_2 plasma (Figure 36E and Section 3.1.1). After removing the sacrificial layer, graphene quality is accessed by optical microscopy (film continuity) and Raman spectroscopy for structural quality and continuity, as shown in Figure 36J.

Previously to the passivation, Al_2O_3 is selectively removed to improve adhesion of the passivation to the chips' surface. Al_2O_3 is kept only at the gate and pads to prevent contact with the stopping layer by patterning 2200 nm thick AZP4110 photoresist and wet etching with alkaline solution (AZ400k 1:4).

A hard coating for passivation is chosen (section 3.2), considering the devices' intended use. The process described in section 3.2.2 is used to fabricate the passivation layer (Figure 36F,G) with a Cu or Ni-based stopping layer (black layer in Figure 23). The final wafer (Figure 36H) was analyzed with EDX to discard the presence of process contaminants (Figure 36I). Characterization using Raman spectroscopy was repeated after processing the wafer to confirm the achieved final quality of graphene (Figure 36J, red spectrum).

Optical images acquired after each fabrication stage (Figure 36) were used to monitor the process, ensuring that the wafer only proceeds to the following fabrication step if the optical images show that the previous step was successfully achieved. Raman spectroscopy of graphene as transferred and after processing shows a slight increase in defect concentration (D peak, 1350 cm^{-1}). The defect-related D mode ratio to the G mode changes from 0.12 (as transferred) to 0.24 (final), but 2D/G ≈ 2.3, indicating graphene quality, is not significantly affected by the fabrication process.

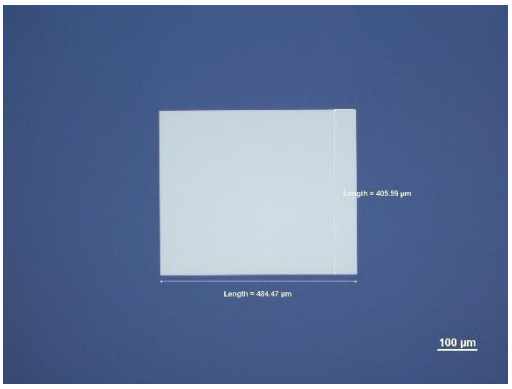
Length = 405.59 µm
Length = 484.47 µm
100 µm

(A)

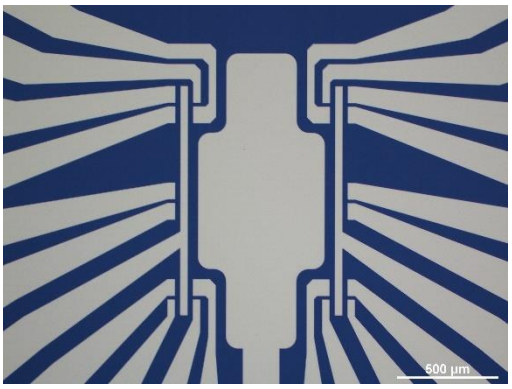
500 µm

(B)

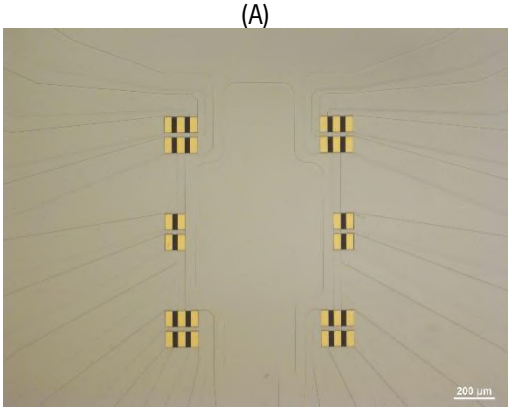
200 µm

(C)

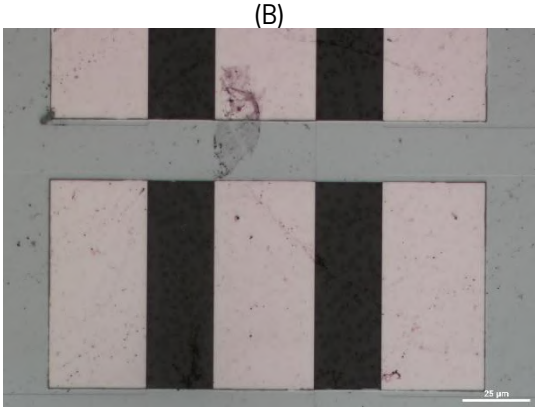
25 µm

(D)

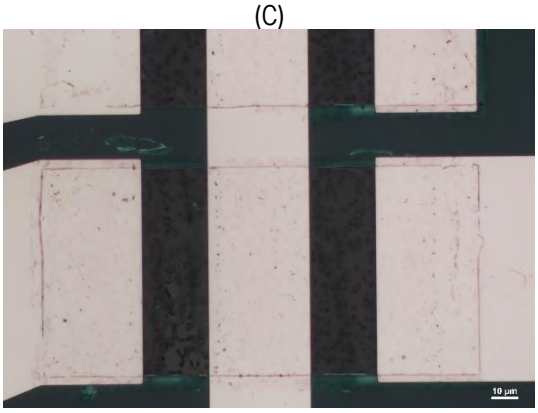
10 µm

(E)

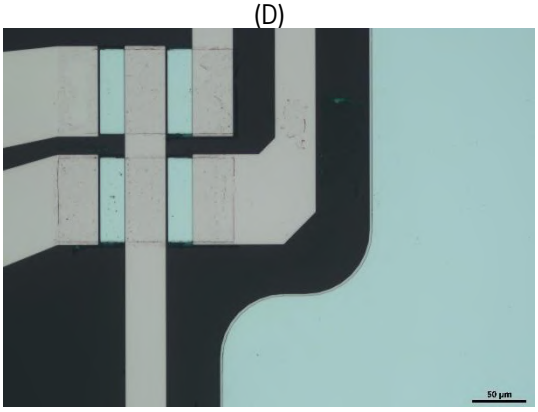
50 µm

(F)

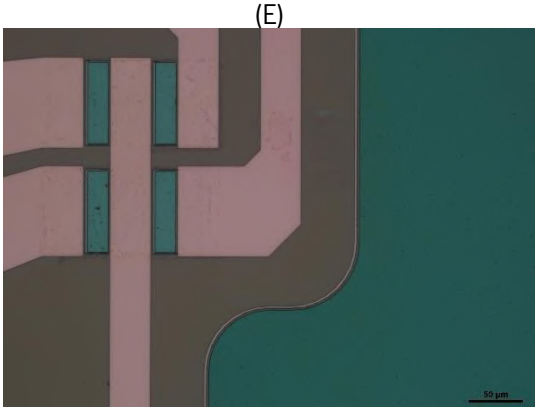
50 µm

(G)

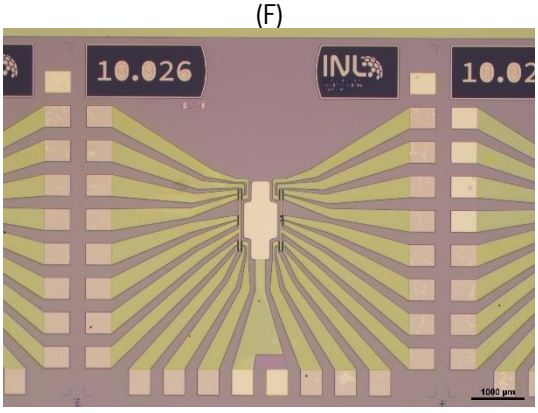
10.026
INL
10.02
1000 µm

(H)

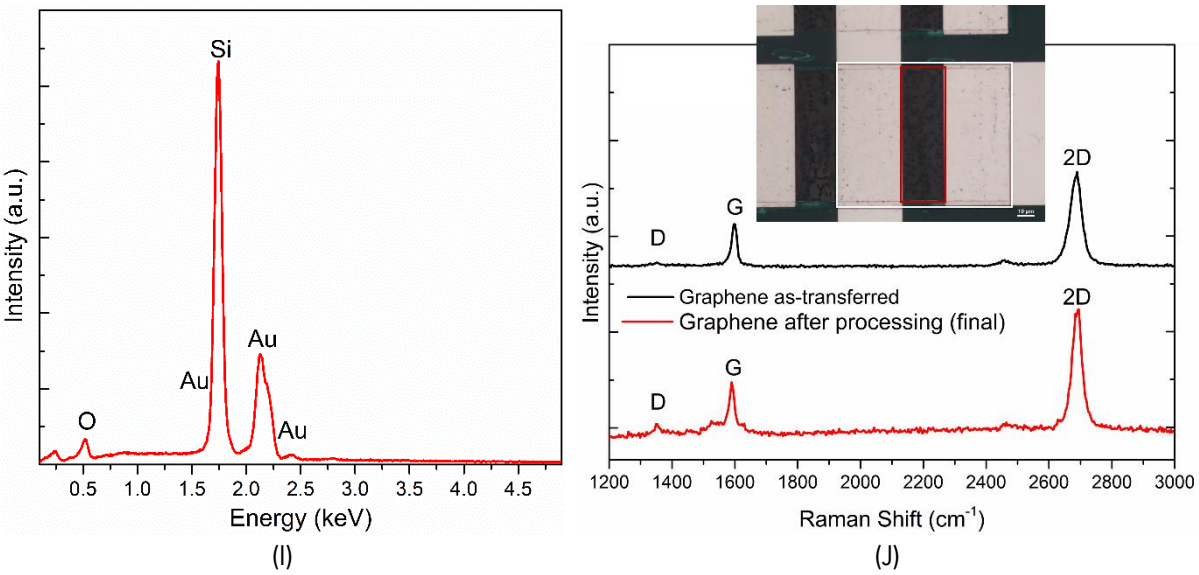

Figure 36. *Optical microscope photographs resuming the steps of the wafer-scale fabrication process of graphene field-effect transistors in which liquid electrolyte replaces the commonly used solid dielectrics (EG-GFETs). (A) Back gate access opened by reactive ion etching (RIE) (20× magnification). Scale bar represents 100 µm. (B) Patterned Au contacts for 20 EG-GFETs with one common in plane gate electrode (5× magnification). Scale bar represents 500 µm. (C) Sacrificial layer for graphene transfer composed of TiW(N), AlSiCu, and TiW(N) (5× magnification). Scale bar represents 200 µm. (D) Surface of the wafer after graphene transfer (50× magnification). Scale bar represents 25 µm. (E) Same area after patterning by O2 plasma and removal of the sacrificial layer (50× magnification). Scale bar represents 10 µm. (F) After preparation of the stopping layer composed by Ni, AlSiCu, and TiW(N) (20× magnification). Scale bar represents 50 µm. (G) After deposition of the dielectric passivation stack (20× magnification). Scale bar represents 50 µm. (H) After RIE patterning of the passivation and removal of the stopping layer (final device, 1× magnification). (I) Energy-dispersive X-ray spectroscopy (EDX) spectrum after complete processing of the wafer to confirm the absence of relevant surface contaminants. (J) Representative Raman spectra of graphene as transferred (black) and after completion of the fabrication process (red), showing the vibrational modes for defects (D), graphitic materials (G) and bi-dimensional characteristic of graphene (2D). (inset) Optical microscope photograph (50× magnification) showing the limits of the patterning and generally good coverage of graphene in the gold contacts (source and drain) and in the channel. The white rectangle limits the source and drain contacts of one EG-GFET, and the red region shows the channel area. The scale bar represents 20 µm.*

3.3.1. Statistical Study of the EG-GFET Channel Resistances Fabricated at the Wafer-Scale

For the devices' electrical characterization, an automated probe station was used to measure either the current or the voltage drop in the channel between source and drain contacts at a fixed voltage of 1 mV or a fixed current of 1 μA, respectively. Then, the measured values were converted to resistances to provide information on the homogeneity of the devices' process and quality (Figure 37).

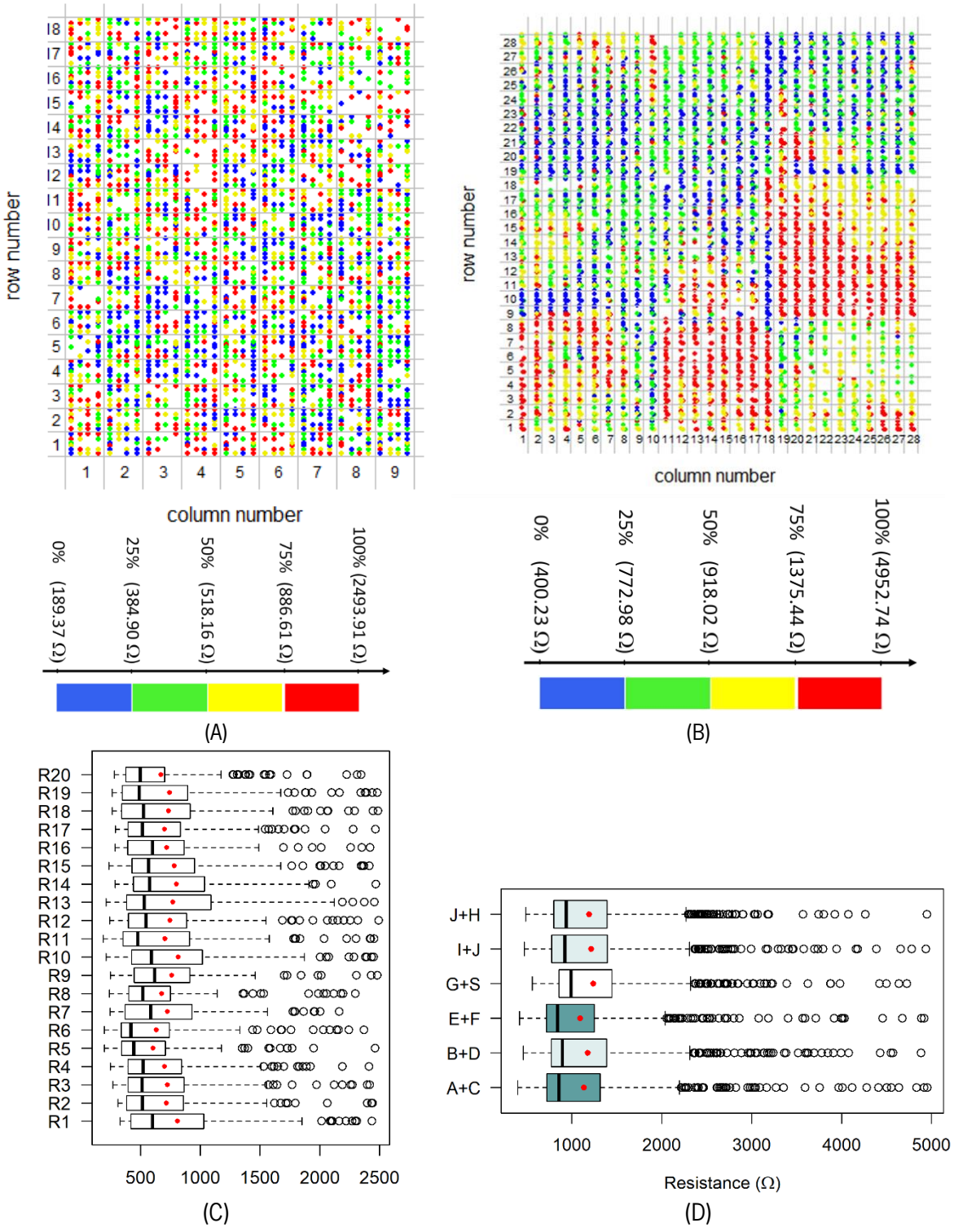

Figure 37. *Analysis of resistance values distribution in the fabricated wafers. (A) Distribution of resistance values in wafer A, with color-coding according to the quartiles of R values' empirical distribution.*

(B) Distribution of resistance values in wafer B, with color-coding according to the quartiles of R values' empirical distribution. (C) Boxplot of the empirical distributions of resistance values per pair of contacts in wafer A. The black line inside each box represents the median, and the red dot represents the mean of each distribution. (D) Boxplot of the empirical distributions of resistance values per pair of contacts (A+C, B+D, . . . see text) in wafer B. The black line inside each box represents the median, and the red dot represents the mean of each distribution.

For the geometry of the transistors (W/L = 3) and the unintentional doping level (see Figure 34) of processed graphene, a channel resistance, R, below ≈1000 Ω is expected in successful devices, while values up to ≈2500 W are still acceptable. Transistors with R > 2500 Ω were rejected and discarded. Two wafers were processed and studied. Wafer A is a shared design wafer containing 9 × 18 chips (see Appendix I – Microfabrication of EG-GFETs), each chip containing 20 transistors with resistances R1 to R20. In this wafer, measured at constant voltage, 63% of the 3240 channels have R < 1000 W (80% of the channels have R < 2500 W). In Figure 37A, each colored dot corresponds to one transistor's location with R < 2500 Ω. The color code refers to four classes of data values according to quartiles, qi (q0 = 189.37 W, q1/4 = 384.90 W, q1/2 = 518.16 W, q3/4 = 886.61 W, q1 = 2493.91 W). The spatial distribution of the resistance values looks random, and no correlation with the graphene patches individually transferred (Figure 38A) is visible. The boxplot charts in Figure 37C display the data distributions per device (see device map in Figure 38B) showing that all contacts behave in a relatively similar way, with medians (averages, red dots) ranging from 421.12 Ω (606.45 Ω) for R6 (R5) to 617.96 Ω (816.83 Ω) for R9 (R10).

A second wafer (wafer B) was processed and measured at constant source–drain current. Figure 37B shows 4107 resistance measurements with values in the range from 400 Ω to 5000 Ω, belonging to 784 chips distributed across the wafer in a square array of 28×28 lines and columns. Each measurement encompasses two transistor channels connected in series. Hence, the acceptable resistance range was multiplied by two. Since six pairs of GFETs were measured per die (the remaining five pairs were not measured due to constraints imposed by the automated measuring system, measured pairs in Figure 38D), we have 6 × 784 = 4704 measurements, of which those with resistance 2R > 5 kΩ were rejected (4704 – 4107 = 597). The x and y-coordinates of each data point corresponding to one pair of resistors. The color code reflects four classes of data values according to quartiles, qi (q0 = 400.23 W, q1/4 = 772.98 W, q1/2 = 918.02 W, q3/4 = 1375.44 W, q1 = 4952.74 W). Figure 37D gives the data distributions per contact pair (A + C, B + D, E + F, G + S, I + J, J + H, see the chip contact map in Figure

38D), in boxplot format. The red dot inside each box represents the mean of each dataset. Medians (means) differ by contact pair, from 843 Ω (1095 Ω) for E + F to 993 Ω (1239 Ω) for G + S, revealing three categories of statistically different medians, as shown by different colors in the plot. The highest median category refers to G + S and the lowest refers to A + C and E + F, which are contacts located in the central part of the die. Variances do not differ statistically between contacts, whereas the empirical distribution tail is slightly longer for contact E + F and slightly shorter for G + S.

Figure 37B suggests the existence of nine regions across the wafer, according to the color code. In the fabrication sequence of wafer B, the graphene transfer process consisted of a succession of nine transfer steps of individual graphene patches, as arranged in Figure 38C. The correspondence of the nine zones between the figures is striking. This result shows that the classes of resistance values found in the measurements correlate with the graphene transfer step—a rather artisanal process—and less with any other fabrication steps.

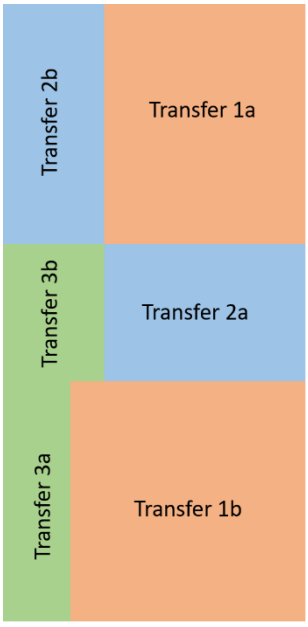

(A)

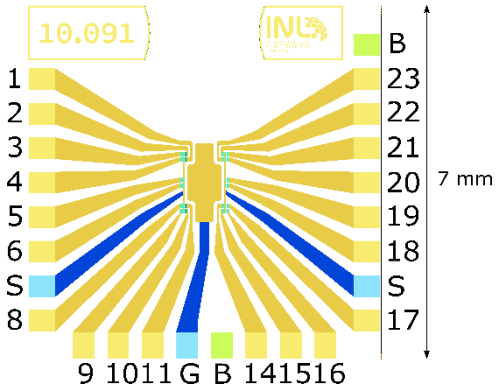

(B)

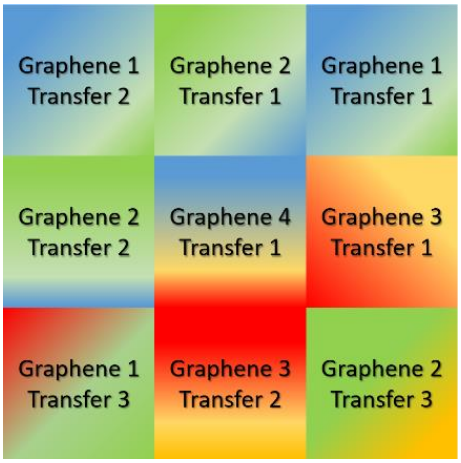

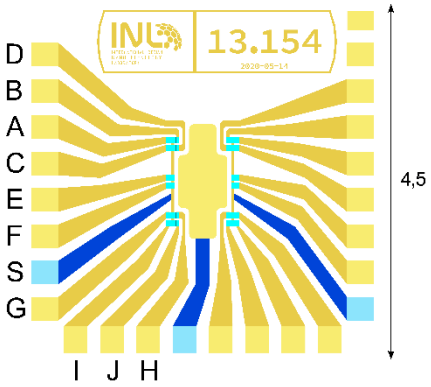

(C) (D)

Figure 38. *Distribution of graphene patches during full-wafer transfer and detailed designs of Wafer A and B. (A) Distribution of graphene patches over wafer A from a single chemical vapor deposition (CVD) batch. (B) Layout of one die from wafer A with the map of contacts used in Figure 36A,C. (C) Distribution of graphene patches over wafer B from CVD batches 1 to 4. Graphene from batches 1 and 2 was divided in three pieces, while that from batch 3 was divided into two pieces, and a single piece was used from batch 4. (D) Layout of one die from wafer B with the map of contacts used in Figure 36B,D. Note that not all the contacts from Wafer B were used in this study.*

4. Conclusions

A process for the fabrication of chips containing graphene electrolyte-gated FETs was developed step by step in this study, having in mind their application as biosensors. Many technical solutions for different process issues were suggested, developed, tested, and critically discussed. Some of them were rejected, given the study's goal, since they do not provide chips with enough chemical or electrical stability. However, for less demanding applications, these solutions could be useful. Dielectric passivation as the final step of the fabrication process allows an improvement of signal stability. It decreases electronic noise, since only the graphene channel and the gate electrode become exposed to the electrolyte during measurements. One of the most relevant results to obtain a useful chemical-resistant chip is the possibility of metal sputtering on top of graphene films without inducing relevant damage. This result can be extended to devices where metallic layers are required on top of graphene without significantly increasing the fabrication time.

A novel approach to improve the surface cleanliness of the chip surface after graphene transfer was also demonstrated. An effective sacrificial layer was developed, allowing the patterning of graphene while protecting the pristine gold surfaces. This optimization is of high importance for using the devices as biosensors. It promotes better inter-device homogeneity and less random molecular adsorption responsible for the sensor signal's random response and noise. The process is general and suitable for other applications or devices with similar requirements.

This study casts light on the critical field of microfabrication of graphene devices for chemical sensors with electric transduction and their chemical stability as a function of the process chosen in a manner that allows researchers in the field to pick, among the results presented, those that better suit their application.

Chapter III – Biofunctionalization of 2D materials

The general contents of this section are present in the publication " Functionalization of single-layer graphene for immunoassays" by Elisabete Fernandes[1], Patrícia D. Cabral[1], Rui Campos, George Machado Jr., M. Fátima Cerqueira, Cláudia Sousa, Paulo P. Freitas, Jérôme Borme, Dmitri Y. Petrovykh and Pedro Alpuim, in Applied Surface Science 480 (2019) 709–716 (https://doi.org/10.1016/j.apsusc.2019.03.004).

[1] These authors contributed equally to the manuscript

Personal Contribution: Methodology development, data processing and analysis, investigation, original draft writing, reviewing, and editing.

1. Introduction

The unique fundamental properties of graphene [44], particularly the chemical stability and extreme sensitivity to near-surface charges and electric fields, suggest its use for biomolecular detection [77–79]. The hydrophobicity and high sensitivity to charges and electrical fields, however, result in strong interference from nonspecific molecular ad- sorption and thus poor selectivity of unmodified graphene sensors for bioanalytes when operating in an aqueous physiological environment. Accordingly, to produce selective and specific biosensors, graphene surfaces need to be functionalized [93,194,195] with specific biomolecular probes, thereby minimizing nonspecific adsorption and ensuring that the surface binding events are dominated by the biorecognition of the target. These molecular binding events can be effectively transduced into electrical signals by using the functionalized single-layer graphene as the channel of a field-effect transistor (FET), or more specifically for biosensing, of an electrolyte-gated FET (EGFET) [93,118,196]. The most common graphene functionalization methods overcome the hydrophobic nature of pristine graphene by oxidation treatments to produce graphene oxide (GO) or reduced GO (rGO), followed by covalent or non-covalent immobilization of biomolecular probes [95,107,120,197]. The aggressive oxidation treatments, however, typically destroy the excellent electronic properties of pristine graphene [198]. To preserve the unique electronic structure of graphene for biosensing applications, non-covalent (π-π stacking) modification of pristine graphene using pyrene derivatives as heterobifunctional linkers is a popular approach [81,93,94,97,118,122,199], for which the detailed mechanistic understanding is still emerging [111–115]. Reports on implementations of this approach to date typically rely on the device performance [81,94,118,122] as an indirect indicator of a successful surface functionalization, rather than using the more direct surface analysis methods to investigate the surface functionalization steps. In other words, the assay performance typically has been implicitly assumed to be a self-sufficient endpoint, from which the success of all the surface functionalization steps was inferred indirectly. In contrast, here we systematically follow by complementary characterization techniques each step of the surface functionalization and biofunctionalization of single-layer graphene produced in-house by chemical vapor deposition (CVD). Particularly, we verify that a combination of a pyrene-derivative heterobifunctional linker and an optimized blocking strategy can be effectively used to immobilize specific biomolecular probes (antibodies) and minimize nonspecific adsorption in the context of an immunoassay. Following the validation of the biofunctionalization strategy, we use it to functionalize a graphene channel in a receded-gate EGFET [39] and to perform proof-of-principle immunoassay measurements for a clinically-relevant biomarker.

2. Materials & Methods

2.1. Materials

Table 4. *Reagents and Biomolecules.*

	Description	Supplier
Solvents	Dimethylformamide (DMF) 99.75% purity Ethyl Acetate, anhydrous 99.8%	Sigma-Aldrich
	Ethanol 99.8%	Honeywell
Chemicals	1-Pyrenebutanoic acid succinimidyl ester (PBSE) Ethanolamine, 98% (ETA) 1-Dodecanethiol (DDT) (≥98%) PMMA 15 kDa, powder	Sigma-Aldrich
	PMMA 550 kDa, powder	Alfa Aesar
	NaH_2PO_4 Na_2HPO_4	Fisher Scientific
Biomolecules	Purified Matrix Metallopeptidase 9 (MMP-9), MW 92 kDa Monoclonal anti-human MMP-9 Polyclonal biotin anti-human MMP-9	Immunostep
	Human Hemoglobin protein (≥95%), MW 66.2 kDa	LifeSpan BioSciences

2.2. Methods

2.2.1. Solutions Preparation

PBSE linker was prepared at 10 mM in DMF as follows: 38.5 mg of PBSE powder were weighted and dissolved in 10 mL of DMF. The solution was stored in a dark bottle at room temperature.

Ethanolamine at 100 mM was prepared in ultrapure water as follows: 60.5 µL of ETA 98% were diluted into 8 mL of ultrapure water. After pH assessment, HCl 2 M was slowly added to the mixture to reduce the pH value to physiological values (pH 7.2 – 7.4). After pH stabilization the volume was completed to 10 mL with ultrapure water.

DDT 2 mM was prepared by dissolution of 5 µL of DDT ≥98% in 10 mL of Ethanol. Fresh solution was prepared for each run.

Phosphate buffer (PB) at 100 mM with pH 7.2 was prepared mixing 70 mL of 200 mM NaH_2PO_4, 180 mL of 200 mM Na_2HPO_4 and 250 mL of water. Dilution for PB 10 mM was done with ultrapure water as required.

PB 10 mM with Tween 20 at 0.05% (PB-Tw20) was prepared by addition of 5 µL of Tween 20 to 10 mL of PB 10 mM. PB-Tw20 was freshly prepared for each run.

2.2.2. Samples preparation

For functionalization studies, 7×7mm² square silicon substrates with 200-nm silicon oxynitride coating and a transferred graphene layer were used as models of the surfaces of graphene channels in EGFET structures. Graphene growth by CVD and transfer to silicon substrates followed the previously published process [39]. Shortly single-layer graphene (SLG) was deposited by Chemical Vapor Deposition (CVD) in a load-locked quartz tube 3-zone furnace (FirstNano EasyTube® 3000) onto high-purity (> 99.99 %) 25 µm-thick copper foils placed inside a graphite susceptor that accepts substrates with area up to 10 cm × 12 cm. An annealing step at 1020 °C for 20 minutes in a H_2 atmosphere (300 sccm, 0.5 Torr) was performed previously to deposition. A gaseous mixture of 300 sccm of H_2 with 50 sccm of CH_4 was used for growth, keeping the same temperature and pressure used in the annealing step. A temporary PMMA substrate was used for graphene transfer. PMMA was spun onto one side of the as-grown graphene/Cu/graphene sample, followed by Cu dissolution by dipping into a 0.5 M $FeCl_3$ solution at 35 °C for 1 h. The PMMA/graphene composite was then cleaned in 2% HCl solution and was further washed in deionized water. The cleaning procedure was repeated three times. After transfer to the silicon/silicon dioxide (Si/SiO_2), the sample was dried with a N_2 flow to flatten the PMMA/graphene film on the substrate, followed by annealing for 7 hours at 180 °C. The PMMA is finally removed using acetone followed by ethyl acetate.

2.2.3. Surface functionalization

The heterobifunctional pyrene linker, 1-Pyrenebutyric acid N-hydroxysuccinimide (NHS) ester (PBSE, 10mM in DMF) was deposited as a 30 µL drop and allowed to interact with the graphene surface for 2 h under a humid atmosphere at room temperature (RT). Anti-MMP-9 antibody was prepared at 250 µg/ml concentration in 10 mM PB, spotted onto the pyrene-modified substrates, and incubated overnight at 4 °C in a humid atmosphere. To prevent nonspecific binding events, ethanolamine 100 mM, was used since previous results showed improved blocking using this agent [42].

2.2.4. Characterization techniques

X-Ray photoelectron spectroscopy (XPS)

Representative graphene surfaces before and after functionalization with PBSE and anti-MMP-9 antibody were characterized in an ESCALAB 250 Xi system (Thermo Scientific) using a monochromated micro-focused Al Kα X-ray source that defined an analysis spot of<1mm2. Peak fitting was performed in Avantage instrument software (Thermo Scientific), choosing a minimal number of components that produced random residuals consistently for all the samples; a convolution of Gaussian and Lorentzian line shapes was used for all the spectral components. Small differential charging encountered for some of the samples was compensated by shifting the binding energy (BE) scale for C 1s and N 1s regions to place the aliphatic C 1s peak associated with the organic/molecular layers on top of graphene at 284.5 ± 0.2 eV, the value consistent with previous measurements of organic [200] or bio- logical [201–203] molecules on metallic surfaces.

Quartz crystal microbalance (QCM)

QCM measurements were performed in a QSense E1 system (Biolin Scientific). AT-cut quartz crystals having gold electrodes of the working surface coated with ca. 50 nm of silicon oxide (QSX 335, Biolin Scientific) were used as substrates for single-layer graphene transfer. Prior to monitoring the anti-MMP-9 antibody immobilization by QCM, these graphene surfaces were functionalized with PBSE (2 h in 10 mM PBSE in DMF). QCM measurements for the fundamental (ca. 4.95 MHz) frequency and at its 6 odd overtones (n=3, 5, 7, 9, 11, 13) were carried out under a flow rate of 0.06 mL/min at a constant temperature of 20 °C (set within<1 °C from RT, at which the solutions have been stabilized prior to the measurements). The frequency shift is reported in the standard ΔFn/n normalization, as recorded by the instrument software. The baseline in the blank 10 mM PB was recorded before and after the antibody immobilization; antibody was immobilized by re-circulating 1 mL of 20 μg/mL solution in the same buffer through the QCM flow cell. The measurement produced consistent results in two repeated depositions on two different QCM crystals. Protein immobilization was carried out using analogously prepared substrates and measurement parameters. Prior to monitoring the immobilization step by QCM, the graphene surfaces were functionalized with PBSE (2 h in 10 mM PBSE in DMF), anti-MMP9 antibody (2 h in 250 μg/mL anti-MMP9 in PB 10 mM) and ethanolamine (100 mM in water, for 1 h at RT). The baseline in the blank 10 mM PB was recorded before and after protein immobilization; MMP-9, Hemoglobin (nonspecific control) and c-Fn protein targets were presented for biorecognition by recirculating 1 mL of 3 μg/mL solution in the same buffer through the QCM flow cell. The capture of each protein target by the anti-MMP9 or anti-c-Fn functionalized graphene was recorded independently, on freshly prepared samples.

3. Results & Discussion

The biofunctionalization studies discussed were performed to complement previous results present in the dissertation "Nanobiosensors based in Graphene Field Effect Transistors for biomarkers detection" which conduced to the master's degree of the author in Biophysics and Bionanosystems by the University of Minho. They should be as such seen as a continuation of the previous work, rather than an independent result.

Each graphene surface functionalization step presented in Figure 39 was carried out and systematically characterized by several complementary techniques. Before chemical functionalization, the single-layer structure of the graphene was confirmed by Raman spectroscopy as reported in [42].

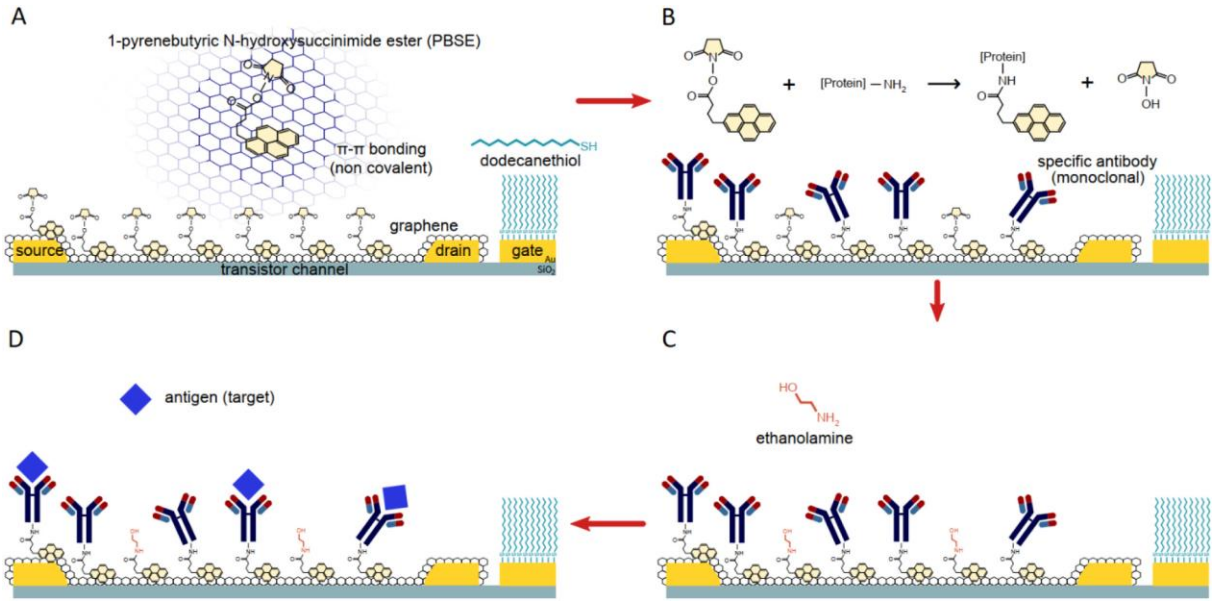

Figure 39. *Functionalization and biorecognition on a single-layer graphene surface of an EGFET. (A) Surface modification with the heterobifunctional linker, PBSE; (B) covalent immobilization of the antibody; (C) blocking with ethanolamine; (D) biorecognition of MMP-9 target.*

3.1. Chemical functionalization

The graphene surface was first modified with PBSE (Figure 39A), a pyrene-based heterobifunctional linker that is expected to attach to the graphene surface via stable non-covalent π-π interactions [204] and to present an NHS-ester ligand for amide coupling of the antibodies in the subsequent biofunctionalization step (Figure 39B). The primary indications of the successful π-π bonding of the pyrene ligands of PBSE to graphene were provided by Raman spectroscopy [42]. The presence of the NHS-ester ligands of PBSE was confirmed by XPS measurements, whereby the peaks characteristic of NHS-esters appear (Figure 40) after the PBSE functionalization for N 1s at 402.3 eV and for C 1s at 289.3 eV [117,205,206]. The

high BE of the N 1s component provides a nearly-unique identification for the electron-deficient N atom in NHS-esters because the main alternative means for producing such a high BE shift for N 1s – the protonation of primary amines in polymers [207,208] or in proteins and peptides [209] – is inconsistent with the chemistry of the compounds that we used to modify the graphene surface. The concomitant observation of the C 1s component at 289.3 eV strengthens the NHS-ester identification of the ligands on the PBSE-modified graphene because the high oxidation states of C atoms that it implies are in excellent agreement with O-C=O and N-C=O configurations [210] in NHS-esters.

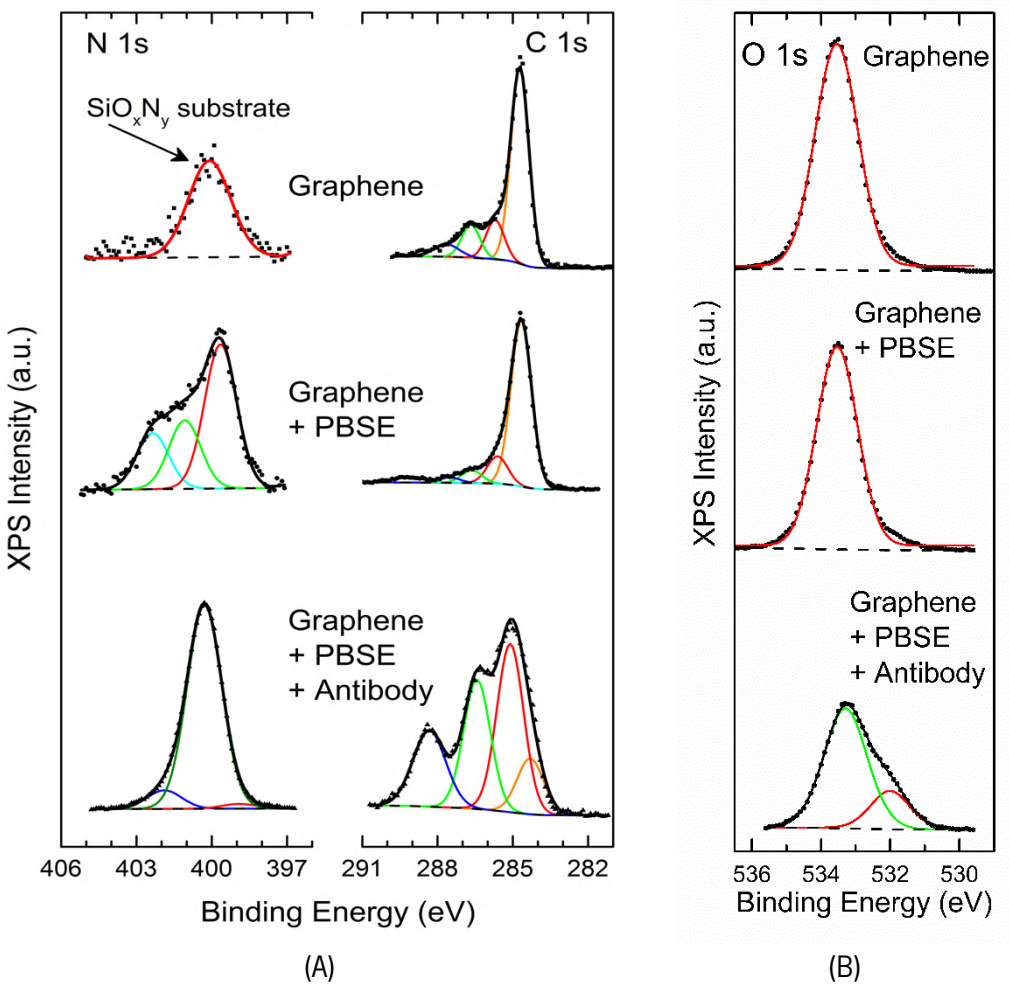

Figure 40. *XPS signatures acquired after individual steps in biofunctionalization of graphene. The N 1s (left, A), C 1s (right, A) and O 1s (B) spectral regions and are shown for the initial graphene surface (top), PBSE-modified graphene (middle), and PBSE-modified graphene after anti-MMP-9 antibody immobilization (bottom). With exception of the top-left panel, all the data are shown after correcting any small differential charging in the raw data to shift the aliphatic C 1s peak to 284.5±0.2 eV; this correction is applied essentially only to the peaks associated with the organic/molecular layers on top of graphene, as verified by observing the protein N 1s component at 400.3 eV (bottom-left). The exception for the top-left N 1s panel is due to the apparent small differential charging between the substrate and the*

organic/molecular layers: the N 1s signal observed for the initial graphene surface (top-left) arises from the silicon oxynitride substrate and is shown after a small BE correction that places the unresolved substrate Si 2p peak at 104.2±0.1 eV (and substrate O 1s at 533.4±0.1 eV, data not shown) for all the samples. Symbols=raw data; thick lines=overall fits; thin colored lines=fit components; dashed lines=background.

3.2. Antibody immobilization

The PBSE-modified graphene surface was biofunctionalized with the anti-MMP9 antibody (Figure 39B), as confirmed by both in situ real-time QCM measurements (Figure 41) and ex situ XPS measurements (Figure 40).

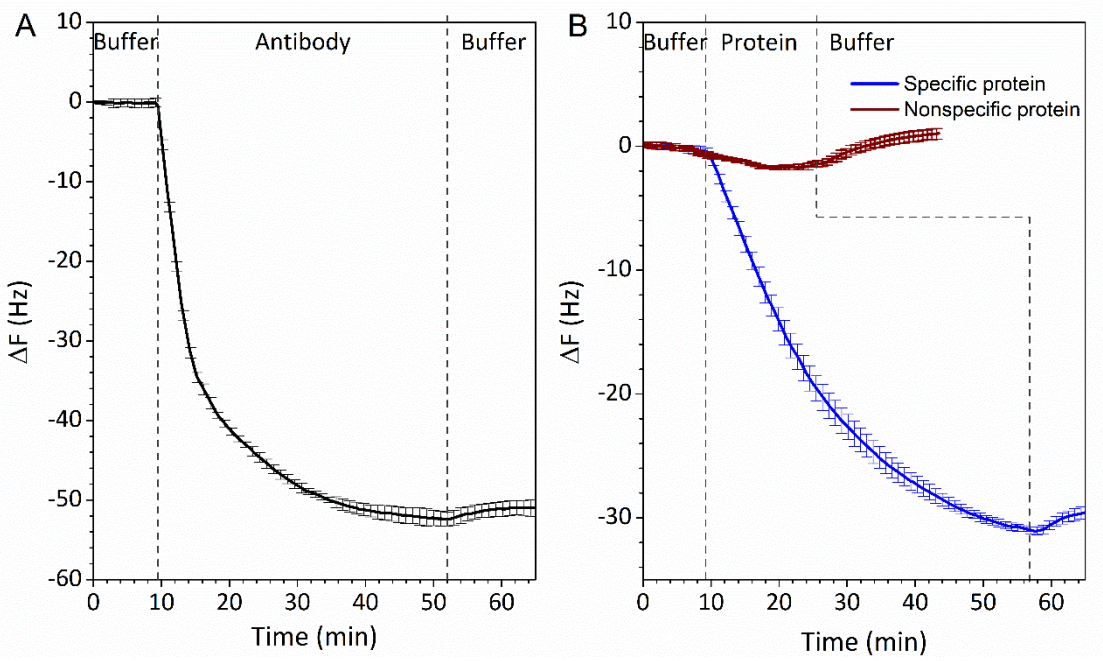

***Figure 41**. QCM characterization of the biofunctionalization of graphene. Real-time QCM data are shown for the anti-MMP9 antibody deposition on PBSE-modified graphene (A) and for the biorecognition of MMP9 (specific protein target) and Hemoglobin (nonspecific control) on fully biofunctionalized (PBSE + anti-MMP9+ethanolamine) graphene (B). The normalized frequency shift in (A) is shown for the 11th overtone, error bars represent the standard deviation based on averaging overtones 5–13 for (A) and overtones 9–13 for (B). The vertical dashed lines indicate, the introduction (ca. 10 min) of the deposition solution into the QCM chamber and the beginning of the post-deposition rinse (at ca. 52 (A) and 25/56 (B) min) in blank buffer.*

In QCM data, when the PBSE-modified graphene was exposed to the antibody solution (dashed line at ca. 10 min in Figure 41A), a rapid and consistent frequency shift was observed for all the overtones, leading

to the quasi-saturation value of -53 ± 1 Hz after ca. 40 min of deposition. Both the initial deposition rate and the overall frequency shift agree with the behavior previously reported in an extensive multi-technique characterization of surface immobilization of a model protein [8], indicating that the QCM kinetic profile in Figure 41A is consistent with a signature of an antibody immobilization onto the PBSE-modified graphene. The XPS results support the identification of the molecular layer deposited onto the PBSE-modified graphene as an antibody. The multi-component N 1s spectrum observed for the PBSE-modified graphene is replaced by a dominant N 1s component at 400.3 eV (Figure 40A), which is characteristic of amide and amine nitrogen in proteins and peptides [201,202,211]. Likewise, the C 1s spectrum after the antibody deposition (Figure 40A) is no longer dominated by the aliphatic component at 284.5 ± 0.2 eV, but rather by the three higher-BE components that exhibit both the BEs and intensity ratios characteristic for the C configurations (C-O, C-N, C=O, O-C=O, N-C=O) in proteins and peptides [201,202,211]. Furthermore, only after the antibody deposition, an O 1s component appears at 531.7 eV (Figure 40B), which is one of the characteristic BEs for O 1s in proteins and peptides [201]. The dominant intensities of the protein-like N 1s and C 1s components are also in agreement with the large frequency shift observed in QCM (Figure 41A), which suggests a near-saturation surface density of the deposited antibody.

3.3. Non-specific surface interactions

The physical mechanism of transduction in graphene EGFETs is based on the near-surface charges and electric fields [77–79], making such biosensors highly sensitive but not selective [212] in terms of differentiating the biorecognition binding events from nonspecific adsorption, e.g., of background molecules. It is critically important, therefore, to validate the strategy (Figure 39C) that can be used to block the nonspecific adsorption onto the biofunctionalized surface. The appropriate blocking strategy is likely to be different for our minimally hydrophilic PBSE-modified graphene surfaces vs those used on the more common GO and rGO. Likewise, immunoassays typically require a blocking strategy different from those used in DNA assays [213–217]. In particular, it is useful to choose validation methodologies independent from that of the intended assay, EGFET in this case, in order to avoid being misdirected by intrinsic artifacts. QCM measurements are a well-established approach for the validation of biorecognition assays [46] allowing to quantitatively evaluate the specificity of antibody-antigen interactions. We used the model QCM crystals biofunctionalized with anti-MMP9 antibodies (Figure 39B, Figure 41A), blocked by ethanolamine (Figure 39C), to quantitatively compare (Figure 41B) biorecognition of the specific protein target (MMP9) and of a nonspecific protein control (human hemoglobin) that has a comparable molecular weight. Observing the nearly 30-fold difference between the QCM responses associated with

specific and nonspecific biorecognition (Figure 41B) validates the specificity of the MMP9 immunoassay components and indicates that the ethanolamine blocking strategy is effective. Additional data on the effectiveness of surface blocking with ethanolamine, comparing with other common blocking strategies (e.g. BSA) is reported in [42].

3.4. Binding of specific biomarkers

The final validation step for our graphene biofunctionalization strategy (Figure 39) is confirming the biorecognition of the target (Figure 39D) by the immobilized antibody. Direct visualization of this biorecognition was provided by an MNP-tagged target binding assay as discussed in [42]. Additionally, the model QCM crystals (Figure 41B) showed specific immobilization of MMP9 as discussed in the sub-section 3.3. To confirm the versatility of the system for different biomarkers, QCM model crystals biofunctionalized with anti-c-Fn antibodies and blocked with ethanolamine were exposed to c-Fn at 3 µg/mL (Figure 41). Exposure to the specific target induced a frequency shift of 11.3 ± 1.7 Hz, indicating that specific detection is possible for different biomarkers, i.e., the functionalization strategy can be adapted for a multiplex detection system.

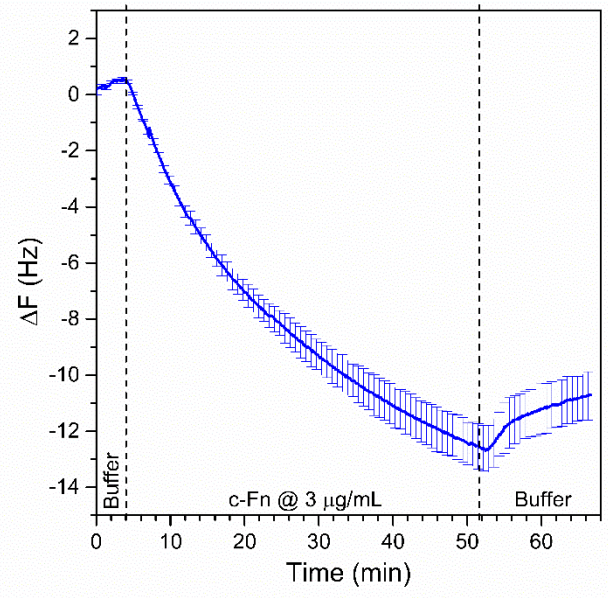

Figure 42. *QCM characterization of the specific detection of c-Fn on functionalized graphene. Real-time QCM data are shown for the biorecognition of c-Fn (specific protein target) on fully biofunctionalized (PBSE + anti-c-Fn + ethanolamine) graphene (B). The normalized frequency shift in (A) is shown for the 11th overtone, error bars represent the standard deviation based on averaging overtones 5–13 for (A) and overtones 9–13 for (B). The vertical dashed lines indicate, the introduction (ca. 10 min) of the deposition*

solution into the QCM chamber and the beginning of the post-deposition rinse (at ca. 52 (A) and 25/56 (B) min) in blank buffer

Still, it is clear an almost 3x difference in the frequency shift observed between specific detection of MMP9 and specific detection of c-Fn. Considering that both targets were prepared at 3 µg/mL and have different molecular weights (92 kDa for MMP9 vs 550 kDa for c-Fn), it is expected to have much less c-Fn proteins in circulation than MMP9 for the same concentration (19.6×10^{12} MMP9 molecules vs. 3.3×10^{12} c-Fn molecules). In fact if the total of protein in circulation is compared to the estimated values of protein that was bound in the functionalized crystal (Appendix II – Graphene functionalization, section 2.1) [8,218] it is observed an 2.5-fold difference in binding efficiency (ratio between bound and circulating target), as reflected in the frequency shift. This difference in the binding efficiency between different proteins can be related with size and availability, meaning that with less protein present (7 times less protein in this situation) the likelihood of detection reduces, as it is expected in other sensing systems [83]. In order to be able to directly compare the frequency shifts obtained for MMP9 and c-Fn, the second one would have to be prepared at a higher, but impracticable concentration (~20 µg/mL) which is not required for the goal of this study.

4. Conclusions

This biofunctionalization study systematically investigated and validated a strategy for biofunctionalization of graphene. Several independent methods have been used to characterize and verify each step in the surface functionalization and biofunctionalization procedure. Finally, we have applied the validated strategy in model QCM crystals as a proof-of-principle of specific detection for MMP9 and c-Fn and non-specific blocking for similar proteins as hemoglobin. The optimized strategy can thus be applied to graphene channels in an EGFET device to perform proof-of-principle measurements of biosensor functionality.

The excellent results obtained with the available CVD-grown graphene and the reduced availability of other 2D materials compel this work in the direction of graphene-based sensors. Development of biofunctionalization procedures and biosensing platforms might be considered for other 2D materials when the throughput of growth of such materials reaches a stage similar to graphene.

Section IV – Assessment of graphene immuno-FETs for the detection of stroke-related biomarkers

The contents of this section are present in the publication "Graphene immuno-FETs for detection of stroke-related biomarkers in human serum" by, Patrícia D. Cabral, Ivo Colmiais., Jérôme Borme, Marco Martins, Pedro Alpuim and Elisabete Fernandes, under preparation for publication.

Personal Contribution: Methodology development, data processing and analysis, investigation, original draft writing, reviewing, and editing.

1. Introduction

Biosensing technologies based on label-free methodologies are of great interest for multiplex detection since there is no limitation on the number of different labels available. Field-effect transistors (FETs) have been widely studied as label-free biosensors due to their ability to respond to changes in the near-surface charges, e.g., due to the presence of a charged analyte, without any modification/labeling of the detection system. More specifically, graphene field-effect transistors (GFETs) are reported for the detection of a variety of molecules/biomolecules and ions [175], including pH [84], glucose [175], deoxyribonucleic acid (DNA) [175], proteins [94], and hormones [175], with different detection ranges. Graphene's particular interest comes from its intrinsic properties, such as high carrier mobility [16,174], low intrinsic electronic noise [16,94], chemical stability [16,94,219], high sensitivity to electric charges in its vicinity [16,174], and record surface-to-volume ratio [94,174]. Operation of graphene FETs in electrolyte gating mode allows to perform detection of biomolecules directly on top of graphene, making use of its properties for the development of biosensors. The functionalization of CVD-graphene followed by the immobilization of molecules that specifically recognize the interested targets allows to improve assays specificity [42]. Antibodies are the preferred biorecognition elements in the biosensing field for the detection of protein biomarkers, also explored with FETs [3]. Additionally, the possibility for large-scale fabrication of EG-GFETs [28] allows adapting/using this system for multiplex detection approaches. The relevance of detecting multiple biomarkers arises from the recurrent need of evaluating and/or identifying complex diseases in a pre-disease state accurately and timely. An example is acute ischemic stroke (AIS) which represents a large public health problem that lacks a diagnostic system to provide personalized treatment to improve patient outcomes [63,64]. Nowadays, a patient with AIS can undergo pharmacological therapy with a recombinant thrombolytic plasminogen activator (r-tPA) that is highly effective to dissolve the blood clot and restore blood circulation but its application is limited to a very narrow time-window administration (< 4.5 hours from stroke onset) [61]. Moreover, the side effects of r-tPA therapy, as the risk of hemorrhagic transformation (HT) [61–63], and the strict inclusion/exclusion criteria (e.g. high blood pressure, overweight, and diabetes type II) decreases the treatment rates. The study of the pathophysiology of ischemic stroke has allowed associating panels of protein biomarkers to the risk of HT. These panels can work as potential tools to use for the stratification of ischemic stroke patients for r-tPA therapy [62,63,65,66]. The protein biomarkers identified have been selected for their role in different physiological processes of ischemic stroke that can lead to HT: Matrix Metalloproteinase-9 (MMP9), cellular Fibronectin (c-Fn), Platelet-Derived Growth Factor-CC (PDGF-CC), Angiopoietin-1 (Ang1), Neuroserpin and Calcium-binding protein S100β. MMP9 is related to loss of microvascular integrity and

disruption of the blood-brain barrier (BBB). High levels of this protein in blood serum (> 140 ng/ml) were correlated with an increased risk of HT in ischemic stroke patients [64,68–70]. High concentrations of c-Fn (> 3.6 μg/ml) have also been associated with vascular injury HT [62,65], since its release into the bloodstream only occurs in the case of disruption of endothelial tissue (blood vessels component). The detection of a single biomarker does not provide enough information on the risk of HT, however, it has been shown that simultaneous detection of MMP9 and c-Fn provides 87 % diagnostics specificity [65]. Ideally, just the simultaneous detection of the complete panel of biomarkers provides high specificity rates, however, simultaneous detection of multiple biomarkers presents several challenges that need to be overcome. As such, only two biomarkers (MMP9 and c-Fn) are studied in this work for biosensing assessment, allowing to study the immune-FET capabilities, limitations, and potential for simultaneous detection of two biomarkers.

This work focused on the development of an immunosensor, based on the EG-GFETs, for the detection of MMP9 and c-Fn in serum. Sensitivity, selectivity, and dynamic range were the analytical parameters explored to understand if the graphene-based sensor fits the clinical need. For that, several parameters must be accessed [220], including the limit-of-blank (LoB) and limit-of-detection (LoD). Assessment of the linear dynamic range allowed to define the range of concentrations that the graphene sensor can quantify above the LoD and below the saturation threshold [220]. The sensitivity related parameters can be quantitated using the standard deviation as a reference, as demonstrated by [220,221] (Appendix III – Baseline measurements with multi-channel acquisition system for EG-GFETs, Eq. 1,2). Assessment of the blank noise (limit of blank), of the lowest readable concentration (LoD) and of the sensor response for each target concentration allow to evaluate the sensitivity of EG-GFETs for a specific target [10,67,221]. Selectivity can then be accessed by comparing the response of the devices to a specific target with the response to a non-specific one, which should be much lower than the specific response to obtain a selective sensor [10].

The EG-GFETs were first tested with phosphate buffer to study the charge effects in the transistor signal and then used with an immunoassay to obtain a dose-dependent response curve for MMP9 and c-Fn. Later, the effects of the biological matrix (detailed in Chapter VI) were also assessed.

2. Materials & Methods

2.1. Materials

Table 5. *Reagents and Biomolecules*

	Description	Supplier
Solvents	Dimethylformamide (DMF) 99.75% purity	Sigma-Aldrich
	Ethanol 99.8%	Honeywell
Chemicals	3140 RTV non-corrosive silicone rubber (flowable)	Dawsil™
	Elastosil® E41, RTV-1 silicone rubber	Wacker Chamie
	1-Pyrenebutanoic acid succinimidyl ester (PBSE) Ethanolamine, 98% (ETA) 1-Dodecanethiol (DDT) (≥98%)	Sigma-Aldrich
	NaH_2PO_4 Na_2HPO_4 Sulfosuccinimidyl 6-(3′-(2-pyridyldithio)propionamido)hexanoate (Sulfo-LC-SPDP)	Fisher Scientific
Biomolecules	Purified Matrix Metallopeptidase 9 (MMP-9), MW 92 kDa Monoclonal anti-human MMP-9 Human Cellular Fibronectin Native Protein (c-Fn), MW 560 kDa Purified monoclonal anti-human Fibronectin	Immunostep
	Bovine Serum Albumin (BSA)	BioWest

2.2. Methods

2.2.1. Solutions Preparation

PBSE linker was prepared at 10 mM in DMF as follows: 3.85 mg of PBSE powder were weighted and dissolved in 1 mL of DMF. The solution was stored in a dark bottle at room temperature. The solution was prepared fresh after 5 experiments to avoid loss of activity of the linker.

Ethanolamine at 100 mM was prepared in ultrapure water as follows: 60.5 µL of ETA 98% were diluted into 8 mL of ultrapure water. After pH assessment, HCl 2 M was slowly added to the mixture to reduce

the pH value to physiological values (pH 7.2 – 7.4). After pH stabilization, the volume was completed to 10 mL with ultrapure water.

DDT 2 mM was prepared by dissolution of 5 µL of DDT ≥98% in 10 mL of Ethanol. A fresh solution was prepared for each run.

Phosphate buffer (PB) at 100 mM, pH 7.2 was prepared by mixing 70 mL of 200 mM NaH_2PO_4, 180 mL of 200 mM Na_2HPO_4, and 250 mL of water. Dilution for PB 10 mM was done with ultrapure water as required.

Bovine Serum Albumine (BSA), was prepared in PB 10 mM at 1 pg/ml, 10 pg/ml, 100 pg/ml, 1 ng/ml, 10 ng/ml, 100 ng/ml and 100 µg/ml for non-specific detection sequential assays.

Monoclonal anti-human Fibronectin and anti-human MMP9 were prepared at 250 µg/ml in PB 10 mM for functionalization of EG-GFETs.

Matrix Metallopeptidase 9 (MMP9) was prepared in PB 10 mM at 1 pg/ml, 10 pg/ml, 100 pg/ml, 1 ng/ml, 10 ng/ml and 100 ng/ml for sequential detection assays.

Cellular Fibronectin (c-Fn) was prepared in PB 10 mM at 1 pg/ml, 10 pg/ml, 100 pg/ml, 1 ng/ml, 10 ng/ml and 100 ng/ml for sequential detection assays.

2.2.2. Microfabrication of EG-GFETs and Graphene Transfer

The microfabrication of EG-GFETs at wafer-scale and graphene transfer methods are reported in detail by [28] and summarized in Chapter III, Section 2.

2.2.3. Chip Preparation

To allow electrical measurements using a multi-channel platform the diced chips were wire-bonded to custom-made PCBs using Aluminum or Gold wire. The wires were protected using 3140 RTV flowable silicone rubber and E41 silicone rubber, which was dried in air, at room temperature for 18 h.

2.2.4. Surface functionalization

Graphene

Functionalization of the graphene channels of EG-GFETs was performed as reported by [42]. Shortly a heterobifunctional pyrene linker, PBSE, 10mM in DMF, was deposited in a 20 µL drop and allowed to interact with the graphene surface for 2 h under a humid atmosphere at room temperature (RT). Antibodies (Anti-MMP9 or Anti-c-Fn) were prepared at 250 µg/ml concentration in PB 10 mM and spotted (5 µL) onto the pyrene-modified surfaces for overnight incubation at 4°C under a humid atmosphere.

Prevention of non-specific binding was done by passivating free PBSE molecules with ethanolamine (ETA) at 100 mM concentration for 1h at RT, under a humid atmosphere. For non-specific detection assays, graphene was only functionalized with PBSE, 10mM in DMF before exposure to the target protein.

Gold Surfaces

For assays where detection is expected to happen in the graphene channel, the gold gate electrode was passivated to prevent non-specific interactions with DDT at 2 mM concentration in ethanol. This step is performed before the initial characterization of the EG-GFETs and biofunctionalization of graphene.
For assays with non-specific detection at the gate electrode, gold was functionalized with, Sulfo-LC-SPDP, 1 mg/ml in PB 10 mM, for 20 minutes at RT, in a humid atmosphere [213], previous to exposure to the target protein.

2.3. Characterization techniques

2.3.1. EG-GFET electrical measurements

The acquisition of transfer curves from EG-GFETs and extraction of curve parameters (e.g., minimum conductivity point) was performed using an in-house built platform and software for sequential data acquisition of the 20 EG-GFETs present in each chip. The acquisition system consisted of an Arduino-like board with 10×6 cm^2 equipped with a microcontroller, digital-to-analog and analog-to-digital converters (DAC, ADC), resistance-controlled current source of 1-100 µA, digital potentiometer, and CMOS matrices (Figure 43). A constant drain-source current (I_{DS}) was applied at 1 µA, or a constant drain-source voltage (V_{SD}). The gate voltage was linearly scanned within a 1 V range with a voltage step of 200 mV using a liquid gate electrode. The waiting time during each measurement of the transfer curve was 18 s. The acquisition software, custom-made with Lab-View™ tools, allowed to control the measurement parameters and automatic extraction of the transfer curve parameters (e.g., minimum conductivity point, linear region slopes). For all functionalization and detection steps, 20 consecutive curves were traced to allow for signal stabilization (Appendix III – Baseline measurements with multi-channel acquisition system for EG-GFETs, Figure Ap12).

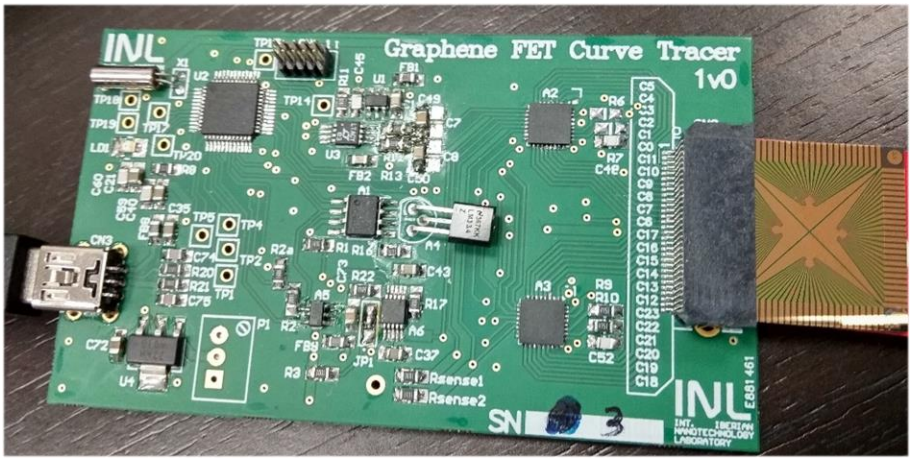

Figure 43. *The in-house built platform for simultaneous acquisition of transfer curves from up to 22 EG-GFETs.*

2.4. Data analysis

The data extracted from the acquisition system was analyzed using Origin® 9 software.

Transfer curves were used for the extraction of charge carrier mobility parameters as reported previously [39].

Overtime parameters (minimum conductivity point) were extracted to evaluate signal stability, and the values from the final 5 runs were used to average the voltage at the minimum conductivity point (V_{CNP}). The averaged V_{CNP} was used as the signal from each EG-GFET and was compared between functionalization steps. After functionalization, exposure to PB 10 mM allowed to stabilize the surface, and a baseline V_{CNP} was extracted for comparison with the V_{CNP} from target exposure.

Comparison of the data from all EG-GFETs in one chip, using the average, mode, and two times standard deviation (2SD) allowed to detect outliers and remove them from the final data analysis (exemplified in Figure 43). When the mode results in a very different value from the average (> 10 mV) it is indicative that the average is being skewed by outliers. As such, initial outliers are considered to have a voltage shift value that is at least 10 mV above or below the mode shift value. After removal of these values, the new average plotted with 2SD is used to filter minor outliers.

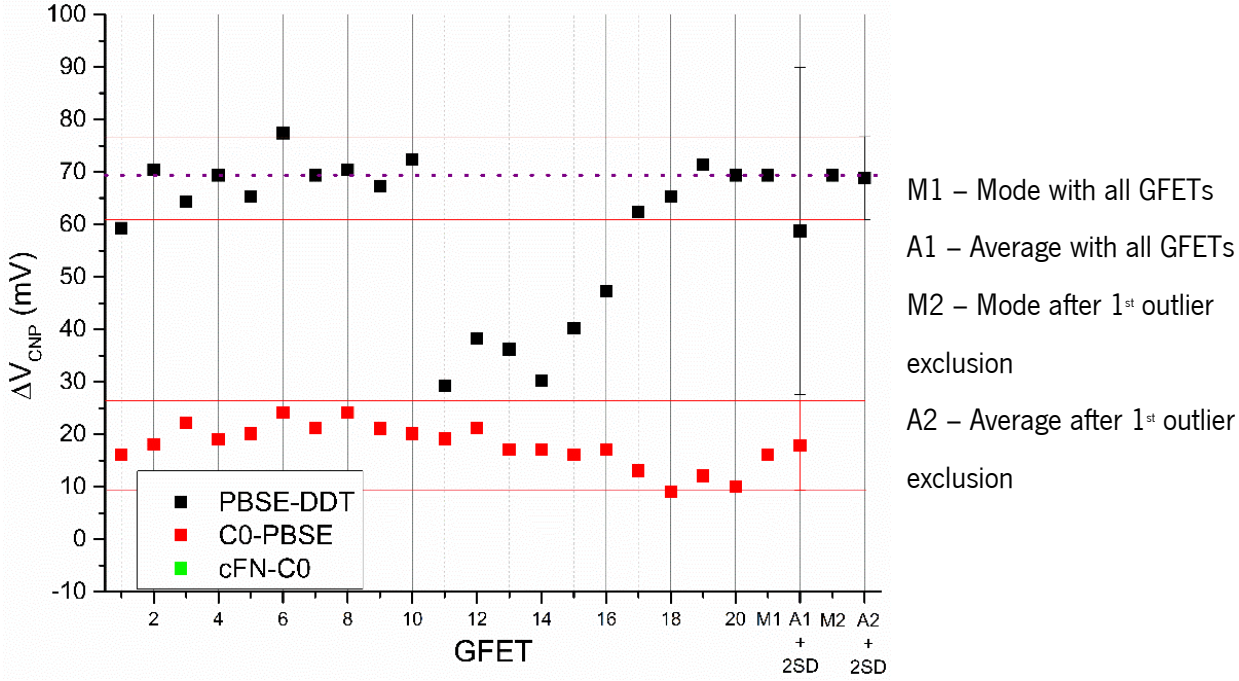

Figure 44. *Examples of outlier detection using the average, mode, and 2SD as parameters. The black squares show an example where a 2-step outlier exclusion is performed. The red squares show an example of a 1-step outlier exclusion. PBSE-DDT (black squares) is the voltage shift of each EG-GFET between passivation of the gate (DDT) and chemical functionalization of graphene (PBSE). C0-PBSE (red squares) represents the voltage shift of each EG-GFET between the chemical functionalization of graphene (PBSE) and the exposure to blank solution (PB 10 mM) after complete functionalization.*

3. Results & discussion

3.1. Initial biosensor response

To study the fabricated EG-GFETs [28] as biosensors, an initial analysis with a standard protein was performed (BSA). Chips from both of the fabricated models (BF19 and BF20, see Appendix I – Microfabrication of EG-GFETs, section 1.3) [28] were functionalized only with the linker (see section 2.6) and exposed to sequential increasing concentrations of BSA, 100 pg/ml, 100 ng/ml and 100 µg/ml. Transfer curves were acquired after each step, and V_{CNP} was followed as the transistor signal (Appendix III – Baseline measurements with multi-channel acquisition system for EG-GFETs, Figure Ap13). Figure 45 shows an example of the transfer curves acquired for an EG-GFET after each step.

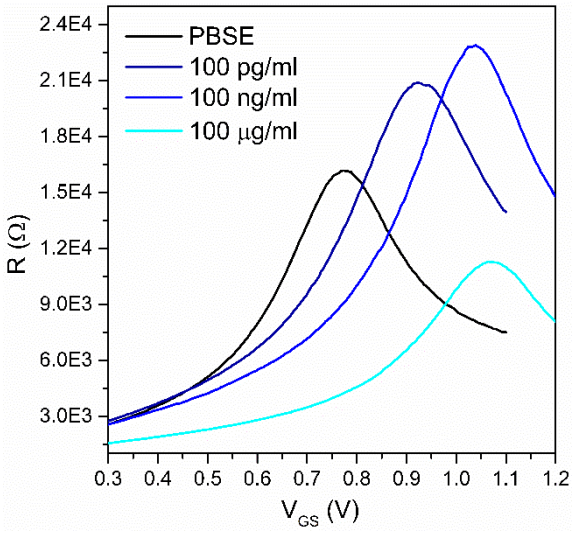

Figure 45. *Transfer curves of an EG-GFET (model BF20) after chemical functionalization (PBSE, black line) and sequential exposure to increasing concentrations of BSA (blue lines). The transfer curves represent the last of the 20 curves acquired for each step.*

In the transfer curves presented in Figure 45, it is possible to observe an increase in V_{CNP} after each 1h incubation with BSA. Figure 46 shows a schematic of the functionalized devices and the shifts of V_{CNP} having as reference the linker step. The plots show that the direction of the shift of V_{CNP} is dependent on the functionalized surface, with a positive shift being observed when the protein is bound to the graphene linker (Figure 46A), and a negative shift being observed when the protein is bound to the gate electrode (Figure 46C).

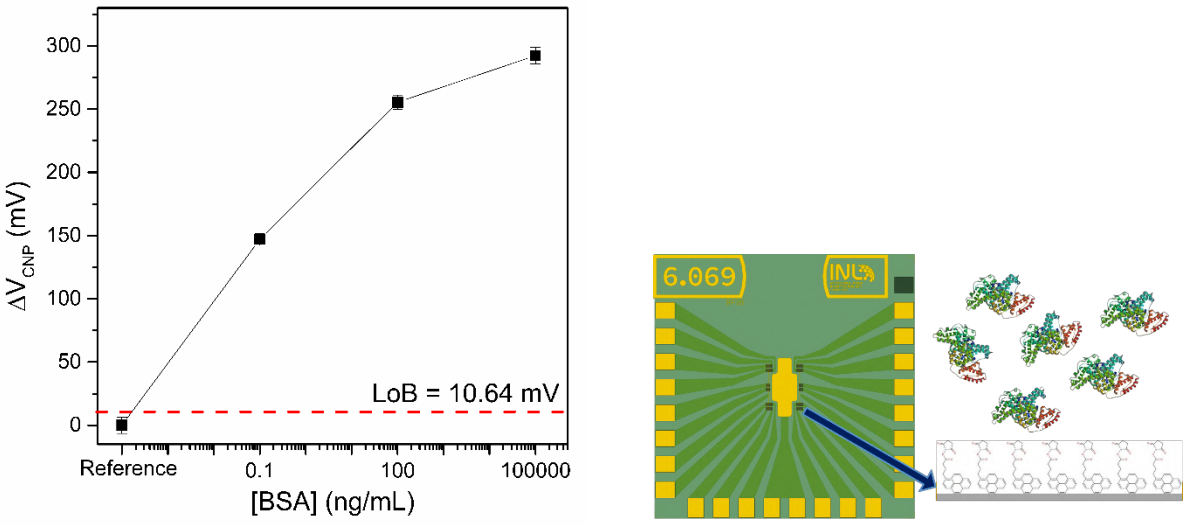

(A) (B)

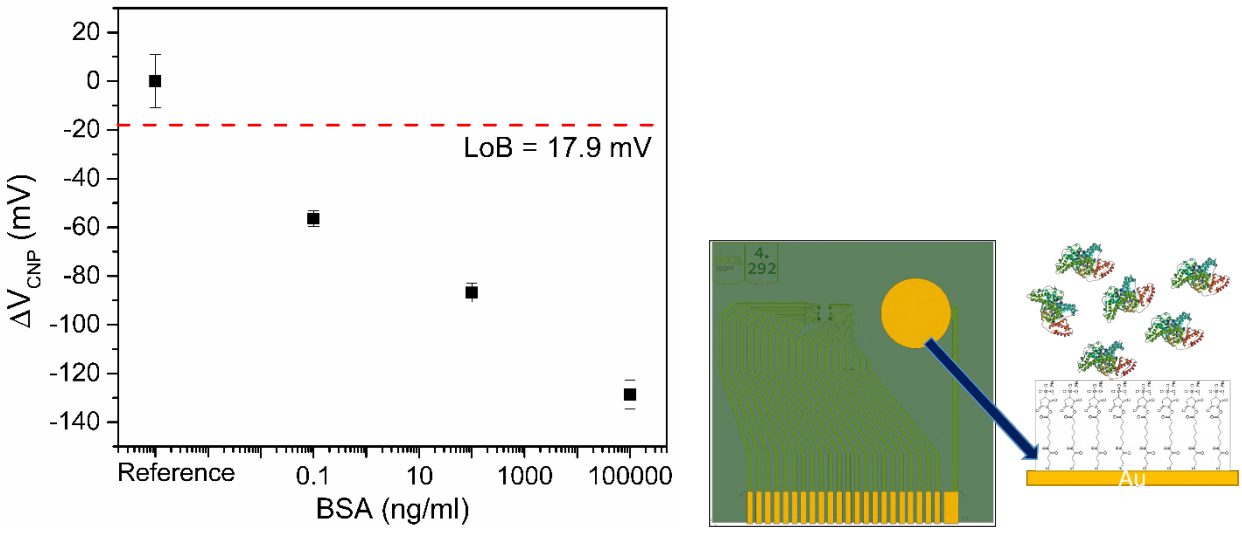

(C) (D)

Figure 46. *Non-specific detection of BSA on chemically functionalized EG-GFETs. (A) Shift of V_{CNP} after 1 h incubation with BSA at concentrations of 100 pg/ml, 100 ng/ml and 100 µg/ml at the graphene channel. (B) Schematic of the functionalization at the graphene channel (BF20), and surface modification/detection. (C) Shift of V_{CNP} after 1 h incubation with BSA at concentrations of 100 pg/ml, 100 ng/ml, and 100 µg/ml at the gate electrode. (D) Schematic of the functionalization at the gate electrode (BF19), and surface modification/detection.*

Here, BSA was used as model protein due to the similarities with the interested biomarkers (MMP9 and c-Fn) with an isoelectric point (pI) below physiological pH (4.5-5.0 [9]), meaning that when prepared in the phosphate buffer with pH 7.2, the protein configuration exposes negatively charged groups. As such, it is expected that when the protein is close to graphene a depletion of electron carriers occurs at the graphene channel [16], increasing the local p-doping and shifting the minimum conductivity point to higher voltages. This behavior is observed in Figure 46A (detection events at the graphene channel) with V_{CNP} increasing with BSA concentration. However, when the detection events occur at the gate electrode, V_{CNP} shifts in the opposite direction. This can be explained due to the accumulation of negative charges at the gate/electrolyte interface that is changing the gate potential (otherwise stable), changing the overall conductivity of the transistor. Understanding these detection mechanisms is key to interpreting the signal in a more complex scenario, i.e., with probe antibodies on the surface, or when exposed to complex samples, even if the focus is the detection at the 2D material interface.

To evaluate if the results obtained with BSA could be translated to the target proteins at the study, EG-GFETs were chemically modified with PBSE and exposed to BSA or MMP9. The incubation time was

reduced from 1h to 20 minutes to decrease assay time (relevant for the clinical application). Figure 47 shows the shifts of V_{CNP} with increasing concentration of BSA (Figure 47A) and MMP9 (Figure 47B).

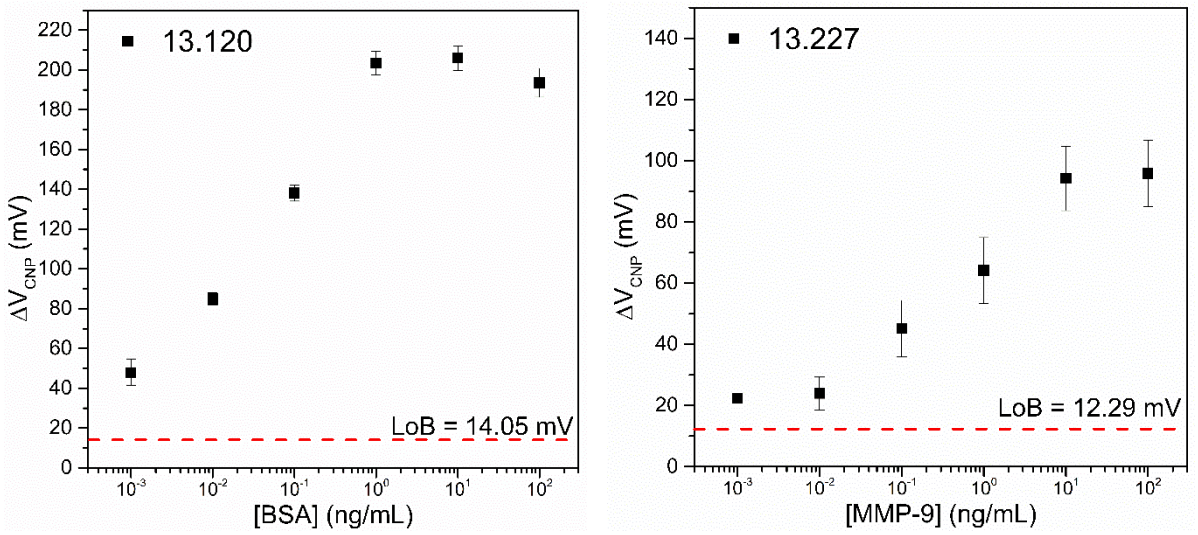

(A) (B)

Figure 47. *The shift of V_{CNP} of PBSE-functionalized EG-GFETs (BF20) with sequentially increasing concentration of BSA (A) and MMP9 (B).*

Comparing the plots from Figure 47 it is observable that even though the signal intensity is smaller for MMP9 than for BSA, a dose-response transistor signal can be achieved.

3.2. Sequential Calibration curves

To access the performance of the fabricated EG-GFETs as biosensors, specific detection of protein biomarkers in Phosphate buffer (PB) was performed. After the functionalization and antibody immobilization step (detailed in section 2.2.4), the sensors were sequentially exposed to PB 10 mM spiked with increasing concentrations of the corresponding target (MMP9 and c-Fn). The transfer curves (acquired with constant I_{SD}) during all the steps of the immunoassay were extracted (Figure 48A-D) and the V_{CNP} shift between the functionalized sensor (after stabilization) and the target exposure, was used as the sensing signal, as shown in Figure 48E and Figure 48F.

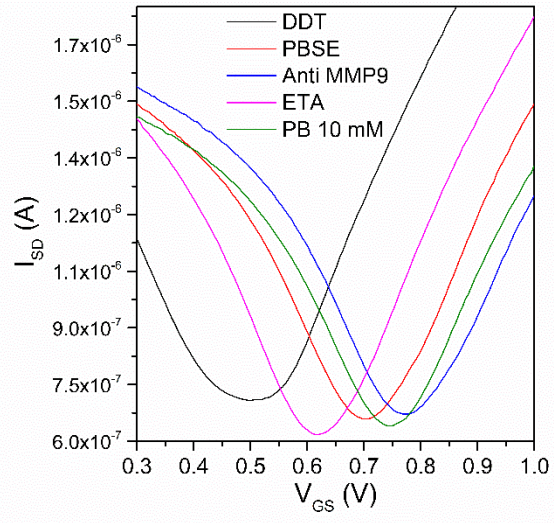
DDT
PBSE
Anti MMP9
ETA
PB 10 mM
I_{SD} (A)
V_{GS} (V)

(A)

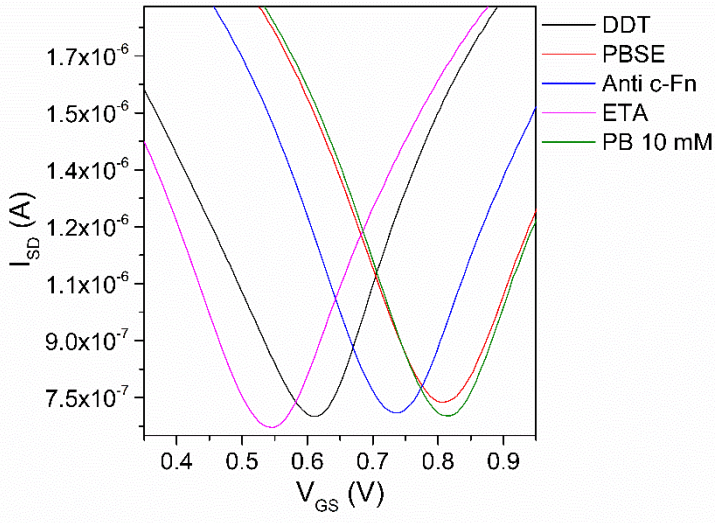
DDT
PBSE
Anti c-Fn
ETA
PB 10 mM
I_{SD} (A)
V_{GS} (V)

(B)

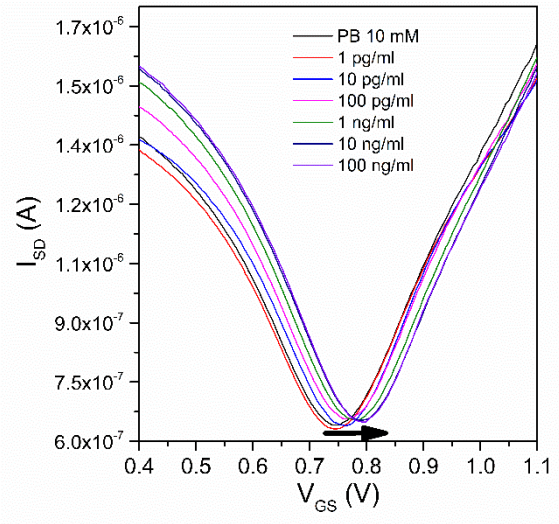
PB 10 mM
1 pg/ml
10 pg/ml
100 pg/ml
1 ng/ml
10 ng/ml
100 ng/ml
I_{SD} (A)
V_{GS} (V)

(C)

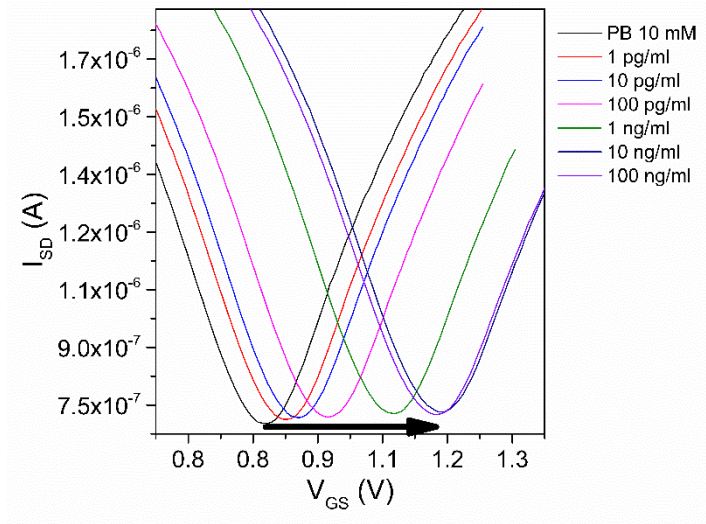
PB 10 mM
1 pg/ml
10 pg/ml
100 pg/ml
1 ng/ml
10 ng/ml
100 ng/ml
I_{SD} (A)
V_{GS} (V)

(D)

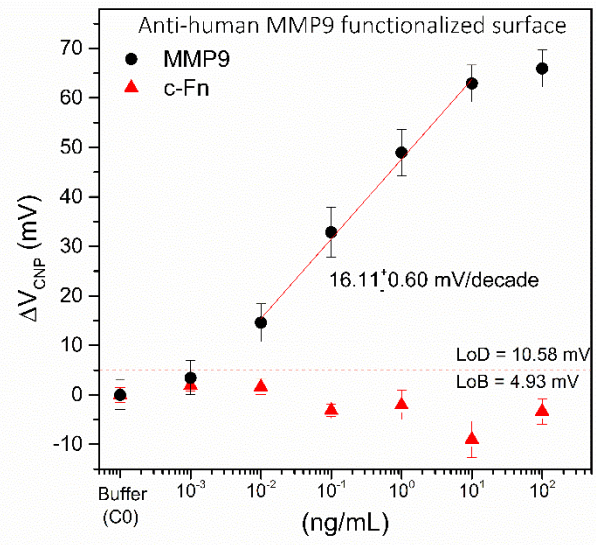
Anti-human MMP9 functionalized surface
MMP9
c-Fn
16.11±0.60 mV/decade
LoD = 10.58 mV
LoB = 4.93 mV
ΔV_{CNP} (mV)
Buffer (C0)
(ng/mL)

(E)

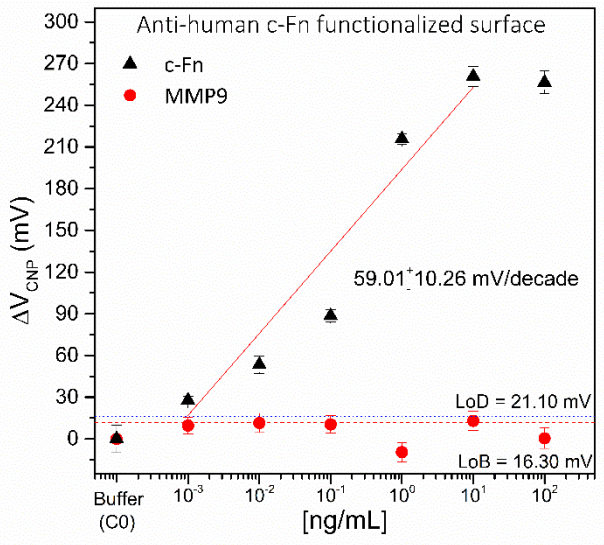
Anti-human c-Fn functionalized surface
c-Fn
MMP9
59.01±10.26 mV/decade
LoD = 21.10 mV
LoB = 16.30 mV
ΔV_{CNP} (mV)
Buffer (C0)
[ng/mL]

(F)

Figure 48. *EG-GFETs response after each step of the immunoassay for MMP9 and c-Fn. (A) Transfer curves after functionalization of an EG-GFET with DDT, PBSE, Anti-human MMP9, ethanolamine, and stabilization in PB 10 mM. (B) Transfer curves after functionalization of an EG-GFET with DDT, PBSE, Anti-human c-Fn, ethanolamine, and stabilization in PB 10 mM. (C) Transfer curves of EG-GFET after specific detection of MMP9 from 1 pg/ml to 100 ng/ml. (D) Transfer curves of EG-GFET after specific detection of c-Fn from 1 pg/ml to 100 ng/ml. (E) The shift of V_{CNP} along with increased concentration for MMP9 and control with c-Fn. (F) The shift of V_{CNP} along with the increased concentration for c-Fn and control with MMP9. The error bars represent the standard deviation of the V_{CNP} shift obtained for 10 to 20 GFETs, after outlier exclusion.*

The transfer curves after chemical functionalization with PBSE show a consistent positive shift of V_{CNP} (Figure 48A,B, red lines) that was observed through all the functionalization experiments (Appendix III – Baseline measurements with multi-channel acquisition system for EG-GFETs, Figure Ap14).

Immobilization of the antibodies resulted in minor random shifts of V_{CNP} (Figure 48A,B, blue lines, Appendix III – Baseline measurements with multi-channel acquisition system for EG-GFETs, Figure Ap15). These random shifts might be related to the orientation of the antibodies during immobilization since this parameter is not controlled. Major effects from the molecules' net charge are not expected since the antibodies used, human Immunoglobulins G, have a pI (6.3-8.4 [222]) close to the pH of the phosphate buffer (pH 7.2), and as such are not as charged as the antigens.

The passivation of non-functionalized sites (with PBSE) with ethanolamine (ETA) results often in negative shifts (Figure 48A,B, pink lines, Appendix III – Baseline measurements with multi-channel acquisition system for EG-GFETs, Figure Ap16) that vary in intensity between chips. It is not clear what is the mechanism behind this shift since the molecule itself is not charged.

A final stabilization step is performed exposing the devices to PB 10 mM for 20 minutes, allowing the functionalized devices and biomolecules to adapt to the intended medium of measurement and target incubation. It is consistently observed that after this exposure V_{CNP} shifts positively when compared with the ETA step (Figure 48A, B, green lines), recovering a position close to the initial PBSE or Antibody step. This difference may be related to the stabilization in a salt composition different from the ETA step (prepared in water) that impacts both the charges in the vicinity of graphene and the antibodies configuration (more stable in buffer solution than water). This step also works as a baseline for the detection of the target, which is prepared in the same buffer, meaning that the signal from the protein is obtained only from its detection, and not from changes in the solvent composition (as it happens between functionalization steps). The V_{CNP} shifts obtained of during the antibody immobilization steps seem to be

independent of the antibodies used (anti-human MMP9 and anti-human c-Fn immobilization result in similar V_{CNP} shifts), as expected, meaning it is possible to replicate and analyze the functionalization process with other antibodies from the same class (Immunoglobulins G, IgG) using EG-GFETs.

When exposed to sequentially increasing amounts of MMP9 (Figure 48C) has an effect similar to that observed without antibodies, suggesting that even though the distance to graphene is increased (by adding the monoclonal antibodies layer) it is still possible to observe the accumulation of the protein charges. This is also reflected in the transfer curves acquired after exposure to increasing concentrations of c-Fn (Figure 48D), which result in a positive V_{CNP} shift.

The increasingly positive V_{CNP} shift observed in Figure 6 E and F plots can be associated with the addition of the target protein at the sensor surface due to its negative surface charge at a physiological pH, which induces p-doping of the graphene channel, as previously explored by Fernandes et al. [42]. Using the parametrization definitions explored by Armbruster et al [221], the baseline standard deviation (SD) and signal intensity can be used to estimate the limit-of-blank (LoB) and the limit-of-detection (LoD) (see Appendix III – Baseline measurements with multi-channel acquisition system for EG-GFETs, section 3.1). The estimated LoB and LoD values, presented in Figure 48E,F, allow to infer that the voltage shift obtained by exposing anti-human MMP9 functionalized EG-GFETs to MMP9 spiked in PB is only reliable for MMP9 concentrations above 10 pg/ml, while for anti-human c-Fn functionalized sensors reliable voltage shifts related to c-Fn detection are obtained for c-Fn at 1 pg/ml. For both targets saturation is reached at 10 ng/ml, meaning that it is possible to achieve detection within 4 orders of magnitude with a sensitivity of 16 mV/decade for MMP9 and of 59 mV/decade for c-Fn. The reason for the signal intensity difference is not clear, since the surface charge of both proteins should be similar (MMP9 pI = 5.69 [223], Fibronectin pI = 5.6-6.1 [224]).

Using the same strategy for non-specific detection of control targets (e.g., expose anti-human c-Fn functionalized sensors to MMP9 spikes) the voltage shifts obtained were of low magnitude and less consistent direction. In both studied situations (red symbols, Figure 48E, F) the voltage shifts were always within the LoB indicating no consistent effects can be extracted from the obtained signal, reinforcing the specificity and selectivity of the monoclonal antibodies as probes.

3.3. Inter-assays

To evaluate the consistency and reproducibility of detection of the protein biomarkers, an assay was designed to expose 5 different chips, with 17 to 20 working EG-GFETs each, to a single spike of one of the biomarkers and check the variability of the voltage shift signal between them. All 5 chips were functionalized and immobilized with specific antibodies for the specific detection of c-Fn. Chips were

exposed to 100 ng/ml of c-Fn (prepared in PB). Figure 49 shows the V_{CNP} shift obtained for each chip after exposure to c-Fn.

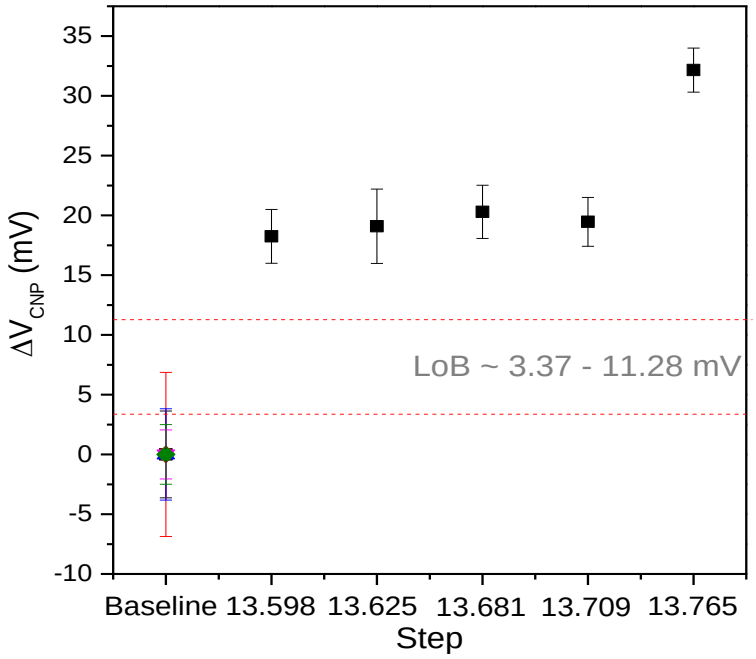

Figure 49. *The shift of V_{CNP} after exposing anti-human c-Fn functionalized EG-GFETs to 100 ng/ml of c-FN. Each data point represents an average of the V_{CNP} shift obtained in the working EG-GFETs of one chip. The error bars represent the standard deviation obtained from the same values.*

Table 6 shows the V_{CNP} shift values extracted and estimations of intra- and inter-variability. Using the average V_{CNP} shift for each chip and corresponding standard deviation, it is possible to calculate the variation coefficient given by:

$$\%\ Coefficient\ of\ Variation\ (CV) = \frac{SD}{Mean} \times 100 \quad [225]$$

For commercial applications, it is considered that the %CV should be lower than 10% in an intra-assay (within the same chip) and lower than 20% in an inter-assay (between different chips) [226]. For the EG-GFETs at study, the intra-assay resulted in a %CV between 5.73% and 16.29%, meaning that in general, the devices provide an initial and reasonable reproducibility with potential for improvement for commercial applications. On the inter-assay, the %CV is 26.57% using all the tested chips, however, if the chip 13.765 is removed from the analysis (due to different behavior/response) a %CV of 4.42% is achieved fitting well within the commercial requirements. This indicates that more data should be obtained for a conclusion, but there is potential to have EG-GFETs performing at clinical applications, suggesting some improvements in the homogeneity of the fabrication, mainly in the graphene transfer methods, as discussed previously [28].

When comparing the V_{CNP} shift obtained for c-Fn at 100 ng/ml in the sequential assay and the reproducibility assay it is noticeable that the intensity of the second is about 20x lower. Although this might seem inconsistent, it is important to remember that in the sequential assay what is being seen by the functionalized graphene channel is an added effect of the tested concentration (100 ng/ml of c-Fn) with the previous exposures to the same protein (1 pg/ml to 10 ng/ml), which is very different from a single exposure to that target concentration.

***Table 6**. Evaluation of reproducibility of VCNP shift after exposure to 100 ng/ml of c-Fn (prepared in PB 10 mM), and using5 independent EG-GFET chips. Each chip with 17 to 20 EG-GFETs.*

Intra-assay				
Chip	**N (GFETs)**	**Mean (V)**	**SD**	**%CV**
13.598	19	0.018248	0.002252	12.34
13.625	20	0.019097	0.003111	16.29
13.681	20	0.020303	0.002226	10.96
13.709	19	0.019465	0.002042	10.49
13.765	17	0.032159	0.001845	5.73
Average				**11.16**
Inter-assay				
	5	**0.021855**	**0.005808**	**26.57**
	4 (Excluding 13.765)	0.019278	0.000852	4.42

4. Conclusions

Detection of charged proteins was achieved directly on graphene with a response compatible with negatively-charged targets, which is in good agreement with the expected charge configuration for the studied proteins with isoelectric point below the phosphate buffer pH.

Specific detection of protein biomarkers by functionalized EG-GFETs was achieved, with sequential detection of MMP9 and c-Fn between 1pg/ml and 100 ng/ml. Sequential detection of MMP9 indicates a detection sensitivity of 16 mV/decade in the linear range, with an LoD of 10 pg/ml and saturation after

10 ng/ml. Detection of c-Fn reaches a sensitivity of 59 mV/decade in the linear range, with 1 pg/ml of LoD and saturation after 10 ng/ml. The reason for the increased sensitivity obtained with c-Fn is not clear, although differences in size or charge distribution might interfere with the sensitivity. Detection of c-Fn in 5 independent chips, containing 17 to 20 EG-GFETs allowed to study the reproducibility of the device, indicating that this first generation of bio-EG-GFETs is close to the commercial application requirements. Improvements to the homogeneity within a chip and between chips could be reached with modifications in the graphene transfer process which remains the most user-dependent task in EG-GFET fabrication.

In general, the EG-GFET devices are suitable for biosensor applications, and the possibility for clinical applications using complex matrices is accessed in the next chapter.

Section V – Biological Matrix studies

The contents of this section are present in the publication "Graphene immuno-FETs for detection of stroke-related biomarkers in human serum" by, Patrícia D. Cabral, Ivo Colmiais., Jérôme Borme, Marco Martins, Pedro Alpuim and Elisabete Fernandes, under preparation for publication.

Personal Contribution: Methodology development, data processing and analysis, investigation, original draft writing, reviewing, and editing.

1. Introduction

Detection of biomarkers in complex biological samples is currently one of the major challenges in the development of biosensing technologies [227]. The possibility to detect biomarkers directly in raw biological samples could help to improve the overall performance of biosensors, allowing for a wider use by non-specialized operators (point-of-care (PoC) platforms). Until today, however, only a few systems [14] were able to reach detection in complex matrices [29,103,228–230]. When multiple biomarkers must be quantified to provide relevant information [231], biosensing systems still present many limitations for multiplex approaches. Cross-reactivity, sensitivity adjustment, and interaction with biological matrices (blood, serum, saliva, etc.) [10,227] are some of the challenges to overcome.

An example is acute ischemic stroke (AIS) which represents a large public health problem that lacks a diagnostic system to provide personalized treatment to improve patient outcomes [63,64]. In acute cases, alteplase, an intravenous recombinant tissue plasminogen activator (rtPA) is the only approved systemic reperfusion treatment, which efficiency is time-dependent (< 4.5 h after symptom onset) [61]. One of the challenges is to predict the severe side effects of r-tPA therapy, hemorrhagic transformation (HT), which causes significant morbidity and mortality [61–63]. Researchers are validating panels of biomarkers that can contribute to predict the risk-benefit of it. Cellular Fibronectin (c-Fn), angiopoietin-1 (ANGIO1), matrix metallopeptidase-9 (MMP-9), and platelet-derived growth factor-CC (PDGF-CC) are potential biomarkers studied in the blood of stroke patients [61–63,65,66,72–75]. These biomarkers at certain levels in blood can accurately predict the risk of HT. Moreover, the detection of independent biomarkers is not specific to provide information on the risk of HT. A diagnostic tool that can provide simultaneous detection of the complete panel of biomarkers is of great interest for this disease. However, one of the limitations for fast detection of the mentioned biomarkers is related to sample processing. First, to decrease the complexity of the sample matrix, a blood sample (approx. of 10 mL) is collected from the patient and goes under centrifugation for plasma or serum separation. Nevertheless, serum samples can also present elevated levels of peptides, free-floating hemoglobin, as well as complex cross-reactivity of proteins such as plasma fibronectin, IgG, or hemoglobin [103,220,228]. Standard methods (e.g. ELISA tests) dilute serum samples to decrease the background noise, however, when low LoDs are required, they lack sensitivity [2,10]. Besides it, these methods are very time-consuming. In acute ischemic stroke, time is a crucial factor for thrombolytic treatment, where delays have a tremendous impact on the patient outcome [61]. Therefore, a system capable of detecting timely the interest biomarkers, and at the clinically relevant ranges is essential to achieve effective stratification of ischemic stroke patients.

As the simultaneous detection of MMP9 and c-Fn provides 87 % HT risk prediction, this work aimed to develop a reliable biosensor for the detection of these biomarkers. Human serum was the sample matrix used for the study, which has inherently high salt concentrations and elevated levels of various proteins [103,220,228]. Specific challenges in EG-GFETs are related to the detection of those biomarkers in salt-rich medium and non-specific adsorption of serum proteins which interfere with the electrical signal due to local charge accumulation and Debye length reduction [228]. Pre-treatment of the biological matrix to improve the detection signal is often reported, with sample filtering, desalting and dilution as the most commonly reported approaches [227]. However sample processing can increase the analysis time and increase variation and error due to additional steps of sample manipulation [227,228]. Other methods for improved detection in complex samples have been reported using control groups for signal comparison [232,233], or cross-validation with two or more transduction mechanisms [234].

The main goal of the presented work was to achieve specific detection events signal in a complex sample matrix within 1 h, considering the time relevance for AIS patient stratification. To distinguish the specific detection signal from other matrix interferences, surface and electrical parameters were evaluated, allowing to understand the main interactions of human serum with the EG-GFETs active surfaces (gate electrode and graphene channel). Specific detection of MMP9 and c-Fn was also evaluated in EG-GFETs. Customized ELISA tests were used for the assessment of specific detection of c-Fn and cross-reactivity studies.

2. Materials & Methods

2.1. Materials

Table 7. *Reagents and biomolecules.*

	Description	Supplier
Solvents	Dimethylformamide (DMF) 99.75% purity	Sigma-Aldrich
	Ethanol 99.8%	Honeywell
Chemicals	3140 RTV non-corrosive silicone rubber (flowable)	Dawsil™
	Elastosil® E41, RTV-1 silicone rubber	Wacker Chamie
	1-Pyrenebutanoic acid succinimidyl ester (PBSE)	Sigma-Aldrich
	Ethanolamine, 98% (ETA)	
	1-Dodecanethiol (DDT) (≥98%)	
	Polyethylene glycol sorbitan monolaurate (Tween® 20)	

	Horseradish Peroxidase-Streptavidin (HRP)	
	3,3′,5,5′-Tetramethylbenzidine (TMB)	
	Sodium bicarbonate ($NaHCO_3$)	
	Sodium Carbonate (Na_2CO_3)	
	NaH_2PO_4	
	Na_2HPO_4	
	Phosphate Buffered Saline (PBS) Tablets	Fisher Scientific
	Sulfosuccinimidyl 6-(3′-(2-pyridyldithio)propionamido)hexanoate (Sulfo-LC-SPDP)	
Biomolecules	Purified Matrix Metallopeptidase 9 (MMP-9), MW 92 kDa	Immunostep
	Monoclonal anti-human MMP-9	
	Polyclonal biotin anti-human MMP-9	
	Human Cellular Fibronectin Native Protein (c-Fn), MW 560 kDa	
	Purified monoclonal anti-human Fibronectin	
	Anti-human Fibronectin Biotin	
	Human Plasma Fibronectin Purified Protein (p-Fn), MW 220 kDa	
	Bovine Serum Albumin (BSA)	BioWest
Others	Human Serum AB Male	Sigma-Aldrich

2.2. Methods

2.2.1. Solutions Preparation

PBSE linker was prepared at 10 mM in DMF as follows: 3.85 mg of PBSE powder were weighted and dissolved in 1 ml of DMF. The solution was stored in a dark bottle at room temperature. The solution was prepared fresh after 5 experiments to avoid loss of activity of the linker.

Ethanolamine at 100 mM was prepared in ultrapure water as follows: 60.5 µL of ETA 98% were diluted into 8 mL of ultrapure water. After pH assessment, HCl 2 M was slowly added to the mixture to reduce the pH value to physiological values (pH 7.2 – 7.4). After pH stabilization, the volume was completed to 10 ml with ultrapure water.

DDT 2 mM was prepared by dissolution of 5 µl of DDT ≥98% in 10 ml of Ethanol. A fresh solution was prepared for each run.

Phosphate buffer (PB) at 100 mM with pH 7.2 was prepared by mixing 70 mL of 200 mM NaH_2PO_4, 180 ml of 200 mM Na_2HPO_4, and 250 ml of dH_2O. The solution was filtered and sterilized and stored at 4 °C until use. Dilution for PB 10 mM was done with ultrapure water as required.

Phosphate Buffer Saline (PBS) 1x was prepared by dissolving 5 tablets in 1 l of dH_2O. The solution was filtered and sterilized and stored at 4 °C until use.

For ELISA plate washing, PBS 1x with Tween® 20 at 0.05% (PBS-Tw20) was prepared by the addition of 2.5 ml of Tween® 20 to 5 l of PBS 1x. The solution was filtered and sterilized and stored at 4 °C until use.

Sodium Carbonate/Sodium Bicarbonate buffer at 50 mM with pH 9.6 was prepared by mixing 16 ml of 200 mM Na_2CO_3, 34 ml of 200 mM $NaHCO_3$, and 150 ml of dH_2O.

Human Serum provided by Sigma-Aldrich (AB Male Human Serum, H4522). Dilutions of serum were prepared as following:1:5, 200 µl of Human serum were diluted in PB 10 mM for a final volume of 1 ml (freshly prepared for each experiment). The depleted serum (prepared fresh for each experiment) was prepared as follows: the human serum was centrifuged at 10 krpm for 30 minutes at 4°C using a Milipore 3 kDa filter (Amicon Ultra-0.5 mL Centrifugal Filters, C82301, Merk) to remove all serum components with MW > 3 kDa. .

BSA (prepared fresh for each experiment day) was prepared at 1 % (10 mg/ml) and 3 % (30 mg/ml) in PBS 1x. .

Monoclonal antibodies for Fibronectin and MMP9 were prepared at 250 µg/ml in PB 10 mM for immobilization on EG-GFETs and QCM crystals. Monoclonal anti-human Fibronectin was prepared at 5 µg/ml in 50 mM Carbonate/Bicarbonate buffer for immobilization in ELISA plates.

Anti-human Fibronectin Biotin at 2 µg/ml or 5 µg/ml was prepared in BSA 1 %.

HRP was diluted 1:20000 and prepared in BSA 1 %.

Cellular Fibronectin (c-Fn) was prepared at 100 ng/ml in PB 10 mM and in serum (raw, diluted and depleted) for the tests carried out using EG-GFETs. For ELISA tests, c-Fn was prepared at the concentrations of 0 µg/ml, 0.01 µg/ml, 0.1 µg/ml, and 1 µg/ml in PBS 1x and serum diluted 1:5.

Plasma Fibronectin (p-Fn) was prepared in PBS 1x at the concentrations of 0 µg/ml, 0.01 µg/ml, 0.1 µg/ml, and 1 µg/ml.

Matrix Metallopeptidase 9 (MMP9) was prepared in PB 10 mM and serum at 100 ng/ml for tests in the EG-GFETs.

2.2.2. Microfabrication of EG-GFETs and Graphene Transfer

The microfabrication of EG-GFETs at wafer-scale and graphene transfer methods are reported in detail by [28] and summarized in Chapter III, Section 2.

2.2.3. EG-GFET chips Preparation

To allow electrical measurements using a multi-channel platform the diced chips were wire-bonded to custom-made PCBs using Aluminum or Gold wire. The wires were protected using 3140 RTV flowable silicone rubber and E41 silicone rubber, which was dried in air, at room temperature for 18 h.

2.2.4. Surface functionalization

Graphene

Functionalization of the graphene channels of EG-GFETs was performed as reported by [42]. Shortly a heterobifunctional pyrene linker, PBSE, 10mM in DMF, was deposited as a 20 µL drop and allowed to interact with the graphene surface for 2 h under a humid atmosphere at room temperature (RT). Antibodies (Anti-MMP9 or Anti-c-Fn) were prepared at 250 µg/ml concentration in PB 10 mM and spotted (5 µL) onto the pyrene-modified surfaces for overnight incubation at 4 °C under a humid atmosphere. Prevention of nonspecific binding was done by passivating free PBSE molecules with ethanolamine (ETA) at 100 mM concentration for 1h at RT, under a humid atmosphere. For blocking efficiency assays, graphene was only functionalized with PBSE, 10mM in DMF and ethanolamine, 100 mM in water before exposure to the human serum.

Gold Surfaces

The gold gate electrode of EG-GFETs was passivated to prevent nonspecific interactions with DDT at 2 mM concentration in ethanol. This step is performed before initial characterization of the EG-GFETs and biofunctionalization of graphene. The same functionalization procedure was applied to gold coated QCM crystals.

2.2.5. Detection strategy in EG-GFETs

For biological matrix effects studies, EG-GFETs functionalized with PBSE, monoclonal antibodies and ethanolamine were exposed for 20 minutes to human serum (5 µl) and rinsed with PB 10 mM before transfer curve acquisition. The same procedure was applied for the specific detection of MMP9 and c-Fn.

2.2.6. Enzyme-linked Immunosorbent Assays (ELISA)

Sandwich assays

Sandwich ELISA assays with matched pairs of antibodies were used to study specific detection of c-Fn and cross-reactivity with p-Fn. 100 µl of primary antibody (Monoclonal anti-human c-Fn) was immobilized on 96 wells plates and incubated overnight at 4 °C. The unbound antibodies were washed with PB-Tw20, followed by a blocking step (300 µl) with BSA 3 % to reduce non-specific binding in free-sites. The plates were incubated for 1 h at 37 °C. After the washing step (PB-Tw20), wells were filled (100 µl) with the target protein (c-Fn or p-Fn) and left incubating for 90 minutes at 37 °C. The secondary antibody (Anti-human c-Fn Biotin at 2 µg/ml) was added (100 µl) and left incubating 1 h at 37°C. HRP-streptavidin at 1:20000 dilution was added to react with the biotinylated secondary antibody and incubated for 30 minutes. After the final washing step, TMB was added to react with the enzyme (HRP) for 2 minutes. After that time, HCl 1 M was added to stop the reaction.

Direct assays

In the reported direct assays, the target protein was immobilized directly on the wells, and only the secondary antibody was used to access the specificity of the binding to c-Fn and p-Fn. Immobilization of the target protein (c-Fn, p-Fn, BSA, human serum) was performed by filling the wells with 100 µl of the target solution and incubating overnight at 4 °C. After removing the unbounded protein with PB-Tw20, the wells were filled (300 µl) with BSA 3 % to reduce non-specific binding. The plates were incubated for 1 h at 37 °C. After the washing step (PB-Tw20), 100 µl of secondary antibody (Anti-human c-Fn Biotin at 2 µg/ml) was added and incubated 1 h at 37 °C. HRP-streptavidin at 1:20000 dilution was added to react with the biotinylated secondary antibody and incubated for 30 minutes. After the final washing step, TMB was added to react with the enzyme for 2 minutes. After that time, HCl 1 M was added to stop the reaction.

2.3. Characterization techniques

2.3.1. Quartz crystal microbalance (QCM)

QCM measurements were performed in a QSense E1 system (Biolin Scientific). AT-cut quartz crystals having gold electrodes of the working surface coated with ca. 50 nm of silicon oxide (QSX 335, Biolin Scientific) were used as substrates for single-layer graphene transfer, to mimic the effects at the EG-GFETs graphene channel. AT-cut quartz crystals having gold electrodes of the working surface coated with ca. 50 nm of gold were used to mimic the effects of the EG-GFETs gate electrode.

Prior to monitoring the effect of human serum by QCM, the graphene surfaces were functionalized with PBSE (2 h in 10 mM PBSE in DMF), Anti-human MMP9 or Anti-human c-Fn (at 250 µg/ml in PB 10 mM,

overnight, at 4 °C) and ethanolamine (100 mM in water, 1h). The gold crystals were functionalized with DDT (2 mM in ethanol, overnight) prior to exposure to human serum in QCM.

QCM measurements for the fundamental (ca. 4.95 MHz) frequency and at its 6 odd overtones (n=3, 5, 7, 9, 11, 13) were carried out under a flow rate of 0.06 mL/min at a constant temperature of 20 °C (set within<1 °C from RT, at which the solutions have been stabilized prior to the measurements). The frequency shift is reported in the standard ΔFn/n normalization, as recorded by the instrument software. The baseline in the blank PB 10 mM was recorded before and after exposure to human serum; exposure to human serum was performed by re-circulating 1 mL of the solution through the QCM flow cell.

2.3.2. EG-GFET electrical measurements

The acquisition of transfer curves from EG-GFETs and extraction of curve parameters (e.g., minimum conductivity point) was performed using an in-house built platform and software for sequential data acquisition of the 20 EG-GFETs present in each chip. The acquisition system consisted of an Arduino-like board with 10×6 cm^2 equipped with a microcontroller, digital-to-analog and analog-to-digital converters (DAC, ADC), resistance-controlled current source of 1-100 μA, digital potentiometer, and CMOS matrices. A constant drain-source current (I_{DS}) was applied at 1 μA, or a constant drain-source voltage (V_{SD}). The gate voltage was linearly scanned within a 1 V range with a voltage step of 200 mV using a liquid gate electrode. The waiting time during each measurement of the transfer curve was 18 s. The acquisition software, custom-made with Lab-View™ tools, allowed to control the measurement parameters and automatic extraction of the transfer curve parameters (e.g., minimum conductivity point, linear region slopes). For all functionalization and detection steps, 20 consecutive curves were traced to allow for signal stabilization (Appendix III – Baseline measurements with multi-channel acquisition system for EG-GFETs, Figure Ap12).

2.3.3. Plate reader

A SYNERGY H1 Microtiter Plate Reader from Biotek is used to read the absorbance values at 450 nm from the finalized 96-wells ELISA plates. The system is programmed to perform a 5 s orbital shake of the plate for sample homogenization before reading the absorbance values.

2.4. Data analysis

The data extracted from the EG-GFETs acquisition system was analyzed using Origin® 9 software. Transfer curves were used for the extraction of charge carrier mobility parameters. Overtime parameters (minimum conductivity point) were extracted to evaluate signal stability, and the values from the final 5

runs were used to average the voltage at the minimum conductivity point (V_{CNP}). The averaged V_{CNP} was used as the signal from each EG-GFET and was compared between functionalization steps. After functionalization, exposure to PB 10 mM allowed to stabilize the surface and a baseline V_{CNP} was extracted for comparison with the V_{CNP} from target exposure. Outlier detection and extraction was performed as reported in chapter V.

3. Results & discussion

3.1. Biological matrix effects on EG-GFET chip

Once the detection of the relevant biomarkers was achieved in PB 10 mM with satisfactory reproducibility (Chapter V), the challenge was to understand how the biological matrix (human serum) could affect the sensor surface and electrical characteristics. As such, to analyze the surface effects, quartz crystals were used to infer non-specific surface adsorption of serum elements in the different available surfaces at the EG-GFET chip: gold quartz crystals (AuQC) to mimic the gate electrode, and SiO_2 quartz crystals (SiO_2QC) with graphene to mimic the graphene channel. AuQC and SiO_2QC were functionalized with DDT and PBSE, respectively, followed by a blocking step with ethanolamine and/or antibody immobilization (anti-human MMP9 or anti-human c-Fn) . Figure 50A shows the frequency shifts obtained after exposure to human serum (dark grey) and depleted human serum (light grey) of the mentioned functionalized surfaces.

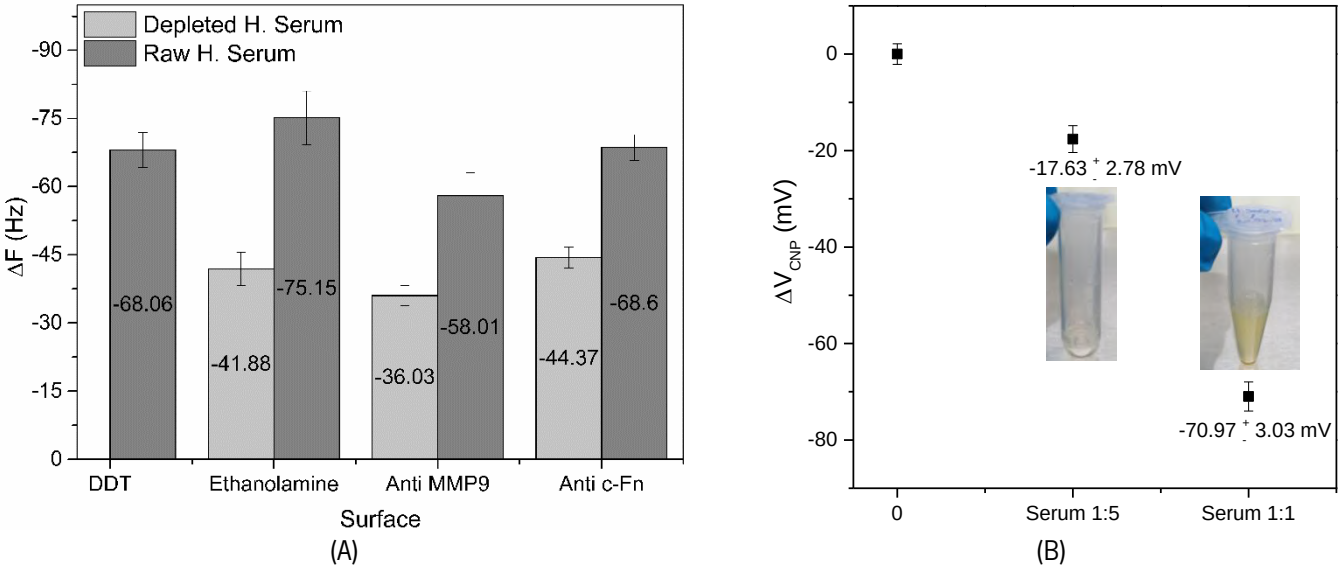

Figure 50. *Effects on the sensor surfaces after exposure to the biological matrix (human serum). (A) Frequency shift caused by the non-specific adsorption of serum components (depleted and non-depleted)*

(in the functionalized gold (DDT) and graphene channel. (B) The V_{CNP} shift of passivated EG-GFETs (DDT + PBSE + ETA) after exposure to diluted serum (1:5) and undiluted serum (1:1).

When the sensor surfaces are passivated with DDT vs. PBSE + Ethanolamine it is possible to observe a significant frequency shift in both exposures (to depleted and non-depleted serum), indicating strong adsorption of serum components to the surfaces (even though they are passivated). On the gold surface, the non-specific adsorption might be due to the reduced efficiency of DDT to block all the surface area [235], when defects or small impurities are present in the surface. In the graphene surface, it is important to consider that unlike the close-packed thiol-binding of DDT on gold [235], PBSE has a large surface area and there is no evidence of rearrangement of the interaction sites for close-packing. Our previous findings using X-ray Photoelectron Spectroscopy (XPS) technique (detailed in Chapter III) [28] allowed to estimate that about 34% of the graphene surface is left uncovered by the pyrene-based linker. Therefore, as the serum is the protein-rich component of blood, the uncovered surface with PBSE could easily trigger cascading adsorption events due to protein denaturation in the presence of a highly hydrophobic surface [42]. Besides QCM allowing mimicking the sensor surface exposed to the biological components, with a similar area of approx. 1 cm^2, it is important to highlight that in the EG-GFETs the surface area of the gold gate electrode is about 370 times bigger than the graphene channel [28]. This difference is reflected in the negative shift of V_{CNP} observed in Figure 50B (which is indicative of the stronger influence of non-specific adsorption events occurring at the gate electrode, than that of the effects at the passivated graphene channels. The non-specific adsorption in the graphene surfaces functionalized with specific antibodies still occurs, but at a lower level. Nevertheless, any presence of non-specific adsorption always reduces the sensor sensitivity. The surface functionalized with anti-human MMP9 is the one reporting better results. The surface functionalized with anti-human c-Fn has about 10 Hz more shift than for MMP9 surface, and this can be explained by the existence of certain cross-reactivity events with plasmatic fibronectin (p-Fn) as 300 to 400 µg/ml of p-Fn is present in the serum of healthy patients [236]. Fibronectin is a multidomain protein, composed of multiple repeated modules, allowing for functional flexibility [236]. The organization and presence of certain modules defines the functionality of the molecule with the major difference between p-Fn and c-Fn being the presence of EIIIA and/or EIIIB modules in the second one [236], meaning that the general structure of the two proteins is similar. However, the same cannot be explained in depleted serum due to the presence of only proteins below 3kDa. Therefore, and as the error bars overlap for depleted-serum through the different surface treatments, it suggests that serum samples will cause a background noise with a frequency shift of approx. -41 Hz, or approximately 20 mV in EG-GFETs (Figure 51). The adsorption effects analyzed in the surface

study are reflected when the EG-GFETs are exposed to the same complex biological matrix. In general, both for MMP9 and c-Fn specific surfaces, exposure to depleted or diluted serum seems to induce some positive shift indicating some interaction occurring at the graphene surfaces, but at levels like those observed with PB 10 mM (which is explained by the stabilization of the surface after complete functionalization). An exception for the background signal in the functionalized EG-GFETs is observed for exposure to undiluted serum in c-Fn specific devices, in which a strong positive shift of V_{CNP} (≈65 mV) indicates additional interferences, which are explored later in this chapter (section 3.3).

3.2. Detection of stroke protein biomarkers in serum

After understanding the background noise of serum in EG-GFETs, samples spiked with 100 ng/ml of the interesting targets (MMP9 and c-Fn) were tested and the shift in V_{CNP} was taken as a measure of the specific detection signal (Figure 51). The transfer curves of each tested EG-GFET chip are shown in Figure Ap18 and Figure Ap19 of Appendix IV – Biological Matrix Effects.

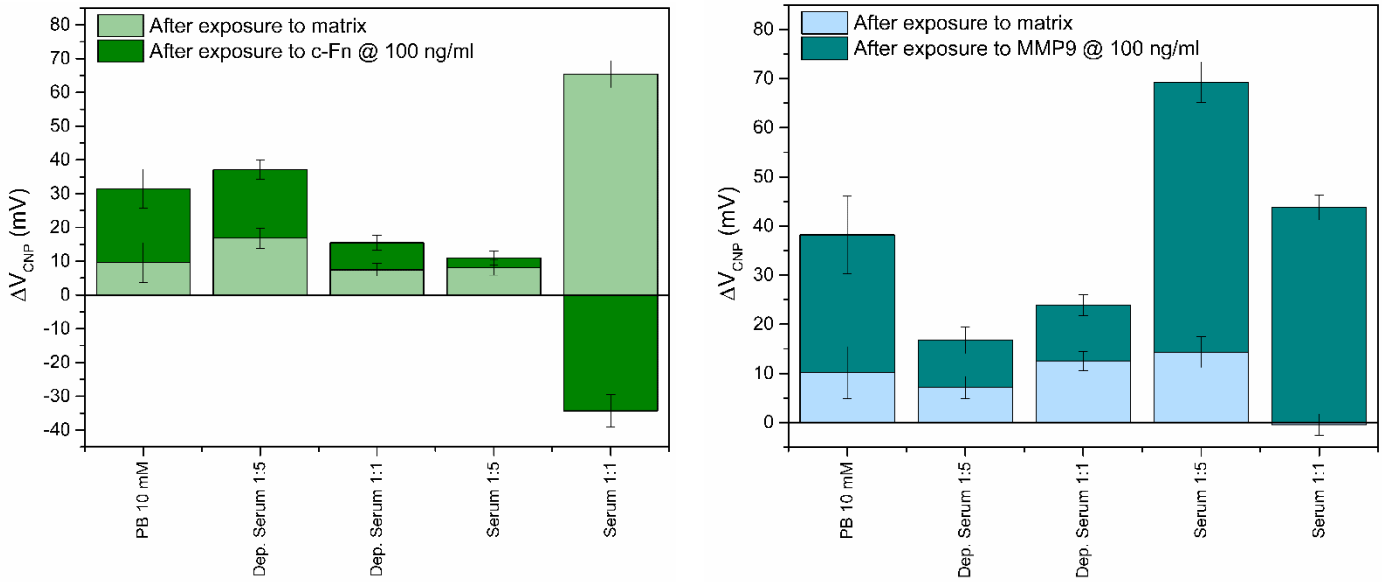

Figure 51. *The shift of V_{CNP} after exposing the functionalized EG-GFETs with immobilized antibodies to the biological matrix (light color bars) and specific targets (MMP9 or c-Fn) (dark color bars) prepared in depleted serum and serum, undiluted (1:1) and diluted (1:5). (A) The V_{CNP} shift of EG-GFETs functionalized with monoclonal anti-human fibronectin, after exposure to different sample matrices and exposure to c-Fn at 100 ng/ml, showing the background signal contribution. (B) The V_{CNP} shift of EG-GFETs,*

functionalized with monoclonal anti-human MMP9, after exposure to different sample matrices and to MMP9 at 100 ng/ml, showing the background signal contribution.

The detection of MMP9 and c-Fn in buffer solution is achieved with similar intensity (20 to 30 mV shift) indicating a similar interaction between the target and the antibodies. The increasing complexity of the matrix (depleted serum and serum, diluted or not) decreases the detection signal for c-Fn. For undiluted serum (1:1), a negative shift of V_{CNP} is observed, which can be indicative of a more complex detection dynamics related with cross-reactivity events with p-Fn as proposed in the previous section and discussed in section 3.3. The detection signal for MMP9 does not seem to be dependent on the matrix complexity, since the V_{CNP} shifts obtained in diluted and non-diluted serum fit well within the values obtained in buffer solutions. However, the detection signal for MMP9 decreases in depleted serum (diluted or not), which could be caused by the instability of the target protein in these mediums, which can easily loose its enzymatic activity in mediums with non-ideal pH [237]. The process of serum depletion can indeed change the pH of the medium, which might decrease the stability of the protein and reduce is viability for detection in a more pronounced fashion than c-Fn. The signal intensity is always higher for the samples spiked in serum, instead of in depleted-serum and PB.

To decrease sample matrix effects, the results obtained suggested that patient samples should be diluted. The 1:5 dilution is already recurrent in analytical techniques (e.g., ELISA tests) to reduce the interferences from the biological matrix, however, when diluting the sample, the interest target is also diluted, and therefore can compromise the assay LoD. Depending on the clinical application, the difficulty of achieving high LoDs can limit the sensor applicability. For ischemic stroke, the cutoff values for MMP9 and c-Fn are still within the dynamic range provided by the EG-GFETs from pg/ml to ng/ml range, and therefore far below from the interest region, which is in the ng/ml to µg/ml range. As such, there is potential on EG-GFETS for ischemic stroke patient stratification.

3.3. Complementary study on p-Fn and c-Fn affinities

Cross-reactivity studies were performed, using ELISA tests, to understand if some affinity exists between plasmatic fibronectin (p-Fn) and the antibodies that are immobilized on the sensor surface for cellular fibronectin (c-Fn). The absorbance values presented in the Figures 52 to 54 can be confirmed in the tables presented in Appendix IV – Biological Matrix Effects (sections 4.2 and 4.3).

The first ELISA test was carried out by using a sandwich assay, where the monoclonal antibody used in EG-GFETS is used as primary antibody, immobilized on 96-well plate, and a biotinylated polyclonal antibody used as a secondary antibody to react with streptavidin-conjugated with horseradish peroxidase

(HRP). Figure 52A shows absorbance values similar for samples spiked with c-Fn and p-Fn. Comparison of detection in sandwich assays using PBS 1x buffer and diluted serum (1:5) reinforces the evidence of the strong interaction between serum components (mainly p-Fn) and the c-Fn specific antibodies (Figure 52B), since the absorbance values obtained in diluted serum samples are equivalent to that obtained for high concentrations of p-Fn (≥ 3 µg/ml) and higher to that obtained for c-Fn samples prepared at the same concentration in PBS 1x.

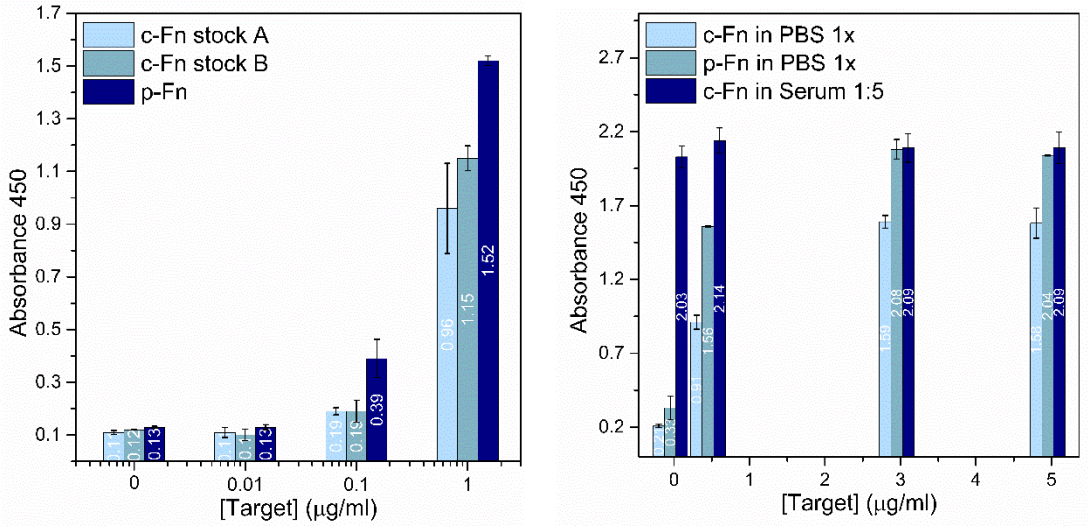

(A) (B)

Figure 52. *Absorbance values at 450 nm from 96-well plates after sandwich-assay ELISA. (A) Absorbance values with increasing concentration of 2 different lots of c-Fn in comparison with p-Fn, between 0.01 µg/ml and 1 µg/ml. (B) Absorbance values with increasing concentration of c-Fn and p-Fn in PBS, and c-Fn in diluted human serum (1:5), between 0.5 µg/ml and 5 µg/ml (interest range for c-Fn in stroke).*

To understand the affinity between the secondary antibody (Anti-human Fibronectin Biotin) and p-Fn, direct assays were performed. Here, p-Fn and c-Fn were immobilized in 96-well plates by physical adsorption, followed by a blocking step and a detection step using the biotinylated antibodies. Plate 1, with the map showed in Appendix IV – Biological Matrix Effects, Table Ap 4, was prepared for two purposes: (a) cross-reactivity of biotinylated antibodies of fibronectin with p-Fn, and (b) events of non-specific binding due to serum matrix components.

The absorbance values for the reaction between the Anti-human Fibronectin Biotin antibody and p-Fn immobilized in PBS 1x are shown in Figure 53 (average absorbance values in Table Ap5, Appendix IV – Biological Matrix Effects). As expected, absorbance increases with antibody concentration, meaning the presence of more antibodies increases the change for non-specific interactions with the target. However,

it is also observable that the absorbance values obtained when the secondary antibody is used at 2 µg/ml are very close to those obtained in the sandwich assays (Figure 52A). This indicates that the affinity issues observed initially are equally attributed to the primary and secondary antibodies.

It is also observed in Figure 53A that the response to diluted human serum is within the window of response to p-Fn. Since the human serum used is obtained from healthy volunteers, it is only expected a minor amount of c-Fn in circulation that would be difficult to detect in this assay. As such, it is likely that the signal comes from the interaction of the secondary antibodies with the immobilized p-Fn occurring naturally in human serum.

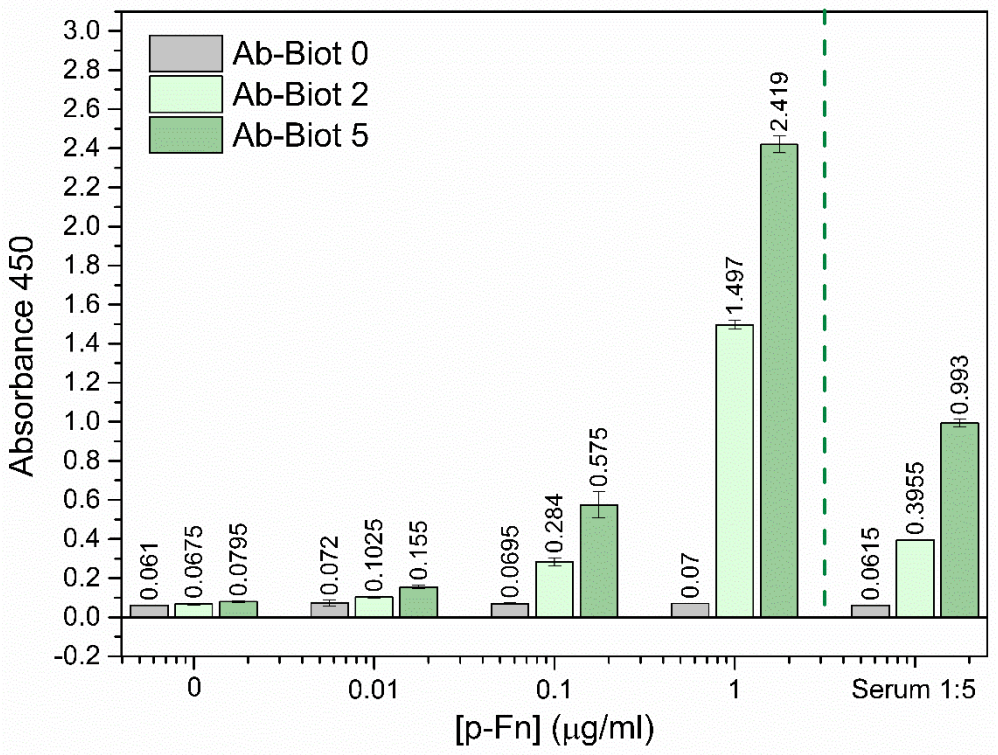

(A)

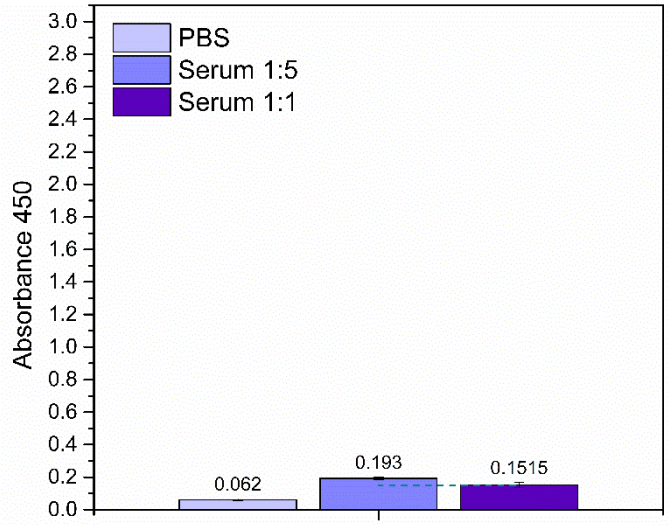

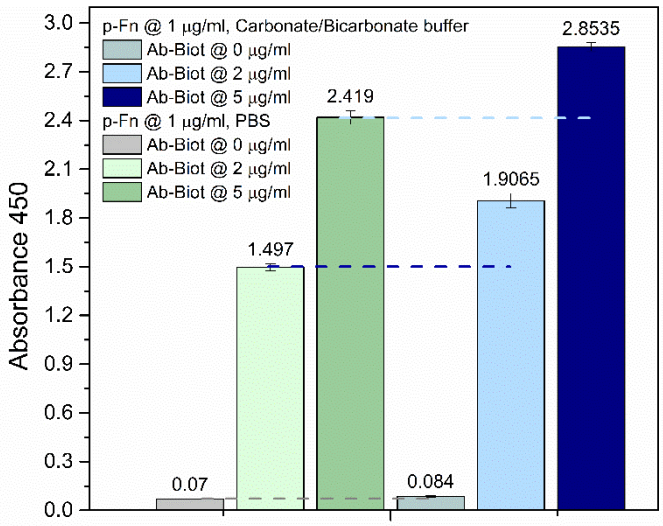

(B) (C)

Figure 53. *Absorbance values from Plate 1, after direct immobilization of p-Fn and human serum, and non-specific detection with Anti-human Fibronectin Biotin antibodies. (A) Absorbance values increase with p-Fn concentration and secondary antibody concentration (after adsorption of human serum). (B) Absorbance values for the wells blocked with BSA 3% and exposed to PBS and human serum, showing effective blocking of the well's walls. (C) Effect of buffer in the immobilization of the target in the wells.*

Figure 53B shows the effectiveness of the passivation of the wells with BSA, indicating that even in the presence of complex solutions (human serum) only a small incidence of adsorption is observed. The comparison of target immobilization with different buffers (Figure 53C), indicates that the carbonate/bicarbonate buffer improves the efficiency of immobilization in the wells, which can be significant for assays where increased reliability and/or quantification are required.

A second study was performed to access the preferential interaction of the antibodies. Up to this point the antibodies only interacted with c-Fn and p-Fn separately, but it was not clear if the mixture of both proteins would lead to preferential detection of one of them. Table Ap 6 in Appendix IV – Biological Matrix Effects shows the distribution of c-Fn and p-Fn in the 96-well plate, with the controls for separate detection and the prepared mixtures.

The absorbance values for the reaction between the Anti-human Fibronectin Biotin antibody and the c-Fn/p-Fn mixtures immobilized in PBS 1x are shown in Figure 54 (average absorbance values in Table Ap7, Appendix IV – Biological Matrix Effects). As observed before in sandwich assays (Figure 52), for the same concentration of protein, the signal intensity obtained for c-Fn (Figure 54A, left group) is lower than that obtained for p-Fn (Figure 54A, grey bars). For the highest concentration of p-Fn tested is not clear if there is effect from adding c-Fn, since the absorbance values overlap for all c-Fn concentrations (Figure 53A, right group). When analyzing the data from the perspective of the specific target (c-Fn) it is possible to see that the absorbance values are similar between samples with only c-Fn and samples with a p-Fn concentration below that of c-Fn (Figure 54B,C). This tendency is lost for p-Fn concentrations equal or above c-Fn concentration, indicating that the specificity limitations faced in human serum samples are related with the great amount of p-Fn present when compared with c-Fn [236].

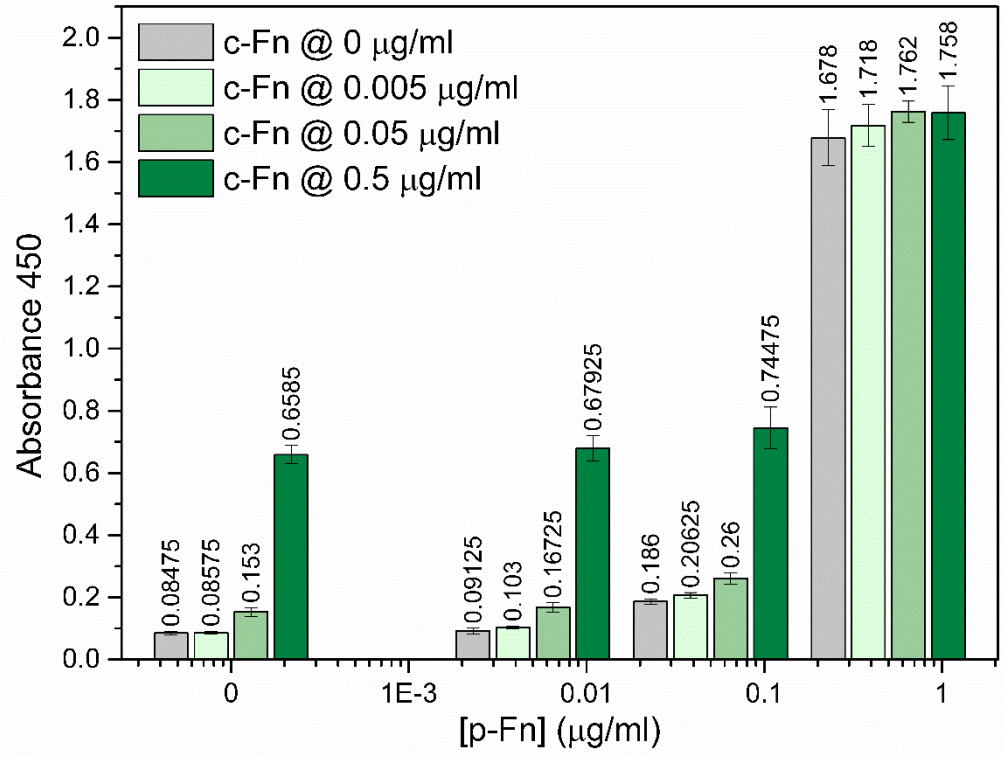

(A)

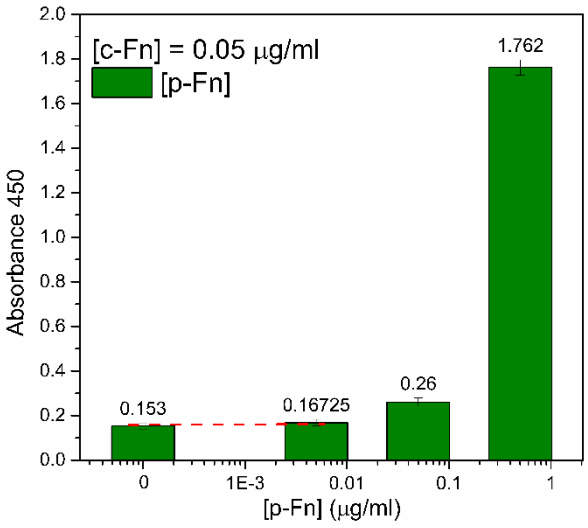

(B)

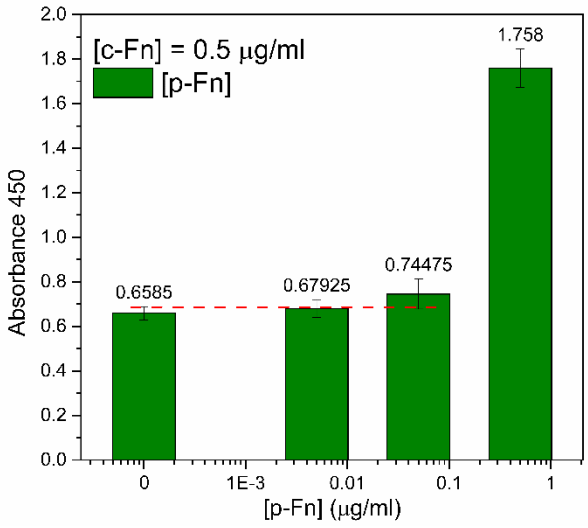

(C)

Figure 54. *Absorbance values from Plate 2, after direct immobilization of c-Fn and p-Fn, and detection with Anti-human Fibronectin Biotin antibodies. (A) Absorbance values increase with c-Fn and p-Fn concentration. (B) Absorbance values for increasing p-Fn concentration with 0.05 µg/ml c-Fn present. (C) Absorbance values for increasing p-Fn concentration with 0.5 µg/ml of c-Fn present.*

4. Conclusions

Exposure of the devices to complex biological samples, revealed some limitations in the surface functionalization process, indicating that the gold and graphene surface passivation requires further investigation. Functionalized surfaces with specific immobilized antibodies for the interesting targets revealed specific and non-specific binding to serum components. Cross-reactivity happens between fibronectin antibodies and p-Fn, and therefore decreasing the specific detection of c-Fn. These cross-reactivity events could occur due to the shared modules between cellular fibronectin and p-Fn which create common molecular binding regions in the two molecules [236]. Our findings suggested that the matrix interferences could be decreased by diluting serum samples, and therefore, obtain a more accurate and specific detection of c-Fn and MMP9, indicating the potential of the studied EG-GFETs for clinical applications.

Section VI – Future work

The work developed under this thesis shows the potential application of EG-GFETs as clinical diagnostic tools. The optimization of the microfabrication process allowed to improve the homogeneity of the transistor's characteristics (e.g., carrier mobility, resistance, surface cleaning), which are now mostly dependent on the graphene quality and transfer. To optimize the throughput of EG-GFETs for biosensor development, microfabrication using physical masks can be used to reduce fabrication time from 1 month to 1-2 weeks [238]. Still, improvements must be achieved in graphene transfer to reduce variability within the wafer. Transfer methods must be optimized to allow large area transfer of graphene (e.g., covering the whole wafer at once).

The detection of MMP9 and c-Fn was achieved with good specificity, and possible to use a biological complex matrix, as human serum. Nevertheless, EG-GFETs are prone to some non-specific binding when exposed to undiluted serum. The results showed some limitations regarding surface passivation/blocking. It is proposed that the 1-Dodecanethiol (DDT) molecules used to passivate gold do not provide effective passivation in a complex medium due to the short length of the molecule. As such, longer molecules could be tested to improve the blocking and avoid the non-specific adsorption at the gate electrode.

In the graphene channels, the results showed that the exposure of non-functionalized graphene areas to human serum led to the strong adsorption of serum proteins, maybe due to denaturation cascades occurring at the hydrophobic interface. It is then proposed to use a surfactant along with ethanolamine to allow passivation of the free graphene surface. Previous results showed a strong interaction between graphene and Tween® 20 (Appendix V – Future Work (preliminary data)), which would allow reducing further interactions with graphene, as well as proposed in the literature [3,116].

Regarding the biological samples, it is preferred to reduce the sample processing through the operator to reduce errors and variability from sample to sample [2]. The detection of cellular fibronectin (c-Fn) showed that the presence of p-Fn in serum strongly interferes with its specific detection. This interference can be overcome by using a pre-recognition step with, for example, functionalized nanoparticles, as reported elsewhere [220]. This implies a 'labeling' of the target, without implications in the measurement in the EG-GFETs, which can be possibly achieved by using a sample preparation device. To explore the potential of this idea, preliminary tests were performed using magnetic nanoparticles (MNPs) functionalized with biotinylated antibodies specific for c-Fn. The results are shown in Appendix V – Future Work (preliminary data), allowing to access the impact of the nanoparticles in the EG-GFETs signal. Detection using samples

prepared with this system was attempted but further optimization of particle ratios is required to reach the required clinical cutoff values. If successful, this extraction system can be integrated into a microfluidics setup allowing the targeting of the interest biomarker from human serum and avoiding sample complexity.

One of the most important parameters for the use of the EG-GFET biosensors for clinical stratification is the linear dynamic range. The results obtained with sequential assays showed that the linear range of the sensors was within the ng/mL range, however for the studied clinical application, the linear range should be in the microgram/mL range. The future developments of this sensing system would imply adjustment of the dynamic range and sensitivity to cover the interest concentrations for diagnosis. The use of diluted serum for this particular clinical case can be beneficial not only to decrease sample complexity but also to decrease sensor sensitivity. Dynamic range can be adjusted by testing different sample dilution, and/or antibody concentrations, which at this point is saturating the surface (Chapter IV, [42]). An alternative can also be the sample preparation process on-chip and taking the benefit of nanoparticles to adjust the ratio of captured protein biomarkers before detection. These proposals require extensive work since adjustment has to be performed for each biomarker depending on the detection range required. Still, only after optimizing detection of the interested biomarker within the clinical and relevant dynamic range, it is possible to access a multiplex detection strategy for biomarkers associated with the risk of hemorrhagic transformation in stroke patients.

REFERENCES

[1] K. Shavanova, Y. Bakakina, I. Burkova, I. Shtepliuk, R. Viter, A. Ubelis, V. Beni, N. Starodub, R. Yakimova, V. Khranovskyy, Application of 2D non-graphene materials and 2D oxide nanostructures for biosensing technology, Sensors (Switzerland). 16 (2016) 1–23. https://doi.org/10.3390/s16020223.

[2] X. Liu, H. Jiang, Construction and potential applications of biosensors for proteins in clinical laboratory diagnosis, Sensors (Switzerland). 17 (2017). https://doi.org/10.3390/s17122805.

[3] A. de Moraes, L. Kubota, Recent Trends in Field-Effect Transistors-Based Immunosensors, Chemosensors. 4 (2016) 20. https://doi.org/10.3390/chemosensors4040020.

[4] P.S. Pakchin, S.A. Nakhjavani, R. Saber, H. Ghanbari, Y. Omidi, Recent advances in simultaneous electrochemical multi-analyte sensing platforms, TrAC - Trends Anal. Chem. 92 (2017) 32–41. https://doi.org/10.1016/j.trac.2017.04.010.

[5] D. Bizzotto, I.J. Burgess, T. Doneux, T. Sagara, H.Z. Yu, Beyond Simple Cartoons: Challenges in Characterizing Electrochemical Biosensor Interfaces, ACS Sensors. 3 (2018). https://doi.org/10.1021/acssensors.7b00840.

[6] Y.-C. Syu, W.-E. Hsu, C.-T. Lin, Review—Field-Effect Transistor Biosensing: Devices and Clinical Applications, ECS J. Solid State Sci. Technol. 7 (2018) Q3196–Q3207. https://doi.org/10.1149/2.0291807jss.

[7] S. Sang, Y. Wang, Q. Feng, Y. Wei, J. Ji, W. Zhang, Progress of new label-free techniques for biosensors: A review, Crit. Rev. Biotechnol. 36 (2016) 465–481. https://doi.org/10.3109/07388551.2014.991270.

[8] S. Ray, R.T. Steven, F.M. Green, F. Höök, B. Taskinen, V.P. Hytönen, A.G. Shard, Neutralized chimeric avidin binding at a reference biosensor surface, Langmuir. 31 (2015) 1921–1930. https://doi.org/10.1021/la503213f.

[9] H.T.M. Phan, S. Bartelt-Hunt, K.B. Rodenhausen, M. Schubert, J.C. Bartz, Investigation of bovine serum albumin (BSA) attachment onto self-assembled monolayers (SAMs) using combinatorial quartz crystal microbalance with dissipation (QCM-D) and spectroscopic ellipsometry (SE), PLoS One. 10 (2015). https://doi.org/10.1371/journal.pone.0141282.

[10] B.A. Prabowo, P.D. Cabral, P. Freitas, E. Fernandes, The Challenges of Developing Biosensors for Clinical Assessment: A Review, Chemosensors. 9 (2021) 299. https://doi.org/10.3390/chemosensors9110299.

[11] H. Ma, D. Wu, Z. Cui, Y. Li, Y. Zhang, B. Du, Q. Wei, Graphene-Based Optical and Electrochemical Biosensors: A Review, Anal. Lett. 46 (2013) 1–17. https://doi.org/10.1080/00032719.2012.706850.

[12] G. Wang, Y. Wang, L. Chen, J. Choo, Nanomaterial-assisted aptamers for optical sensing, Biosens. Bioelectron. 25 (2010) 1859–1868. https://doi.org/10.1016/j.bios.2009.11.012.

[13] W. Putzbach, N.J. Ronkainen, Immobilization techniques in the fabrication of nanomaterial-based electrochemical biosensors: A review, Sensors (Switzerland). 13 (2013) 4811–4840. https://doi.org/10.3390/s130404811.

[14] M. Kaisti, Detection principles of biological and chemical FET sensors, Biosens. Bioelectron. 98 (2017) 437–448. https://doi.org/10.1016/j.bios.2017.07.010.

[15] J. Sun, Y. Liu, Matrix Effect Study and Immunoassay Detection Using Electrolyte-Gated Graphene Biosensor, Micromachines. 9 (2018) 142. https://doi.org/10.3390/mi9040142.

[16] W. Fu, L. Jiang, E.P. van Geest, L.M.C. Lima, G.F. Schneider, Sensing at the Surface of Graphene Field-Effect Transistors, Adv. Mater. 29 (2017) 1603610. https://doi.org/10.1002/adma.201603610.

[17] R. Stine, S.P. Mulvaney, J.T. Robinson, C.R. Tamanaha, P.E. Sheehan, Fabrication, optimization, and use of graphene field effect sensors, Anal. Chem. 85 (2013) 509–521. https://doi.org/10.1021/ac303190w.

[18] Z. Meng, R.M. Stolz, L. Mendecki, K.A. Mirica, Electrically-Transduced Chemical Sensors Based on Two-Dimensional Nanomaterials, Chem. Rev. 119 (2019) 478–598. https://doi.org/10.1021/acs.chemrev.8b00311.

[19] B.G. Sonmez, O. Ertop, S. Mutlu, Modelling and Realization of a Water-Gated Field Effect Transistor (WG-FET) Using 16-nm-Thick Mono-Si Film, Sci. Rep. 7 (2017) 12190. https://doi.org/10.1038/s41598-017-12439-8.

[20] V.M. Aguilella, J. Pellicer, M. Aguilella-Arzo, Gibbs' dividing surface between a fixed-charge membrane and an electrolyte solution. Application to electrokinetic phenomena in charged pores, Langmuir. 15 (1999) 6156–6162. https://doi.org/10.1021/la980773p.

[21] R. Forsyth, A. Devadoss, O.J. Guy, Graphene Field Effect Transistors for Biomedical Applications: Current Status and Future Prospects, Diagnostics. 7 (2017) 45. https://doi.org/10.3390/diagnostics7030045.

[22] A. V. Lakhin, V.Z. Tarantul, L. V. Gening, Aptamers: Problems, Solutions and Prospects, Acta Naturae. 5 (2013) 34–43. https://doi.org/10.32607/20758251-2013-5-4-34-43.

[23] A.L. Nelson, Antibody fragments, MAbs. 2 (2010) 77–83. https://doi.org/10.4161/mabs.2.1.10786.

[24] D. Saerens, L. Huang, K. Bonroy, S. Muyldermans, Antibody fragments as probe in biosensor development, Sensors. 8 (2008) 4669–4686. https://doi.org/10.3390/s8084669.

[25] A. Zhang, C.M. Lieber, Nano-Bioelectronics, Chem. Rev. 116 (2017) 215–257. https://doi.org/10.1021/acs.chemrev.5b00608.Nano-Bioelectronics.

[26] Y. ZHANG, R. CHEN, L. XU, Y. NING, S. XIE, G.-J. ZHANG, Silicon Nanowire Biosensor for Highly Sensitive and Multiplexed Detection of Oral Squamous Cell Carcinoma Biomarkers in Saliva, Anal. Sci. 31 (2015) 73–78. https://doi.org/10.2116/analsci.31.73.

[27] N.H. Lee, S.H. Nahm, I.S. Choi, Real-time monitoring of a botulinum neurotoxin using all-carbon nanotube-based field-effect transistor devices, Sensors (Switzerland). 18 (2018) 1–12. https://doi.org/10.3390/s18124235.

[28] P.D. Cabral, T. Domingues, G. Machado, A. Chicharo, F. Cerqueira, E. Fernandes, E. Athayde, P. Alpuim, J. Borme, Clean-Room Lithographical Processes for the Fabrication of Graphene Biosensors, Materials (Basel). 13 (2020) 5728. https://doi.org/10.3390/ma13245728.

[29] Ó. Gutiérrez-Sanz, N.M. Andoy, M.S. Filipiak, N. Haustein, A. Tarasov, Direct, Label-Free, and Rapid Transistor-Based Immunodetection in Whole Serum, ACS Sensors. 2 (2017) 1278–1286. https://doi.org/10.1021/acssensors.7b00187.

[30] Ó. Gutiérrez-Sanz, N. Haustein, M. Schroeter, T. Oelschlaegel, M.S. Filipiak, A. Tarasov, Transistor-based immunosensing in human serum samples without on-site calibration, Sensors Actuators B Chem. 295 (2019) 153–158. https://doi.org/10.1016/j.snb.2019.05.043.

[31] Y. Hirano, K. Ooe, K. Tsuchiya, T. Hosokawa, K. Koike, S. Sasa, Design And Evaluation Of The MOSFET Type Glucose Biosensing System, Adv. Mater. Lett. 4 (2013) 108–114. https://doi.org/10.5185/amlett.2012.6367.

[32] S.-W. Huang, I. Sarangadharan, P.-H. Chen, W.-C. Kuo, Y.-L. Wang, Study of Stability and Sensitivity of Cardiac Troponin I Based on FET Sensor, ECS Trans. 89 (2019) 57–63. https://doi.org/10.1149/08906.0057ecst.

[33] L. Zhou, K. Wang, H. Sun, S. Zhao, X. Chen, D. Qian, H. Mao, J. Zhao, Novel Graphene Biosensor Based on the Functionalization of Multifunctional Nano-bovine Serum Albumin for the Highly Sensitive Detection of Cancer Biomarkers, Nano-Micro Lett. 11 (2019). https://doi.org/10.1007/s40820-019-0250-8.

[34] K. Zhou, Z. Zhao, L. Pan, Z. Wang, Silicon nanowire pH sensors fabricated with CMOS compatible sidewall mask technology, Sensors Actuators B Chem. 279 (2019) 111–121. https://doi.org/10.1016/j.snb.2018.09.114.

[35] Y.K. Yen, Y.C. Lai, W.T. Hong, Y. Pheanpanitporn, C.S. Chen, L.S. Huang, Electrical detection of C-reactive protein using a single free-standing, thermally controlled piezoresistive microcantilever for highly reproducible and accurate measurements, Sensors (Switzerland). 13 (2013) 9653–9668. https://doi.org/10.3390/s130809653.

[36] A. Hess-Dunning, C.A. Zorman, Electrical interfaces for recording, stimulation, and sensing, in: Implant. Biomed. Microsystems, Elsevier, 2015: pp. 13–38. https://doi.org/10.1016/B978-0-323-26208-8.00002-9.

[37] Y. Chen, X.L. Gong, J.G. Gai, Progress and Challenges in Transfer of Large-Area Graphene Films, Adv. Sci. 3 (2016) 1–15. https://doi.org/10.1002/advs.201500343.

[38] D.-C. Mao, S.-A. Peng, S.-Q. Wang, D.-Y. Zhang, J.-Y. Shi, X. Wang, Z. Jin, Towards a cleaner graphene surface in graphene field effect transistor via N,N-Dimethylacetamide, Mater. Res. Express. 3 (2016) 095011. https://doi.org/10.1088/2053-1591/3/9/095011.

[39] N.C.S. Vieira, J. Borme, G. MacHado, F. Cerqueira, P.P. Freitas, V. Zucolotto, N.M.R. Peres, P. Alpuim, Graphene field-effect transistor array with integrated electrolytic gates scaled to 200 mm, J. Phys. Condens. Matter. 28 (2016) 85302. https://doi.org/10.1088/0953-8984/28/8/085302.

[40] J. Sun, M. Muruganathan, H. Mizuta, Room temperature detection of individual molecular physisorption using suspended bilayer graphene, Sci. Adv. 2 (2016) 1–8. https://doi.org/10.1126/sciadv.1501518.

[41] N.O. Weiss, H. Zhou, L. Liao, Y. Liu, S. Jiang, Y. Huang, X. Duan, Graphene: An emerging electronic material, Adv. Mater. 24 (2012) 5782–5825. https://doi.org/10.1002/adma.201201482.

[42] E. Fernandes, P.D. Cabral, R. Campos, G. Machado, M.F. Cerqueira, C. Sousa, P.P. Freitas, J. Borme, D.Y. Petrovykh, P. Alpuim, Functionalization of single-layer graphene for immunoassays, Appl. Surf. Sci. 480 (2019) 709–716. https://doi.org/10.1016/j.apsusc.2019.03.004.

[43] C. Riedl, Epitaxial Graphene on Silicon Carbide Surfaces: Growth, Characterization, Doping and Hydrogen Intercalation, Friedrich-Alexander-Universität, 2010. https://doi.org/10.1088/1751-8113/44/8/085201.

[44] K.S. Novoselov, Electric Field Effect in Atomically Thin Carbon Films, Science (80-.). 306 (2004) 666–669. https://doi.org/10.1126/science.1102896.

[45] Y. Hernandez, V. Nicolosi, M. Lotya, F.M. Blighe, Z. Sun, S. De, I.T. McGovern, B. Holland, M. Byrne, Y.K. Gun'Ko, J.J. Boland, P. Niraj, G. Duesberg, S. Krishnamurthy, R. Goodhue, J. Hutchison, V. Scardaci, A.C. Ferrari, J.N. Coleman, High-yield production of graphene by liquid-phase exfoliation of graphite, Nat. Nanotechnol. 3 (2008) 563–568. https://doi.org/10.1038/nnano.2008.215.

[46] S. Majee, M. Song, S.L. Zhang, Z. Bin Zhang, Scalable inkjet printing of shear-exfoliated graphene transparent conductive films, Carbon N. Y. 102 (2016) 51–57. https://doi.org/10.1016/j.carbon.2016.02.013.

[47] A.E. Del Rio Castillo, V. Pellegrini, A. Ansaldo, F. Ricciardella, H. Sun, L. Marasco, J. Buha, Z. Dang, L. Gagliani, E. Lago, N. Curreli, S. Gentiluomo, F. Palazon, M. Prato, R. Oropesa-Nuñez, P.S. Toth, E. Mantero, M. Crugliano, A. Gamucci, A. Tomadin, M. Polini, F. Bonaccorso, High-yield production of 2D crystals by wet-jet milling, Mater. Horizons. 5 (2018) 890–904. https://doi.org/10.1039/C8MH00487K.

[48] D.R. Cooper, B. D'Anjou, N. Ghattamaneni, B. Harack, M. Hilke, A. Horth, N. Majlis, M. Massicotte, L. Vandsburger, E. Whiteway, V. Yu, Experimental review of graphene, 2012 (2011).

https://doi.org/10.5402/2012/501686.

[49] Y. Hao, M.S. Bharathi, L. Wang, Y. Liu, H. Chen, S. Nie, X. Wang, H. Chou, C. Tan, B. Fallahazad, H. Ramanarayan, C.W. Magnuson, E. Tutuc, B.I. Yakobson, K.F. McCarty, Y.-W. Zhang, P. Kim, J. Hone, L. Colombo, R.S. Ruoff, The Role of Surface Oxygen in the Growth of Large Single-Crystal Graphene on Copper, Science (80-.). 342 (2013) 720–723. https://doi.org/10.1126/science.1243879.

[50] J. Pezard, M. Lazar, N. Haddour, C. Botella, P. Roy, J.B. Brubach, D. Wysocka, B. Vilquin, P.R. Romeo, F. Buret, Realization of a graphene gate field effect transistor for electrochemical detection and biosensors, Thin Solid Films. 617 (2016) 150–155. https://doi.org/10.1016/j.tsf.2016.04.031.

[51] R.A. Hartvig, M. Van De Weert, J. Østergaard, L. Jorgensen, H. Jensen, Protein adsorption at charged surfaces: The role of electrostatic interactions and interfacial charge regulation, Langmuir. 27 (2011) 2634–2643. https://doi.org/10.1021/la104720n.

[52] A. Gupta, T. Sakthivel, S. Seal, Recent development in 2D materials beyond graphene, Prog. Mater. Sci. 73 (2015) 44–126. https://doi.org/10.1016/j.pmatsci.2015.02.002.

[53] X. Gan, H. Zhao, X. Quan, Two-dimensional MoS2: A promising building block for biosensors, Biosens. Bioelectron. 89 (2017) 56–71. https://doi.org/10.1016/j.bios.2016.03.042.

[54] Y. Fan, G. Hao, S. Luo, X. Qi, H. Li, L. Ren, J. Zhong, Synthesis, characterization and electrostatic properties of WS2 nanostructures, AIP Adv. 4 (2014). https://doi.org/10.1063/1.4875915.

[55] L. Wang, Y. Wang, J.I. Wong, T. Palacios, J. Kong, H.Y. Yang, Functionalized MoS2 Nanosheet-Based Field-Effect Biosensor for Label-Free Sensitive Detection of Cancer Marker Proteins in Solution, Small. 10 (2014) 1101–1105. https://doi.org/10.1002/smll.201302081.

[56] J. Shan, J. Li, X. Chu, M. Xu, F. Jin, X. Wang, L. Ma, X. Fang, Z. Wei, X. Wang, High sensitivity glucose detection at extremely low concentrations using a MoS 2 -based field-effect transistor, RSC Adv. 8 (2018) 7942–7948. https://doi.org/10.1039/C7RA13614E.

[57] Y. Huang, J. Guo, Y. Kang, Y. Ai, C.M. Li, Two dimensional atomically thin MoS2 nanosheets and their sensing applications, Nanoscale. 7 (2015) 19358–19376. https://doi.org/10.1039/C5NR06144J.

[58] D. Sarkar, W. Liu, X. Xie, A.C. Anselmo, S. Mitragotri, K. Banerjee, MoS2 field-effect transistor for next-generation label-free biosensors, ACS Nano. 8 (2014) 3992–4003. https://doi.org/10.1021/nn5009148.

[59] J. Lee, P. Dak, Y. Lee, H. Park, W. Choi, M. a Alam, S. Kim, Two-dimensional layered MoS_2 biosensors enable highly sensitive detection of biomolecules., Sci. Rep. 4 (2014) 7352. https://doi.org/10.1038/srep07352.

[60] H. Nam, B.R. Oh, P. Chen, J.S. Yoon, S. Wi, M. Chen, K. Kurabayashi, X. Liang, Two different device physics principles for operating MoS2transistor biosensors with femtomolar-level detection limits, Appl. Phys. Lett. 107 (2015). https://doi.org/10.1063/1.4926800.

[61] M. Gelderblom, M. Neumann, P. Ludewig, C. Bernreuther, S. Krasemann, P. Arunachalam, C. Gerloff, M. Glatzel, T. Magnus, Deficiency in Serine Protease Inhibitor Neuroserpin Exacerbates Ischemic Brain Injury by Increased Postischemic Inflammation, PLoS One. 8 (2013) 1–9. https://doi.org/10.1371/journal.pone.0063118.

[62] G.C. Jickling, F.R. Sharp, Blood Biomarkers of Ischemic Stroke, Neurotherapeutics. 8 (2011) 349–360. https://doi.org/10.1007/s13311-011-0050-4.

[63] M. Rodríguez-Yáñez, M. Blanco, T. Sobrino, S. Arias-Rivas, J. Castillo, Update on the research of serum biomarkers to assess stroke, Drugs Future. 37 (2012) 283. https://doi.org/10.1358/dof.2012.037.04.1769799.

[64] O. Moldes, T. Sobrino, M. Millan, M. Castellanos, N. Perez de la Ossa, R. Leira, J. Serena, J. Vivancos, A. Davalos, J. Castillo, High Serum Levels of Endothelin-1 Predict Severe Cerebral

Edema in Patients With Acute Ischemic Stroke Treated With t-PA, Stroke. 39 (2008) 2006–2010. https://doi.org/10.1161/STROKEAHA.107.495044.

[65] I. Maestrini, A. Ducroquet, S. Moulin, D. Leys, C. Cordonnier, R. Bordet, Blood biomarkers in the early stage of cerebral ischemia, Rev. Neurol. (Paris). 172 (2016) 198–219. https://doi.org/10.1016/j.neurol.2016.02.003.

[66] G.J.L. Ng, A.M.L. Quek, C. Cheung, T. V. Arumugam, R.C.S. Seet, Stroke biomarkers in clinical practice: A critical appraisal, Neurochem. Int. 107 (2017) 11–22. https://doi.org/10.1016/j.neuint.2017.01.005.

[67] E. Fernandes, T. Sobrino, V.C. Martins, I. Lopez-loureiro, F. Campos, J. Germano, M. Rodríguez-Pérez, S. Cardoso, D.Y. Petrovykh, J. Castillo, P.P. Freitas, Point-of-care quantification of serum cellular fibronectin levels for stratification of ischemic stroke patients, Nanomedicine Nanotechnology, Biol. Med. 30 (2020) 102287. https://doi.org/10.1016/j.nano.2020.102287.

[68] G.C. Jickling, D. Liu, B. Stamova, B.P. Ander, X. Zhan, A. Lu, F.R. Sharp, Hemorrhagic transformation after ischemic stroke in animals and humans, J. Cereb. Blood Flow Metab. 34 (2014) 185–199. https://doi.org/10.1038/jcbfm.2013.203.

[69] M. Ramos-Fernandez, M.F. Bellolio, L.G. Stead, Matrix metalloproteinase-9 as a marker for acute ischemic stroke: A systematic review, J. Stroke Cerebrovasc. Dis. 20 (2011) 47–54. https://doi.org/10.1016/j.jstrokecerebrovasdis.2009.10.008.

[70] M. Rodriguez-Yanez, T. Sobrino, S. Arias, F. Vazquez-Herrero, D. Brea, M. Blanco, R. Leira, M. Castellanos, J. Serena, J. Vivancos, A. Davalos, J. Castillo, Early Biomarkers of Clinical-Diffusion Mismatch in Acute Ischemic Stroke, Stroke. 42 (2011) 2813–2818. https://doi.org/10.1161/STROKEAHA.111.614503.

[71] M. Castellanos, R. Leira, J. Serena, M. Blanco, S. Pedraza, J. Castillo, A. Dávalos, Plasma cellular-fibronectin concentration predicts hemorrhagic transformation after thrombolytic therapy in acute ischemic stroke, Stroke. 35 (2004) 1671–1676. https://doi.org/10.1161/01.STR.0000131656.47979.39.

[72] R. Rodríguez-González, M. Blanco, M. Rodríguez-Yáñez, O. Moldes, J. Castillo, T. Sobrino, Platelet derived growth factor-CC isoform is associated with hemorrhagic transformation in ischemic stroke patients treated with tissue plasminogen activator, Atherosclerosis. 226 (2013) 165–171. https://doi.org/10.1016/j.atherosclerosis.2012.10.072.

[73] K. Kawamura, T. Takahashi, M. Kanazawa, H. Igarashi, T. Nakada, M. Nishizawa, T. Shimohata, Effects of angiopoietin-1 on hemorrhagic transformation and cerebral edema after tissue plasminogen activator treatment for ischemic stroke in rats, PLoS One. 9 (2014) 1–9. https://doi.org/10.1371/journal.pone.0098639.

[74] R. Rodríguez-González, T. Sobrino, M. Rodríguez-Yáñez, M. Millán, D. Brea, E. Miranda, O. Moldes, J. Pérez, D.A. Lomas, R. Leira, A. Dávalos, J. Castillo, Association between neuroserpin and molecular markers of brain damage in patients with acute ischemic stroke, J. Transl. Med. 9 (2011) 58. https://doi.org/10.1186/1479-5876-9-58.

[75] C. Foerch, M.T. Wunderlich, F. Dvorak, M. Humpich, T. Kahles, M. Goertler, J. Alvarez-Sabín, C.W. Wallesch, C.A. Molina, H. Steinmetz, M. Sitzer, J. Montaner, Elevated serum S100B levels indicate a higher risk of hemorrhagic transformation after thrombolytic therapy in acute stroke, Stroke. 38 (2007) 2491–2495. https://doi.org/10.1161/STROKEAHA.106.480111.

[76] H.Y. Park, S.R. Dugasani, D.H. Kang, G. Yoo, J. Kim, B. Gnapareddy, J. Jeon, M. Kim, Y.J. Song, S. Lee, J. Heo, Y.J. Jeon, S.H. Park, J.H. Park, M-DNA/Transition Metal Dichalcogenide Hybrid Structure-based Bio-FET sensor with Ultra-high Sensitivity, Sci. Rep. 6 (2016) 1–9. https://doi.org/10.1038/srep35733.

[77] S.J. Rodríguez, L. Makinistian, E.A. Albanesi, Graphene for amino acid biosensing: Theoretical study of the electronic transport, Appl. Surf. Sci. 419 (2017) 540–545.

https://doi.org/10.1016/J.APSUSC.2017.05.031.

[78] K.S. Novoselov, V.I. Fal'Ko, L. Colombo, P.R. Gellert, M.G. Schwab, K. Kim, A roadmap for graphene, Nature. 490 (2012) 192–200. https://doi.org/10.1038/nature11458.

[79] P. Li, B. Zhang, T. Cui, Towards intrinsic graphene biosensor: A label-free, suspended single crystalline graphene sensor for multiplex lung cancer tumor markers detection, Biosens. Bioelectron. 72 (2015) 168–174. https://doi.org/10.1016/j.bios.2015.05.007.

[80] S. Mao, K. Yu, J. Chang, D.A. Steeber, L.E. Ocola, J. Chen, Direct Growth of Vertically-oriented Graphene for Field-Effect Transistor Biosensor, Sci. Rep. 3 (2013) 1696. https://doi.org/10.1038/srep01696.

[81] S. Afsahi, M.B. Lerner, J.M. Goldstein, J. Lee, X. Tang, D.A. Bagarozzi, D. Pan, L. Locascio, A. Walker, F. Barron, B.R. Goldsmith, Novel graphene-based biosensor for early detection of Zika virus infection, Biosens. Bioelectron. 100 (2018) 85–88. https://doi.org/10.1016/j.bios.2017.08.051.

[82] Y. Chen, R. Ren, H. Pu, X. Guo, J. Chang, G. Zhou, S. Mao, M. Kron, J. Chen, Field-Effect Transistor Biosensor for Rapid Detection of Ebola Antigen, Sci. Rep. 7 (2017) 4–11. https://doi.org/10.1038/s41598-017-11387-7.

[83] R. Campos, J. Borme, J.R. Guerreiro, G. Machado, M.F. Cerqueira, D.Y. Petrovykh, P. Alpuim, Attomolar Label-Free Detection of DNA Hybridization with Electrolyte-Gated Graphene Field-Effect Transistors, ACS Sensors. 4 (2019) 286–293. https://doi.org/10.1021/acssensors.8b00344.

[84] Y. Ohno, K. Maehashi, Y. Yamashiro, K. Matsumoto, Electrolyte-Gated Graphene Field-Effect Transistors for Detecting pH and Protein Adsorption, Nano Lett. 9 (2009) 3318–3322. https://doi.org/10.1021/nl901596m.

[85] S. Siddique, M.Z. Iqbal, H. Mukhtar, Cholesterol immobilization on chemical vapor deposition grown graphene nanosheets for biosensors and bioFETs with enhanced electrical performance, Sensors Actuators, B Chem. 253 (2017) 559–565. https://doi.org/10.1016/j.snb.2017.06.170.

[86] S. Mao, K. Yu, G. Lu, J. Chen, Highly sensitive protein sensor based on thermally-reduced graphene oxide field-effect transistor, Nano Res. 4 (2011) 921–930. https://doi.org/10.1007/s12274-011-0148-3.

[87] X. Dong, Y. Shi, W. Huang, P. Chen, L.-J. Li, Electrical Detection of DNA Hybridization with Single-Base Specificity Using Transistors Based on CVD-Grown Graphene Sheets, Adv. Mater. 22 (2010) 1649–1653. https://doi.org/10.1002/adma.200903645.

[88] Z. Yin, Q. He, X. Huang, J. Zhang, S. Wu, P. Chen, G. Lu, P. Chen, Q. Zhang, Q. Yan, H. Zhang, Real-time DNA detection using Pt nanoparticle-decorated reduced graphene oxide field-effect transistors, Nanoscale. 4 (2012) 293–297. https://doi.org/10.1039/C1NR11149C.

[89] M. Larisika, C. Kotlowski, C. Steininger, R. Mastrogiacomo, P. Pelosi, S. Schütz, S.F. Peteu, C. Kleber, C. Reiner-Rozman, C. Nowak, W. Knoll, Electronic Olfactory Sensor Based on A. mellifera Odorant-Binding Protein 14 on a Reduced Graphene Oxide Field-Effect Transistor, Angew. Chemie Int. Ed. 54 (2015) 13245–13248. https://doi.org/10.1002/anie.201505712.

[90] T.-Y. Chen, P.T.K. Loan, C.-L. Hsu, Y.-H. Lee, J. Tse-Wei Wang, K.-H. Wei, C.-T. Lin, L.-J. Li, Label-free detection of DNA hybridization using transistors based on CVD grown graphene, Biosens. Bioelectron. 41 (2013) 103–109. https://doi.org/10.1016/j.bios.2012.07.059.

[91] M.B. Lerner, F. Matsunaga, G.H. Han, S.J. Hong, J. Xi, A. Crook, J.M. Perez-Aguilar, Y.W. Park, J.G. Saven, R. Liu, a T.C. Johnson, Supporting information: Scalable Production of Highly Sensitive Nanosensors Based on Graphene Functionalized with a Designed G Protein-Coupled Receptor, Nano Lett. 14 (2014) 2709–2714. https://doi.org/10.1021/nl5006349.

[92] M.B. Lerner, D. Pan, Y. Gao, L.E. Locascio, K.Y. Lee, J. Nokes, S. Afsahi, J.D. Lerner, A. Walker, P.G. Collins, K. Oegema, F. Barron, B.R. Goldsmith, Large scale commercial fabrication of high

quality graphene-based assays for biomolecule detection, Sensors Actuators, B Chem. 239 (2017) 1261–1267. https://doi.org/10.1016/j.snb.2016.09.137.

[93] S. Xu, S. Jiang, C. Zhang, W. Yue, Y. Zou, G. Wang, H. Liu, X. Zhang, M. Li, Z. Zhu, J. Wang, Ultrasensitive label-free detection of DNA hybridization by sapphire-based graphene field-effect transistor biosensor, Appl. Surf. Sci. 427 (2018) 1114–1119. https://doi.org/10.1016/j.apsusc.2017.09.113.

[94] C. Haslam, S. Damiati, T. Whitley, P. Davey, E. Ifeachor, S. Awan, Label-Free Sensors Based on Graphene Field-Effect Transistors for the Detection of Human Chorionic Gonadotropin Cancer Risk Biomarker, Diagnostics. 8 (2018) 5. https://doi.org/10.3390/diagnostics8010005.

[95] D. Kim, I. Yung, J.-H. Jung, O. Ja, N.-E. Lee, I.Y. Sohn, J.-H. Jung, O.J. Yoon, N.-E. Lee, J.-S. Park, Reduced graphene oxide field-effect transistor for label-free femtomolar protein detection, Biosens. Bioelectron. 41 (2013) 621–626. https://doi.org/10.1016/j.bios.2012.09.040.

[96] B. Cai, S. Wang, L. Huang, Y. Ning, Z. Zhang, G.-J. Zhang, Ultrasensitive Label-Free Detection of PNA–DNA Hybridization by Reduced Graphene Oxide Field-Effect Transistor Biosensor, ACS Nano. 8 (2014) 2632–2638. https://doi.org/10.1021/nn4063424.

[97] Y. Ohno, K. Maehashi, K. Matsumoto, Label-Free Biosensors Based on Aptamer-Modified Graphene Field-Effect Transistors, J. Am. Chem. Soc. 132 (2010) 18012–18013. https://doi.org/10.1021/ja108127r.

[98] C. Reiner-Rozman, C. Kotlowski, W. Knoll, Electronic Biosensing with Functionalized rGO FETs, Biosensors. 6 (2016) 17. https://doi.org/10.3390/bios6020017.

[99] Q. He, S. Wu, S. Gao, X. Cao, Z. Yin, H. Li, P. Chen, H. Zhang, Transparent, Flexible, All-Reduced Graphene Oxide Thin Film Transistors, ACS Nano. (2011) 5038–5044.

[100] C. Zheng, L. Huang, H. Zhang, Z. Sun, Z. Zhang, G.-J. Zhang, Fabrication of Ultrasensitive Field-Effect Transistor DNA Biosensors by a Directional Transfer Technique Based on CVD-Grown Graphene, ACS Appl. Mater. Interfaces. 7 (2015) 16953–16959. https://doi.org/10.1021/acsami.5b03941.

[101] L. Zhou, H. Mao, C. Wu, L. Tang, Z. Wu, H. Sun, H. Zhang, H. Zhou, C. Jia, Q. Jin, X. Chen, J. Zhao, Label-free graphene biosensor targeting cancer molecules based on non-covalent modification, Biosens. Bioelectron. 87 (2017) 701–707. https://doi.org/10.1016/j.bios.2016.09.025.

[102] C. Wang, Y. Li, Y. Zhu, X. Zhou, Q. Lin, M. He, High-κ Solid-Gate Transistor Configured Graphene Biosensor with Fully Integrated Structure and Enhanced Sensitivity, Adv. Funct. Mater. 26 (2016) 7668–7678. https://doi.org/10.1002/adfm.201602960.

[103] N.M. Andoy, M.S. Filipiak, D. Vetter, Ó. Gutiérrez-Sanz, A. Tarasov, Graphene-Based Electronic Immunosensor with Femtomolar Detection Limit in Whole Serum, Adv. Mater. Technol. 3 (2018) 1800186. https://doi.org/10.1002/admt.201800186.

[104] G. Saltzgaber, P. Wojcik, T. Sharf, M.R. Leyden, J.L. Wardini, C.A. Heist, A.A. Adenuga, V.T. Remcho, E.D. Minot, Supporting Information : Scalable Graphene Field-Effect Sensors for Specific Protein Detection, Nanotechnology. 24 (2013).

[105] C. Wang, X. Cui, Y. Li, H. Li, L. Huang, J. Bi, J. Luo, L.Q. Ma, W. Zhou, Y. Cao, B. Wang, F. Miao, A label-free and portable graphene FET aptasensor for children blood lead detection, Sci. Rep. 6 (2016) 1–8. https://doi.org/10.1038/srep21711.

[106] Y. Zhu, Y. Hao, E.A. Adogla, J. Yan, D. Li, K. Xu, Q. Wang, J. Hone, Q. Lin, A graphene-based affinity nanosensor for detection of low-charge and low-molecular-weight molecules, Nanoscale. 8 (2016) 5815–5819. https://doi.org/10.1039/C5NR08866F.

[107] M.B. Lerner, F. Matsunaga, G.H. Han, S.J. Hong, J. Xi, A. Crook, J.M. Perez-Aguilar, Y.W. Park, J.G. Saven, R. Liu, a T.C. Johnson, Scalable Production of Highly Sensitive Nanosensors Based on Graphene Functionalized with a Designed G Protein-Coupled Receptor, Nano Lett. 14 (2014)

2709–2714. https://doi.org/10.1021/nl5006349.
[108] K. Settu, J.T. Liu, C.J. Chen, J.Z. Tsai, Development of carbon–graphene-based aptamer biosensor for EN2 protein detection, Anal. Biochem. 534 (2017) 99–107. https://doi.org/10.1016/j.ab.2017.07.012.
[109] G. Saltzgaber, P.M. Wojcik, T. Sharf, M.R. Leyden, J.L. Wardini, C.A. Heist, A.A. Adenuga, V.T. Remcho, E.D. Minot, Scalable graphene field-effect sensors for specific protein detection, Nanotechnology. 24 (2013) 355502. https://doi.org/10.1088/0957-4484/24/35/355502.
[110] N. Gao, T. Gao, X. Yang, X. Dai, W. Zhou, A. Zhang, C.M. Lieber, Specific detection of biomolecules in physiological solutions using graphene transistor biosensors, Proc. Natl. Acad. Sci. 113 (2016) 14633–14638. https://doi.org/10.1073/pnas.1625010114.
[111] T. Kuamit, M. Ratanasak, C. Rungnim, V. Parasuk, Effects of shape, size, and pyrene doping on electronic properties of graphene nanoflakes, J. Mol. Model. 23 (2017) 355. https://doi.org/10.1007/s00894-017-3521-7.
[112] M.Z. Miskin, C. Sun, I. Cohen, W.R. Dichtel, P.L. McEuen, Measuring and Manipulating the Adhesion of Graphene, Nano Lett. 18 (2018) 449–454. https://doi.org/10.1021/acs.nanolett.7b04370.
[113] C. Lechner, A.F. Sax, Towards atomic-level mechanics: Adhesive forces between aromatic molecules and carbon nanotubes, Appl. Surf. Sci. 420 (2017) 606–617. https://doi.org/10.1016/j.apsusc.2017.05.170.
[114] L. Xu, X. Yang, Molecular dynamics simulation of adsorption of pyrene-polyethylene glycol onto graphene, J. Colloid Interface Sci. 418 (2014) 66–73. https://doi.org/10.1016/j.jcis.2013.12.005.
[115] S. Bailey, D. Visontai, C.J. Lambert, M.R. Bryce, H. Frampton, D. Chappell, A study of planar anchor groups for graphene-based single-molecule electronics, J. Chem. Phys. 140 (2014). https://doi.org/10.1063/1.4861941.
[116] C.S. Park, H. Yoon, O.S. Kwon, Graphene-based nanoelectronic biosensors, J. Ind. Eng. Chem. 38 (2016) 13–22. https://doi.org/10.1016/j.jiec.2016.04.021.
[117] C.Y. Lim, N.A. Owens, R.D. Wampler, Y. Ying, J.H. Granger, M.D. Porter, M. Takahashi, K. Shimazu, Succinimidyl ester surface chemistry: Implications of the competition between aminolysis and hydrolysis on covalent protein immobilization, Langmuir. 30 (2014) 12868–12878. https://doi.org/10.1021/la503439g.
[118] S. Xu, J. Zhan, B. Man, S. Jiang, W. Yue, S. Gao, C. Guo, H. Liu, Z. Li, J. Wang, Y. Zhou, Real-time reliable determination of binding kinetics of DNA hybridization using a multi-channel graphene biosensor, Nat. Commun. 8 (2017) 14902. https://doi.org/10.1038/ncomms14902.
[119] P.T.K. Loan, D. Wu, C. Ye, X. Li, V.T. Tra, Q. Wei, L. Fu, A. Yu, L.J. Li, C. Te Lin, Hall effect biosensors with ultraclean graphene film for improved sensitivity of label-free DNA detection, Biosens. Bioelectron. 99 (2018) 85–91. https://doi.org/10.1016/j.bios.2017.07.045.
[120] J. Basu, S. Datta, C. Roy, A graphene field effect capacitive Immunosensor for sub-femtomolar food toxin detection, Biosens. Bioelectron. 68 (2015) 544–549. https://doi.org/10.1016/j.bios.2015.01.046.
[121] T.C. Chiu, C.C. Huang, Aptamer-functionalized nano-biosensors, 2009. https://doi.org/10.3390/s91210356.
[122] S.J. Afsahi, L.E. Locascio, D. Pan, Y. Gao, A.E. Walker, F.E. Barron, B.R. Goldsmith, M.B. Lerner, Towards Novel Graphene-Enabled Diagnostic Assays with Improved Signal-to-Noise Ratio, MRS Adv. 2 (2017) 3733–3739. https://doi.org/10.1557/adv.2017.431.
[123] M. Sajid, A. Osman, G.U. Siddiqui, H.B. Kim, S.W. Kim, J.B. Ko, Y.K. Lim, K.H. Choi, All-printed highly sensitive 2D MoS2based multi-reagent immunosensor for smartphone based point-of-care diagnosis, Sci. Rep. 7 (2017) 1–11. https://doi.org/10.1038/s41598-017-06265-1.

[124] C.H. Naylor, N.J. Kybert, C. Schneier, J. Xi, G. Romero, G. Saven, R. Liu, A.T.C. Johnson, Scalable Production of Molybdenum Disul fi de Based Biosensors, ACS Nano. 10 (2016) 6173–6179. https://doi.org/10.1021/acsnano.6b02137.

[125] B. Ryu, H. Nam, B.-R. Oh, Y. Song, P. Chen, Y. Park, W. Wan, K. Kurabayashi, X. Liang, Cyclewise Operation of Printed MoS 2 Transistor Biosensors for Rapid Biomolecule Quantification at Femtomolar Levels, ACS Sensors. 2 (2017) 274–281. https://doi.org/10.1021/acssensors.6b00795.

[126] S.P. Pujari, L. Scheres, A.T.M. Marcelis, H. Zuilhof, Covalent surface modification of oxide surfaces, Angew. Chemie - Int. Ed. 53 (2014) 6322–6356. https://doi.org/10.1002/anie.201306709.

[127] C.H. Naylor, N.J. Kybert, C. Schneier, J. Xi, G. Romero, J.G. Saven, R. Liu, A.T.C. Johnson, Scalable Production of Molybdenum Disulfide Based Biosensors, ACS Nano. 10 (2016) 6173–6179. https://doi.org/10.1021/acsnano.6b02137.

[128] Y.-H. Lin, C. Chu, C. Lin, H. Liao, H. Tsai, Y. Juang, Extended-gate field-effect transistor packed in micro channel for glucose, urea and protein biomarker detection, Biomed. Microdevices. 17 (2015) 111. https://doi.org/10.1007/s10544-015-0020-4.

[129] S. Hideshima, R. Sato, S. Inoue, S. Kuroiwa, T. Osaka, Detection of tumor marker in blood serum using antibody-modified field effect transistor with optimized BSA blocking, Sensors Actuators B Chem. 161 (2012) 146–150. https://doi.org/10.1016/j.snb.2011.10.001.

[130] S. Hideshima, S. Kuroiwa, M. Kimura, S. Cheng, T. Osaka, Effect of the size of receptor in allergy detection using field effect transistor biosensor, Electrochim. Acta. 110 (2013) 146–151. https://doi.org/10.1016/j.electacta.2013.07.113.

[131] B. Khamaisi, O. Vaknin, O. Shaya, N. Ashkenasy, Electrical Performance of Silicon-on-Insulator Field-Effect Transistors with Multiple Top-Gate Organic Layers in Electrolyte Solution, ACS Nano. 4 (2010) 4601–4608. https://doi.org/10.1021/nn100936h.

[132] H. Qian, Y. Huang, X. Duan, X. Wei, Y. Fan, D. Gan, S. Yue, W. Cheng, T. Chen, Fiber optic surface plasmon resonance biosensor for detection of PDGF-BB in serum based on self-assembled aptamer and antifouling peptide monolayer, Biosens. Bioelectron. 140 (2019). https://doi.org/10.1016/j.bios.2019.111350.

[133] J. Zhang, Y. Yuan, S. biXie, Y. Chai, R. Yuan, Amplified amperometric aptasensor for selective detection of protein using catalase-functional DNA-PtNPs dendrimer as a synergetic signal amplification label, Biosens. Bioelectron. 60 (2014) 224–230. https://doi.org/10.1016/j.bios.2014.04.024.

[134] J.-W. Park, S. Jin Lee, E.-J. Choi, J. Kim, J.-Y. Song, M. Bock Gu, An ultra-sensitive detection of a whole virus using dual aptamers developed by immobilization-free screening., Biosens. Bioelectron. 51 (2014) 324–9.

[135] T.-C. Chang, C.-C. Wu, S.-C. Wang, L.-K. Chau, W.-H. Hsieh, Using a fiber optic particle plasmon resonance biosensor to determine kinetic constants of antigen-antibody binding reaction., Anal. Chem. 85 (2013) 245–50.

[136] M.M. Ali, D.-K. Kang, K. Tsang, M. Fu, J.M. Karp, W. Zhao, Cell-surface sensors: Lighting the cellular environment, Wiley Interdiscip. Rev. Nanomedicine Nanobiotechnology. 4 (2012) 547–561. https://doi.org/10.1002/wnan.1179.

[137] Y. Chen, R. Ren, H. Pu, J. Chang, S. Mao, J. Chen, Field-effect transistor biosensors with two-dimensional black phosphorus nanosheets, Biosens. Bioelectron. 89 (2017) 505–510. https://doi.org/10.1016/j.bios.2016.03.059.

[138] X.P.A. Gao, G. Zheng, C.M. Lieber, Subthreshold regime has the optimal sensitivity for nanowire FET biosensors, Nano Lett. 10 (2010) 547–552. https://doi.org/10.1021/nl9034219.

[139] S. Mao, J. Chang, H. Pu, G. Lu, Q. He, H. Zhang, J. Chen, Two-dimensional nanomaterial-based

field-effect transistors for chemical and biological sensing, Chem. Soc. Rev. 46 (2017) 6872–6904. https://doi.org/10.1039/C6CS00827E.

[140] E. Comini, C. Baratto, G. Faglia, M. Ferroni, A. Vomiero, G. Sberveglieri, Quasi-one dimensional metal oxide semiconductors: Preparation, characterization and application as chemical sensors, Prog. Mater. Sci. 54 (2009) 1–67. https://doi.org/10.1016/j.pmatsci.2008.06.003.

[141] B.A. Prabowo, A. Purwidyantri, B. Liu, H.C. Lai, K.C. Liu, Gold nanoparticle-assisted plasmonic enhancement for DNA detection on a graphene-based portable surface plasmon resonance sensor, Nanotechnology. 32 (2021). https://doi.org/10.1088/1361-6528/abcd62.

[142] P. Ramnani, N.M. Saucedo, A. Mulchandani, Carbon nanomaterial-based electrochemical biosensors for label-free sensing of environmental pollutants, Chemosphere. 143 (2016) 85–98. https://doi.org/10.1016/j.chemosphere.2015.04.063.

[143] G. Xu, J. Abbott, L. Qin, K.Y.M. Yeung, Y. Song, H. Yoon, J. Kong, D. Ham, Electrophoretic and field-effect graphene for all-electrical DNA array technology, Nat. Commun. 5 (2014) 1–9. https://doi.org/10.1038/ncomms5866.

[144] S. Mao, G. Lu, K. Yu, Z. Bo, J. Chen, Specific protein detection using thermally reduced graphene oxide sheet decorated with gold nanoparticle-antibody conjugates, Adv. Mater. 22 (2010) 3521–3526. https://doi.org/10.1002/adma.201000520.

[145] A. Purwidyantri, T. Domingues, J.R. Guerreiro, A. Ipatov, C.M. Abreu, M. Martins, P. Alpuim, M. Prado, Influence of the Electrolyte Salt Concentration on DNA Detection with Graphene Transistors, Biosensors. 11 (2021) 24. https://doi.org/10.3390/bios11010024.

[146] D.-W. Lee, J. Lee, I.Y. Sohn, B.-Y. Kim, Y.M. Son, H. Bark, J. Jung, M. Choi, T.H. Kim, C. Lee, N.-E. Lee, Field-effect transistor with a chemically synthesized MoS2 sensing channel for label-free and highly sensitive electrical detection of DNA hybridization, Nano Res. 8 (2015) 2340–2350. https://doi.org/10.1007/s12274-015-0744-8.

[147] P. Chen, X. Shu, H. Cao, K. Sugden, High-sensitivity and large-dynamic-range refractive index sensors employing weak composite Fabry-Perot cavities., Opt. Lett. 42 (2017) 3145–3148. https://doi.org/10.1364/OL.42.003145.

[148] B.A. Prabowo, I.D.P. Hermida, R.V. Manurung, A. Purwidyantri, K.-C. Liu, Nano- film aluminum-gold for ultra-high dynamic-range surface plasmon resonance chemical sensor, Front. Optoelectron. (2019). https://doi.org/10.1007/s12200-019-0864-y.

[149] B.A. Prabowo, The Trade-Off Performance of Surface Plasmon Resonance Sensing Utilizing Thin Layer Oxide Under the Metal Layer, in: 2019 Int. Conf. Radar, Antenna, Microwave, Electron. Telecommun., 2019. https://doi.org/10.1109/icramet47453.2019.8980455.

[150] V. Kamat, A. Rafique, Designing binding kinetic assay on the bio-layer interferometry (BLI) biosensor to characterize antibody-antigen interactions, Anal. Biochem. 536 (2017) 16–31. https://doi.org/10.1016/j.ab.2017.08.002.

[151] S. Sharma, H. Byrne, R.J. O'Kennedy, Antibodies and antibody-derived analytical biosensors, Essays Biochem. 60 (2016). https://doi.org/10.1042/EBC20150002.

[152] J.M. Stroot, K.M. Leach, P.G. Stroot, D. V. Lim, Capture antibody targeted fluorescence in situ hybridization (CAT-FISH): Dual labeling allows for increased specificity in complex samples, J. Microbiol. Methods. 88 (2012). https://doi.org/10.1016/j.mimet.2011.12.009.

[153] M. Duman, E. Piskin, Detection of Mycobacterium tuberculosis complex and Mycobacterium gordonae on the same portable surface plasmon resonance sensor., Biosens. Bioelectron. 26 (2010) 908–12. https://doi.org/10.1016/j.bios.2010.06.071.

[154] D. Chauhan, Pooja, V. Nirbhaya, C.M. Srivastava, R. Chandra, S. Kumar, Nanostructured transition metal chalcogenide embedded on reduced graphene oxide based highly efficient biosensor for cardiovascular disease detection, Microchem. J. 155 (2020). https://doi.org/10.1016/j.microc.2020.104697.

[155] K. Deng, Y. Xiang, L. Zhang, Q. Chen, W. Fu, An aptamer-based biosensing platform for highly sensitive detection of platelet-derived growth factor via enzyme-mediated direct electrochemistry, Anal. Chim. Acta. 759 (2013) 61–65. https://doi.org/10.1016/j.aca.2012.11.018.

[156] B.P. Xie, G.H. Qiu, P.P. Hu, Z. Liang, Y.M. Liang, B. Sun, L.P. Bai, Z.H. Jiang, J.X. Chen, Simultaneous detection of Dengue and Zika virus RNA sequences with a three-dimensional Cu-based zwitterionic metal–organic framework, comparison of single and synchronous fluorescence analysis, Sensors Actuators, B Chem. 254 (2018) 1133–1140. https://doi.org/10.1016/j.snb.2017.06.085.

[157] M.-C. Sin, S.-H. Chen, Y. Chang, Hemocompatibility of zwitterionic interfaces and membranes, Polym. J. 46 (2014) 436–443.

[158] H. Chen, M. Zhang, J. Yang, C. Zhao, R. Hu, Q. Chen, Y. Chang, J. Zheng, Synthesis and characterization of antifouling poly(N-acryloylaminoethoxyethanol) with ultralow protein adsorption and cell attachment., Langmuir. 30 (2014) 10398–409.

[159] T. Riedel, C. Rodriguez-Emmenegger, A. de los Santos Pereira, A. Bědajánková, P. Jinoch, P.M. Boltovets, E. Brynda, Diagnosis of Epstein-Barr virus infection in clinical serum samples by an SPR biosensor assay., Biosens. Bioelectron. 55 (2014) 278–84.

[160] T. Špringer, J. Homola, Biofunctionalized gold nanoparticles for SPR-biosensor-based detection of CEA in blood plasma, Anal. Bioanal. Chem. 404 (2012) 2869–75. https://doi.org/10.1007/s00216-012-6308-9.

[161] G. Liu, A.S. Gurung, W. Qiu, Lateral flow aptasensor for simultaneous detection of platelet-derived growth factor-BB (PDGF-BB) and thrombin, Molecules. 24 (2019). https://doi.org/10.3390/molecules24040756.

[162] J. Chen, L. Kong, X. Sun, J. Feng, Z. Chen, D. Fan, Q. Wei, Ultrasensitive photoelectrochemical immunosensor of cardiac troponin I detection based on dual inhibition effect of Ag@Cu2O core-shell submicron-particles on CdS QDs sensitized TiO2nanosheets, Biosens. Bioelectron. 117 (2018) 340–346. https://doi.org/10.1016/j.bios.2018.05.037.

[163] O. Averseng, A. Hagège, F. Taran, C. Vidaud, Surface plasmon resonance for rapid screening of uranyl affine proteins, Anal. Chem. 82 (2010) 9797–802. https://doi.org/10.1021/ac102578y.

[164] M.J. Duffy, Biomarkers for prostate cancer: Prostate-specific antigen and beyond, Clin. Chem. Lab. Med. 58 (2020) 326–339. https://doi.org/10.1515/cclm-2019-0693.

[165] V.A. Afrăsânie, M.V. Marinca, T. Alexa-Stratulat, B. Gafton, M. Păduraru, A.M. Adavidoaiei, L. Miron, C. Rusu, KRAS, NRAS, BRAF, HER2 and microsatellite instability in metastatic colorectal cancer-practical implications for the clinician, Radiol. Oncol. 53 (2019) 265–274. https://doi.org/10.2478/raon-2019-0033.

[166] T. Muinao, H.P. Deka Boruah, M. Pal, Multi-biomarker panel signature as the key to diagnosis of ovarian cancer, Heliyon. 5 (2019). https://doi.org/10.1016/j.heliyon.2019.e02826.

[167] S. Gilgunn, P.J. Conroy, R. Saldova, P.M. Rudd, R.J. O'Kennedy, Aberrant PSA glycosylation - A sweet predictor of prostate cancer, Nat. Rev. Urol. 10 (2013) 99–107. https://doi.org/10.1038/nrurol.2012.258.

[168] B.A. Wood, K.P. O'Halloran, S. VandeWoude, Development and validation of a multiplex microsphere-based assay for detection of domestic cat (Felis catus) cytokines, Clin. Vaccine Immunol. 18 (2011) 387–392. https://doi.org/10.1128/CVI.00289-10.

[169] J. Lee, J.Y. Yun, W.C. Lee, S. Choi, J. Lim, H. Jeong, D.-S. Shin, Y.J. Park, A reference electrode-free electrochemical biosensor for detecting MMP-9 using a concentric electrode device, Sensors Actuators B Chem. 240 (2017) 735–741. https://doi.org/10.1016/j.snb.2016.09.026.

[170] S. Mohseni, T.T. Moghadam, B. Dabirmanesh, S. Jabbari, K. Khajeh, Development of a label-free SPR sensor for detection of matrixmetalloproteinase-9 by antibody immobilization on carboxymethyldextran chip, Biosens. Bioelectron. 81 (2016) 510–516.

https://doi.org/10.1016/j.bios.2016.03.038.

[171] G. Ruiz-Vega, A. García-Robaina, M. Ben Ismail, H. Pasamar, T. García-Berrocoso, J. Montaner, M. Zourob, A. Othmane, F.J. del Campo, E. Baldrich, Detection of plasma MMP-9 within minutes. Unveiling some of the clues to develop fast and simple electrochemical magneto-immunosensors, Biosens. Bioelectron. 115 (2018) 45–52. https://doi.org/10.1016/j.bios.2018.05.020.

[172] A. Sankiewicz, L. Romanowicz, M. Pyc, A. Hermanowicz, E. Gorodkiewicz, SPR imaging biosensor for the quantitation of fibronectin concentration in blood samples, J. Pharm. Biomed. Anal. 150 (2018) 1–8. https://doi.org/10.1016/j.jpba.2017.11.070.

[173] A. Biela, M. Watkinson, U.C. Meier, D. Baker, G. Giovannoni, C.R. Becer, S. Krause, Disposable MMP-9 sensor based on the degradation of peptide cross-linked hydrogel films using electrochemical impedance spectroscopy, Biosens. Bioelectron. 68 (2015) 660–667. https://doi.org/10.1016/j.bios.2015.01.060.

[174] A. Pandey, Y. Gurbuz, V. Ozguz, J.H. Niazi, A. Qureshi, Graphene-interfaced electrical biosensor for label-free and sensitive detection of foodborne pathogenic E. coli O157:H7, Biosens. Bioelectron. 91 (2017) 225–231. https://doi.org/10.1016/j.bios.2016.12.041.

[175] X. Liu, C. Ye, X. Li, N. Cui, T. Wu, S. Du, Q. Wei, L. Fu, J. Yin, C. Te Lin, Highly sensitive and selective potassium ion detection based on graphene hall effect biosensors, Materials (Basel). 11 (2018) 1–9. https://doi.org/10.3390/ma11030399.

[176] R. Campos, G. Machado, M.F. Cerqueira, J. Borme, P. Alpuim, Wafer scale fabrication of graphene microelectrode arrays for the detection of DNA hybridization, Microelectron. Eng. 189 (2018) 85–90. https://doi.org/10.1016/j.mee.2017.12.015.

[177] M. Donnelly, D. Mao, J. Park, G. Xu, Graphene field-effect transistors: the road to bioelectronics, J. Phys. D. Appl. Phys. 51 (2018) 493001. https://doi.org/10.1088/1361-6463/aadcca.

[178] I. Rodríguez-Ruiz, A. Llobera, J. Vila-Planas, D.W. Johnson, J. Gómez-morales, J.M. García-ruiz, L.D.E. Cristalográficos, I. Csic, A. De, Analysis of the structural integrity of SU-8 based optofluidic systems for small molecule crystallization studies, Anal. Chem. 85 (2013) 9678–9685. https://doi.org/10.1021/ac402019x.

[179] T. Rodrigues, Assessment of graphene transistors for measurement of stroke relevant biomarker cutoff value, Univerity of Minho, 2019. http://hdl.handle.net/1822/73644.

[180] N. Yogeswaran, W.T. Navaraj, S. Gupta, F. Liu, V. Vinciguerra, L. Lorenzelli, R. Dahiya, Piezoelectric graphene field effect transistor pressure sensors for tactile sensing, Appl. Phys. Lett. 113 (2018). https://doi.org/10.1063/1.5030545.

[181] E. Schilirò, R. Lo Nigro, F. Roccaforte, F. Giannazzo, Recent Advances in Seeded and Seed-Layer-Free Atomic Layer Deposition of High-K Dielectrics on Graphene for Electronics, C — J. Carbon Res. 5 (2019) 53. https://doi.org/10.3390/c5030053.

[182] B. Fallahazad, K. Lee, G. Lian, S. Kim, C.M. Corbet, D.A. Ferrer, L. Colombo, E. Tutuc, Scaling of Al 2 O 3 dielectric for graphene field-effect transistors, Appl. Phys. Lett. 100 (2012) 093112. https://doi.org/10.1063/1.3689785.

[183] T. Kobayashi, M. Bando, N. Kimura, K. Shimizu, K. Kadono, N. Umezu, K. Miyahara, S. Hayazaki, S. Nagai, Y. Mizuguchi, Y. Murakami, D. Hobara, Production of a 100-m-long high-quality graphene transparent conductive film by roll-to-roll chemical vapor deposition and transfer process, Appl. Phys. Lett. 102 (2013) 023112. https://doi.org/10.1063/1.4776707.

[184] P.A. De Carvalho Gomes, Optimization of Graphene Deposition Conditions by Chemical Vapour Deposition: Impact of Temperature, IST-Técnico, Lisbon University, 2017. https://fenix.tecnico.ulisboa.pt/cursos/meft/dissertacao/1691203502343037.

[185] K. Yambe, N. Kuramoto, Y. Inagaki, Dependence of plasma current on object condition in atmospheric pressure non-thermal equilibrium argon plasma, AIP Adv. 9 (2019) 085202. https://doi.org/10.1063/1.5116268.

[186] M.R. Tesauro, G. Roche, In-Situ Measurement of the Relative Thermal Contributions of Chemical Reactions and Ions During Plasma Etching M.R. Tesauro, ECS Trans. 13 (2008) 3–15. https://doi.org/10.1149/1.3035362.

[187] N. Moldovan, R. Divan, H. Zeng, J.A. Carlisle, Nanofabrication of sharp diamond tips by e-beam lithography and inductively coupled plasma reactive ion etching, J. Vac. Sci. Technol. B Microelectron. Nanom. Struct. 27 (2009) 3125. https://doi.org/10.1116/1.3263174.

[188] A.S. da Silva Sobrinho, M. Latrèche, G. Czeremuszkin, J.E. Klemberg-Sapieha, M.R. Wertheimer, Transparent barrier coatings on polyethylene terephthalate by single- and dual-frequency plasma-enhanced chemical vapor deposition, J. Vac. Sci. Technol. A Vacuum, Surfaces, Film. 16 (1998) 3190–3198. https://doi.org/10.1116/1.581519.

[189] W. Huang, X. Wang, M. Sheng, L. Xu, F. Stubhan, L. Luo, T. Feng, X. Wang, F. Zhang, S. Zou, Low temperature PECVD SiNx films applied in OLED packaging, Mater. Sci. Eng. B. 98 (2003) 248–254. https://doi.org/10.1016/S0921-5107(03)00045-X.

[190] X. Sun, P. Cheng, H. Wang, H. Xu, L. Dang, Z. Liu, Z. Lei, Activation of graphene aerogel with phosphoric acid for enhanced electrocapacitive performance, Carbon N. Y. 92 (2015) 1–10. https://doi.org/10.1016/j.carbon.2015.02.052.

[191] J. Valle, D. Fernandez, J. Madrenas, Experimental Analysis of Vapor HF Etch Rate and Its Wafer Level Uniformity on a CMOS-MEMS Process, J. Microelectromechanical Syst. 25 (2016) 401–412. https://doi.org/10.1109/JMEMS.2016.2533267.

[192] H.C. Lee, H. Bong, M.S. Yoo, M. Jo, K. Cho, Copper-Vapor-Assisted Growth and Defect-Healing of Graphene on Copper Surfaces, Small. 14 (2018) 1801181. https://doi.org/10.1002/smll.201801181.

[193] A. Ferreira, J. Viana-Gomes, J. Nilsson, E.R. Mucciolo, N.M.R. Peres, A.H. Castro Neto, Unified description of the dc conductivity of monolayer and bilayer graphene at finite densities based on resonant scatterers, Phys. Rev. B. 83 (2011) 165402. https://doi.org/10.1103/PhysRevB.83.165402.

[194] M. Pumera, Graphene in biosensing, Mater. Today. 14 (2011) 308–315. https://doi.org/10.1016/S1369-7021(11)70160-2.

[195] Y. Song, Y. Luo, C. Zhu, H. Li, D. Du, Y. Lin, Recent advances in electrochemical biosensors based on graphene two-dimensional nanomaterials, Biosens. Bioelectron. 76 (2016) 195–212. https://doi.org/10.1016/J.BIOS.2015.07.002.

[196] Y.Y. Wang, P.J. Burke, Polyelectrolyte multilayer electrostatic gating of graphene field-effect transistors, Nano Res. 7 (2014) 1650–1658. https://doi.org/10.1007/s12274-014-0525-9.

[197] X. Ren, H. Ma, T. Zhang, Y. Zhang, T. Yan, B. Du, Q. Wei, Sulfur-Doped Graphene-Based Immunological Biosensing Platform for Multianalysis of Cancer Biomarkers, ACS Appl. Mater. Interfaces. 9 (2017) 37637–37644. https://doi.org/10.1021/acsami.7b13416.

[198] F. Perreault, A. Fonseca de Faria, M. Elimelech, Environmental applications of graphene-based nanomaterials, Chem. Soc. Rev. 44 (2015) 5861–5896. https://doi.org/10.1039/C5CS00021A.

[199] S. Viswanathan, T.N. Narayanan, K. Aran, K.D. Fink, J. Paredes, P.M. Ajayan, S. Filipek, P. Miszta, H.C. Tekin, F. Inci, U. Demirci, P. Li, K.I. Bolotin, D. Liepmann, V. Renugopalakrishanan, Graphene–protein field effect biosensors: glucose sensing, Mater. Today. 18 (2015) 513–522. https://doi.org/10.1016/j.mattod.2015.04.003.

[200] D.Y. Petrovykh, H. Kimura-Suda, A. Opdahl, L.J. Richter, M.J. Tarlov, L.J. Whitman, Alkanethiols on Platinum: Multicomponent Self-Assembled Monolayers, Langmuir. 22 (2006) 2578–2587. https://doi.org/10.1021/la050928a.

[201] K.P. Fears, D.Y. Petrovykh, S.J. Photiadis, T.D. Clark, Circular Dichroism Analysis of Cyclic beta-Helical Peptides Adsorbed on Planar Fused Quartz, Langmuir. 29 (2013) 10095–10101.

https://doi.org/10.1021/la401544c.

[202] K.P. Fears, D.Y. Petrovykh, T.D. Clark, Evaluating protocols and analytical methods for peptide adsorption experiments, Biointerphases. 8 (2013) 1–15. https://doi.org/10.1186/1559-4106-8-20.

[203] D.Y. Petrovykh, H. Kimura-Suda, M.J. Tarlov, L.J. Whitman, Quantitative Characterization of DNA Films by X-ray Photoelectron Spectroscopy, Langmuir. 20 (2004) 429–440. https://doi.org/10.1021/la034944o.

[204] M. Cao, A. Fu, Z. Wang, J. Liu, N. Kong, X. Zong, H. Liu, J.J. Gooding, Electrochemical and Theoretical Study of π–π Stacking Interactions between Graphitic Surfaces and Pyrene Derivatives, J. Phys. Chem. C. 118 (2014) 2650–2659. https://doi.org/10.1021/jp411979x.

[205] E. Delamarche, G. Sundarababu, H. Biebuyck, B. Michel, C. Gerber, H. Sigrist, H. Wolf, H. Ringsdorf, N. Xanthopoulos, H.J. Mathieu, Immobilization of Antibodies on a Photoactive Self-Assembled Monolayer on Gold, Langmuir. 12 (1996) 1997–2006. https://doi.org/10.1021/la950836t.

[206] L. Jiang, A. Glidle, A. Griffith, C.J. McNeil, J.M. Cooper, Characterising the formation of a bioelectrochemical interface at a self-assembled monolayer using X-ray photoelectron spectroscopy, Bioelectrochemistry Bioenerg. 42 (1997) 15–23. https://doi.org/10.1016/S0302-4598(96)05173-2.

[207] N.D. Bassim, W.J. Dressick, K.P. Fears, R.M. Stroud, T.D. Clark, D.Y. Petrovykh, Layer-by-layer assembly of heterogeneous modular nanocomposites, J. Phys. Chem. C. 116 (2012) 1694–1701. https://doi.org/10.1021/jp207912b.

[208] W.J. Dressick, K.J. Wahl, N.D. Bassim, R.M. Stroud, D.Y. Petrovykh, Divalent-anion salt effects in polyelectrolyte multilayer depositions, Langmuir. 28 (2012) 15831–15843. https://doi.org/10.1021/la3033176.

[209] K.P. Fears, Measuring the p K /p I of Biomolecules Using X-ray Photoelectron Spectroscopy, Anal. Chem. 86 (2014) 8526–8529. https://doi.org/10.1021/ac5020386.

[210] E.H. Lock, D.Y. Petrovykh, P. Mack, T. Carney, R.G. White, S.G. Walton, R.F. Fernsler, Surface composition, chemistry, and structure of polystyrene modified by electron-beam-generated plasma, Langmuir. 26 (2010) 8857–8868. https://doi.org/10.1021/la9046337.

[211] K.P. Fears, T.D. Clark, D.Y. Petrovykh, Residue-dependent adsorption of model oligopeptides on gold, J. Am. Chem. Soc. 135 (2013) 15040–15052. https://doi.org/10.1021/ja404346p.

[212] S. Pullano, C. Critello, I. Mahbub, N. Tasneem, S. Shamsir, S. Islam, M. Greco, A. Fiorillo, EGFET-Based Sensors for Bioanalytical Applications: A Review, Sensors. 18 (2018) 4042. https://doi.org/10.3390/s18114042.

[213] S. Cherré, E. Fernandes, J. Germano, T. Dias, S. Cardoso, M.S. Piedade, N. Rozlosnik, M.I. Oliveira, P.P. Freitas, Rapid and specific detection of cell-derived microvesicles using a magnetoresistive biochip, Analyst. 142 (2017) 979–986. https://doi.org/10.1039/c6an02651f.

[214] E. Fernandes, V.C.C. Martins, C. Nóbrega, C.M.M. Carvalho, F.A.A. Cardoso, S. Cardoso, J. Dias, D. Deng, L.D.D. Kluskens, P.P.P. Freitas, J. Azeredo, A bacteriophage detection tool for viability assessment of Salmonella cells, Biosens. Bioelectron. 52 (2014) 239–246. https://doi.org/10.1016/J.BIOS.2013.08.053.

[215] P. Gong, C.-Y. Lee, L.J. Gamble, D.G. Castner, D.W. Grainger, Hybridization behavior of mixed DNA/alkylthiol monolayers on gold: characterization by surface plasmon resonance and 32P radiometric assay., Anal. Chem. 78 (2006) 3326–34. https://doi.org/10.1021/ac052138b.

[216] V.C. Martins, F.A. Cardoso, J. Germano, S. Cardoso, L. Sousa, M. Piedade, P.P. Freitas, L.P. Fonseca, Femtomolar limit of detection with a magnetoresistive biochip., Biosens. Bioelectron. 24 (2009) 2690–5. https://doi.org/10.1016/j.bios.2009.01.040.

[217] C.-Y. Lee, L.J. Gamble, D.W. Grainger, D.G. Castner, Mixed DNA/oligo (ethylene glycol)

functionalized gold surfaces improve DNA hybridization in complex media, Biointerphases. 1 (2006) 82–92. https://doi.org/10.1116/1.2219110.

[218] X. Huang, Q. Bai, J. Hu, D. Hou, A practical model of quartz crystal microbalance in actual applications, Sensors (Switzerland). 17 (2017) 1–9. https://doi.org/10.3390/s17081785.

[219] N.C.S.S. Vieira, J. Borme, G. Machado, F. Cerqueira, P.P. Freitas, V. Zucolotto, N.M.R.R. Peres, P. Alpuim, G.M. Jr, F. Cerqueira, P.P. Freitas, V. Zucolotto, Graphene field-effect transistor array with integrated electrolytic gates scaled to 200 mm, J. Phys. Condens. Matter. 28 (2016) 11–17. https://doi.org/10.1088/0953-8984/28/8/085302.

[220] E. Fernandes, T. Sobrino, V.C. Martins, I. Lopez-loureiro, F. Campos, J. Germano, M. Rodríguez-Pérez, S. Cardoso, D.Y. Petrovykh, J. Castillo, P.P. Freitas, Point-of-care quantification of serum cellular fibronectin levels for stratification of ischemic stroke patients, Nanomedicine Nanotechnology, Biol. Med. 30 (2020) 102287. https://doi.org/10.1016/j.nano.2020.102287.

[221] D.A. Armbruster, T. Pry, Limit of blank, limit of detection and limit of quantitation., Clin. Biochem. Rev. 29 Suppl 1 (2008) S49-52. http://www.ncbi.nlm.nih.gov/pubmed/18852857%0Ahttp://www.pubmedcentral.nih.gov/articlerender.fcgi?artid=PMC2556583.

[222] D. Yang, R. Kroe-Barrett, S. Singh, T. Laue, IgG Charge: Practical and Biological Implications, Antibodies. 8 (2019) 24. https://doi.org/10.3390/antib8010024.

[223] A. Jaiswal, A. Chhabra, U. Malhotra, S. Kohli, V. Rani, Comparative analysis of human matrix metalloproteinases: Emerging therapeutic targets in diseases., Bioinformation. 6 (2011) 23–30. https://doi.org/10.6026/97320630006023.

[224] B.J. Boughton, A.W. Simpson, The Biochemical and Functional Heterogeneity of Circulating Human Plasma Fibronectin, Ekp. 119 (1984) 1174–1180. https://www.sciencedirect.com/science/article/abs/pii/0006291X84908994?via%3Dihub.

[225] O.C. Schultheiss, S.J. Stanton, Assessment of Salivary Hormones A Primer on Concepts and Measurement Issues in Behavioral Endocrinology, Methods Soc. Neurosci. (2009).

[226] S. Angeloni, R. Cordes, S. Dunbar, C. Garcia, G. Gibson, C. Martin, V. Stone, xMAP Cookbook, 2nd ed., Luminex, 2014.

[227] J. Choi, T.W. Seong, M. Jeun, K.H. Lee, Field-Effect Biosensors for On-Site Detection: Recent Advances and Promising Targets, Adv. Healthc. Mater. 6 (2017) 1700796. https://doi.org/10.1002/adhm.201700796.

[228] S. Park, M. Kim, D. Kim, S.H. Kang, K.H. Lee, Y. Jeong, Interfacial charge regulation of protein blocking layers in transistor biosensor for direct measurement in serum, Biosens. Bioelectron. 147 (2020) 111737. https://doi.org/10.1016/j.bios.2019.111737.

[229] C.H. Chu, I. Sarangadharan, A. Regmi, Y.W. Chen, C.P. Hsu, W.H. Chang, G.Y. Lee, J.I. Chyi, C.C. Chen, S.C. Shiesh, G. Bin Lee, Y.L. Wang, Beyond the Debye length in high ionic strength solution: Direct protein detection with field-effect transistors (FETs) in human serum, Sci. Rep. 7 (2017) 1–15. https://doi.org/10.1038/s41598-017-05426-6.

[230] I. Sarangadharan, S.-W. Huang, W.-C. Kuo, P.-H. Chen, Y.-L. Wang, Rapid detection of NT-proBNP from whole blood using FET based biosensors for homecare, Sensors Actuators B Chem. 285 (2019) 209–215. https://doi.org/10.1016/J.SNB.2019.01.066.

[231] R. Hidi, Multiplex Immunoassays in Clinical Bioanalysis: The Promise and Challenges to Implementation in Clinical Development, Life Sci. | Tech. Bull. (2010) 4.

[232] S. Mansouri Majd, A. Salimi, B. Astinchap, Label-free attomolar detection of lactate based on radio frequency sputtered of nickel oxide thin film field effect transistor, Biosens. Bioelectron. 92 (2017) 733–740. https://doi.org/10.1016/j.bios.2016.09.097.

[233] Y. Chen, R. Ren, H. Pu, J. Chang, S. Mao, J. Chen, Field-effect transistor biosensors with two-dimensional black phosphorus nanosheets, Biosens. Bioelectron. 89 (2017) 505–510.

https://doi.org/10.1016/j.bios.2016.03.059.

[234] S. Liu, Y. Zhao, J.W. Parks, D.W. Deamer, A.R. Hawkins, H. Schmidt, Correlated electrical and optical analysis of single nanoparticles and biomolecules on a nanopore-gated optofluidic chip, Nano Lett. 14 (2014) 4816–4820. https://doi.org/10.1021/nl502400x.

[235] J. Tkac, J.J. Davis, An optimised electrode pre-treatment for SAM formation on polycrystalline gold, J. Electroanal. Chem. 621 (2008) 117–120. https://doi.org/10.1016/j.jelechem.2008.04.010.

[236] W.S. To, K.S. Midwood, Plasma and cellular fibronectin: Distinct and independent functions during tissue repair, Fibrogenes. Tissue Repair. 4 (2011) 1–17. https://doi.org/10.1186/1755-1536-4-21.

[237] G.F. Fasciglione, S. Marini, S. D'Alessio, V. Politi, M. Coletta, pH- and temperature-dependence of functional modulation in metalloproteinases. A comparison between neutrophil collagenase and gelatinases A and B, Biophys. J. 79 (2000) 2138–2149. https://doi.org/10.1016/S0006-3495(00)76461-7.

[238] M. V. Pugachev, A.I. Duleba, A.A. Galiullin, A.Y. Kuntsevich, Micromask Lithography for Cheap and Fast 2D Materials Microstructures Fabrication, Micromachines. 12 (2021) 850. https://doi.org/10.3390/mi12080850.

[239] X. Huang, Q. Bai, J. Hu, D. Hou, A Practical Model of Quartz Crystal Microbalance in Actual Applications, Sensors. 17 (2017) 1785. https://doi.org/10.3390/s17081785.

1. Appendix I – Microfabrication of EG-GFETs

1.1. Previous layouts

After the initial proof-of-concept measurements showed in [42], a new generation of EG-GFETs was required to provide enough devices for biosensor development. An initial proposal, here referred to as Wafer 3, was made to use an SU-8 like passivation to reduce fabrication time and allow passivation of the source and drain contacts. The proposed design is presented in Figure Ap1.

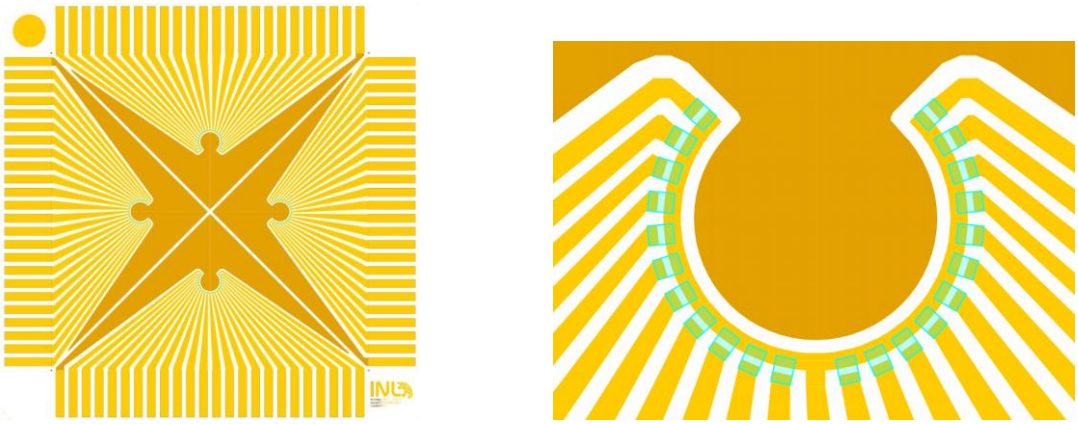

(A) (B)

Figure Ap1. *Proposed layout for Wafer 3. (A) Design for 1 chip with contacts available on the four sides, to allow multiple use. Each die has 20×20 mm. (B) Close-up on the graphene channels, showing a common source electrode and 22 individual drain electrodes.*

After contacts fabrication and graphene transfer, an epoxy similar to SU-8 was used for passivation, DWL1x that allowed to passivate the contacts with a 1 µm thick layer, leaving only the graphene channels, gate electrode, and connection pads uncovered. Tests with old layouts were performed to ensure adhesion of the passivation to the chip surface and its endurance to cleaning (with ethyl acetate), as shown in Figure Ap2. As only slight changes were observed after the cleaning step, it was considered that the passivation should be stable enough for the process.

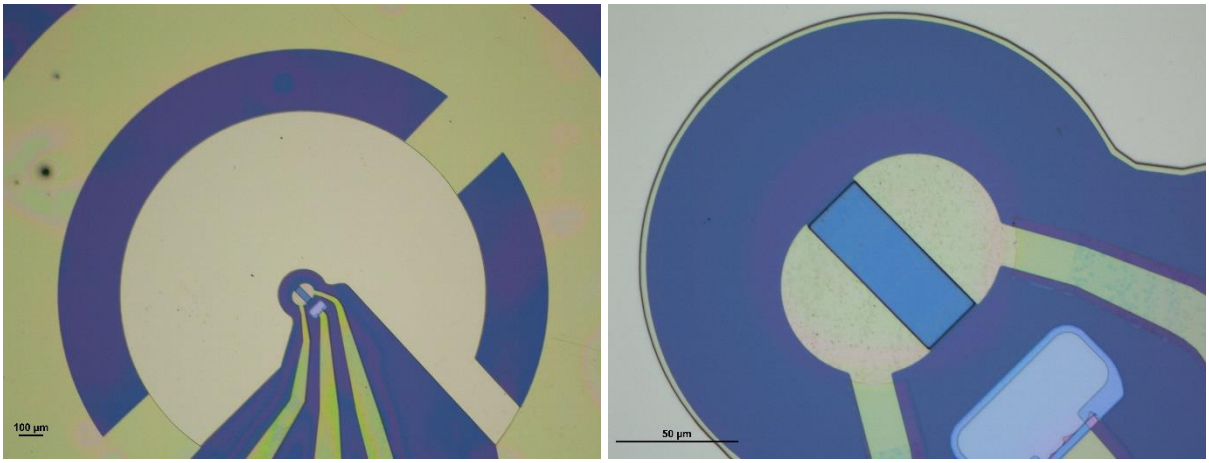

(A) (B)

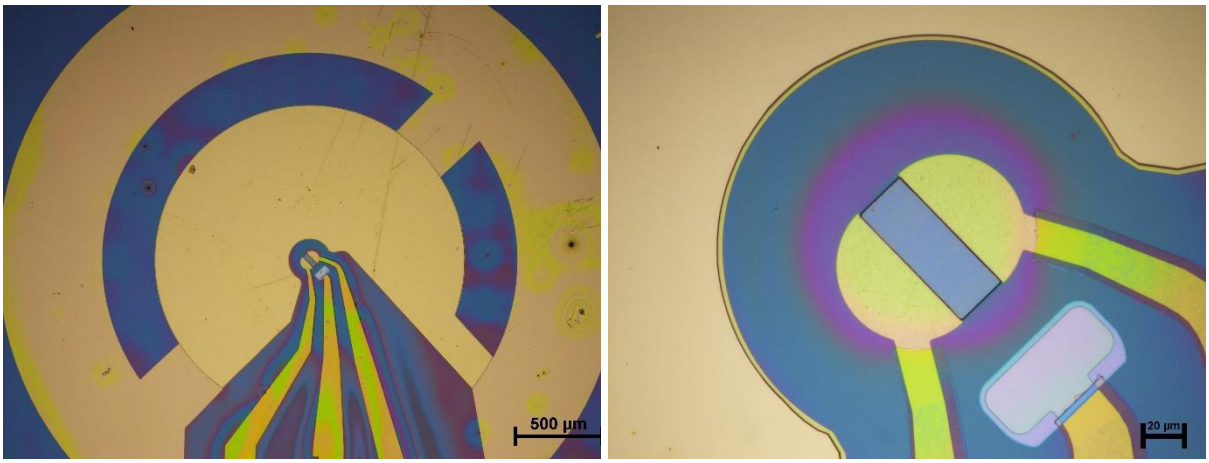

(C) (D)

Figure Ap2. *Initial testing for passivation using DWL 1x. After exposure by optical lithography and development a well-defined structure was observed, with the gate electrode (A) and graphene channel (B) exposed. After immersion of the sample in ethyl acetate for 2 h (cleaning step) the passivation seems to be slightly attacked, with infiltration of the solvent through the mask borders.*

Application of this process to Wafer 3, resulted in a homogeneous passivation as shown in Figure Ap3. However, as it is also possible to observe the gate electrode surface obtained is not clean, with a great amount of graphene transfer-related residues on top. This can be a limitation in the application of the fabricated devices as biosensors due to random adsorption events as discussed in chapter IV.

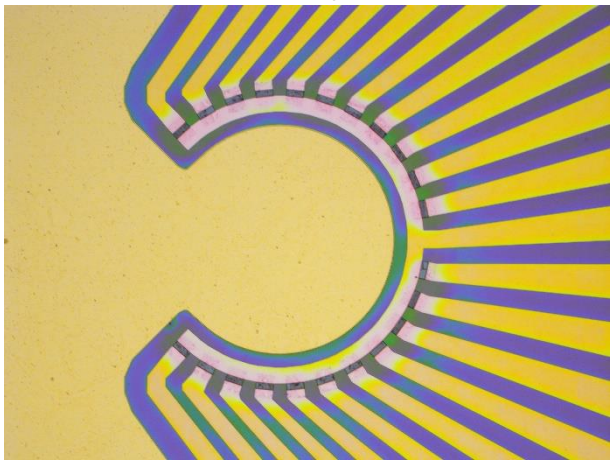

(A)

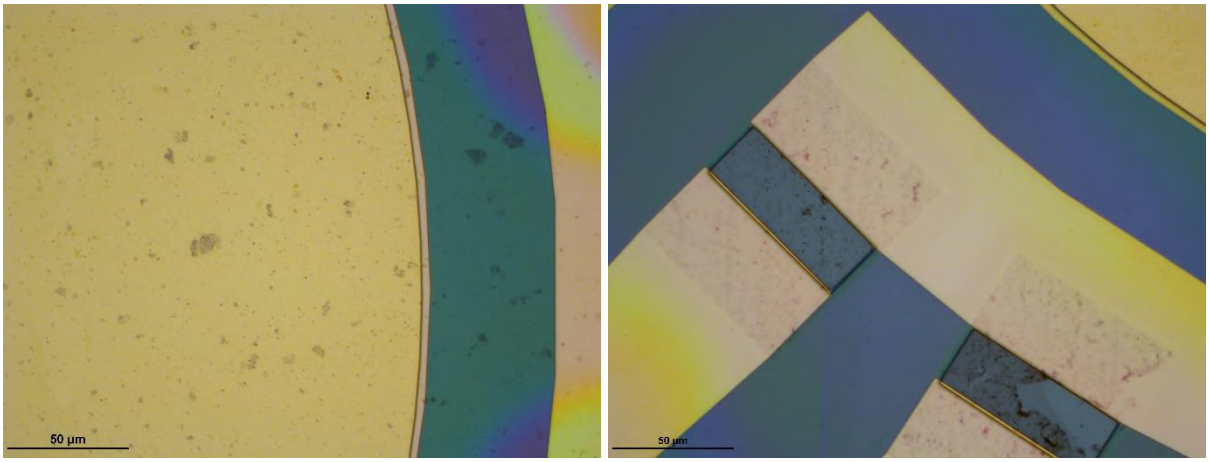

(B) (C)

Figure Ap3. Wafer 3 after full process, showing a homogeneous passivation with DWL 1x (A) with the expected overlapping at the gate electrode (B) and only a slight misalignment at the graphene channels (C).

Still the devices were tested for acquisition of transistor transfer curves, and signal stability studies. Simultaneous acquisition of the transfer curves of the 22 EG-GFETs was performed using an in-lab customized platform, as seen in Figure Ap4A, which applies a fixed source-drain current (I_{SD}) through and ADC and a variable gate-source voltage (V_{GS}) through a DAC microcontroller. The current and voltage are applied to the EG-GFETs as a series as defined by matrix connectors, and the correspondent source-drain voltage (V_{SD}) is the output signal. A schematic of the platform concept is shown in Figure Ap4B. The transfer curves acquired showed excellent homogeneity in terms of the voltage of the minimum conductivity point (V_{CNP}), as shown in Figure Ap4C.

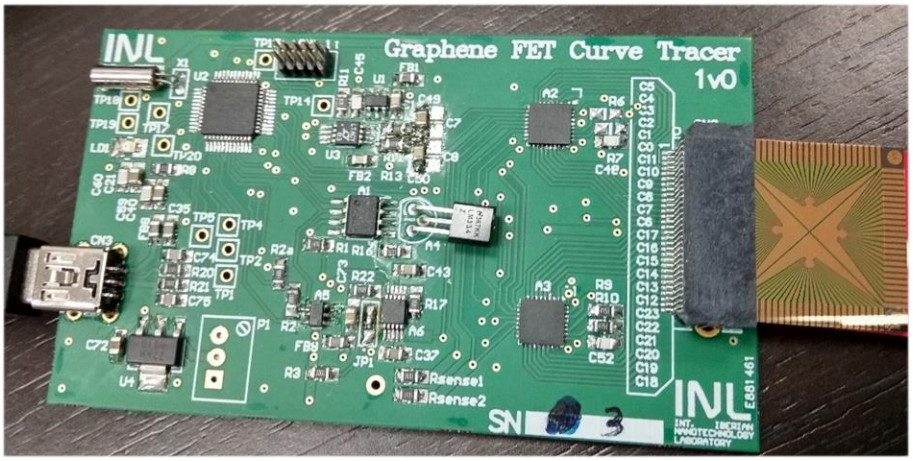

(A)

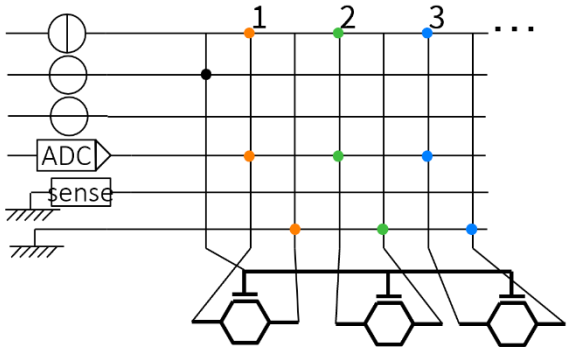

(B)

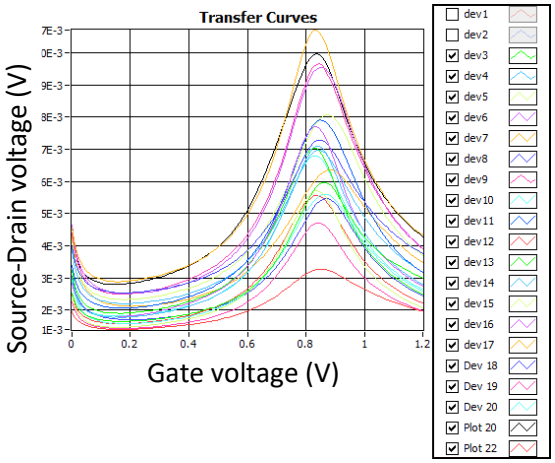

(C)

Figure Ap4. *System for multiple acquisition of EG-GFET transfer curves. (A) Photograph of the first model of the platform with a chip from Wafer 3 inserted for measurements. (B) Schematic of the principle of operation of the FET Curve Tracer platform. (C) Example of transfer curves as taken from the software*

built to work with the acquisition platform, showing 20 out of 22 EG-GFETs working, with very similar position of V_{CNP}.

For stability studies, the minimum conductivity point voltage (V_{CNP}) was extracted overtime to evaluate signal changes, as this is the intended signal for the biosensing studies. Figure Ap5 shows the overtime variation of V_{CNP} using a standard acquisition or a pulse-modulated acquisition. The standard mode applied a gate voltage value followed by the next, while the pulsed modulation implied a drop to zero gate voltage between each step of the gate voltage sweep. With this pulsed mode it is expected to reduce charge trapping in the channels, reducing drift of the signal. Indeed, the signal acquired in this mode (Figure Ap5, right side) shows reduced drift and faster stabilization of the signal. This also showed the importance of grounding the contacts of the EG-GFETs for some time between measurements to reduce charge trapping effects that destabilize the devices.

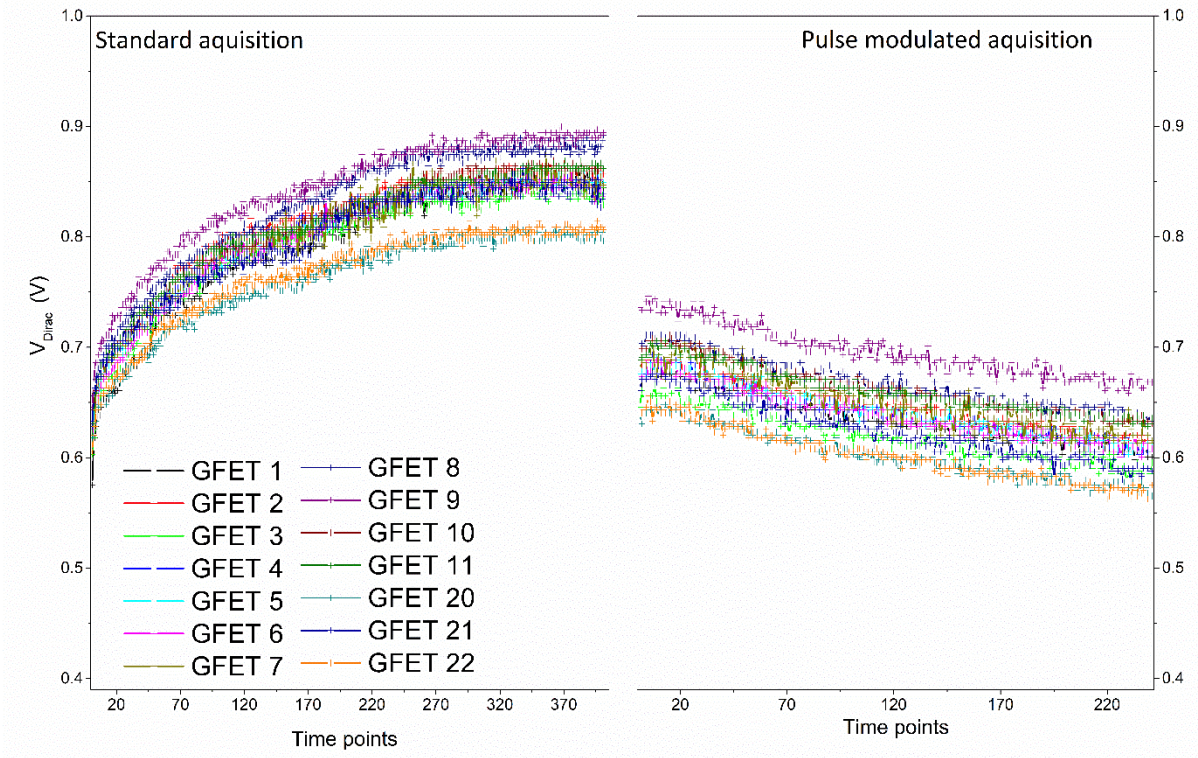

(A)

Figure Ap5. *Overtime variation of V_{CNP} of 22 EG-GFETs (chip 3.5, side 3), using a standard acquisition of the transfer curves (left side) or a pulse-modulated acquisition (right side).*

After determining the signal acquisition conditions, devices from wafer 3 were used for functionalization and bio detection studies, however with many limitations. The first limitation encountered was related with the functionalization with PBSE. As shown in Figure Ap6B, after exposure to DMF (the solvent used for PBSE) the borders of the passivation are attacked, and Raman spectroscopy reveals the appearance of a photoluminescence band (PL band, Figure Ap6C, blue spectra) indicating residues from the passivation might have deposited over the graphene channel.

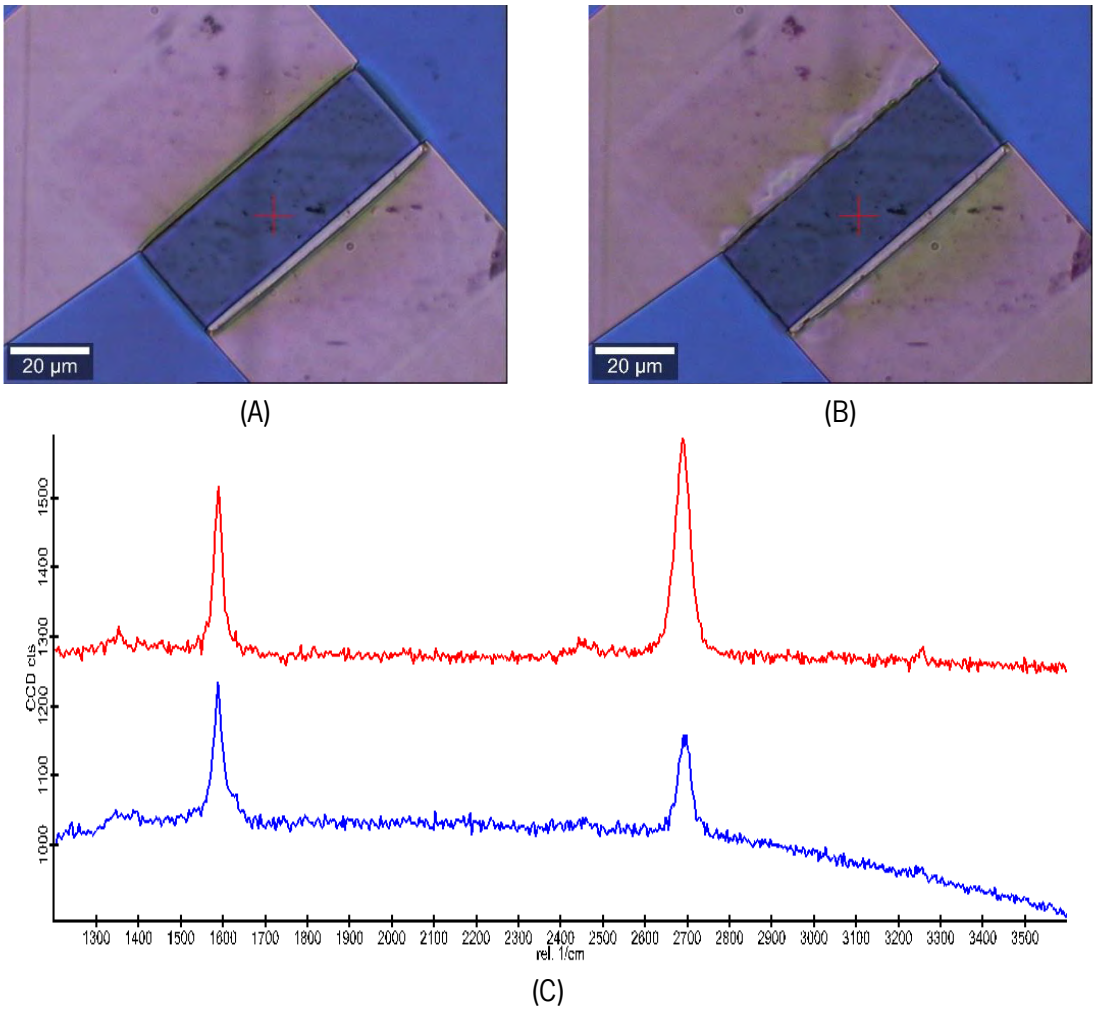

Figure Ap6. *Effects of DMF exposure on DWL 1x passivation. (A) Transistor channel as fabricated. (B) The same channel after 2h exposure to DMF, showing degradation of the passivation borders. (C) Raman spectra of the channel before (red) and after (blue) exposure to DMF.*

As a result, alternatives for PBSE preparation were sought. A range of solvents were tested, but most of them were non-compatible for PBSE dissolution (e.g., IPA, Benzene, Hexane, Ethanol). Ethyl acetate worked as a solvent but evaporated too fast, not allowing for the optimized 2h incubation. As such, it was proposed to use one of the milder solvents (ethanol) mixed with DMF, to reduce the content of DMF, but still allow dissolution of PBSE. Tests were performed with a mixture of 7% DMF and 93% ethanol for PBSE preparation. A sample like that of Figure Ap6 was tested, and this time no damage was observed in the passivation.

Functionalization studies in samples analyzed by XPS and QCM, however, showed limitations in this approach. Figure Ap7A,B shows the XPS N1s spectra obtained in a graphene sample before and after functionalization with PBSE prepared in the mixture 7%/93% of DMF and ethanol, respectively. Using the fitting parameters and equation (1) it is possible to have an approximate estimation of the amount of PBSE on the analyzed surface, which for the analyzed samples resulted in an estimated value between 3 to 5 × 10^{14} molecules per cm^2. When comparing this with the footprint of the molecule, which would expectedly provide a binding density around 10^{13} molecules per cm^2, it is expected that part of the signal from PBSE comes from aggregated molecules instead of singular molecules in the surface. Additionally,

when functionalizing a QCM crystal (after graphene transfer) with PBSE prepared in pure DMF or the mixture (Figure Ap7C), a clear difference is observed in antibodies immobilization, indicative that the solvent is not as stable as expected and is hindering the functionalization process.

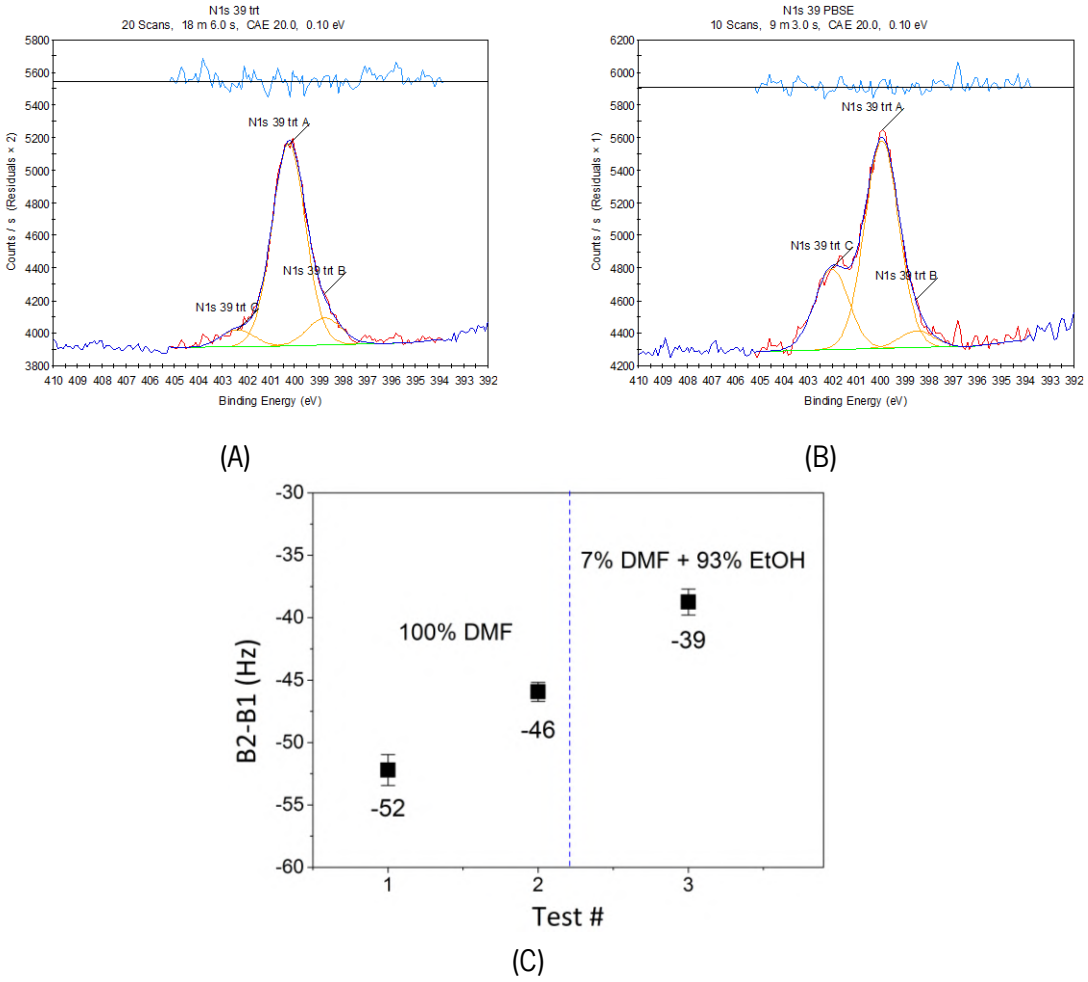

Figure Ap7. Analysis of the effect of the use of 7% DMF and 93% ethanol mixture as a solvent for PBSE. (A) XPS spectra of the N1s range of the graphene surface before functionalization, showing the characteristic peak from the SiO_2N_x substrate. (B) XPS spectra of the N1s range of the graphene surface after functionalization showing the higher energy peak associated with the N of the NHS-ester group of PBSE. (C) Frequency shifts of QCM crystals after antibody immobilization in surfaces functionalized with PBSE prepared in DMF and the mixture of 7% DMF and 93% ethanol.

$$n_s = \left(\frac{I_{element}}{I_{metal}} . \frac{\sigma_{element}}{\sigma_{metal}}\right)\left(\frac{T_{metal}}{T_{element}} . L^Q_{metal} . N^Q_{metal}\right) \qquad (1)$$

Considering this, the passivation for the final layout was chosen to be resistant to strong solvents to avoid the mentioned limitations.

1.2. Fabrication of the Dielectric Passivation Layer

1.2.1. Combined Reactive Ion Etching and Wet Etch Strategy

In order to test the possibility of using combined dry and wet etch for the patterning of the hard passivation (SiO_2 and SiN_x based) layer as the final step of the fabrication, two test wafers were prepared to measure the dry and wet etch rates of the passivation layer, as follows: Si wafers are coated, using PECVD, with 90 nm of SiO_2 and 50 nm of SiN_x on Test Wafer #1, and 120 nm of SiO_2 and 50 nm of SiN_x on Test Wafer #2. For thickness estimation with interferometer, millimeter-sized patterns were patterned by optical lithography, as exemplified in the mask on Figure Ap8A. After RIE on Test Wafer #1, it was observed that all SiO2 had been etched away, contrary to the intended purpose. As such, the results bellow are referent to Test Wafer #2. Figure Ap8B shows the wafer after RIE. After extraction of the thickness values of SiO_2 (Table Ap1), the wafer was exposed to KOH 1 M at 45 °C for 1h, but an etch rate equivalent to that of room temperature was achieved, being to slow for our process (5 ± 0.95 nm/h). To improve the etch rate, the wafer was cut into small samples which were immersed in KOH 1M at 60 °C for different times (examples of samples in Figure Ap8C). The SiO_2 thickness measured in the interferometer showed it was possible to remove all SiO_2 within a reasonable amount of time. The interferometer values allowed then to extract the estimated etched thickness, which is presented in Chapter IV.

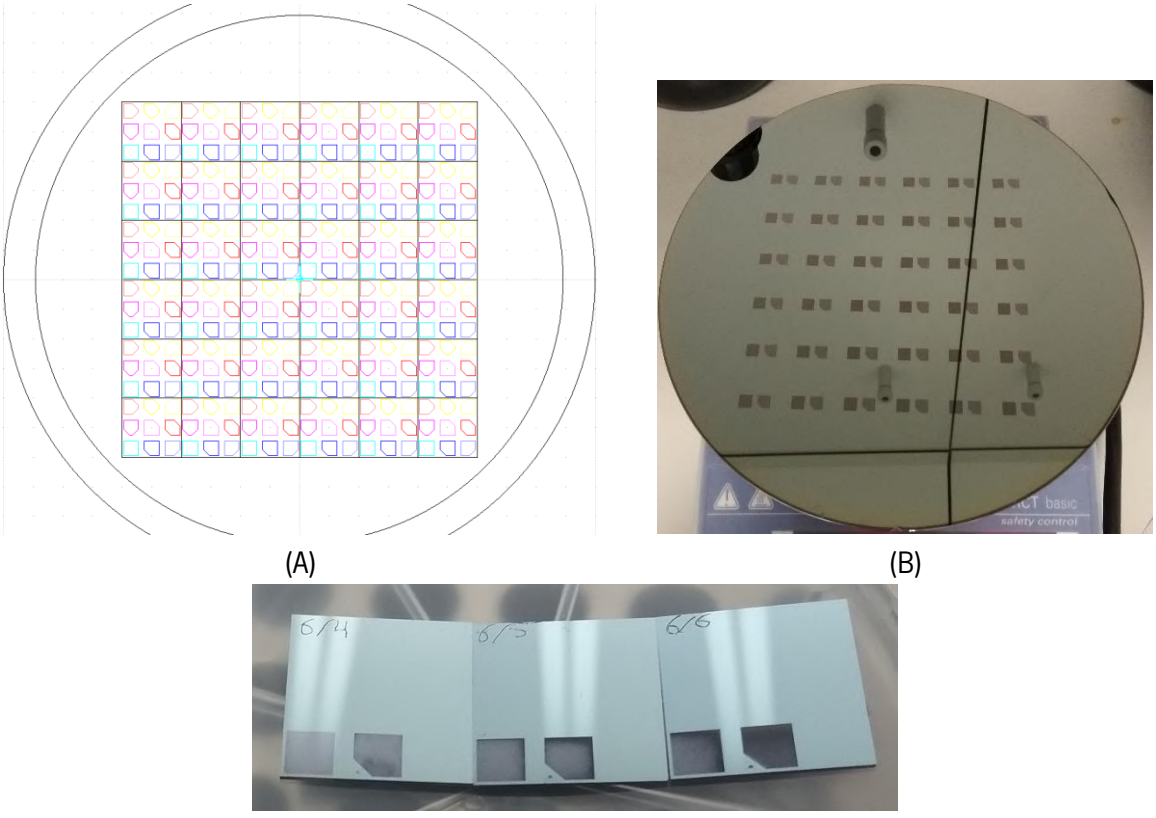

Figure Ap8. *Etch rate test wafers and samples. (A) Mask for millimeter-sized patterns for the Test Wafers, to allow measurements in the interferometer. (B) Test Wafer #2 after RIE for 30 s (25 + 5 s). (C) Three samples from Test Wafer #2 before exposure to KOH 1M at 60 °C.*

Table Ap1. *Measured SiO_2 thickness in the millimeter-sized features after each etching step tested.*

After RIE (25 + 5 s)						KOH 45ºC (1h)						KOH 60ºC					
C1	C2	C3	C4	C5	C6	C1	C2	C3	C4	C5	C6	C1	C2	C3	C4	C5	C6

L6	29.9	35.1	39.5	41.2	40.4	38.6	26.8	30.7	33.9	35.1	34.4	32.8				0	0	0
																1h	2h	3h
L4	33	41.1	47.1	48.4			28.7	36.1	42.1	42.7	40.2	34.9	19.1	20.1	14.9			
													15min	30min	45min			

1.2.2. Stopping Layer-Assisted Reactive Ion Etching of Dielectric Passivation

To perform patterning of the stopping layer by lift-off, a strategy was optimized to avoid the use of ultrasonication that would damage graphene. It was proposed to perform a pre-development of the photoresist before exposure in optical lithography to harden the top layer of the photoresist. Figure Ap9 shows a sample after exposure and development using different exposure parameters (Energy and CD bias) to correct for size variations arising from the hardened photoresist. It was recommended to increase the energy of the laser to be able to go through the hardened photoresist. Values of +15%, +20% and +25% of energy (in reference to the standard value for AZ1505) with no clear difference in terms of exposure quality. As such, the intermediate value of +20% of energy was kept for further testing. Variation of the CD bias showed that without this correction, the features had a ~0.5 µm increase in size when compared to the layout size (4.5 µm). Positive bias correction increased even more the size (Figure Ap9D), but the use of a negative correction bias (-600) reduced the feature size in ~0.5 µm. This was indicative that the CD bias value should be within 0 to -600. As such exposure was performed with -300 correction to provide feature sizes closer to the designed layouts.

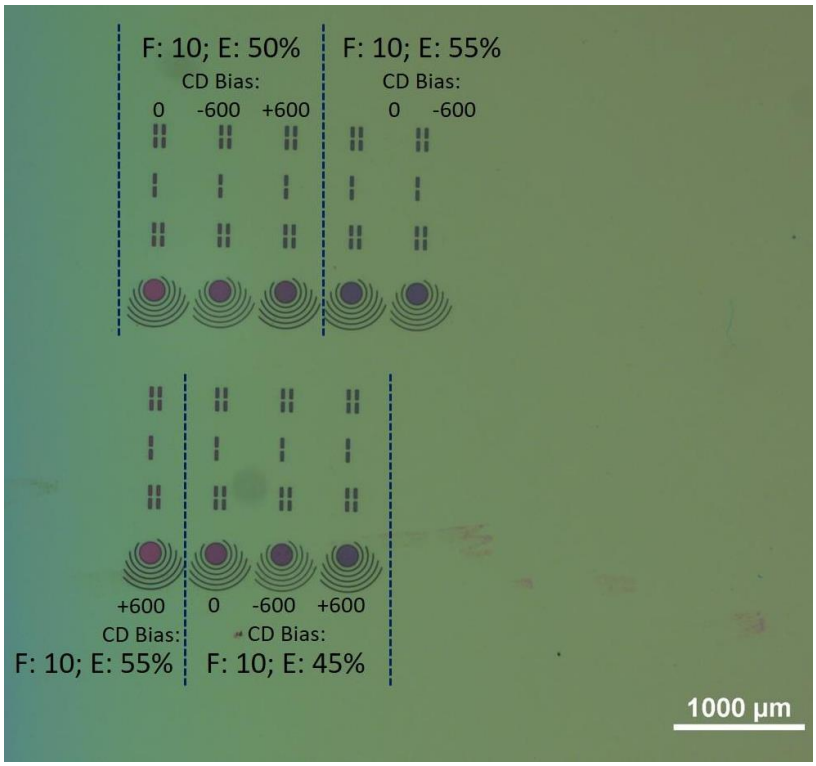

(A)

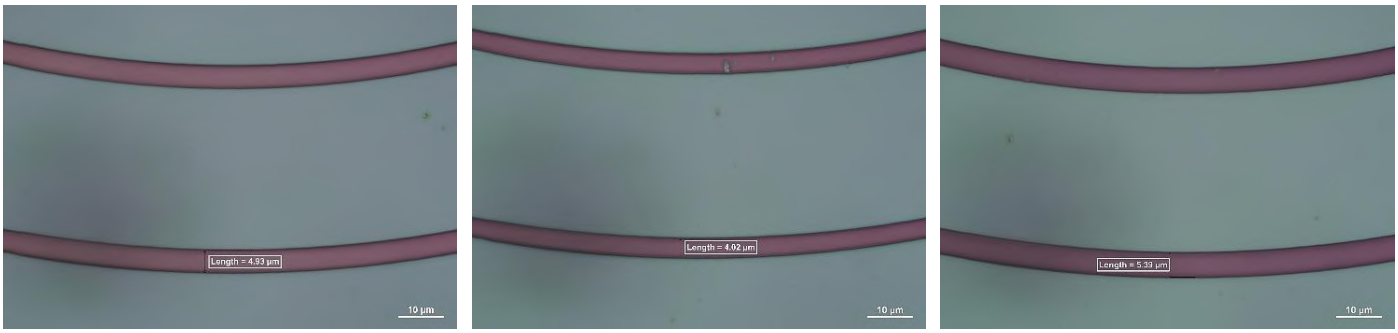

(B) (C) (D)

Figure Ap9. *Test sample after exposure and development of AZ1505 using the soaking methodology. (A) Full sample showing the different parameters used for laser exposure. (B) Feature size using CD Bias of 0, is 4.93 µm. (C) Feature size using CD Bias of -600, is 4.02 µm. (D) Feature size using CD Bias of +600, is 5.39 µm.*

Using the optimized parameters, devices were prepared for the stopping layer patterning. Figure Ap10 shows the sample after lithography and development, and after patterning by lift-off without ultrasonication. After lithography and development, the features have the expected size (Figure Ap10B), and SEM imaging (after metal sputtering) shows the typical mushroom-hat like borders of the photoresist (Figure Ap10C, D). After immersion and rinsing with acetone, well-defined features were obtained (Figure Ap10F), showing that this is a suitable strategy for the patterning of layers by lift-off using milder conditions.

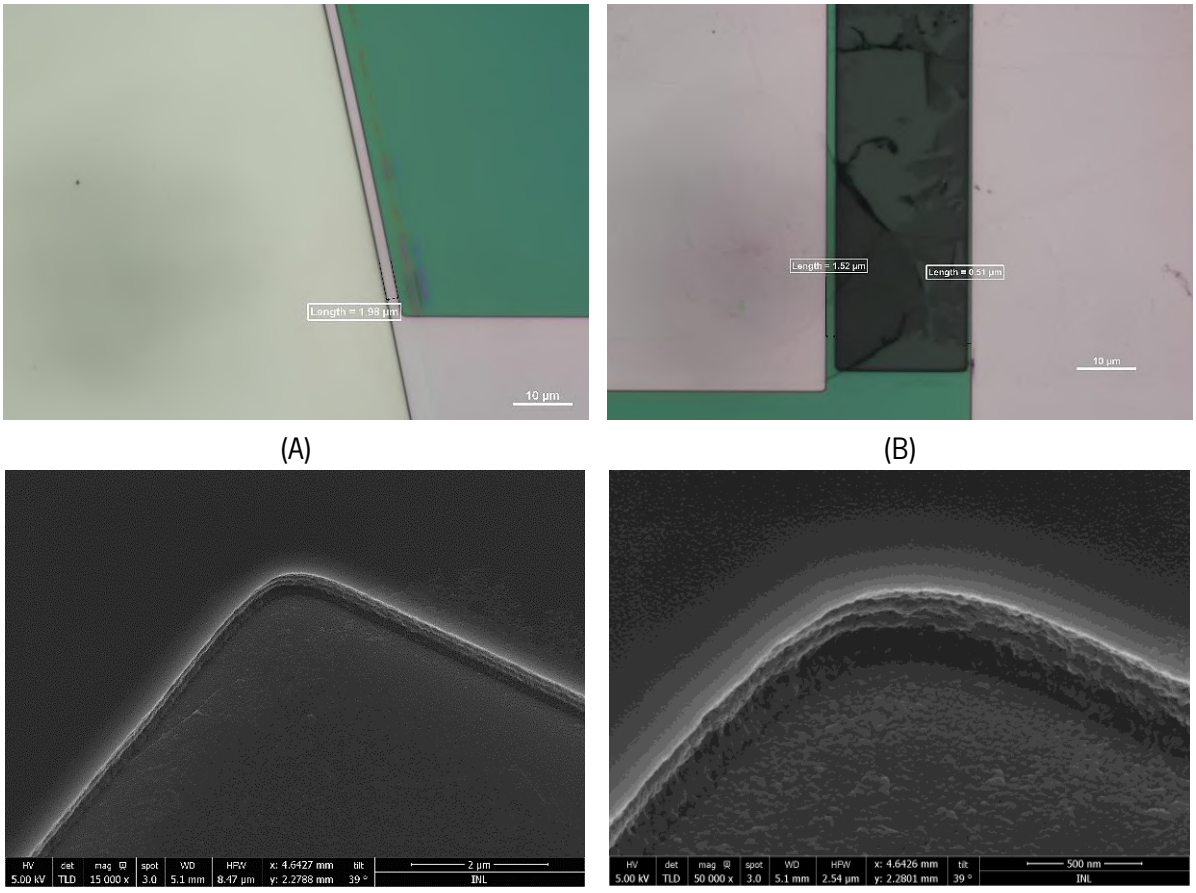

(A) (B)

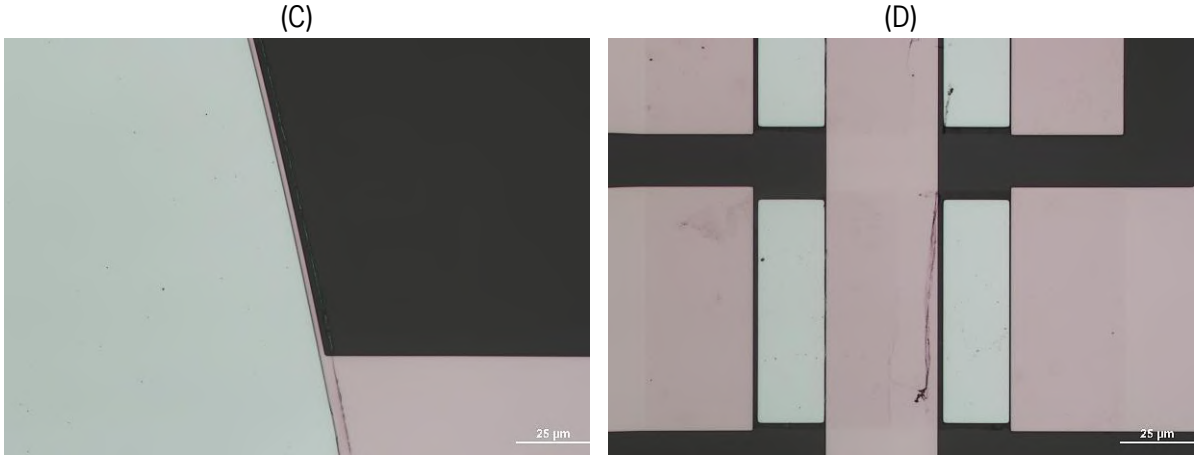

Figure Ap10. Optical microscopy photographs of an EG-GFET chip for preparation of the stopping layer. After optical lithography and development with optimized parameters the sample shows features with the expected size (A, B). After sputtering of the stopping layer materials, SEM was used to check the characteristic features of the photoresist using the soak method (C, D). After immersion in acetone and rinsing with a acetone wash bottle, a well-defined stopping layer is achieved (E, F).

1.3. Case Study: Fabrication at 200 mm Wafer Scale of Graphene Electrolyte Gated FETs

Wafer A layout:

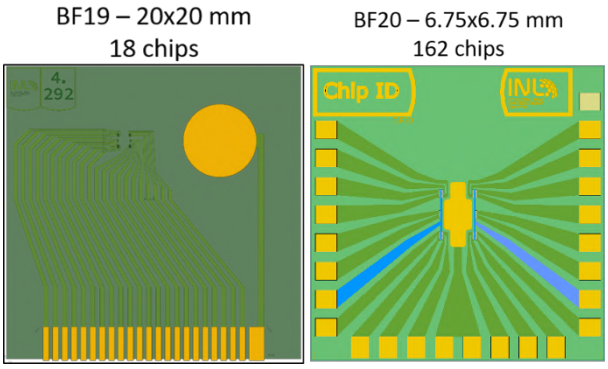

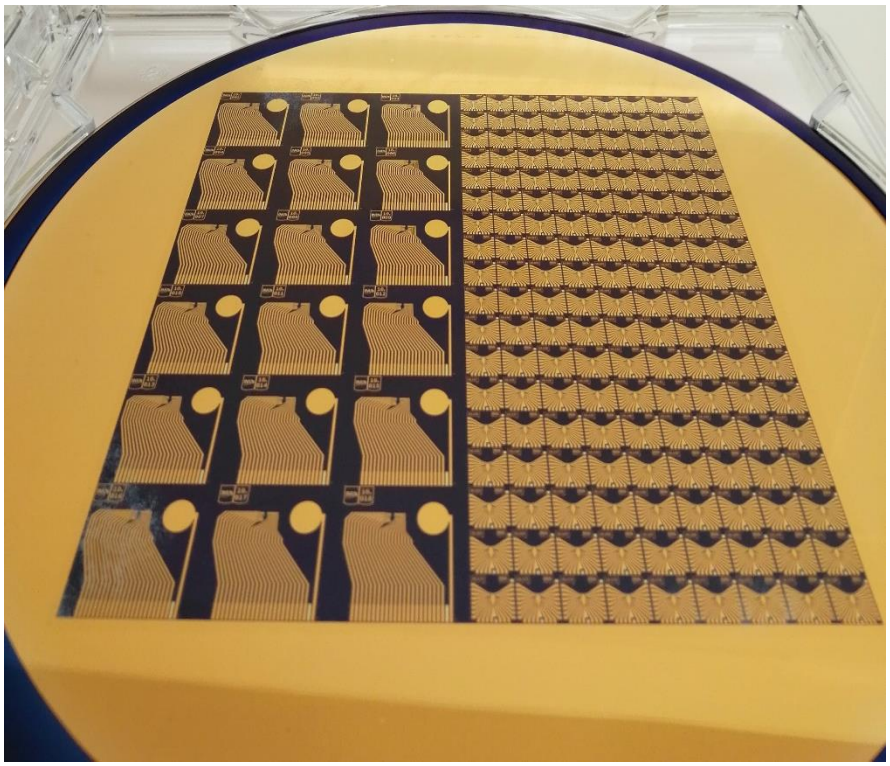

Figure Ap11. *Proposed chip layouts for Wafer A (top), distributed to occupy half of the wafer area with each proposal (bottom). The BF19 layout was designed for assays with biosensing occurring at the gate electrode, for comparison with the effects of biosensing at the graphene channel (BF20).*

2. Appendix II – Graphene functionalization

2.1. Binding of specific biomarkers – complementary calculations

Binding efficiency was estimated using QCM frequency shifts after specific binding of MMP9 and c-Fn each circulating at 3 µg/ml.

First the total protein in circulation is estimated considering the protein molecular weight.

MMP9

V_{Total} = 1 ml; W_{MMP9} = 3×10^{-6} g

MW_{MMP9} = 92 kDa = 92000 g/mol

N_A = 6.022×10^{23} mol^{-1}

$n = \frac{W_{MMP9}}{MW_{MMP9}} = \frac{3\times10^{-6}}{92000} = 3.26 \times 10^{-11}\ mol$

$N = n \times N_A = 19.64 \times 10^{12}$ MMP9 molecules

c-Fn

V_{Total} = 1 ml; W_{MMP9} = 3×10^{-6} g

MW_{MMP9} = 550 kDa = 550000 g/mol

N_A = 6.022×10^{23} mol^{-1}

$n = \frac{W_{MMP9}}{MW_{MMP9}} = \frac{3\times10^{-6}}{550000} = 5.45 \times 10^{-12}\ mol$

$N = n \times N_A = 3.28 \times 10^{12}$ c-Fn molecules

The estimation of amount of circulating protein, shows that for the same concentration there is 6x more MMP9 in circulation than c-Fn. This can lead to decreased binding in the c-Fn specific surface due to the reduced chance of the protein reaching the surface. Indeed, this is reflected in the QCM frequency shift. The frequency shifts can therefore be used to estimate the amount of bound protein to extract the binding efficiency.

MMP9

$\Delta m = -C_{QCM} \times \Delta f$; C_{QCM} = 17.7 $ng.cm^{-2}.Hz^{-1}$ [239]

(QCM crystal area ~ 1 cm^2)

Δm ~ 506.22 ng ⟶ N_{bound} = 2.85×10^{12} MMP9 molecules immobilized (considering molecular hydration correction of 14% [8])

$Binding\ Efficiency\ = \frac{N_{bound}}{N_{total}} \times 100 = 14.5\ \%$

c-Fn

$\Delta m = -C_{QCM} \times \Delta f$; C_{QCM} = 17.7 $ng.cm^{-2}.Hz^{-1}$ [239]

(QCM crystal area ~ 1 cm^2)

Δm ~ 200.19 ng ⟶ N_{bound} = 1.90×10^{11} MMP9 molecules immobilized (considering molecular hydration correction of 14% [8])

$Binding\ Efficiency\ = \frac{N_{bound}}{N_{total}} \times 100 = 5.8\ \%$

As expected, reducing the amount of circulating protein also reduced the binding efficiency although not linearly, as the 6x decrease in protein (from MMP9 to c-Fn) only reflected a 2.5x decrease in the binding efficiency. To understand better the mechanisms behind these differences a study using different concentrations of the same protein could be performed, however it was not the focus of the presented work.

3. Appendix III – Baseline measurements with multi-channel acquisition system for EG-GFETs

3.1. LoB and LoD according to [221]:

The limit-of-blank (LoB) is the highest apparent analyte concentration expected to be found when replicates of a blank sample containing no analyte are tested.
The limit-of-detection (LoD) is the lowest analyte concentration likely to be reliably distinguished from the LoB. LoD is determined by utilizing both the measured LoB and test replicates of a sample known to contain a low concentration of analyte.

$$LoB = mean_{blank} + 1.645(SD_{blank}) \quad \text{(Eq. 1)}$$

$$LoD = LoB + 1.645(SD_{low\ concentration\ sample}) \quad \text{(Eq. 2)}$$

3.2. Signal stabilization

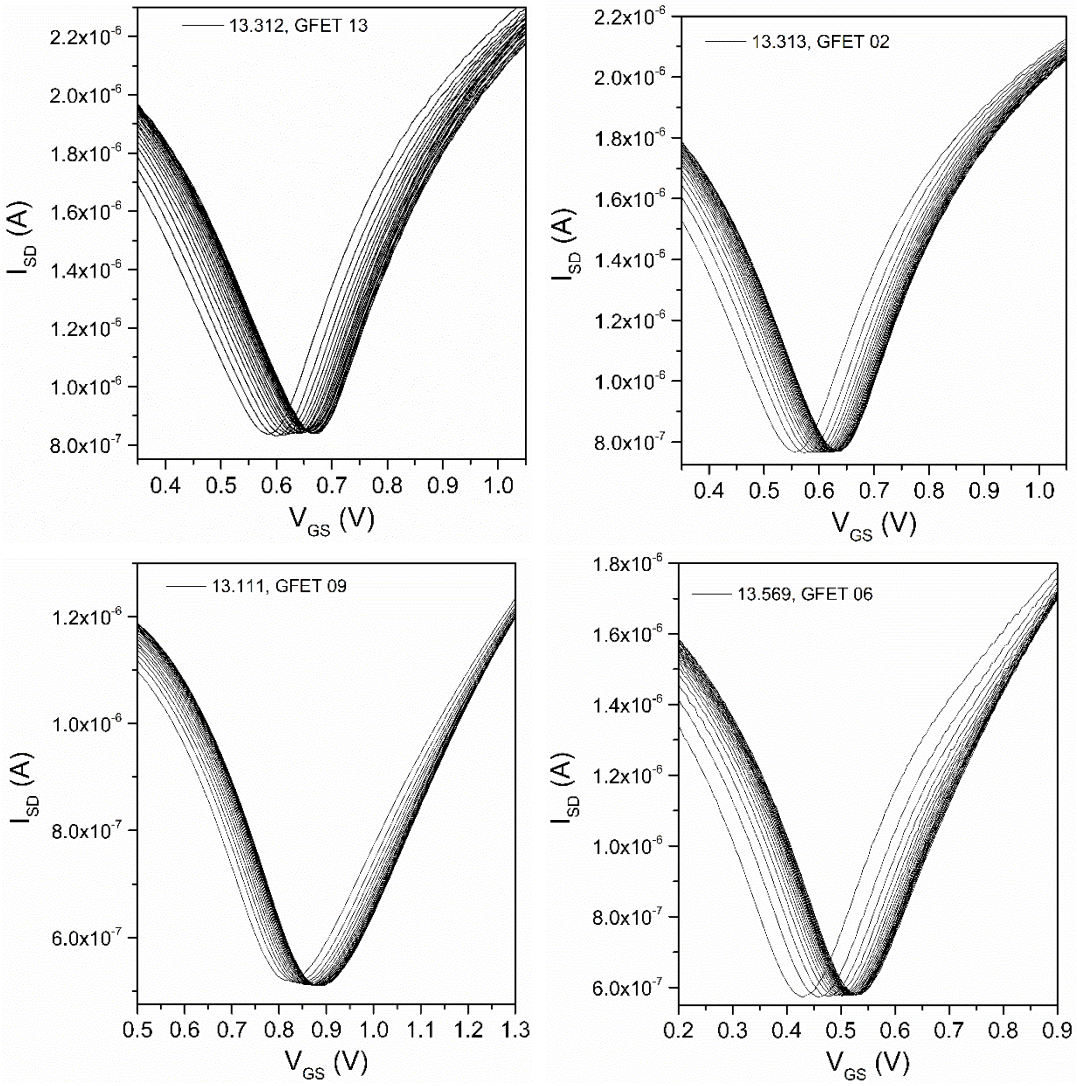

Figure Ap12. *Transfer curves in representative devices showing drift and stabilization of the signal over the 20 acquisitions performed after each surface modification/ detection step.*

3.3. BSA detection in graphene and gold

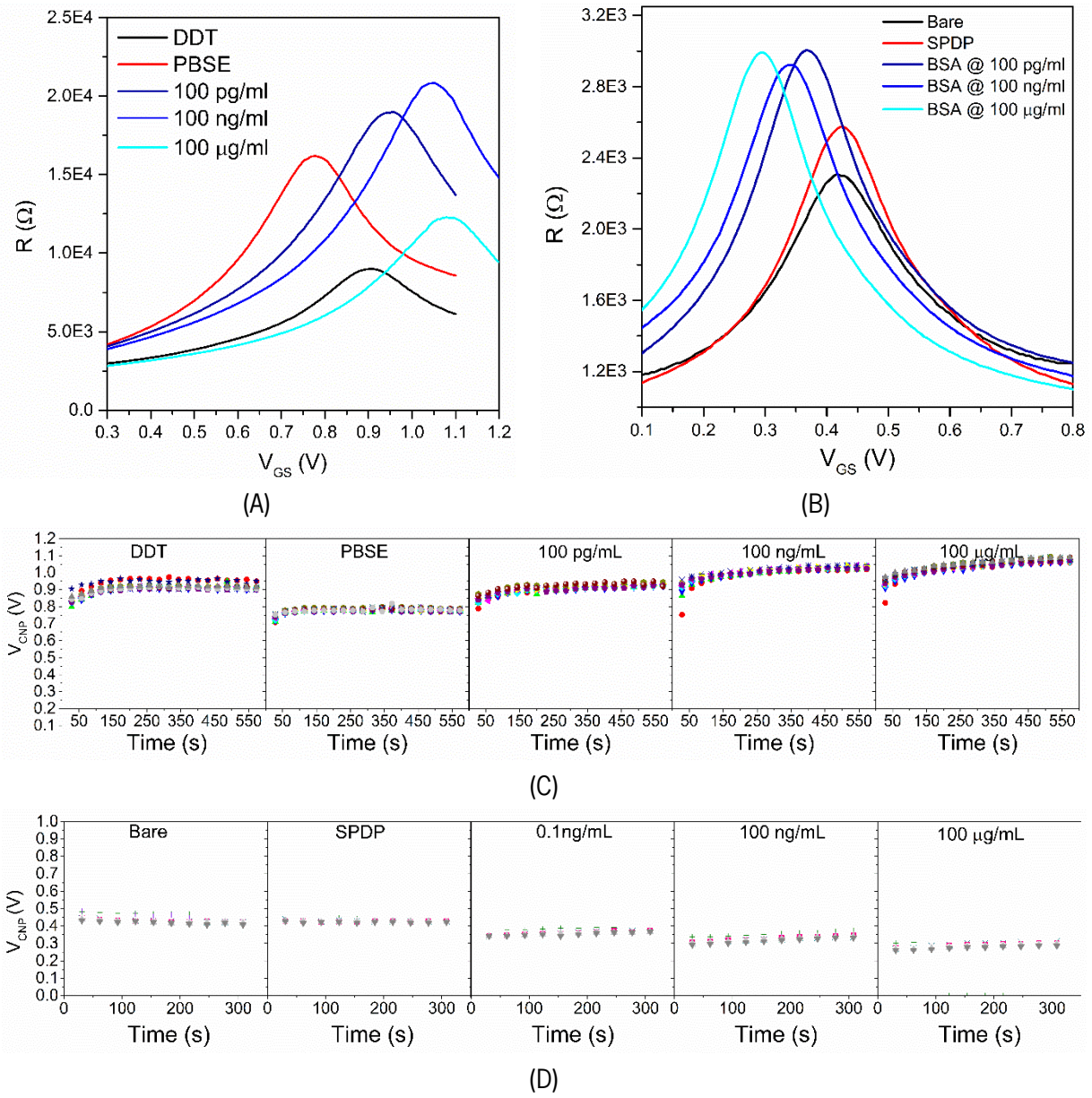

Figure Ap13. *Transfer curves and overtime acquisition of V_{CNP} after chemical functionalization and exposure to BSA. (A) Last transfer curve of each 20-loops measured after passivation of gold (black line), functionalization of graphene with PBSE (red line) and exposure to BSA at 100 pg/ml, 100 ng/ml and 100 µg/ml (blue lines). (B) Last transfer curve of each 20-loops measured after functionalization of gold with Sulfo-LC-SPDP (red line) and exposure to BSA at 100 pg/ml, 100 ng/ml and 100 µg/ml (blue lines). (C) Extracted V_{CNP} for each working EG-GFET at each transfer curve measurement (20 measures), after each step of functionalization and detection on graphene channels (BF20 model). (D) Extracted V_{CNP} for*

each working EG-GFET at each transfer curve measurement (20 measures), after each step of functionalization and detection on the gate electrode (BF19 model).

3.4. Standard response of EG-GFETs to functionalization

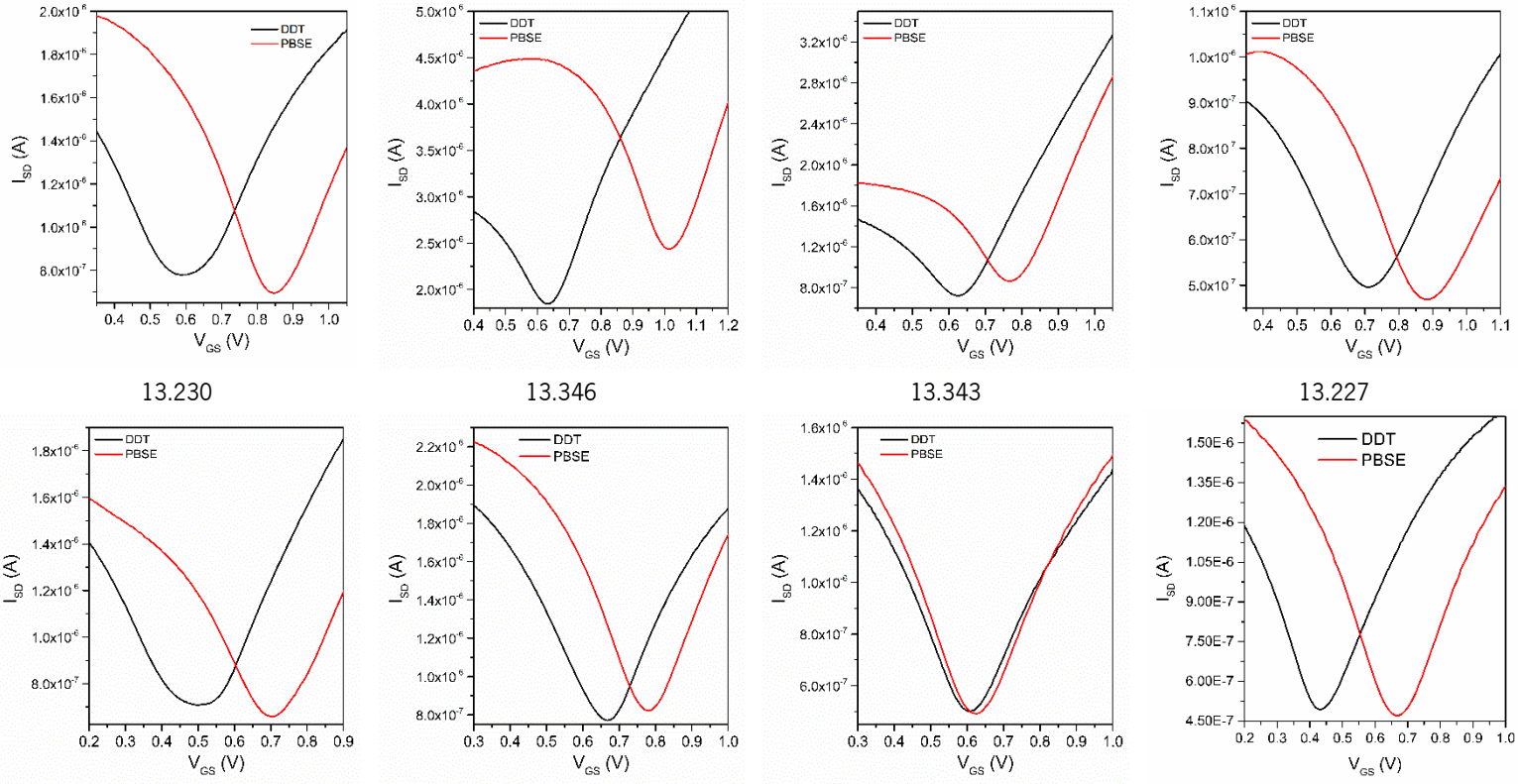

13.230 13.346 13.343 13.227

13.235 13.312 13.598 13.765

Figure Ap14. *Transfer curves in representative devices showing the consistent positive shift of V_{CNP} after chemical functionalization of graphene with PBSE (red curves), when compared with bare graphene (black curves).*

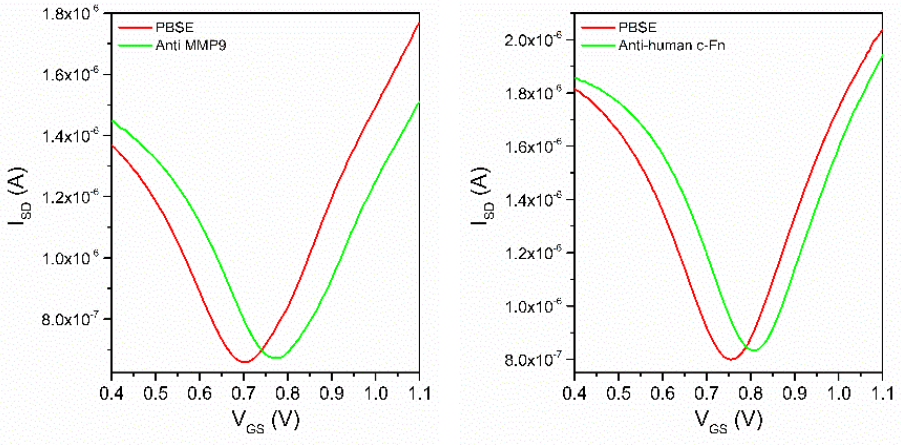

13.235 13.236

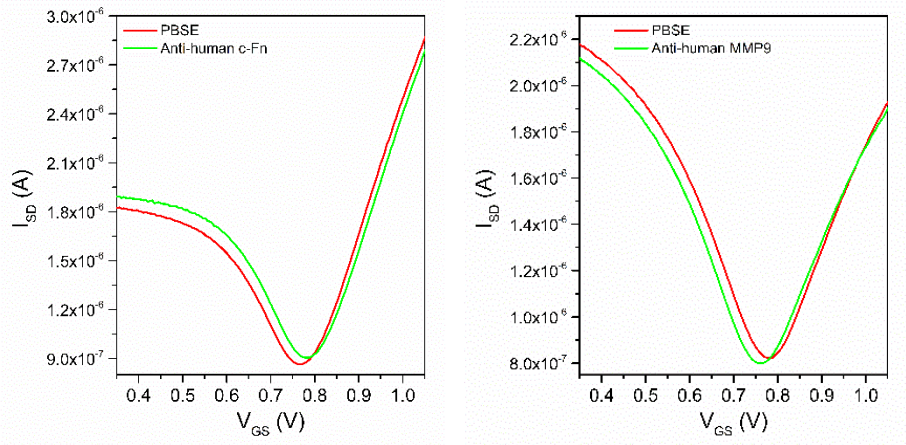

13.343 13.312

Figure Ap15. *Transfer curves in representative devices showing a non-consistent minor shift of V_{CNP} after antibody immobilization (green curves) on the PBSE-modified graphene (red curves). The direction and intensity of the shift does not seem to be related with the use of Anti-human MMP9 or Anti-human c-Fn.*

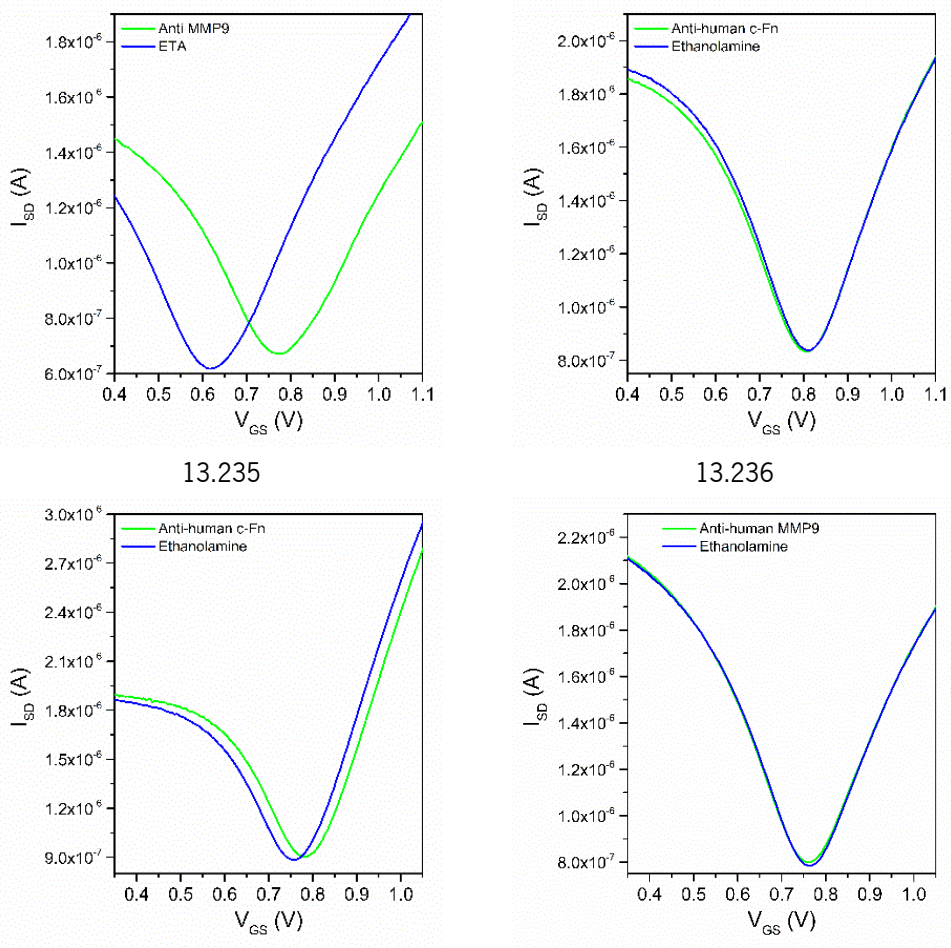

13.235 13.236

13.343 13.312

Figure Ap16. *Transfer curves in representative devices showing a negative shift of V_{CNP} after blocking with ethanolamine (blue curves) on the PBSE + Antibody modified graphene (green curves). The shift is generally negative, but some situations exhibit no V_{CNP} shift. The shift intensity is not consistent between samples, even in the same assay (e.g., 13.235 and 13.236).*

4. Appendix IV – Biological Matrix Effects

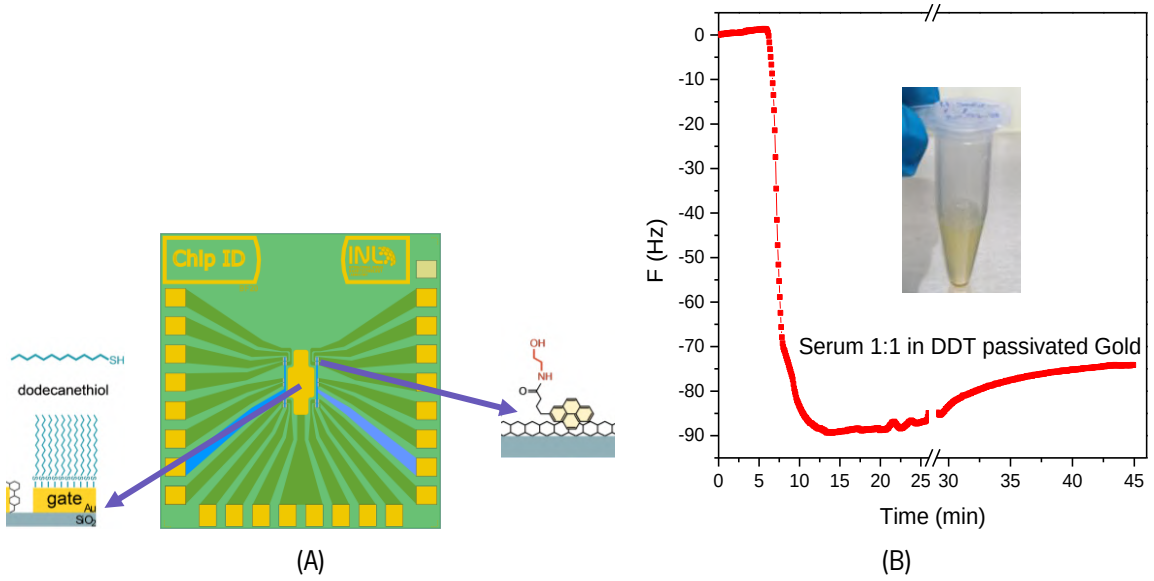

Figure Ap17. *Effects of exposure of human blood serum to passivated graphene and gold surfaces. (A) Schematic of EG-GFETs surfaces and respective functionalization applied for initial testing with human serum (both surfaces passivated). (B) Frequency shift in real-time during exposure of a gold QCM crystal blocked with DDT, to undiluted human serum.*

4.1. EG-GFETs transfer curves

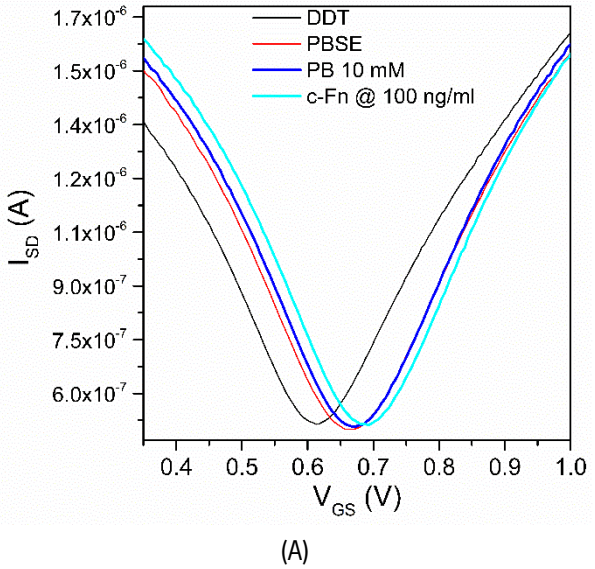

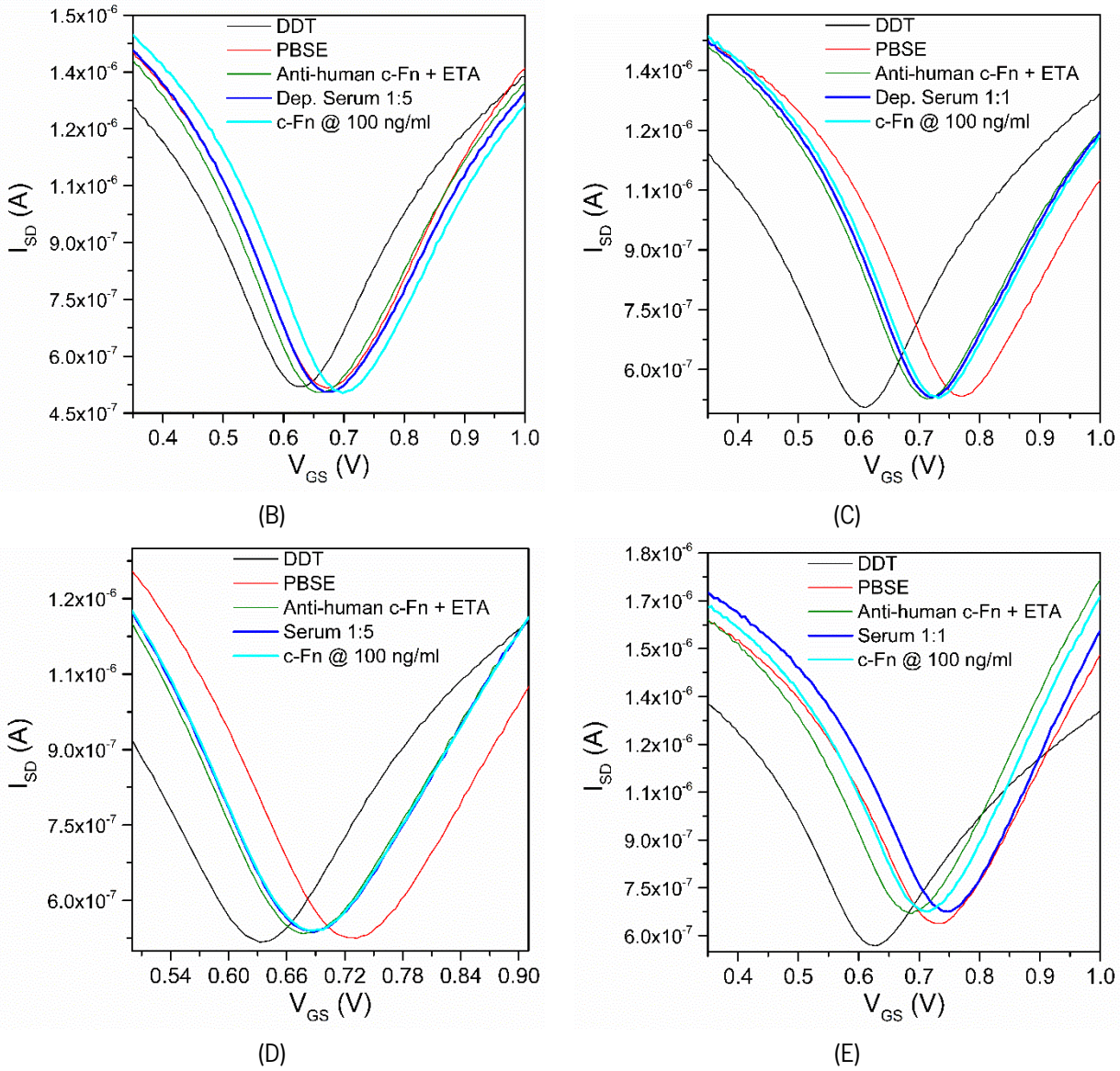

Figure Ap18. *Transfer curves after exposure of Anti-human c-Fn functionalized EG-GFETs to human serum solutions for 20 minutes and respective exposure to c-Fn at 100 ng/ml (20 minutes) prepared in the same medium. (A) PB 10 mM. (B) Diluted depleted serum (Dep. Serum 1:5). (C) Depleted serum (Dep. Serum 1:1). (D) Diluted human serum (Serum 1:5). (E) Human serum (Serum 1:1).*

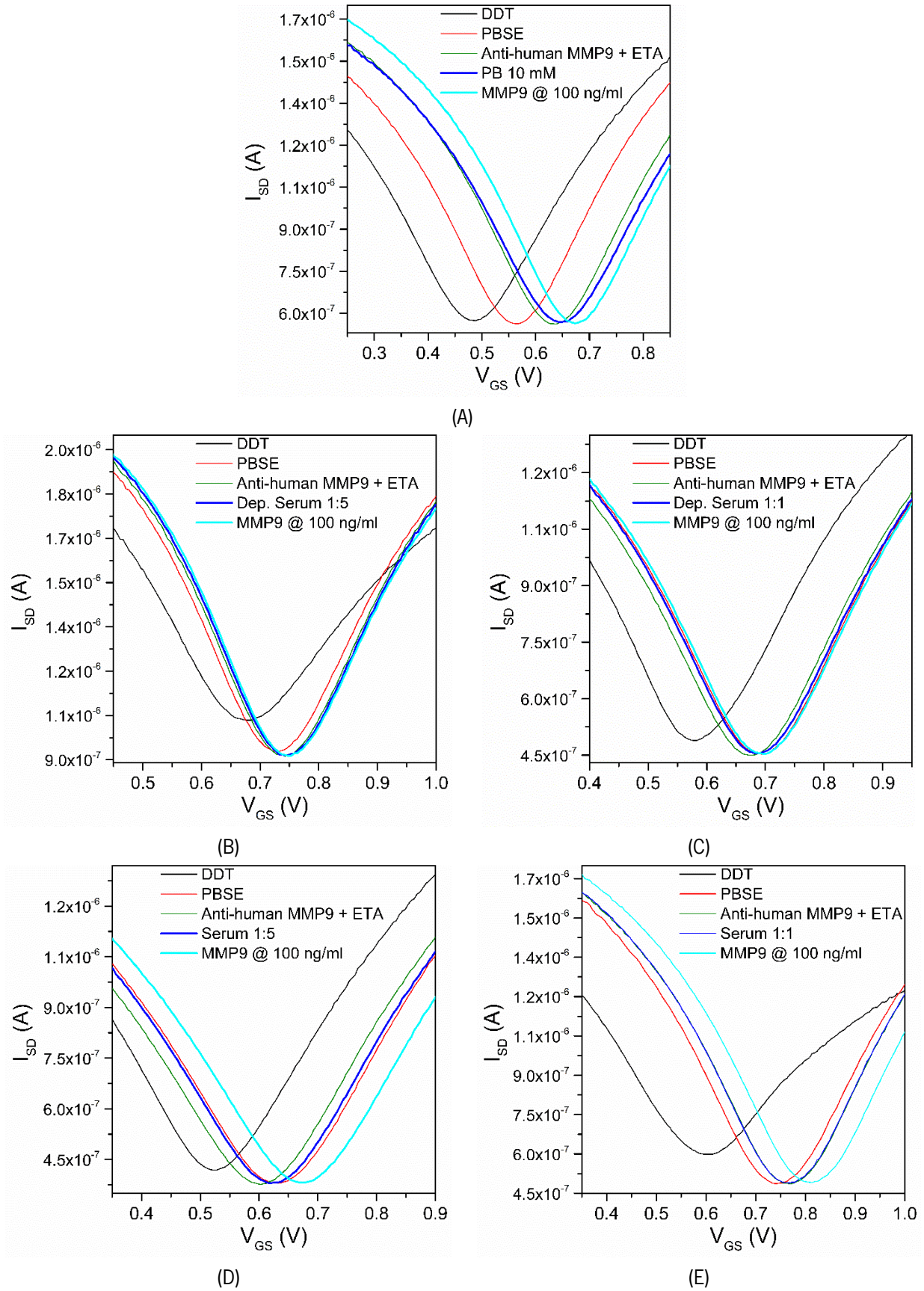

Figure Ap19. Transfer curves after exposure of Anti-human MMP9 functionalized EG-GFETs to human serum solutions for 20 minutes and respective exposure to MMP9 at 100 ng/ml (20 minutes) prepared

in the same medium. (A) PB 10 mM. B) Diluted depleted serum (Dep. Serum 1:5). (C) Depleted serum (Dep. Serum 1:1). (D) Diluted human serum (Serum 1:5). (E) Human serum (Serum 1:1).

4.2. ELISA sandwich-assays

Table Ap2. *Absorbance at 450 nm from an ELISA sandwich assay, after exposure to the specific target (c-Fn) and non-specific protein (p-Fn) in PBS. The left column of each exposure represents the standard deviation from the plate duplicates.*

	c-Fn (Stock A)		**c-Fn (stock B)**		**p-Fn**	
[Target]	Average	SD	Average	SD	Average	SD
0	0.113	0.007	0.116	0.002	0.129	0.003
0.01	0.1145	0.019	0.099	0.022	0.129	0.010
0.1	0.189	0.013	0.195	0.041	0.386	0.073
1	0.958	0.171	1.153	0.047	1.519	0.018

Table Ap3. *Absorbance at 450 nm from an ELISA sandwich assay, after exposure to the specific target (c-Fn) and non-specific protein (p-Fn) in PBS and in human serum diluted 1:5. The left column of each exposure represents the standard deviation from the plate duplicates.*

	c-Fn in PBS 1x		**p-Fn in PBS 1x**		**c-Fn in Serum 1:5**	
[Target]	Average	SD	Average	SD	Average	SD
0	0.213	0.012	0.332	0.080	2.03	0.073
0.5	0.910	0.047	1.564	0.005	2.137	0.085
3	1.594	0.042	2.08	0.066	2.088	0.098
5	1.582	0.101	2.039	0.004	2.087	0.105

4.3. ELISA direct assays

Table Ap 4. *Configuration of the 96-well plate used to access affinity of the secondary Anti-human c-Fn antibody to p-Fn and serum elements. The concentration of p-Fn in PBS 1x increases from line to line up to 1 µg/ml. Comparison with c-Fn at 1 µg/ml prepared in Carbonate/bicarbonate buffer is performed to access differences in protein immobilization due to the buffer used. Diluted human serum is used for cross-reactivity testing with the secondary Anti-human c-Fn antibody. Line G is blocked with BSA 3% before exposure to buffer and human serum to access the quality of the blocking step (secondary Anti-human c-Fn antibody used at 2 µg /ml in this line). The red values in columns 1 to 6 represent the concentration of secondary Anti-human c-Fn antibody in µg/ml.*

Plate 1	**HRP**	1:20000											
		Ab-biot c-Fn (µg/ml)											
[p-Fn] µg/mL		**1** **0**	**2** **0**	**3** **2**	**4** **2**	**5** **5**	**6** **5**	**7**	**8**	**9**	**10**	**11**	**12**
0	**A**												
0.01	**B**												
0.1	**C**												
1	**D**												

1	**E**							(In carbonate buffer)					
Serum 1:5	**F**												
BSA 3%	**G**	PBS	PBS	Serum 1:5	Serum 1:5	Serum 1:1	Serum 1:1	Ab-biot (2 µg/ml)					
	H												

Table Ap5. *Absorbance at 450 nm from an ELISA direct assay, after immobilization of p-Fn and diluted human serum and exposure to increasing concentrations of Anti-human Fibronectin Biotin antibodies (Ab-biot c-Fn). The left column of each exposure represents the standard deviation from the plate duplicates.*

	Ab-biot 0 µg/ml		**Ab-biot 2 µg/ml**		**Ab-biot 5 µg/ml**	
[p-Fn] µg/ml	Average	SD	Average	SD	Average	SD
0	0.061	0.001	0.067	0.005	0.079	0.003
0.01	0.072	0.015	0.102	0.003	0.155	0.010
0.1	0.069	0.003	0.284	0.020	0.575	0.066
1	0.070	0.001	1.497	0.021	2.419	0.042
1 (C/biC)	0.084	0.006	1.906	0.044	2.853	0.025
Serum 1:5	0.061	0.001	0.395	0.002	0.993	0.020
BSA + Serum	0.062	0.007	0.193	0.008	0.151	0.018

Table Ap 6. *Configuration of the 96-well plate used to access the preferential affinity of the secondary Anti-human c-Fn antibody to c-Fn or p-Fn. The concentration of p-Fn in PBS 1x increases from line to line up to 1 µg/ml. The concentration of c-Fn in PBS 1x increases from column to column up to 1 µg/ml (red values). Both targets are immobilized in duplicates, creating quadruplicates for each concentration mixture.*

Plate 2	**HRP**	1:20000											
		Ab-biot c-Fn (2 µg/mL)											
[p-Fn] µg/mL	[c-Fn] µg/ml	**1** **0**	**2** **0**	**3** **0.005**	**4** **0.005**	**5** **0.05**	**6** **0.05**	**7** **0.5**	**8** **0.5**	**9**	**10**	**11**	**12**
0	**A**												
0	**B**												
0.005	**C**												
0.005	**D**												
0.05	**E**												
0.05	**F**												
0.5	**G**												
0.5	**H**												

Table Ap7. *Absorbance at 450 nm from an ELISA direct assay, after immobilization of p-Fn and c-Fn mixtures and exposure to 2 µg/ml of Anti-human Fibronectin Biotin antibodies (Ab-biot c-Fn). The left column of each exposure represents the standard deviation from the plate duplicates.*

[c-Fn] (µg/ml)	**0**		**0.005**		**0.05**		**0.5**	
[p-Fn] (µg/ml)	Average	SD	Average	SD	Average	SD	Average	SD

0	0.085	0.006	0.086	0.005	0.153	0.014	0.658	0.030
0.005	0.091	0.009	0.103	0.0045	0.167	0.015	0.679	0.040
0.05	0.186	0.009	0.206	0.009	0.260	0.018	0.745	0.067
0.5	1.678	0.090	1.718	0.067	1.762	0.034	1.758	0.086

5. Appendix V – Future Work (preliminary data)

5.1. Surfactant effect on EG-GFETs

5.1.1. Methodology

Functionalization of the graphene channels of EG-GFETs was performed as reported by [42]. Shortly, the gold gate electrode was passivated with 1-Dodecanethiol (DDT, Sigma-Aldrich) at 2 mM in ethanol, by immersion, overnight at room temperature. A heterobifunctional pyrene linker, 1-Pyrenebutanoic acid succinimidyl ester (PBSE, Sigma-Aldrich), 10mM in DMF, was deposited as a 20 µl drop and allowed to interact with the graphene surface for 2 h under a humid atmosphere at room temperature (RT). Anti-human MMP9 antibodies (Immunostep) were prepared at 250 µg/ml concentration in PB 10 mM and spotted (5 µl) onto the pyrene-modified surfaces for overnight incubation at 4 ºC under a humid atmosphere. Prevention of nonspecific binding was done by passivating free PBSE molecules with ethanolamine (ETA, Sigma-Aldrich) at 100 mM concentration for 1h at RT, under a humid atmosphere. Purified Matrix Metallopeptidase 9 (MMP9, Immunostep) was prepared for detection on the functionalized EG-GFETs, in Phosphate buffer with 0.05 % of Tween® 20. Incubation with the target solution was done for 1 h, in a wet chamber, at room temperature.

5.1.2. Assessment of Tween® 20 effect on EG-GFETs

Using functionalized devices from Wafer 3 (Appendix I) for specific detection of MMP9, resulted in negative shifts of V_{CNP}, contrary to expected for this protein [42] (Figure Ap20A). It was also observed that the blank sample (no MMP9 present) resulted an equivalent negative shift of V_{CNP} indicating that the observed effect could be from the medium itself instead of the biomarker. To confirm this hypothesis, EG-GFETs functionalized for MMP9 detection were incubated with PB 10 mM containing different percentages of the surfactant used in the preparation of MMP9 (0 %, 0.02 % and 0.05%). Figure Ap20B shows the V_{CNP} shifts obtained after exposure to the PB-Tw20 solutions. The plot of Figure Ap20B clearly shows that without Tween® 20 in solution, the V_{CNP} shifts positively, which fits the later observations in more recent EG-GFETs, associated with stabilization of the surface/antibodies after the ethanolamine step (in water, less stable for antibodies). However, increasing the amount of Tween® 20 in solution seems to shift V_{CNP} negatively, with the shift increasing with Tween® 20 concentration. In fact, the shift obtained in the samples exposed to PB-Tw20 at 0.05% are comparable to those obtained in Figure Ap20A, reinforcing the idea that the shifts from the first plot were not due to MMP9, but due to interactions of Tween® 20 at the graphene surface. These results led to the removal of Tween® 20 from the medium for protein dilution (use only PB 10 mM).

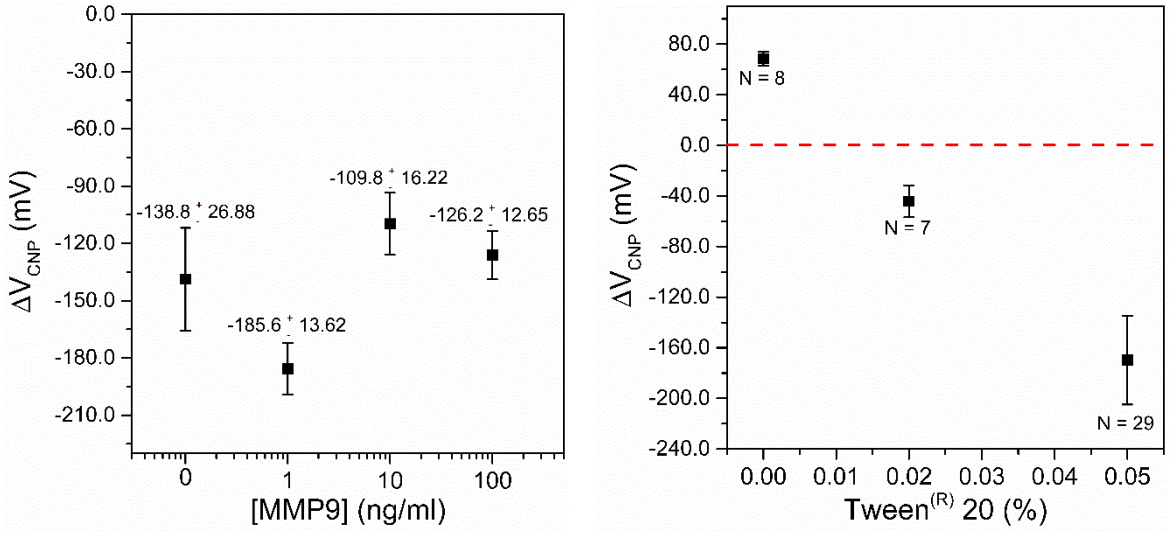

Figure Ap20. *Shift of V_{CNP} in functionalized EG-GFETs after exposure to MMP9 prepared in PB-Tw20 0.05 % (A), and exposure to PB-Tw20 with varying percentage of surfactant (B).*

5.2. MNPs for sample pre-recognition

Preliminary tests were performed using Streptavidin-coated magnetic nanoparticles (MNPs) to access the possibility of using this system to control target capture, and with that adjust the dynamic range of the studied EG-GFETs (Chapters V and VI), as proposed in Figure Ap21. The idea would be to shift the saturation range (10-100 ng/ml) to become the detection limit, and allow detection in the µg/ml range.

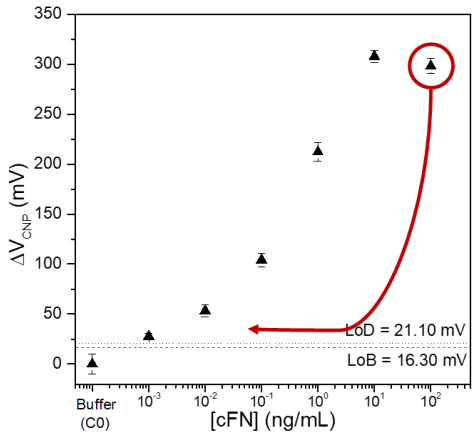

Figure Ap 21. Dynamic range adjustment principle.

5.2.1. Methodology

Functionalization of the graphene channels of EG-GFETs was performed as reported by [42]. Shortly, the gold gate electrode was passivated with 1-Dodecanethiol (DDT, Sigma-Aldrich) at 2 mM in ethanol, by immersion, overnight at room temperature. A heterobifunctional pyrene linker, 1-Pyrenebutanoic acid succinimidyl ester (PBSE, Sigma-Aldrich), 10mM in DMF, was deposited as a 20 µl drop and allowed to interact with the graphene surface for 2 h under a humid atmosphere at room temperature (RT). Purified monoclonal anti-human Fibronectin antibodies (Immunostep) were prepared at 250 µg/ml concentration in PB 10 mM and spotted (5 µl) onto the pyrene-modified surfaces for overnight incubation at 4 ºC under

a humid atmosphere. Prevention of nonspecific binding was done by passivating free PBSE molecules with ethanolamine (ETA, Sigma-Aldrich) at 100 mM concentration for 1h at RT, under a humid atmosphere.

Streptavidin-coated magnetic nanoparticles (MNPs, 250 nm, $4.9x10^{11}$ particles.ml^{-1}, Nanomag-D, Micromod), 250 nm wide, were prepared for exposure to functionalized EG-GFETs as follows:

Bare MNPs (2 µL) were diluted in PB-Tween20 0.05% 100 mM (500 µL), for washing and the eppendorf was placed in the magnetic concentrator. After 2 minutes the solution was discarded. The MNPs were re-suspended in PB 10 mM for final dilutions of 1:8, 1:6, 1:4 and 1:1. Dilutions 1:4 and 1:1 were used without functionalization.

For specific capture of c-Fn the MNPs were incubated with Anti-human Fibronectin Biotin antibodies (Immunostep) prepared at 50 µg/ml, for 1 h at room temperature. Passivation of streptavidin free-sites was performed by incubating the antibody-functionalized MNPs with BSA at 50 mg/ml for 40 minutes at room temperature. Finally, specific capture was performed by incubation of the functionalized particles with c-Fn at 100 ng/ml for 1 h at room temperature. After capture the EG-GFETs were exposed to the MNPs with c-Fn.

5.1.2. Results

Initial assessment of the MNPs effect was performed with passivated graphene channels (PBSE + ethanolamine) and non-functionalized MNPs. Exposure to MNPs led a negative shift of V_{CNP} (Figure Ap22A) that increased with MNPs concentration in the droplet. The negative shifts could be indicating reactions at the gate electrode, since the channels were also passivated, which was confirmed by optical microscopy. Figure Ap23 shows optical images of the gate electrode at 5x magnification before (Figure Ap23A) and after exposure to non-functionalized MNPs (Figure Ap23B,C), clearly indicating accumulation of MNPs at the gate electrode surface.

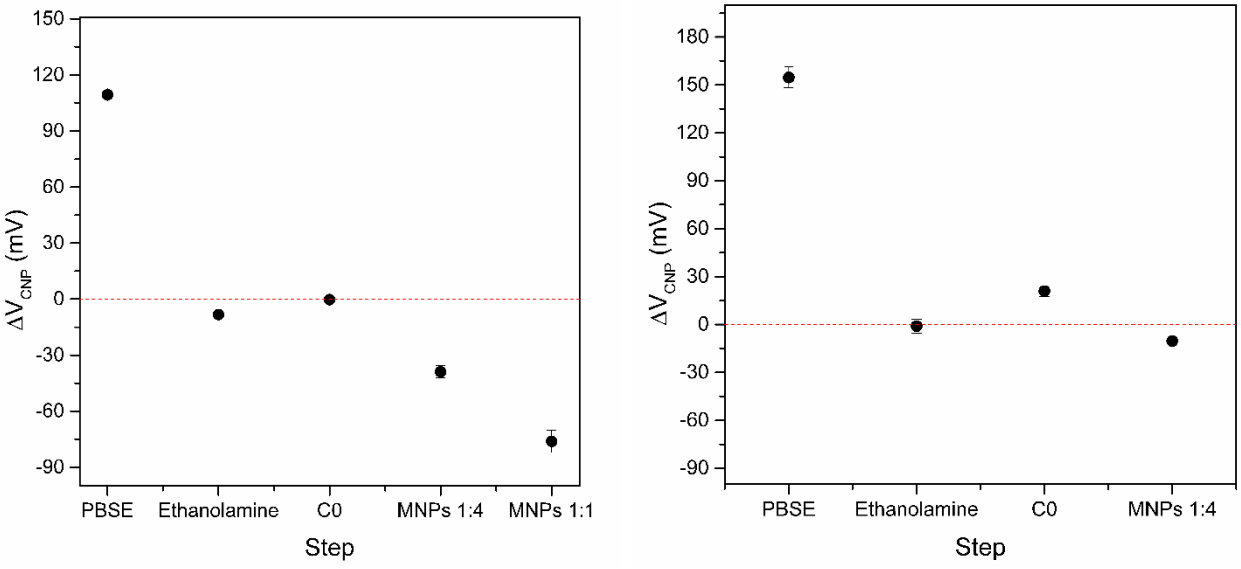

Figure Ap22. *V_{CNP} shift of EG-GFETs after each step of functionalization of the graphene channels and exposure to non-functionalized MNPs (A) and functionalized MNPs (B).*

It was proposed that the exposure of free streptavidin of the MNPs was promoting the random binding of the particles in the EG-GFETs. To counteract that effect, EG-GFETs with the same functionalization scheme were exposed to functionalized MNPs (antibodies + BSA), since the MNPs are always to be used in the functionalized state. Exposure to the functionalized MNPs reduced about 4 times the negative shift associated with MNPs interaction at the gate electrode (Figure Ap22B), which was also confirmed by optical microscopy (Figure Ap23D) with a great reduction of MNPs accumulation at the gate surface. This result indicates, there is the possibility to use the functionalized MNPs on EG-GFETs with reduced interference in the target signal.

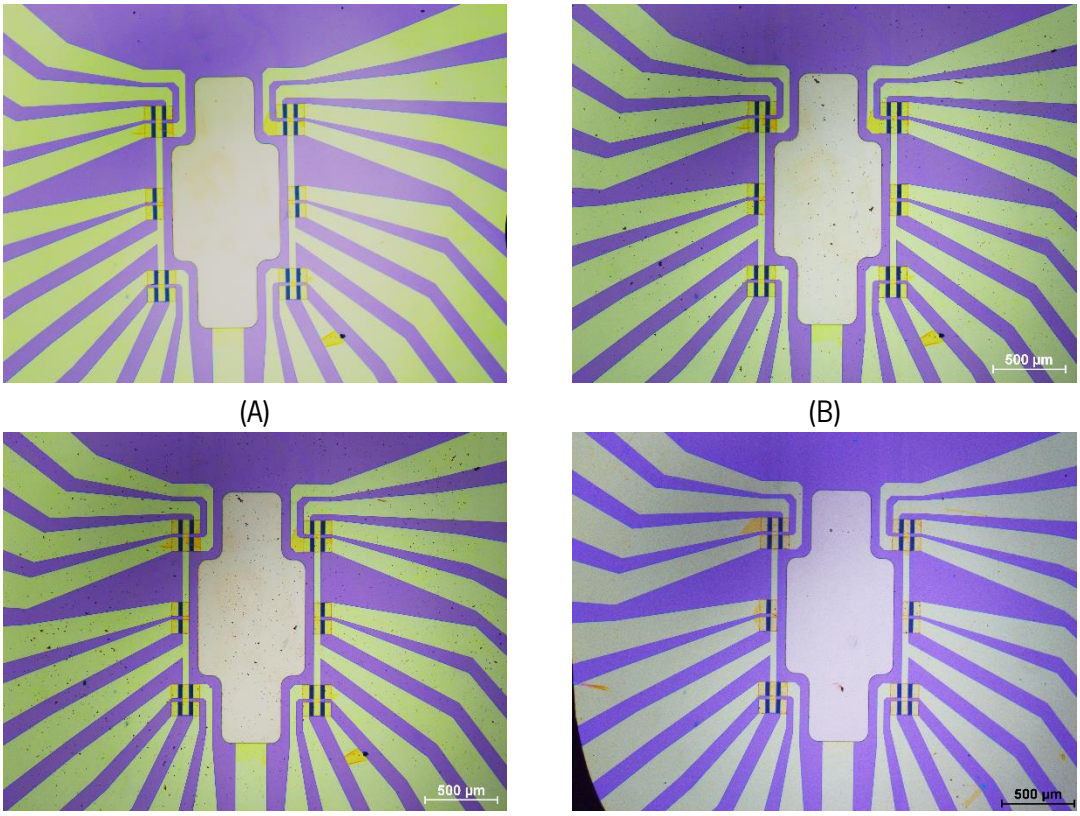

Figure Ap23. *Optical microscope photographs of the gate electrode of EG-GFETs before use (A), after exposure to non-functionalized MNPs at 1:4 dilution (B) and 1:1 dilution (C), and after exposure to functionalized MNPs at 1:4 dilution (D).*

To further access the potential of the particles for the dynamic range adjustment studies, functionalized MNPs prepared at 1:8, 1:6 and 1:4 dilutions were exposed to c-Fn at 100 ng/ml to evaluate the ratios of particles that could be more suitable for our application. After target capture, The MNPs were placed on the anti-human fibronectin functionalized EG-GFETs for specific recognition of c-Fn. The shifts of V_{CNP}, shown in Figure Ap24, show that pre-recognition with functionalized MNPs can indeed reduce the response when compared with a control of direct detection of c-FN (first data point). The results showed that detection was possible with 1:4 dilution of MNPs with a V_{CNP} of about half of that obtained in the

control, however detection was not achieved with 1:6 and 1:8 dilutions. Although the response reduction seems promising, the results with 1:6 and 1:8 dilutions were not consistent indicating further work must be done to optimize the MNPs ratios for the dynamic range adjustment.

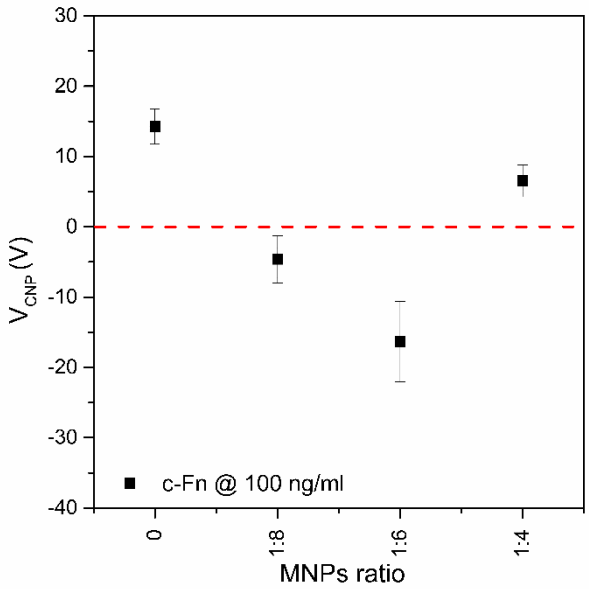

Figure Ap24. *Shift of V_{CNP} of functionalized EG-GFETs after direct exposure to c-Fn at 100 ng/ml (first data point) and exposure to different ratios of functionalized MNPs after pre-recognition of c-Fn at 100 ng/ml.*